DOCTORAL THESIS

Beauty to Open Charm Measurements at LHCb and Other Flavourful Friends

Author:
Jonathan E DAVIES

Supervisor:
Dr. Conor FITZPATRICK
Dr. Stefan SCHACHT

A thesis submitted to the University of Manchester
for the degree of Doctor of Philosophy

in the

School of Natural Sciences
Faculty of Science and Engineering

2024

Contents

List of Figures

List of Tables

List of Abbreviations

SM	**S**tandard **M**odel
BSM	**B**eyond **S**tandard **M**odel
CPV	**C**harge **P**arity **V**iolation
LHC	**L**arge **H**adron **C**ollider
LHCb	**L**arge **H**adron **C**ollider **b**eauty
CERN	**C**onseil **E**uropéen de **R**echerche **N**ucléaire (European Organisation for Nuclear Research)
BAU	**B**aryon **A**symmetry of the **U**niverse
CMB	**C**osmic **M**icrowave **B**ackground
CG	**C**lebsch-**G**ordan
QFT	**Q**uantum **F**ield **T**heory
QED	**Q**uantum **E**lectro**D**ynamics
QCD	**Q**uantum **C**hromo**D**ynamics
EW	**E**lectro**W**eak
MC	**M**onte **C**arlo

THE UNIVERSITY OF MANCHESTER

Abstract

Faculty of Science and Engineering
School of Natural Sciences

Doctor of Philosophy

Beauty to Open Charm Measurements at LHCb and Other Flavourful Friends

by Jonathan E DAVIES

The Standard Model (SM) of particle physics, which seeks to provide a fundamental description of the universe's smallest constituents, is an incredibly successful theory by many metrics. There is, however, good reason to believe that it does not provide the full picture. The exact nature of such a new theory remains uncertain, and there is currently limited experimental evidence of significant deviations from the SM. Observation of such deviations is an essential prerequisite for the emergence of a new fundamental theory that provides a more consistent description of all empirical observations. This, in turn, requires high-precision measurements. LHCb is an experiment designed explicitly with the precision paradigm in mind, particularly for beauty and charm physics, and has recently undergone extensive upgrades. For measurements taken by this new detector to be relied upon, its early data must first be validated, and this thesis details efforts towards this goal, particularly through production cross-sections of beauty hadrons. Such Early Measurements utilise "Beauty to Open Charm" channels, which have recently shown hints of a theory-experiment discrepancy, and both experimental and theoretical analyses seeking to clarify this situation are also explained here. Firstly, I outline an LHCb analysis probing for the influence of New Physics in $\bar{B}^0_s \to D^+_s \pi^-$ through measurements of its CP asymmetry, an observable expected to be sensitive to such effects. A symmetry-based analysis of the theoretical side of this puzzle comes later, where it is concluded that excess symmetry breaking cannot be attributed as the source of the observed tensions. This was limited somewhat by a lack of experimental data, but the data situation is more bountiful for $B \to DD'$, which also benefits from access to direct CP violation. A more in-depth analysis using a similar method was therefore also applied to this family of decays, and the details of this can also be found here. The predictions from this analysis were found to be consistent with the experimental data; however, they had improved precision, and predictions were possible for observables yet to be determined experimentally. Evidence for breaking of the traditional assumption of isospin symmetry in production was also shown at a significance of 2.5σ.

THE UNIVERSITY OF MANCHESTER

Lay Abstract

Faculty of Science and Engineering
School of Natural Sciences

Doctor of Philosophy

Beauty to Open Charm Measurements at LHCb and Other Flavourful Friends

by Jonathan E DAVIES

Why do we exist? I mean this not as a philosophical question but a physical one. A better phrasing might be "how is it that we, as entities made of matter (stuff, if you will), happily exist, billions of years after the universe began?". Not so catchy and possibly still not particularly clear. Almost everything we see is made of matter- people, cats, trees, stars, etc. To get a bit more technical, they're all made of atoms. This doesn't immediately sound extraordinary, but there is another type of substance that things can be made of- antimatter. Many are surprised to hear that this is not only real but also relatively everyday. In fact, a banana produces $\sim$ 1 million antimatter particles a day due to being *slightly* radioactive. Antimatter is matter's opposite- put an electron next to an anti-electron and the two will cancel each other out and disappear- and the two are identical (or exactly opposite) in many respects. Here comes the punchline. If all of this is true then we would expect that at, the birth of the universe, matter and anti-matter were created in equal amounts. Every particle would then cancel out its antimatter partner- no atoms, no world, no us! Our existence is all the evidence we need to convince us that not all particles are created equal- nature clearly has a bit of a preference for the stuff we're made of, which we call "matter". Our theory does allow for such imbalances but there's just one problem though; it's nowhere near enough to explain how we all got here! So maybe our theory is wrong. Over the last 50 years, our theory has made incredibly precise and accurate predictions, so we can't just bin it, but it isn't a perfect picture e.g. astronomers see that the night sky is filled with a substance (dark matter) that just doesn't fit into our theory. The best thing seems to be to measure this matter/anti-matter imbalance and look for something unexpected. This would mean recreating the state of the universe just after its birth, and require an enormous amount of energy. Thankfully, there's a machine that is able to do just this- the Large Hadron Collider (translation: a huge underground ring in which we smash together millions of protons travelling near light-speed). Running this thing is a monumental task, requiring the effort of thousands of people across the world. For a few years I have been one of them and what follows is an account of the small part I have played in that time.

Declaration of Authorship

I, Jonathan E DAVIES, declare that this thesis titled, “Beauty to Open Charm Measurements at LHCb and Other Flavourful Friends” and the work presented in it are my own. I confirm that:

- This work was done wholly or mainly while in candidature for a research degree at this University.
- Where any part of this thesis has previously been submitted for a degree or any other qualification at this University or any other institution, this has been clearly stated.
- Where I have consulted the published work of others, this is always clearly attributed.
- Where I have quoted from the work of others, the source is always given. With the exception of such quotations, this thesis is entirely my own work.
- I have acknowledged all main sources of help.
- Where the thesis is based on work done by myself jointly with others, I have made clear exactly what was done by others and what I have contributed myself.

Copyright Statement

"I wish it need not have happened in my time," said Frodo. "So do I," said Gandalf, "and so do all who live to see such times. But that is not for them to decide. All we have to decide is what to do with the time that is given us."

J.R.R. Tolkien, *The Fellowship of the Ring*

Acknowledgements

I'd like to acknowledge my supervisors Dr. Conor Fitzpatrick and Dr. Stefan Schacht for their abundance of patience with me and for giving me the support I needed to make this process as painless as possible. Thanks also to Dr Nicole Skidmore for much invaluable assistance throughout my PhD; on the technicalities of LHCb software when my code kept crashing, providing much practical guidance in analysis activities, and aiding me in my preparation for interviews. I must acknowledge the support of European Research Council Starting grant 852642 'Beauty2Charm' for making this process financially possible. Significant acknowledgement must also be given to my family, without whose support I may have given up on this a while ago. I am thankful for those along the way who have gone some way to alleviating the emotional challenge that this process has proved to be, getting me out of the house and helping me to feel slightly less alone. Credit must also go to The Wolf and Owl podcast, a mid-week boost that is a highlight of the day amongst a busy work schedule. Thanks for the laughs.

Icons used for chapter headings taken from Freepik.com

Dedicated to all those who feel they're a bit different…

Preface

I was born in Shrewsbury, birthplace of notable scientist Charles Darwin, and grew up nearby in the countryside of North Shropshire. A curious mind and envy of on-screen mad professors naturally led me towards the sciences. I remember the hype surrounding the switch-on of the LHC around my transition from village primary school to state secondary and was inspired to consider a career in particle physics aged 14 following the discovery of the Higgs boson in 2012. As a determined individual, my ambition did not waver over the next 10 years, which culminated in me finally visiting CERN. My journey to the completion of this document has been a somewhat surreal experience, and serves as a example of the possibility of big dreams. The journey has, though, not been without challenge, with continuing long-standing mental health issues being brought to the fore.

The thesis is structured as follows:

- **Chapter 1** introduces the reader to the state-of-the-art in high energy physics, providing the context for and motivating the analyses later detailed.
- **Chapter 2** provides a theoretical background to the Standard Model of particle physics, providing motivation for the analyses that follow, and a starting point for theoretical discussions.
- **Chapter 3** describes the operations of the LHC and LHCb Experiment (in both Runs 2 and 3), as well as providing some historical context to flavour physics measurements.
- **Chapter 4** outlines my contributions to the a^s_{fs} CP violation measurement of $B_s \to D_s\pi$, which was also detailed in Ref. [1].
- **Chapter 5** explores the work performed on preparing to make Early Measurements of beauty hadron production cross-sections with through decays via open-charm to hadronic final states, part of which was included as part of Ref. [2].
- **Chapter 6** describes my phenomenological analysis of $B \to DD'$ [3], using $\mathrm{SU}(3)_F$ symmetry to predict CP asymmetries and test the Standard Model.
- **Chapter 7** describes my work on the phenomenology of $B \to Dh$ decays [4], investigating the current tension between theory and experiment.
- **Chapter 8** concludes with a summary of the outcomes and potential future directions of the work described in the preceding chapters.

Prior to my PhD, I had participated in a few research projects over the course of my undergraduate degree. In summer 2018, I worked with Imperial College's Data Science Institute and Prof. Roberto Trotta in the Astrophysics department to create a visualisation of the observable universe. The following summer, as part of a research exchange, I worked at MIT's LIGOLab on Bayesian inference for Gravitational Wave Power Spectral Densities, resulting in a publication [5]. Finally, I completed a MSci Project using Run 2 CMS data to put constraints on dimension-6 operators that could source New Physics on top of the Standard Model using an Effective Field Theory formalism. In addition, during the PhD I took part in several roles and initiatives:

- I was an organiser of the 2022 edition of the LHCb Starterkit, providing first year PhD students with tutorials in the main software packages of the collaboration.
- I was also an organiser of the monthly LHCb UK Student seminars
- I attained the Associate Fellowship of Advance HE, for my participation in teaching in Higher Education. I also acted as an assessor for the applications of other candidates.
- I acted as a liaison between the B2OC, EMTF and RTA working groups
- I acted as an RTA software shifter
- Data Manager Shifts in the LHCb Control Room
- Co-author on a HSF paper on onboarding and training at CERN experiments [6]
- Wherever possible, I've got involved with outreach opportunities:
  - I acted as a co-coordinator of the LHCb collaboration's involvement in the "I'm a Scientist, Get Me Out of Here!" initiative, which hosts regular live chats with secondary school students.
  - Having participated in the Pint of Science festival as a speaker in 2021 and 2022 in Manchester, I helped to organise CERN-supported events in Geneva and St Genis in 2023.
  - I was a member of the committee for producing LHCb merchandise.
  - I also worked as a tour guide at many CERN visit points, including underground, where I supported both public visits, school visits and protocol visits.

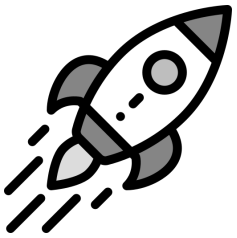

1 Introduction

"Opportunity is missed by most people because it is dressed in overalls and looks like work."

- Thomas Edison

Plato once said, "God ever geometrises" [7]. Indeed, the progress of science over many centuries marks the attempt to find simplicity in a complex world. The language of mathematics evolved and created a world full of patterns and symmetry, and elegance or beauty is often a motivation for mathematicians. Paul Dirac even went as far as to suggest that the beauty of a theory was strongly linked to its validity, and said "The research worker, in his efforts to express the fundamental laws of nature in mathematical form, should strive mainly for mathematical beauty" [7]. As John Keats said, "Beauty is truth", and anecdotally this poem may have been the inspiration behind the names of the "truth" and "beauty" quarks, two types of particle that make up matter at the fundamental level[1]. In the conventional sense of beauty, it is often said to rely on symmetry; symmetrical faces are generally perceived as more "attractive" [8]. Naturally then, in the search for elegant models, symmetries crop up a great deal in physics theories, and interesting consequences arise when these are broken. This point seems especially pertinent in the context of the ongoing struggle for equality and balance in the modern world. The beauty quark, as the heaviest type of elementary particle that can combine with others to form longer-lived and more-easily-measurable composite particles, has been the primary focus of numerous experiments, with appropriate names like BELLE and LHCb[2]. Theoretically, these particles are also interesting from the perspective that, as will be explored in the later chapters, their considerable masses permit approximate symmetries to emerge, dramatically improving the feasibility of certain types of calculation. It is the latter of these experiments (if the title did not give it away) that is the main theme of this thesis, which sits at an interesting convergence of "beauty" and "symmetry" in multiple senses of these words.

[1] Therefore, this statement is somewhat confusing in a particle physics context.

[2] An early proposal to name LHCb "BEAST" (Beauty Experiment At Small Theta) was unfortunately shot down, to the dismay of many of its physicists who wanted to sound cool.

Experiments like LHCb work at the cutting edge and, just as mobile phone companies constantly bring out new models, every few years it is necessary to upgrade the detector to implement the latest advances in technology, providing a more precise instrument with which to measure fundamental physics. After several years of excellent work with the original detector in the first two data runs of the *Large Hadron Collider* (LHC), the period of shutdown from late 2018 presented an opportunity for the collaboration to bring out its version 2.0. The changes that were made were considerable, with new flashy features including the ability to filter experimental data with software alone, at a rate higher than ever. As the experiment prepared for the start of the LHC's Run 3 in 2022, the new LHCb detector significantly differed from the previous one. Much work was therefore needed to test this new machine and understand its quirks, and much of that year was spent commissioning the new detector from the perspective of subdetector performance.

While the hardware and software may have changed in the upgrade, it is important to note that physics has not, and all the subdetectors and the reconstruction chain can be thoroughly checked at once through reference measurements of quantities that are known well. Ideally, these measurements can be performed with a small amount of data, and are given the simple but sufficiently-descriptive name of *Early Measurements*. In 2020, I started, and throughout my PhD continued to work on, such an Early Measurement analysis, though factors beyond our control (COVID pandemic, delays to subdetector installation, VELO vacuum incident) meant that less data was collected than would be needed to produce a competitive measurement. These measurements concern the probabilities that certain composite particles containing a b quark, called B hadrons, get produced in proton collisions. Though these quantities have been measured previously, their determination will mark a first for the experiment in using hadronic (quark-filled) final states to do this, and are studied through the very versatile *Beauty to Open Charm (B2OC)* decays, *charm* being another type of quark and *open* charm referring to hadrons containing just one such quark. Hadrons containing both a c quark and its antimatter equivalent are described as *hidden* charm[3]. Preliminary studies were made using the available 2023 data, with much time spent in the run-up to this preparing with simulated data, and it is expected that data taken during 2024 will enable the measurement to be concluded.

One of the specialities of the LHCb experiment is performing measurements of *CP violation* (CPV), imbalances between matter and antimatter interaction rates necessary to explain the dominance of the former over the latter in the universe. Such measurements are also excellent probes for the presence of new physics, and I participated in an analysis to measure CP violation in $\bar{B}^0_s \to D^+_s \pi^-$ with this goal in mind. This, and other similar $B \to Dh$ decay modes, have recently shown significant tensions with the theoretical predictions of QCD factorisation (QCDF). I also worked to understand the theoretical side of this tension using a different approach to QCDF, based on simple particle symmetry assumptions. This symmetry-based approach is a powerful tool and, in addition to

[3]Such terminology can also be applied to describe particles containing b quarks, permitting in this case the legitimate (though rarely seen) usage of *open bottom*. The converse of *hidden beauty* has much more of a ring to it.

$B \to Dh$, I applied it also to $B \to DD'$ channels in an update of Ref. [9], using branching ratio and CP asymmetry measurements. This approach allows the derivation of approximate predicted relations between B2OC decays, which can be tested by measurements. Significant breaking of these relations could indicate the presence of new physics. Updates to the experimental inputs since the publication of the original $B \to DD'$ paper provides more precise knowledge of hadronic matrix elements, and hence make for better theoretical predictions.

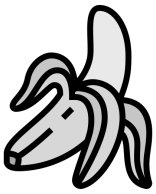

2 Theoretical Background

"The greatest danger for most of us is not that our aim is too high and we miss it, but that it is too low and we reach it."

- Michelangelo

2.1 The Standard Model

2.1.1 Elementary Particles

The Standard Model of Particle Physics, commonly referred to as the *Standard Model* or just the *SM*, was developed in the 1960s and 1970s in order to make some sense of the variety of subatomic phenomena that had been observed by that time [10]. It remains the best fundamental theory of physics on these small scales, and postulates the existence of six types (or *flavours*) of elementary particle called *quarks*[1], namely up, down, strange, charm, bottom (beauty), and top (truth), which make up composite particles like protons and neutrons that, in turn, make up atoms [13]. The common shorthand of $\{u, d, s, c, b, t\}$ to abbreviate these names will be used throughout. The masses of these particles cover several orders of magnitude, a theoretical puzzle that remains unexplained.

Just as protons have an electric charge, designated by the *elementary charge*,

$$e \approx 1.6 \times 10^{-19}\,\mathrm{C}, \tag{2.1}$$

so too do quarks, which can be *up-type* (u, c, t) with a charge of $+\frac{2}{3}e$, or *down-type* (d, s, b) with a charge of $-\frac{1}{3}e$. To be more precise, quarks are charged under the *electromagnetic* interaction, the fundamental force of nature responsible for explaining both electric and magnetic phenomena. As shown in Figure 2.1, such interactions between charged particles can be explained by the exchange of *photons*, massless particles with an infinite

[1] A popular origin story for the origin of this term is that it came from James Joyce's Finnegan's Wake [11], though there is debate as to the correct pronunciation; rhyming with "mark", as implied by the poem, or rhyming with "stork" as the originator of the term, Murray-Gellman, intended [12].

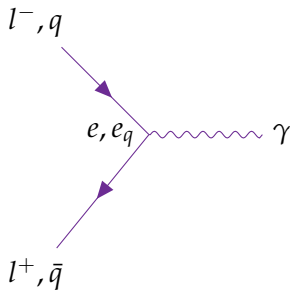

FIGURE 2.1: The electromagnetic interaction diagram. The strength of the interaction is characterised by the vertex factor; the elementary charge e for leptons or the quark charge, e_q, for quarks.

range, which are manifestations of electromagnetic fields, or "light" as they are referred to in everyday life. Electrons, with a charge of $-e$ and mass of 511 keV, alongside protons and neutrons, complete the fundamental picture of atoms[2]. In the SM, they are part of the *lepton* class of particles, which also contains two heavier, equivalently-charged versions called the *muon* and the *tau*, with masses of 105.7 and 1776.8 MeV respectively [14], as well as chargeless *neutrino*[3] versions of each of these. In the SM, neutrinos are also considered to be massless, but the observation of neutrino oscillations[4] [16] showed this not to be the case. This inconsistency, along with other anomalies discussed in Section 2.2, has motivated theorists to postulate numerous extensions to the Standard Model. Quarks and leptons themselves fall into the category of *fermions* because they all possess half-integer spins, in this case equal to $+\frac{1}{2}$. These make up the particles of *matter*, as summarised in Table 2.1. There is, however, also an *antimatter* version (denoted as $\bar{q}$ for a quark q) of each of these that is treated equivalently in the SM, apart from some quantum numbers that are exactly opposite, such as electromagnetic charge. In contrast to fermions, *bosons* are particles with integer spins, which complete the SM through their mediation of fundamental interactions, and are summarised in Table 2.2. The photon, introduced above, is one such particle.

Unlike leptons, quarks are never found alone but always in bound states (*hadrons*[5]); in pairs (*mesons*), threes (*baryons* like protons and neutrons), and even fours and fives (*tetraquarks* and *pentaquarks*). The exact nature of these hadrons with more than three quarks is currently unclear; it is yet to be determined whether they are exotic bound states or simply "molecules" containing two- or three-quark bound states. The LHCb experiment is one of the world leaders in the study of these particles. This tight binding of quarks

[2]To be dimensionally correct, masses should have units of eV/c^2 (with appropriate prefix). It is typical, however, to work in "natural units" where one sets $c = 1$, which is the convention throughout this thesis. The same goes for momenta, which would otherwise have units of eV/c.

[3]The "-ino" suffix here will be familiar to Italian-speakers as a diminutive. The influence of Enrico Fermi, this raises the suggestion that the plural of neutrino should be neutrini.

[4]This discovery won the 2015 Nobel Prize for Takaaki Kajita and Arthur McDonald, exactly 20 years after Frederick Reines' win for first detecting the neutrino [15]. This award was shared with Martin L. Perl for his discovery of the tau that opened the door to the third generation.

[5]Named from the ancient Greek for "stout" or "thick", this shares its etymology with the Hadrosaur, one of my favourite dinosaurs as a child. "Baryon" has a similar origin, sharing its reference to "heaviness" with "bariatric".

	Particle	Mass (MeV)	Charge (e)	Interacts via
Quarks	u	2.2	$+\frac{2}{3}$	EM, Strong, Weak
	c	1.28×10^3		
	t	1.73×10^5		
	d	4.7	$-\frac{1}{3}$	
	s	96		
	b	4.18×10^3		
Leptons	e	0.511	-1	EM, Weak
	μ	106		
	τ	1.78×10^3		
	ν_e	$\lesssim 0.8 \times 10^{-6}$ (†)	0	Weak
	ν_μ			
	ν_τ			

TABLE 2.1: The matter content of the Standard Model. Values taken from Ref. [14] with the (u, d, s) and (c, b) masses being the $\overline{MS}$ masses at the scale $\mu = 2\,\text{GeV}$ and at the $\overline{MS}$ mass, i.e. $m = m(\mu = m)$, respectively. The t mass is extracted from event kinematics. †The neutrino masses are predicted to be zero, however experimental evidence points to them having small but non-zero masses. The value quoted here is the bound on the average neutrino mass from ^3H decay [17].

Boson	Interaction	Mass (GeV)	Range (m)
γ	Electromagnetic	0	∞
g	Strong Nuclear	0	10^{-10}
$W^\pm$	Weak Nuclear	80.369 ± 0.013	10^{-15}
Z^0	Weak Nuclear	91.188 ± 0.002	10^{-15}
$(Graviton, G)$	*(Gravity)*	*(0)*	(∞)
H	Higgs	125.20 ± 0.11	∞

TABLE 2.2: The gauge boson content of the Standard Model plus the hypothesised graviton. Values taken from Ref [14].

is due to the properties of the *strong force*, another fundamental force of nature, which is responsible for holding hadrons together. This interaction, shown in Figure 2.2, can be described in a similar way to electromagnetism by the exchange of massless particles, this time called *gluons*. In contrast to electromagnetism, the potential of this force grows with distance from the source, and gluons exhibit self-interaction. This latter property restricts the range of the interaction to the scale of the atom $\sim 10^{-10}\,\text{m}$, which is known as *confinement*.

Both quarks and leptons participate in a third fundamental force, the *weak force*, which again can be described by particle exchange, this time by *W* and *Z bosons*. Charged **W**eak bosons, with masses of 80.4 GeV and charges of $\pm e$, allow for reactions that change the type of particle (*flavour-changing*), i.e. between an up-type quark and a down-type quark, and between a charged lepton and its neutrino counterpart, as seen in Figure 2.3. Being electromagnetically neutral and having a mass of 91.1 GeV, the **Z**ero-charged boson is like a heavy version of the photon, which may also contribute to the same diagrams, as

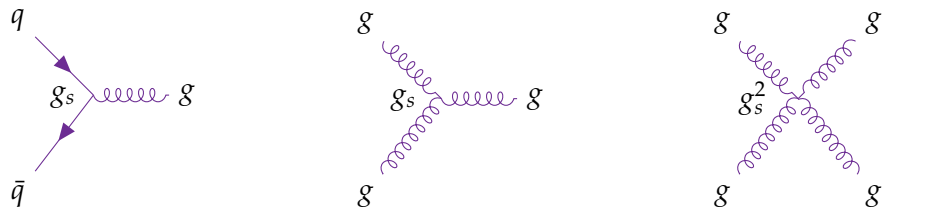

(A) Quark-gluon interaction (B) 3-gluon self-interaction (C) 4-gluon self-interaction

FIGURE 2.2: The strong interaction diagrams. The strength of the interaction is characterised by powers of the strong coupling, g_s, with higher powers corresponding to more suppressed diagrams.

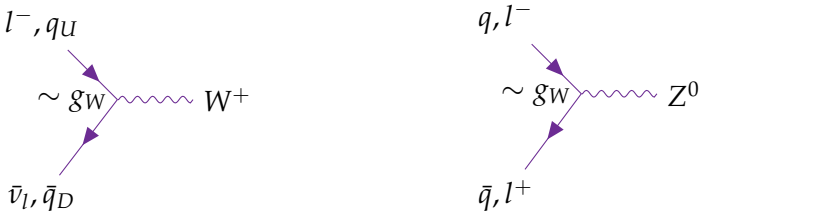

(A) Charged-current fermion interaction. (B) Neutral-current fermion interaction.

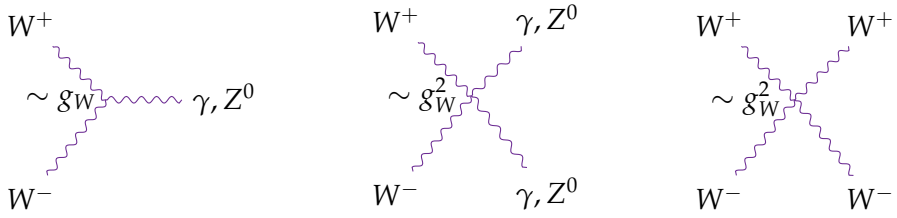

(C) Interactions between the electroweak bosons.

FIGURE 2.3: The weak interaction diagrams. Powers of the weak coupling g_W characterise the interaction strength, and diagrams with higher powers are suppressed. As will be seen, there are additional factors which affect the sizes of these contributions, such as CKM factors and the Weinberg mixing angle.

will be seen later. Considering the Yukawa potential [18],

$$V_{\text{Yukawa}}(r) = -g^2 \frac{e^{-\alpha m r}}{r}, \tag{2.2}$$

which confines the potential due to the interchange of a particle of mass m to a range $r_0 \sim \frac{1}{\alpha m}$, the considerable masses of the weak bosons mean that this interaction is only relevant within the nucleus, at ranges of $\sim 10^{-15}$ m. The weak bosons may also interact with each other.

The last of the Standard Model gauge bosons summarised in Table 2.2, is the Higgs boson, named after Peter Higgs[6], which was introduced as a mechanism by which particles can acquire mass [14], with interactions shown in Figure 2.4. Following the 2012 discovery of a Higgs boson by the ATLAS and CMS experiments with a mass of 125 GeV [20,21],

[6]To appropriately credit everyone who significantly contributed theoretically would necessitate calling it something like the ABEGHHK'tH boson (for Anderson, Brout, Englert, Guralnik, Hagen, Higgs, Kibble, and 't Hooft) [19]. Peter Higgs sadly passed away during the writing of this thesis.

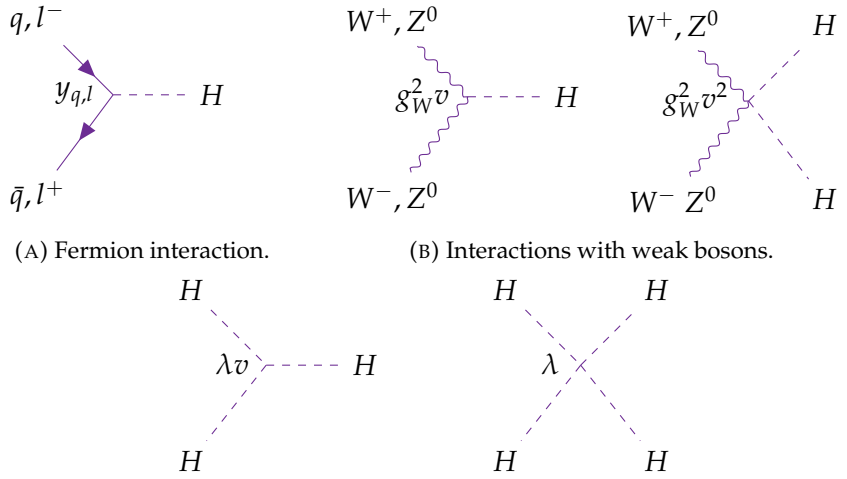

(A) Fermion interaction.

(B) Interactions with weak bosons.

(C) 3- and 4-Higgs self-interactions.

FIGURE 2.4: The Higgs boson interaction diagrams. The vertex factors characterising the strength of the interactions come from a range of sources, which will be further explained later; the Yukawa couplings, $y_{q,l}$, the weak coupling, g_W, the Higgs vacuum expectation value, v, and the Higgs self-coupling, λ.

all of the particles predicted by the SM have since been experimentally confirmed, and the theory has been incredibly successful in terms of the precision of its predictions and in its ability to explain much of the observed phenomena in particle physics [10]. An example of its extraordinary success is the fact that the measured value of the electron's anomalous magnetic dipole moment[7] agrees with its predicted value to nine significant figures, making it one of the most accurately validated quantities in physics [22, 23].

Having introduced the elementary particles, one can understand the SM on a deeper level through the concept of symmetries of nature[8]. A *gauge symmetry* view of the fundamental SM interactions will be explored in Section 2.1.3, but it makes sense to first review the mathematical foundation upon which this interpretation sits: group theory. The following section will give a brief overview of this topic, with more details to be found in Ref. [25].

2.1.2 Group Theory and Symmetries

In Mathematics, a *group* G is defined as a set of elements ($\{g_1, g_2, ...g_n\}$) and a binary operation ($\bullet$) that may be applied between two of its members to generate an element belonging to that same set

$$g_1 \bullet g_2 = g_3, \quad g_1, g_2, g_3 \in G. \tag{2.3}$$

[7] The first determination of this quantity won Polykarp Kusch the Nobel Prize in 1955 [15].
[8] An idea pioneered by Emmy Noether in Ref. [24].

There must also be an identity element $e \in G$ such that

$$g \bullet e = e \bullet g = g \quad \forall g \in G, \tag{2.4}$$

and every group element $g \in G$ has an inverse $g^{-1} \in G$ such that

$$g \bullet g^{-1} = g^{-1} \bullet g = e. \tag{2.5}$$

Finally, the operation $\bullet$ must be associative

$$g_1 \bullet (g_2 \bullet g_3) = (g_1 \bullet g_2) \bullet g_3, \quad \forall g_1, g_2, g_3 \in G. \tag{2.6}$$

Groups are not necessarily commutative, i.e. satisfying

$$g_1 \bullet g_2 = g_2 \bullet g_1, \quad g_1, g_2 \in G, \tag{2.7}$$

but those with this property are referred to as *Abelian* groups. A group may have a finite or infinite number of elements, and it is this latter case, *Lie groups*, that is most relevant in particle physics.

Elements of Lie groups can be "labelled" according to some parameter ϕ (which may have multiple components ϕ_i), so

$$g = G(\phi), \quad g \in G, \tag{2.8}$$

with the identity element e typically being defined as equal to $G(0)$. For a group G of quantum operators (denoted by "hats") to be considered to be continuous, an infinitesimal change, $\delta\phi$, from the identity operator, $\hat{\mathbb{1}}$, must satisfy

$$G(\delta\phi) = \hat{G}(\delta\phi) = e^{i\hat{H}(\delta\phi)} = 1 + i\hat{H}(\delta\phi) = \hat{\mathbb{1}} + i\sum_{j=1}^{n^2} \delta\phi_j \hat{\lambda}_j, \tag{2.9}$$

where $\hat{\lambda}_j$ are the *group generators* [26]. A *representation* of a group is a way of writing the group elements as square matrices of the same size. More formally, it is a vector space of $\hat{\lambda}_i$ with an operation called the *Lie bracket* [27] that maps onto the same vector space

$$[\hat{\lambda}_i, \hat{\lambda}_j] = f_{ijk}\hat{\lambda}_k, \tag{2.10}$$

where the structure constants, f_{ijk}, are simply numbers and satisfy the Jacobi identity

$$[\hat{\lambda}_i, [\hat{\lambda}_j, \hat{\lambda}_k]] + [\hat{\lambda}_j, [\hat{\lambda}_k, \hat{\lambda}_i]] + [\hat{\lambda}_k, [\hat{\lambda}_i, \hat{\lambda}_j]] = 0. \tag{2.11}$$

Unitary operators frequently appear in quantum mechanics since they preserve the lengths of vectors and so also probability amplitudes [26]. Such a $\hat{U}$ satisfies $\hat{U}^\dagger\hat{U} = \hat{U}\hat{U}^\dagger = \hat{\mathbb{1}}$ and its exponent, $\hat{H}$, is a *hermitian* ($\hat{H} = \hat{H}^\dagger$) operator with the same dimension, n, as $\hat{U}$. All such $n \times n$ matrix operators form a group, denoted $U(n)$, under matrix

multiplication. Since $\hat{H}$ is hermitian, its diagonal elements are real,

$$\hat{H}_{ii}^{*} = \hat{H}_{ii} \quad \text{and} \quad \hat{H}_{ij}^{*} = \hat{H}_{ji} \quad \text{for} \quad i,j = 1,2,...,n. \tag{2.12}$$

Thus $\hat{H}$, and therefore also $\hat{U}$, permits n^2 real independent parameters and thus n^2 generators $\hat{\lambda}_j$. Restricting $\det(\hat{U}) = 1$, produces the group $SU(n)$ with $n^2 - 1$ generators. Such symmetries form the backbone of the current understanding of particle physics through the Standard Model, encapsulated mathematically by its *Lagrangian*, which is explored in the following section.

2.1.3 Gauge Theories

The Standard Model is often described more formally with a Lagrangian with a $SU(3) \times SU(2) \times U(1)$ *gauge symmetry*. This means it is invariant under three different types of symmetry operations corresponding to the $SU(3)$, $SU(2)$, and $U(1)$ Lie groups, as introduced in Section 2.1.2. Details on this topic can be found in Refs. [14, 28]. A Lagrangian, L, is a general function[9] that encodes the relevant dynamics of a physical system

$$L(\varphi_i, \dot{\varphi}_i, t) = \int \mathcal{L}(\varphi_i, \dot{\varphi}_i, t) d^3x, \tag{2.13}$$

where φ_i are generalised coordinates on which the system depends and $\mathcal{L}$ is the *Lagrangian density* typically used in field theory. *Equations of motion* of the system can be deduced according to the *principle of least action*, i.e. nature always seeks to minimise a dimensionless quantity called the action, S, given by

$$S = \int L\, dt = \int \mathcal{L}\, d^4x. \tag{2.14}$$

In natural units, where universal physical constants such as $\hbar$ and c are set to unity, space-time coordinates, x^μ, have dimensions of $[\text{Energy}]^{-1}$, and so $\mathcal{L}$ necessarily has units of $[\text{Energy}]^4$. The solution to this minimisation problem can then be retrieved using the *Euler-Lagrange* equations

$$\frac{\partial \mathcal{L}}{\partial \varphi_i} = \partial_\mu \left(\frac{\partial \mathcal{L}}{\partial(\partial_\mu \varphi_i)} \right), \tag{2.15}$$

where ∂_μ is the partial derivative with respect to x^μ.

Quantum Electrodynamics (QED)

A good starting point to understand electromagnetism in the context of particle physics is the *Dirac equation*. This applies special relativity to the Schrödinger equation from quantum mechanics and describes the electromagnetic properties of a charged spin-1/2 particle with mass, m, represented by a four-component *spinor*, ψ [14, 28]

$$(i\partial\!\!\!/ - m)\psi = 0. \tag{2.16}$$

[9] Named after Joseph-Louis Lagrange or, as he was born, Giuseppe Lodovico Lagrangia

Here $\not{\partial} = \partial_\mu \gamma^\mu$ involves the Dirac matrices, which may be represented as

$$\gamma^0 = \begin{pmatrix} 0 & 1 \\ 1 & 0 \end{pmatrix}, \quad \gamma^i = \begin{pmatrix} 0 & \sigma^i \\ \sigma^i & 0 \end{pmatrix} \quad (i = 1, 2, 3). \tag{2.17}$$

The σ^i are the *Pauli matrices* (given in Ref. [26]) associated with quantum mechanical spin, which will be encountered again later. The four components of the spinor correspond to particle wavefunctions for the two spin states, and for both matter and antimatter. The Dirac equation is an equation of motion of the Lagrangian

$$\mathcal{L} = i\bar{\psi}\not{\partial}\psi - m\bar{\psi}\psi, \tag{2.18}$$

where $\bar{\psi} = \psi^\dagger \gamma^0$. It can be noted from this equation that spinor fields have a mass dimension of 3/2. This equation is invariant under a *global* U(1) transformation $\psi \to e^{-i\theta}\psi$, where θ is constant, however not for a *local* transformation, $\theta = \theta(x)$, which would require the addition of a term $\bar{\psi}(\partial_\mu \theta(x))\psi$. This motivates defining the *covariant derivative*, $\mathcal{D}_\mu = \partial_\mu - iqA_\mu$, with

$$A_\mu(x) \to A_\mu(x) - \frac{1}{q}\partial_\mu \theta(x), \tag{2.19}$$

such that Eq. (2.18) can be made to be locally invariant through the replacement of $\not{\partial}$ by $\not{\mathcal{D}}$. This introduces a new degree of freedom to the system, a *vector field* with an associated charge, q. For generality, one must then also add a term

$$-\frac{1}{4}\mathcal{F}^{\mu\nu}\mathcal{F}_{\mu\nu},$$

where

$$\mathcal{F}_{\mu\nu} = \partial_\mu A_\nu - \partial_\nu A_\mu. \tag{2.20}$$

Combining all of these contributions yields Quantum Electrodynamics (QED)[10]:

$$\mathcal{L}_{\text{QED}} = -\frac{1}{4}\mathcal{F}^{\mu\nu}\mathcal{F}_{\mu\nu} + i\bar{\psi}\not{\mathcal{D}}\psi - m\bar{\psi}\psi. \tag{2.21}$$

The corresponding equation of motion for A_μ is essentially a relativistic version of the inhomogeneous Maxwell's equations, with $A^\mu = (\rho, \vec{A})$ and $J^\mu = \bar{\psi}\gamma^\mu\psi$, and it becomes clear that A^μ describes the photon. Requiring that the covariant derivatives satisfy the Jacobi identity, Eq. (2.11), imposes the Bianchi identity for electromagnetism [10],

$$\partial_\alpha F_{\beta\gamma} + \partial_\beta F_{\gamma\alpha} + \partial_\gamma F_{\alpha\beta} = 0, \tag{2.22}$$

which is a formulation of the homogeneous Maxwell's equations.

[10] First developed by Paul Dirac. No doubt the relation to *quod erat demonstrandum*, a common phrase used to end a mathematical proof, was not lost on him.

Quantum Chromodynamics (QCD)

In order to include the strong interaction, one can start with a similar set of terms as for electromagnetism [14,28]. It was found [29,30] that, on symmetry grounds, quarks must possess another degree of freedom, called *colour* charge, of which there are three types (red, green, and blue). One would anticipate an invariance under transformations

$$\psi_i \to M_{ij}\psi_j, \quad i,j \in \{r,g,b\}, \tag{2.23}$$

where $\mathbf{M}$ is a 3×3 matrix. Since unitarity is a common requirement, one can look to SU(3) as the group whose members will generate the necessary transformations:

$$\psi_i \to (\delta_{ij} - ig_s\theta_a(T^a)_{ij})\psi_j, \tag{2.24}$$

where T^a are the generators of SU(3), which are typically represented by the Gell-Mann matrices (given in Ref. [26]), scaled by a factor of a half. SU(3) has eight generators, and so in a locally invariant theory there must be eight vector fields A^a_μ (*gluon fields*), which transform as

$$A^a_\mu \to A^a_\mu + D^{ab}_\mu \theta^b(x), \tag{2.25}$$

with

$$D^{ab}_\mu = \delta^{ab}\partial_\mu - ig_s A^c_\mu (T^c)^{ab}. \tag{2.26}$$

The labels $\{a,b,c\}$ are *adjoint* indices running from one to eight, and the generators are typically taken from the adjoint representation where they are related to the structure constants of SU(3), i.e. $(T^c)^{ab} = -if^{abc}$. This quantity D^{ab}_μ is similar in structure to the covariant derivative

$$(D_\mu)_{ij} = \delta_{ij}\partial_\mu - ig_s A^a_\mu (T^a)_{ij}, \tag{2.27}$$

where i and j are colour indices and the generators T^a are once again represented by the Gell-Mann matrices. Interactions with gluons may change the colour of a quark, with the gluon carrying a colour and an anti-colour label, to match those of the two quarks involved [31]. With three colours, there are nine possible linearly-independent combinations, however one of these would be a colour singlet, which would permit long-range interactions. Since such a phenomenon has not been observed experimentally, the remaining eight gluons provide an accurate description of the strong force consistent with SU(3) symmetry.

One must introduce a field strength tensor similar to that of QED, but here the non-Abelian nature of SU(3) (e.g. matrices do not generally commute) requires the inclusion of an additional term that allows for gluon self-interaction

$$G^a_{\mu\nu} = \partial_\mu A^a_\nu - \partial_\nu A^a_\mu + g_s f^{abc} A^b_\mu A^c_\nu, \tag{2.28}$$

and hence the full QCD Lagrangian is

$$\mathcal{L}_{QCD} = -\frac{1}{2}G^{\mu\nu a}G^{a}_{\mu\nu} + i\bar{\psi}_i \not{D}_{ij}\psi_j - m\delta_{ij}\bar{\psi}_i\psi_j. \tag{2.29}$$

Generality demands an additional term to be present in the QCD Lagrangian,

$$\theta\frac{\alpha_s}{8\pi}G^{a}_{\mu\nu}\tilde{G}^{a\mu\nu},$$

where $\alpha_S = \frac{g_S}{4\pi}$, θ is a free parameter that must be measured, and $\tilde{G}^{a\mu\nu} = \frac{1}{2}\epsilon_{\mu\nu\sigma\rho}G^{a\sigma\rho}$, with $\epsilon_{\mu\nu\sigma\rho}$ being the fully anti-symmetric Levi-Civita symbol. This term violates Charge-Parity symmetry (see Section 2.3). However, experimental limits on ultra-cold neutrons and atomic mercury constrain the QCD vacuum angle to satisfy $|\theta| \lesssim 10^{-10}$ [32, 33], and so, for good reason, this term is typically omitted. This term is discussed further in Section 2.2.

On account of the self-interacting nature of gluons, the strong coupling constant, α_s, depends on energy transfer, Q, satisfying:

$$Q^2\frac{d\alpha_s}{dQ^2} \equiv -b_0\alpha_s^2 + \mathcal{O}(\alpha_s^3), \quad b_0 = \frac{11N_c - 4T_R n_f}{12\pi}, \tag{2.30}$$

which has the solution

$$\alpha_s(Q) = \frac{1}{b_0 \ln\left(\frac{Q^2}{\Lambda^2_{QCD}}\right)}(1 + ...), \tag{2.31}$$

where N_c is the number of colours, $T_R = 1/2$ is the colour factor for a gluon to split to a $q\bar{q}$ pair, n_f in the number of quark flavours, and $\Lambda_{QCD} \sim 200\,\text{MeV}$ is the *QCD scale*, a characteristic energy for the interaction [14, 28]. The ellipsis refers to terms further suppressed by $\ln\left(\frac{Q^2}{\Lambda^2_{QCD}}\right)$. The coupling constant is most significant for small energies, tending to unity and leading to the property of confinement in this regime. In such a scenario, higher-order terms cannot be neglected, which makes such calculations challenging. For large energies, the coupling constant becomes small, and quarks display *asymptotic freedom*[11] and behave as if they were free. In this regime, the theory becomes perturbative, like electromagnetism, and calculations become more feasible. The "energy-scale" at which α_S is evaluated is often also denoted by μ.

Electroweak (EW) Theory

Chirality for a Dirac fermion ψ is defined through the (parity) operator $\gamma^5 = i\gamma^0\gamma^1\gamma^2\gamma^3$, which has eigenvalues of +1 for *right-handed* or -1 for *left-handed* particles. Any Dirac field can thus be projected into its left- or right-handed component by acting with the projection operators $P_L = \frac{1}{2}(1-\gamma^5)$ or $P_R = \frac{1}{2}(1+\gamma^5)$ on ψ. In the relativistic limit ($v \to c$), these eigenstates are equivalent to those of *helicity*, which parameterises the projection of

[11] Work on this by David Gross, Hugh David Politzer, and Frank Wilczek earned them the Nobel Prize in 2004 [15].

a particle's spin onto the direction of its momentum. In this limit, right-/left-handed particles have spins pointing in the same/opposite direction to their momenta, respectively. So far, with the electromagnetic and strong interactions, this property hasn't required much consideration, however this is particularly relevant for the weak interaction.

In analogy to the above, for the strong interaction, the contribution to the SM Lagrangian from the weak interaction can be written as [14, 28]

$$\mathcal{L}_W = -\frac{1}{2}W^{\mu\nu a}W^a_{\mu\nu} + i\bar{Q}_i\not{D}_{ij}Q_j + i\bar{u}_i\not{D}_{ij}u_j + i\bar{d}_i\not{D}_{ij}d_j + i\bar{L}_i\not{D}_{ij}L_j + i\bar{e}_i\not{D}_{ij}e_j, \tag{2.32}$$

where there are separate terms for the different pairings of particles that can interact and a labels up-type/down-type. For left-handed fermions, we now consider two-component objects that group together charged leptons with their corresponding neutrino, and up-type quarks, U, with the appropriate down-type quark, D, in the same generation[12]

$$L = \begin{pmatrix} l^- \\ \nu_l \end{pmatrix}, \quad Q = \begin{pmatrix} U \\ D \end{pmatrix}. \tag{2.33}$$

This dimensionality means that it is the SU(2) symmetry that is relevant here. Experimentally, no W interactions involving right-handed fermions (or left-handed anti-fermions) have been observed. This is the violation of parity symmetry that Chien-Shiung Wu demonstrated in her famous experiment [34]. Therefore, right-handed charged fermions (e_i, u_i, d_i) enter as singlets, while right-handed neutrinos are not included at all. The generators of this group are the two-dimensional Pauli Matrices, of which there are three $(= 2^2 - 1)$, which appear in quantum mechanics as the operators for the three components of spin. In fact, these generators are related to a quantity called *isopsin*, which will be explored later.

Higgs Field

In a general renormalisable Lagrangian with an energy dimension of four, there should also be a complex *scalar field* ϕ (energy dimension one), with a kinetic term

$$\mathcal{L}_{kin} = D^\mu\phi(D_\mu\phi)^*, \tag{2.34}$$

and a potential term

$$V(\phi) = \mu^2\phi\phi^* + \lambda^2(\phi\phi^*)^2. \tag{2.35}$$

For $\mu^2 > 0$, the minimum of the potential or *vacuum expectation value* (vev) is at $\phi = 0$, but if $\mu^2 < 0$ then this minimum value, ϕ_0, is non-zero;

$$|\phi_0| = \frac{v}{\sqrt{2}} = \frac{|\mu|}{\sqrt{2\lambda}}$$

[12] The identification of the doublet structure of leptons was awarded by the 1988 Nobel Prize for Leon M. Lederman, Melvin Schwartz, and Jack Steinberger [15].

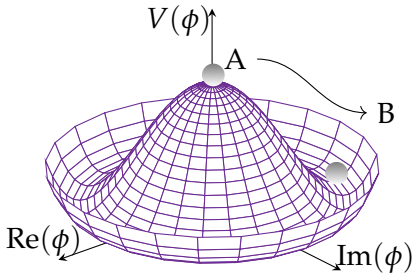

FIGURE 2.5: The Higgs potential, as given in Eq. (2.35) with $\mu^2 < 0$. It is clear that the point $\phi = 0$ at A is not a minimum, and so one can talk of the Higgs acquiring a vev as it rolls down to the degenerate minimum at B. This is the mechanism by which SM particles acquire their masses.

In this latter scenario, the previous symmetry of the system is broken, a phenomenon known as *Spontaneous Symmetry Breaking* or *SSB*.

For a coupling to the weak interaction, the field must be a doublet, $\phi^* \to \phi^\dagger$, and the usual convention for the vacuum expectation value is

$$\phi_0 = \begin{pmatrix} 0 \\ \frac{v}{\sqrt{2}} \end{pmatrix}. \tag{2.36}$$

Perturbations about this minimum can be encoded in a field, h, and gauge transformations can be made to remove imaginary parts and confine ϕ to the lower part of the doublet to give [35]

$$\phi = \begin{pmatrix} 0 \\ \frac{v+h}{\sqrt{2}} \end{pmatrix}. \tag{2.37}$$

Substituting this into the potential generates the following contributions involving h, in addition to higher-order terms:

$$\lambda v^2 h^2 + \lambda v h^3 + \frac{\lambda}{4} h^4, \tag{2.38}$$

i.e. the potential of a particle of mass $m_H = \sqrt{2\lambda} v$ with tri-boson and quartic self-interaction terms, where λ parameterises the interaction strengths. The *Higgs field* is such a scalar field with $v = 246\,\text{GeV}$ [14] (potential shown in Figure 2.5), and the particle H is interpreted as the *Higgs boson*, the mediator of the interaction.

In the case of a $SU(2) \times U(1)$ *electroweak* symmetry[13], combining EM and weak interactions with vector fields W^a_μ and B_μ, the covariant derivative becomes

$$D_\mu = \partial_\mu - igW^a_\mu T^a - i\frac{g'}{2} B_\mu Y, \tag{2.39}$$

[13] Work on this theory was rewarded by not one but two Nobel Prizes, in 1979 for Sheldon Glashow, Abdus Salam, and Steven Weinberg, and in 1999 for Gerard t'Hooft and Martin Veltman [15]. The experimental discovery of the W and Z bosons was also recognised by the award of the Nobel Prize to Carlo Rubbia and Simon van der Meer in 1984.

where Y is the *hypercharge* associated with B_μ. Since the hypercharge of the Higgs is taken to be 1, this produces kinetic terms involving

$$\frac{1}{2}\frac{v^2}{4}\left[g^2W_\mu^1W^{1\mu}+g^2W_\mu^2W^{2\mu}+(-gW_\mu^3+g'B_\mu)(-gW^{3\mu}+g'B^\mu)\right], \tag{2.40}$$

which can be interpreted as three massive gauge bosons, as we expect from Section 2.1.1. To link with the physical flavour states that we're more accustomed to encountering, we can look to the lepton kinetic term $\bar{L}D_\mu L$, which has a part proportional to

$$\begin{pmatrix}\bar{\nu}_{e_L} & \bar{e}_L\end{pmatrix}\begin{pmatrix}W_\mu^3 & W_\mu^1-iW_\mu^2\\ W_\mu^1+iW_\mu^2 & -W_\mu^3\end{pmatrix}\begin{pmatrix}\nu_{e_L}\\ e_L\end{pmatrix}.$$

Thus, we see the connection between $W_\mu^{1,2}$ and $W_\mu^{+,-}$:

$$W_\mu^\pm=\frac{1}{\sqrt{2}}(W_\mu^1\mp iW_\mu^2),\quad m_W=\frac{gv}{2} \tag{2.41}$$

and the third massive boson, Z_μ^0,

$$Z_\mu^0=\cos\theta_W W_\mu^3-\sin\theta_W B_\mu,\quad m_Z=\frac{gv}{2\cos\theta_W}. \tag{2.42}$$

For simplicity, here we have defined the third term of Eq. (2.40) in terms of the weak mixing (Weinberg) angle $\theta_W\equiv\arctan(g'/g)$. In effect, the W and Z bosons have gained their masses from the breaking of the electroweak symmetry $SU(2)_L\times U(1)_Y$ to $U(1)_{EM}$. There is also a component orthogonal to Z_μ^0, which is necessarily massless and is indeed the familiar photon field:

$$A_\mu=\sin\theta_W W_\mu^3+\cos\theta_W B_\mu,\quad m_\gamma=0. \tag{2.43}$$

Such a substitution allows the covariant derivative to be re-expressed in terms of the photon field, A_μ

$$\partial_\mu-ieA_\mu Q+..., \tag{2.44}$$

where

$$Q=T^3+\frac{Y}{2}\mathbb{1}=\frac{1}{2}\begin{pmatrix}Y+1 & 0\\ 0 & Y-1\end{pmatrix} \tag{2.45}$$

is the generator for electric charge and

$$e=g\sin\theta_W=g'\cos\theta_W=gg'/\sqrt{g^2+g'^2}. \tag{2.46}$$

This annihilates the minimum of the Higgs potential for $Y=1$ and the expected charges for the SM particles can be retrieved with the following choices for hypercharge:

- $Y=\frac{1}{3}$ for left-handed quark doublets, Q_i
- $Y=-1$ for left-handed lepton doublets, L_i

- $Y = \frac{4}{3}$ for right-handed up-type quark singlets, u_i
- $Y = -\frac{2}{3}$ for right-handed down-type quark singlets, d_i
- $Y = -2$ for right-handed lepton singlets, e_i

The QED Lagrangian from earlier essentially gets subsumed within the electroweak Lagrangian, $\mathcal{L}_W \rightarrow \mathcal{L}_{EW}$, but QED is recovered following Electroweak Spontaneous Symmetry Breaking (EWSSB) at energies below the *electroweak scale* ($v = v_{EW}$).

For generality, we must also add a final set of terms to the Lagrangian that are gauge-invariant and renormalisable

$$\mathcal{L}_Y = Y^u_{ij}\bar{Q}_i\phi u_j + Y^d_{ij}\bar{Q}_i\phi d_j + Y^e_{ij}\bar{L}_i\phi e_j. \tag{2.47}$$

Through unitary transformations, the Yukawa matrices, Y, can be diagonalised

$$Y^f \rightarrow M^f_{\text{diag}} = V^f_L Y^f V^{f\dagger}_R,$$

and after SSB one obtains terms of the form

$$\mathcal{L}_Y = y^q_i \frac{v^2}{2}\bar{q}_i q_i + y^e_i \frac{v^2}{2}\bar{e}_i e_j. \tag{2.48}$$

These have the appearance of mass terms with $m^{q,e}_i = \sqrt{y_i}v$, and so the origin of fermion masses also becomes clear. This diagonalisation procedure, however, also affects the kinetic terms from Eq. (2.32), which become [14]

$$-\frac{g}{\sqrt{2}}\bar{Q}_L\gamma^\mu W^+_\mu T^+ V^{CKM} Q_L + \text{h.c.}, \quad V^{CKM} = V^u_L V^{d\dagger}_L.$$

T^+ is the "isospin-raising" operator

$$\frac{1}{\sqrt{2}}(T^1 + iT^2) = \begin{pmatrix} 0 & 1 \\ 0 & 0 \end{pmatrix}, \tag{2.49}$$

which will be seen again later, and here pairs up-type and down-type quarks through the interaction with a charged W boson

$$-\frac{g}{\sqrt{2}}\bar{U}_i\gamma^\mu W^+_\mu V^{CKM}_{ij} D_j + h.c.$$

Here $U = (u, c, t)$, $D = (d, s, b)$, and it is taken as given that the charged weak interaction couples only to left-handed fermions. The matrix V^{CKM} introduces a rich phenomenology and is explored further in the following section, but I will conclude by summarising the combined Standard Model Lagrangian;

$$\mathcal{L}_{SM} = \mathcal{L}_{QCD} + \mathcal{L}_{EW} + \mathcal{L}_Y + \mathcal{L}_{\text{kin}} - V(\phi), \tag{2.50}$$

where the present state of the universe follows EWSSB.

2.1.4 The CKM Matrix and Unitarity Triangles

The matrix V^{CKM} introduced in the previous section is called the Cabibbo-Kobayashi-Maskawa (CKM) matrix[14] and gives the relative couplings of the weak interaction for transitions between up-type and down-type quarks [14,36]:

$$V^{CKM} = \begin{bmatrix} V_{ud} & V_{us} & V_{ub} \\ V_{cd} & V_{cs} & V_{cb} \\ V_{td} & V_{ts} & V_{tb} \end{bmatrix}. \tag{2.51}$$

Were this an identity matrix (i.e. $V_{ud} = V_{cs} = V_{tb} = 1$, off-diagonal entries $= 0$), flavour eigenstates would be equivalent to mass eigenstates, and the diagonalisation of the Yukawa matrices wouldn't have affected the kinetic terms. In reality, the off-diagonal elements are non-zero with the hierarchy $|V_{us}|, |V_{cd}| (\sim \lambda) \gg |V_{cb}|, |V_{ts}| (\sim \lambda^2) \gg |V_{ub}|, |V_{td}| (\sim \lambda^3)$. This counting parameter λ is typically defined as

$$\frac{|V_{us}|}{\sqrt{|V_{ud}|^2 + |V_{us}|^2}},$$

with an experimental value from the CKM global fit of 0.2250 ± 0.0002 [37]. As a complex 3×3 unitary matrix, this can be parameterised using nine independent real numbers, though the five independent rotations applied to diagonalise the Yukawa terms reduces the number of free parameters to four [28]. There are several parameterisations that can be used but one of the most popular is the Wolfenstein parameterisation [14], which makes the above hierarchy in λ explicit. In addition, the Wolfenstein parameterisation uses the parameters A, ρ, and η, approximating the matrix as

$$V^{CKM} \approx \begin{bmatrix} 1 - \frac{1}{2}\lambda^2 - \frac{1}{8}\lambda^4 & \lambda & A\lambda^3(\rho - i\eta) \\ -\lambda + \frac{1}{2}A^2\lambda^5[1 - 2(\rho + i\eta)] & 1 - \frac{1}{2}\lambda^2 - \frac{1}{8}\lambda^4(1 + 4A^2) & A\lambda^2 \\ A\lambda^3[1 - (1 - \frac{1}{2}\lambda^2)(\rho + i\eta)] & -A\lambda^2 + \frac{1}{2}A\lambda^4[1 - 2(\rho + i\eta)] & 1 - \frac{1}{2}A^2\lambda^4 \end{bmatrix}, \tag{2.52}$$

up to terms $\mathcal{O}(\lambda^6)$, where η here parameterises the amount of CP violation (as introduced in Chapter 1 and elaborated in Section 2.3). Note that these parameters are not predicted but must be measured experimentally.

The fact that the Standard Model expects the CKM matrix to be unitary imposes constraints on the values of its elements, for instance

$$V_{ud}V_{ub}^* + V_{cd}V_{cb}^* + V_{td}V_{tb}^* = 0. \tag{2.53}$$

In fact, this particular constraint is a special one since it has the unique property of having all three terms of the same size ($\sim \lambda^3$). One can graphically represent such a condition

[14] Kobayashi and Maskawa won the Nobel Prize in 2008 for their development of this matrix, shared with Yoichiro Nambu for his work on broken symmetries.

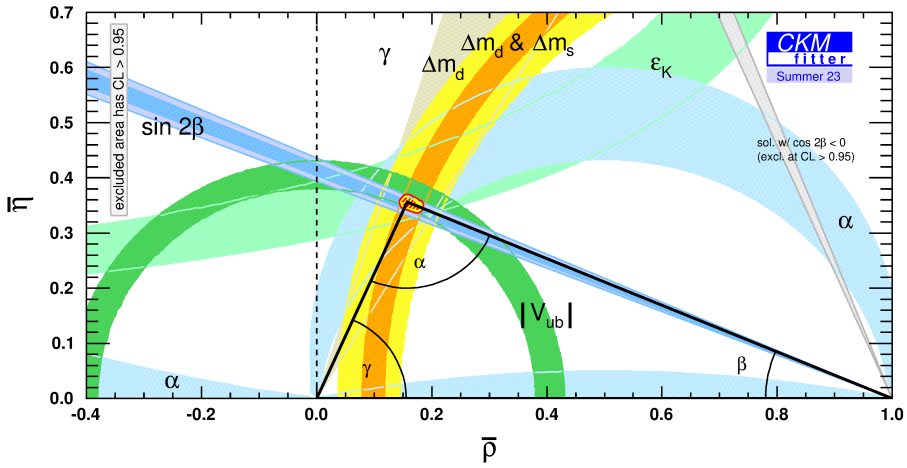

FIGURE 2.6: The current constraints from CKMfitter on the CKM triangle. Figure taken from Ref. [38].

as a *unitarity triangle* in the complex plane, as shown in Figure 2.6, normalised to $V_{cd}V_{cb}^*$. This is typically referred to as *the* unitarity triangle; though there are several, it is the only one where the sides are all of similar length. It is of particular interest to measure these side-lengths,

$$\frac{V_{ud}V_{ub}^*}{V_{cd}V_{cb}^*} \quad \text{and} \quad \frac{V_{td}V_{tb}^*}{V_{cd}V_{cb}^*},$$

as well as the angles of the triangle, which are explicitly defined as

$$\alpha \equiv \arg\left(-\frac{V_{td}V_{tb}^*}{V_{ud}V_{ub}^*}\right), \quad \beta \equiv \arg\left(-\frac{V_{cd}V_{cb}^*}{V_{td}V_{tb}^*}\right), \quad \gamma = \arg\left(-\frac{V_{ud}V_{ub}^*}{V_{cd}V_{cb}^*}\right). \tag{2.54}$$

The apex of this triangle is located at $(\bar{\rho}, \bar{\eta})$, i.e. the real and imaginary parts of $-(V_{ud}V_{ub}^*)/(V_{cd}V_{cb}^*)$, which can be approximated by $\bar{\rho} \approx \rho(1-\lambda^2/2)$ and $\bar{\eta} \approx \eta(1-\lambda^2/2)$. B_s^0 meson oscillation studies require consideration of an analogous triangle involving the second and third columns of V_{CKM}, since these are the appropriate vertex factors. Here $V_{us}V_{ub}^* \ll V_{cs}V_{cb}^*, V_{ts}V_{tb}^*$ and so the mixing phase is related to the interference between these latter two terms, i.e. the angle

$$\beta_s \equiv \arg\left(-\frac{V_{ts}V_{tb}^*}{V_{cs}V_{cb}^*}\right). \tag{2.55}$$

Following on alphabetically, $\delta = \arg(\rho - i\eta)$ is also used as a proxy for the degree of CP violation, with $\delta = 0$ indicating conservation.

If the measurements of these quantities are inconsistent with the triangle hypothesis, i.e. $\alpha + \beta + \gamma \neq \pi$, then this is evidence for the presence of physics *Beyond the Standard Model (BSM)*. In fact, all angles of the unitarity triangle have been measured in hadronic B decays, and the first measurement of this class of modes confirmed the Kobayashi-Maskawa mechanism [39] as the primary source of CP violation in the SM (see Refs. [37, 40] and references therein). The current state of the measurements is shown graphically in Figure 2.6, where BSM effects could manifest themselves as non-closure at the apex.

FIGURE 2.7: Visible light image of the Bullet Cluster, superimposed with the x-ray image in pink and the matter distribution from gravitational lensing in blue. (Credit: x-ray: NASA/CXC/CfA/M. Markevitch et al. [46]; optical: NASA/STScI, Magellan/U. Arizona/D. Clowe et al. [47]; lensing map: NASA/STScI ESO WFI, Magellan/U. Arizona/D. Clowe et al. [47])

2.2 Beyond the Standard Model

2.2.1 Evidence

Indeed, a few pieces of observational evidence point towards the fact that the SM is not the full picture[15]. Astronomical and cosmological data, for instance galaxy rotation curves [42] and strong gravitational lensing [43], indicate the existence of *dark matter* i.e. a form of matter that is, as yet, unaccounted for in the SM (see also Figure 2.7). The observation of neutrino oscillations [16] also suggests that neutrinos are massive, while the precise mechanism for this to occur in the Standard Model remains unknown. The SM also does not include gravity in its description of fundamental interactions [44] and receives critiques on "naturalness" grounds such as the hierarchy problem [45], i.e. explaining why the Higgs mass parameter is many orders of magnitude smaller than what would be assumed from dimensional arguments ($M_P \sim 10^{19}$ GeV). Finally, and most relevant for this work, the universe appears to be overwhelmingly dominated by matter, with antimatter only found in very small abundances. This is most relevant for baryons, more specifically protons and neutrons, which combine to form the atoms that make up the vast majority of the matter content of the universe. If matter and antimatter had been treated equally in the early universe, the matter would have annihilated with the antimatter, and there would have been no mechanism to produce the sizeable net number of baryons that is observed in the universe today [48]. This imbalance (termed the *Baryon Asymmetry of the Universe* or *BAU*) is far larger than what can be currently accounted for in the Standard Model [49]. All of these reasons mean that one of the primary objectives of particle physics in recent years has been to find BSM physics that could explain these anomalous phenomena.

[15] If you're into philosophy, we are the prisoners in Plato's cave allegory [41].

Recent Tensions

In contrast to the electron's anomalous moment, that of the muon has shown tension with SM predictions, most recently with the updated average of the quantity from the g-2 experiment [50]. This experimental average lies more than 5σ from the latest theoretical prediction from the Muon g-2 Theory Initiative [51]. This prediction used measurements of $\sigma(e^+e^- \to \text{hadrons})$ to determine the dominant hadronic contribution. However, tensions were found between this experimental data and both lattice QCD calculations from the BMW collaboration [52] and a preliminary measurement of the $e^+e^- \to \pi^+\pi^-$ cross-section from the CMD-3 experiment [53]. Producing a theoretical prediction that reconciles these individual analyses is currently an ongoing process [54], and it is expected that such a combined result will be more consistent with the SM. This, however, remains one of the most tantalising hints of directly-measured BSM physics.

Similarly, the most recent combination of measurements of $R_{D^{(*)}}$ [55], i.e. the ratio of the branching ratio of $B^- \to D^{0(*)}\tau^-\bar{\nu}_\tau$ to $B^- \to D^{0(*)}l^-\bar{\nu}_l$ $(l = e, \mu)$, appears to violate *lepton flavour universality*, the SM predicts that the W boson couples equally to all leptons, at 3.3σ [56]. The individual R_D and R_{D^*} are, however, consistent with no violation at 1.6σ and 2.5σ, respectively. The similar observable of $R_{K^{(+,*)}}$, the ratio of branching ratios of $\mathcal{B}(B^{(+,0)} \to K^{(+,*)}\mu^+\mu^-)$ to $\mathcal{B}(B^{(+,0)} \to K^{(+,*)}e^+e^-)$, had initially shown tensions (particularly R_K [57]), however a later simultaneous LHCb Run1+Run2 measurement for $q^2 \in [0.1, 1.1]$ GeV^2 and $q^2 \in [1.1, 6.0]$ GeV^2 showed consistency with the SM at 0.2σ [57].

Another interesting discrepancy currently standing concerns the branching ratios of $B^0_{(s)} \to D^{(*)-}_{(s)}h^+$, $h \in \{\pi, K^{(*)}, \rho\}$ decays, some of which disagree with the predictions of QCD factorisation (a theoretical technique explained further in Section 2.5) with a high significance [14, 58, 59]. It is currently an open question as to the source of this discrepancy, and Chapters 4 and 7 detail attempts to resolve this through both experimental and theoretical analyses.

New Particles?

In general, a New Physics theory would introduce new particles whose current non-observation suggests a mass beyond current experimental reach, or else very small couplings. Direct searches aim to produce real (or *on-shell*) versions of these particles, which would appear as a bump in a spectrum of *invariant mass* of decay products ($\sqrt{E^2 - p^2}$ for total energy and momentum E and p, respectively). While such approaches have not yet born fruit, the influence of new particles may equally be seen if they occur *virtually* in loop diagrams. Heisenberg's Energy-Time Uncertainty Principle, $\Delta E \Delta t \geq \hbar$, allows for particles to be produced for a short period of time, Δt, even in instances where their mass ($\sim \Delta E$) is far in excess of the centre-of-mass energy. Such particles that break the relativistic mass-energy equation, $E^2 = m^2c^4 + p^2c^2$, are termed *off-shell*, and their "virtual" nature refers to the fact that they are not material for any appreciable period [60]. The contributions of these particles would introduce some small deviation $\sim 1/M$ to a

precision measurement. The following describes a few popular candidates for such new particles [14].

2.2.2 Leptoquarks

Leptoquarks, described in Ref. [14], are hypothetical particles that carry both baryon- and lepton-numbers, and hence couple quarks to leptons. Naturally-occurring in *Grand Unified Theories* that extend the gauge group to $SU(5)$ or $SO(10)$, they allow for a variety of anomalous behaviour; for example TeV-scale leptoquarks serve as good candidates to explain the recent anomalies found in $R_{D^{(*)}}$ [14]. Tree-level flavour-changing neutral currents, which violate lepton number, could also result if such particles coupled to quark/lepton mass states from multiple generations. Finally, there is the possibility that leptoquarks couple to both left- and right-handed quarks simultaneously, and so these particles could influence the muon anomalous magnetic moment. Both direct and indirect constraints have already been placed on leptoquark models from collider experiments.

2.2.3 Supersymmetry

Supersymmetry (SUSY) is another theory that could be a realisation of larger gauge groups and potentially offers the unification of particle physics and gravity at M_P [14]. It also acts as a possible resolution to the hierarchy problem, which concerns the large difference in scales between this energy scale and the electroweak scale $M_{EW} \sim 100\,\text{GeV}$. The symmetry refers to a transformation of fermions into bosons and vice versa. Hence, in such a theory, every Standard Model particle would have a supersymmetric partner (squarks, sleptons, and bosinos), which would differ in spin by half a unit and be degenerate in mass before symmetry breaking. In this theory, there is also an extended Higgs sector consisting of additional complex Higgs doublets, their higgsino fermionic superpartners, and the corresponding antiparticles. No such particles have been confirmed experimentally as yet, despite thorough searches.

2.2.4 Extended Boson Sectors

The W' and Z' bosons are massive hypothetical particles of spin-1 and electric charge ± 1 and 0, respectively [14]. These are colour singlets and are predicted in several extensions of the Standard Model (SM). The dimensionless coupling coefficients for such a W' term in the Lagrangian would be complex and provide the possibility for couplings to right-handed neutrinos. The SM W couplings can be reproduced through particular choices of these constants. The coupling coefficients for the Z' are real, and these couplings to fermions may generally be generation-dependent. One can assume that these bosons also come from a spontaneously-broken gauge symmetry, the simplest extension being $SU(2)_L \times SU(2)_R \times U(1)$.

2.2.5 Right-handed/Heavy Neutrinos

As previously explained, the SM assumption of massless neutrinos is inconsistent with experimental observations. This can be remedied by adding m *sterile* neutrinos, ν_s, that have an even more feeble effective interaction strength with other matter than their SM counterparts, ν_L. Their influence can be only felt through mixing with SM neutrinos, as their direct SM couplings must be zero. Assuming the same gauge symmetries, two gauge-invariant, renormalisable operators emerge, giving two mass terms [14]

$$-\mathcal{L}_{M_\nu} = M_{D_{ij}} \bar{\nu}_{si} \nu_{Lj} + \frac{1}{2} M_{N_{ij}} \bar{\nu}_{si} \nu^c_{sj} + \text{h.c.}, \tag{2.56}$$

where ν^c is the charge-conjugated neutrino field, M_D is a complex matrix of dimension $m \times 3$, and M_N is a symmetric $m \times m$ matrix [14]. The first (*Dirac*) term is like the mass term for charged fermions

$$Y^\nu_{ij} \bar{\nu}_{si} \tilde{\varphi}^\dagger L_{Lj} \implies M_{D_{ij}} = Y^\nu_{ij} \frac{v}{\sqrt{2}}, \tag{2.57}$$

and introduces sterile neutrinos as the right-handed component of a four-spinor neutrino field. This, however, does not present the SM as a good low-energy effective theory and fails to explain the tiny (but non-zero) neutrino masses inferred from experiments. The second (bare mass) term is more promising, with these *Majorana* neutrinos being their own anti-particles ($\nu_M = \nu^c_M$). If the mass eigenvalues of M_N are much higher than v_{EW}, the diagonalisation of M_ν gives the familiar three light neutrinos, as well as m heavy neutrinos, with masses M^l and M^h, respectively. These masses are given by

$$M^l \approx V_l^T M_D^T M_N^{-1} M_D V_l, \quad M^h \approx V_h^T M_N V_h. \tag{2.58}$$

V_l and V_h are 3×3 and $m \times m$ unitary matrices, respectively. The masses of the heavy states (predominantly composed of right-handed flavour states) are proportional to M_N while the light ones (predominantly composed of left-handed flavour states) scale with M_N^{-1}. This is known as the *see-saw mechanism* due to the inverse relationship between heavy and light masses, and this naturally emerges from several SM extensions.

2.2.6 Dark Matter

Observations of gravitational lensing effects and rotation curves of far-off galaxies indicate that the amount of "visible" matter (i.e. that interacts electromagnetically) in the universe is significantly less than the total amount that interacts gravitationally [61]. Measurements of the *Cosmic Microwave Background* (CMB) imply that the total mass-energy of this "invisible" or "dark" matter (DM) in the universe exceeds that of the baryonic matter by a factor of around five [61]. Explanations due to compact objects (MACHOs) and modified gravity have been largely ruled out [61]. Such a substance has no representation within the Standard Model, and so there is an active effort to account for this additional electromagnetically neutral massive component. In addition to the sterile

neutrinos addressed previously, there are several other possible solutions, including the following [14]:

- **WIMPs:** Weakly Interacting Massive Particles (WIMPs) are leading candidates since they often arise in BSM scenarios that address the hierarchy problem. This solution is favoured due to the WIMP miracle, i.e. a weakly-interacting particle with a mass around the Higgs vev would have a density in the early universe consistent with cosmological observations [62]. The neutralino, the lightest particle in the minimal SUSY extension to the SM, could be such a WIMP.

- **Axions and axion-like particles**: The QCD axion provides a solution to the strong CP problem. Such ultra-light, bosonic DM could imprint quantum effects on macroscopic scales, with its de Broglie wavelength expected to be of a similar size to that of the smallest observed gravitationally-collapsed structures.

- **Dark photons:** Dark matter may, in fact, not interact with the gauge bosons of the SM but rather via a "dark force" mediated by some new, as-yet-undiscovered type of vector boson, with only a feeble coupling to SM particles[16] [63]. A leading candidate is the "dark photon", produced in the early universe through kinetic mixing with its SM counterpart, and would be stable if its mass is below $2m_e$ [14]. These are particles that LHCb is searching for.

2.2.7 Gravity

Gravity, which is best described by Einstein's Field Equations of General Relativity

$$R_{\mu\nu} + \left(\Lambda - \frac{R}{2}\right) g_{\mu\nu} = \frac{8\pi G}{c^4} T_{\mu\nu}, \tag{2.59}$$

is currently difficult to combine with the Standard Model [64]. Here $R_{\mu\nu}$ is the partially-contracted Riemann tensor (describing spacetime curvature) and R is its trace, $g_{\mu\nu}$ is the spacetime metric, Λ is the cosmological constant (which accounts for accelerating expansion of the universe), and $T_{\mu\nu}$ is the energy-momentum tensor of matter [65]. Much effort has, though, been put into quantising gravity, and the *graviton* has been put forward as the gauge boson of this interaction. The source of the scalar (0 indices) Higgs field is spin-0, and the sources of the vector fields (1 index) of the Electromagnetic, Strong, and Weak interactions are spin-1. Therefore, since the source of gravity is a tensor object with two indices, it is assumed that the graviton must be spin-2. With an infinite range and no electromagnetic interaction, it is also assumed to be both massless and chargeless [66].

[16] The dark side of the force is not strong with these ones. That was my very "feeble" attempt at a Star Wars reference.

2.3 CP Violation

A probe of where new physics may arise, most pertinent to the issue of explaining the BAU, regards the phenomenon known as Charge-Parity (CP) violation resulting from the complex part of the CKM matrix in Section 2.1.4. Both the electromagnetic and strong nuclear forces are invariant under charge transformation (C) where the signs of the charges of all the particles are swapped $Q \to -Q$, as well as parity transformation (P) where a reflection in spatial coordinates $\vec{x} \to -\vec{x}$. They are also unaffected by time-inversion (T), $t \to -t$.

Chien-Shiung Wu showed that the weak nuclear force violates parity symmetry [34], but it was thought at the time that the interaction may be invariant under a combined operation of C and P, displaying *CP symmetry* [67]. Indeed, shortly afterwards Lederman confirmed that charge was also violated by the decays [68]. This assumption of CP conservation was, however, very soon dismissed itself when Cronin and Fitch [69] demonstrated a small violation of this proposed symmetry in the decays of neutral kaons to pions[17]. QFT operates under the assumption of no CPT violation [71, 72], and thus T symmetry must necessarily also be violated.

Practically speaking, CP violation implies reactions proceeding at different rates under the exchange of matter and anti-matter. This is one of the three Sakharov Conditions [48] required to explain the observed BAU introduced in the previous section, the other two being non-conservation of baryon number (an accidental symmetry of the SM) and departure from thermal equilibrium in the early universe. The matter-antimatter asymmetry in the early universe is often parameterised by[18]

$$\eta = \frac{n_B - n_{\bar{B}}}{n_\gamma}, \tag{2.60}$$

where n_B is the number density of baryons, $n_{\bar{B}}$ is the number density of antibaryons, and n_γ is the number density of photons [73]. Astrophysical and cosmological observations, including studies of the CMB, indicate a small imbalance of $\eta \sim 10^{-10}$, but even this is far larger than what the Standard Model predicts from experimental data [74]. Since CP is not a fundamental symmetry of nature [14], there is no reason why it should be respected in new physics, and so any general new physics theory would be expected to have $\mathcal{O}(1)$ weak phases, and thus potentially significant CP asymmetries. For these reasons, measurements of CP asymmetries can be excellent tests of the SM.

[17] Benefiting from kaons' "strange" properties of having longer-than-expected lifetimes [70]. This work won them the Nobel Prize in 1980 [15].

[18] Note that this η is not the same quantity as in Eq. (2.52).

2.3.1 Theoretical Foundation

Adapting the notation of Ref. [14], the amplitude of a meson, M, or its CP-conjugate, $\bar{M}$, decaying to final state, f, or its CP-conjugate, $\bar{f}$, can be expressed as follows:

$$\begin{aligned} A_f &= \langle f | \mathcal{H} | M \rangle , \qquad \bar{A}_f = \langle f | \mathcal{H} | \bar{M} \rangle , \\ A_{\bar{f}} &= \langle \bar{f} | \mathcal{H} | M \rangle , \qquad \bar{A}_{\bar{f}} = \langle \bar{f} | \mathcal{H} | \bar{M} \rangle , \end{aligned} \tag{2.61}$$

where $\mathcal{H}$ is the Hamiltonian governing weak interactions. The mass eigenstates of this Hamiltonian, denoted as $|M_L\rangle$ and $|M_H\rangle$ for the light and heavy states, are not the same as those of the strong interaction, $|M^0\rangle$ and $|\bar{M}^0\rangle$. As such, the mass eigenstates can be expressed as a linear superposition of strong eigenstates:

$$|M_L\rangle \propto p |M^0\rangle + q |\bar{M}^0\rangle , \quad |M_H\rangle \propto p |M^0\rangle - q |\bar{M}^0\rangle , \tag{2.62}$$

with the normalisation $|q|^2 + |p|^2 = 1$.

The time evolution of quantum states is governed by the Hamiltonian, and after a time t each mass eigenstate acquires a phase $\sim e^{-iEt}$, where E is the energy of the eigenstate. Consequently, if a particle is produced in the $|M^0\rangle$ state there is a non-zero probability that it could be measured at a later time in the $|\bar{M}^0\rangle$ state. This phenomenon is known as *neutral meson oscillations*, or *mixing*, as the relative probabilities of measuring one or the other state vary sinusoidally over time. The eigenvalues of the Hamiltonian, $\omega_{L,H}$, are complex and are related to the masses and lifetimes of the mass eigenstates as:

$$\Delta m \equiv m_H - m_L = \mathcal{R}e(\omega_H - \omega_L), \quad \Delta\Gamma \equiv \Gamma_H - \Gamma_L = \mathcal{I}m(\omega_H - \omega_L). \tag{2.63}$$

2.3.2 Categories

There are three categories when it comes to CP violation, as outlined below.

1. CP violation in decay. CP violation for charged mesons, which cannot oscillate, appears exclusively through this category, though neutral mesons can also exhibit this kind of CP violation. This classification is defined by

$$|\bar{A}_{\bar{f}} / A_f| \neq 1, \tag{2.64}$$

and the CP asymmetry can be expressed as

$$\mathcal{A}_{CP} = \frac{\Gamma(M^- \to f^-) - \Gamma(M^+ \to f^+)}{\Gamma(M^- \to f^-) + \Gamma(M^+ \to f^+)} = \frac{|\bar{A}_{f^-} / A_{f^+}|^2 - 1}{|\bar{A}_{f^-} / A_{f^+}|^2 + 1}. \tag{2.65}$$

Such decay asymmetries of $B \to D^{(*)}K^{(*)}$ processes provide input to the latest experimental world average of γ

$$\gamma = \left(66.2^{+3.4}_{-3.6}\right)^\circ .$$

$K^{\mp}\pi^{\pm}$ final states were the first to show signs of CP violation for both B^0 and B_s^0, and in principle such decay asymmetries could be used as further input to the average of γ. The achievable precision is, though, limited by the fact that the relative magnitude and strong phase of the contributing amplitudes are as-yet not well understood [14]. The first observation of CP violation of this variety in the charm sector was made by LHCb for $D^0 \to K^+K^-$ and $D^0 \to \pi^+\pi^-$ decays [75].

$$\begin{aligned}\Delta a_{CP} &= \frac{\left|\bar{A}(K^+K^-)/A(K^+K^-)\right|^2 - 1}{\left|\bar{A}(K^+K^-)/A(K^+K^-)\right|^2 + 1} - \frac{\left|\bar{A}(\pi^+\pi^-)/A(\pi^+\pi^-)\right|^2 - 1}{\left|\bar{A}(\pi^+\pi^-)/A(\pi^+\pi^-)\right|^2 + 1} \\ &= (-0.164 \pm 0.028) \times 10^{-2}\end{aligned} \tag{2.66}$$

2. CP violation in mixing. This applies to neutral mesons with

$$|q/p| \neq 1,$$

and, in the absence of CP violation in decay, the asymmetry is typically given by

$$\mathcal{A}_{CP}(t) = \frac{d\Gamma/dt[\bar{M}^0_{\text{phys}}(t) \to \bar{f}] - d\Gamma/dt[M^0_{\text{phys}}(t) \to f]}{d\Gamma/dt[\bar{M}^0_{\text{phys}}(t) \to \bar{f}] + d\Gamma/dt[M^0_{\text{phys}}(t) \to f]} = \frac{1 - |q/p|^4}{1 + |q/p|^4}, \tag{2.67}$$

where $M^0_{\text{phys}}(t)$ and $\bar{M}^0_{\text{phys}}(t)$ refer to the meson being in the M^0 or $\bar{M}^0$ state at time t. Note that this is, in fact, time-independent. CP violation in neutral kaon mixing has been measured for semi-leptonic decays of the long-lived mass eigenstate [14]:

$$\frac{\Gamma(K_L^0 \to \pi^-\ell^+\nu_\ell) - \Gamma(K_L^0 \to \pi^+\ell^-\bar{\nu}_\ell)}{\Gamma(K_L^0 \to \pi^-\ell^+\nu_\ell) + \Gamma(K_L^0 \to \pi^+\ell^-\bar{\nu}_\ell)} = (3.32 \pm 0.06) \times 10^{-3}. \tag{2.68}$$

3. CP violation in interference between decays with and without mixing. This occurs where both M^0 and $\bar{M}^0$ decay to the same final state, f, and is defined by

$$\arg(\lambda_f) + \arg(\lambda_{\bar{f}}) \neq 0, \tag{2.69}$$

where

$$\lambda_f = \frac{q}{p}\left(\frac{\bar{A}_f}{A_f}\right), \tag{2.70}$$

and for B meson decays, this first factor can be written as

$$\frac{q}{p} = e^{-i\phi\left(B^0_{(s)}\right)} = \frac{V^*_{tb}V_{td(s)}}{V^*_{td(s)}V_{tb}}. \tag{2.71}$$

For the case of CP eigenstates, f_{CP}, in the final state, Eq. 2.69 simplifies to

$$\mathcal{I}m(\lambda_{f_{CP}}) \neq 0, \tag{2.72}$$

and the asymmetry can be measured as

$$\begin{aligned}\mathcal{A}_{CP}(t) &= \frac{d\Gamma/dt[\bar{M}^0_{\text{phys}}(t) \to f_{CP}] - d\Gamma/dt[M^0_{\text{phys}}(t) \to f_{CP}]}{d\Gamma/dt[\bar{M}^0_{\text{phys}}(t) \to f_{CP}] + d\Gamma/dt[M^0_{\text{phys}}(t) \to f_{CP}]} \\ &= \frac{S_f \sin \Delta m t - C_f \cos \Delta m t}{\cosh \Delta\Gamma t/2 - A_f^{\Delta\Gamma} \sinh \Delta\Gamma t/2},\end{aligned} \tag{2.73}$$

for B meson decays, where

$$S_f \equiv \frac{2\mathcal{I}m(\lambda_f)}{1+|\lambda_f|^2}, \quad C_f \equiv \frac{1-|\lambda_f|^2}{1+|\lambda_f|^2}, \quad A_f^{\Delta\Gamma} \equiv \frac{-2\mathcal{R}e(\lambda_f)}{1+|\lambda_f|^2}. \tag{2.74}$$

For decays where $\Delta\Gamma \approx 0$, the denominator of Eq. (2.73) is unity, and CP asymmetries are often parameterised in terms of S_f and C_f. This is a valid assumption for B^0 decays but not for those of the B^0_s meson. Δm has been measured for both B_d and B^0_s, most recently in Refs. [76] and [77]. This variety of CP violation has been observed in the $B^0 \to J/\psi K^0$ channel:

$$S_{\psi K^0} \approx \mathcal{I}m(\lambda_{\psi K^0}) = +0.709 \pm 0.011,$$

as well as in numerous other channels.

2.4 Flavour symmetries

Moving on from asymmetries, a well-known approximate *symmetry* for heavy-flavour physics is the SU(3) symmetry, relating decays with u, d, and s quarks interchanged. Since these three light quarks have masses much smaller than Λ_{QCD}, they can be approximated to have the same mass. This is known as the *SU(3) limit* and acts as a way of obtaining leading-order predictions. Such first-order results can only be predicted to be accurate to within around $\sim 30\%$, and it is then possible to include corrections at higher orders - the first set of SU(3)$_F$-breaking terms would be expected to be $\sim 10\%$ accurate. Following on from Section 2.1.2, Section 2.4.3 elaborates and formalises the theoretical foundations behind this approach, while Section 2.4.4 summarises the important ideas that will be utilised later on, particularly in Chapters 6 and 7.

2.4.1 Isospin

Immediately after the discovery of the neutron[19] in 1932, the strong similarity between the proton and neutron prompted nuclear physicists to interpret both particles as two states of the same particle, the *nucleon*. The masses of the proton and neutron are indeed nearly equal, a requirement for this interpretation to be meaningful, with the small difference being partly explained by the different electromagnetic interactions of the two particles. The wave function of this nucleon state can then be labelled with the coordinate τ, to distinguish between the two charge states, in addition to the space-time coordinates

[19] Which won the 1935 Nobel Prize for James Chadwick [15].

r and t, and the spin state s. The convention is taken that $\psi_p = \psi(r,t,s,\tau = +1)$ is the proton state and $\psi_n = \psi(r,t,s,\tau = -1)$ is the neutron state[20] [26].

One can represent the wavefunction of the nucleon, ψ, as a state within a vector-space with basis vectors corresponding to these proton and neutron states

$$\psi = \begin{pmatrix} u_1(r,t,s) \\ u_2(r,t,s) \end{pmatrix}, \tag{2.75}$$

where $|u_1(r,t,s)|^2$ is the probability density for a proton at position r, time t with spin projection s and $|u_2(r,t,s)|^2$ analogously for a neutron. Under this basis, the eigenstates of τ are then

$$\chi_p = \begin{pmatrix} \chi(r,t,s) \\ 0 \end{pmatrix} \quad \text{and} \quad \chi_n = \begin{pmatrix} 0 \\ \chi(r,t,s) \end{pmatrix}, \tag{2.76}$$

i.e. a proton and neutron in the state $\chi(r,t,s)$, respectively, and the appropriate eigenvalues can be retrieved with the following 2×2 matrix operator

$$\hat{\tau} = \begin{pmatrix} 1 & 0 \\ 0 & -1 \end{pmatrix}. \tag{2.77}$$

Strong similarities with the description of spin can be seen here, and one could interpret τ as representing the two possible projections of a vector of unit length; "up" and "down". Indeed, one can introduce "raising" ($\hat{\tau}_+$) and "lowering" ($\hat{\tau}_-$) operators to transform between the two states. As with spin, we choose τ to be the 3rd component of a three-dimensional vector, $\hat{\boldsymbol{\tau}} = (\hat{\tau}_1, \hat{\tau}_2, \hat{\tau}_3 = \hat{\tau})$, with

$$\hat{\tau}_1 = \hat{\tau}_+ + \hat{\tau}_- = \begin{pmatrix} 0 & 1 \\ 1 & 0 \end{pmatrix}, \quad \hat{\tau}_2 = -i(\hat{\tau}_+ - \hat{\tau}_-) = \begin{pmatrix} 0 & i \\ -i & 0 \end{pmatrix}. \tag{2.78}$$

In fact, the three generators $\hat{\tau}_1, \hat{\tau}_2, \hat{\tau}_3$ are the very same Pauli matrices that appear as the operators for spin in quantum mechanics, albeit scaled by a factor of two. This new property is called *isospin*, with operators typically defined as $\hat{T}_k = \frac{1}{2}\hat{\tau}_k$, which are also the same as the operators associated with the electroweak bosons in Section 2.1.1. The property of isospin is often alternatively denoted by I, but this notation will be avoided for the time-being to prevent confusion with the identity matrix. The isospinor ψ then transforms according to $\psi(r,t,s) \to \exp\left(-i\epsilon_v \hat{T}_v\right)\psi(r,t,s)$. In this *isospin group*, a representation of $SU(2)$, one can sort particles with the same T into *charge multiplets*, where each multiplet has a particle state for each integer multiple of e in some range between Q_{min} and Q_{max}. In general, the "centre of charge", $\frac{1}{2}(Q_{\text{min}} + Q_{\text{max}})$, may differ from zero, i.e. $|Q_{\text{min}}| \neq |Q_{\text{max}}|$, and to symmetrise the situation, the isospin component T_3 counts the charge of a particle relative to the centre of charge. This centre of charge happens to be related to the hypercharge as $\frac{1}{2}Y$, and hence the allowed charges for a given isospin

[20] This concept of a vector pointing "up" and "down" motivated the naming of the u and d quarks [70], after the elucidation of the non-fundamental nature of nucleons through the Nobel-Prize-winning work of Robert Hofstadter [15], among that of others.

are given by the Gell-Mann-Nishijima relation [78,79],

$$Q = \frac{1}{2}Y + T_3, \quad T_3 = \{x \in \mathbb{Z} | -T \leq x \leq T\},$$

similar to what was seen in Section 2.1.3. Since the maximum value of T_3 is T, then

$$T = (Q_{\max} - Q_{\min})/2.$$

2.4.2 Quarks and SU(3)

SU(3) has eight generators with the $\hat{\lambda}_j$ obeying the Lie algebra $[\hat{\lambda}_i, \hat{\lambda}_j] = 2if_{ijk}\hat{\lambda}_k$, where f_{ijk} are the structure constants for SU(3). As was seen in Section 2.1.3, the Gell-Mann matrices are one such representation. Let us look at the smallest non-trivial representation of SU(3). Since the isospin doublet with T = 1/2 is the smallest non-trivial description of the isospin group SU(2), one can construct all higher multiplets from this representation. The *Clebsch-Gordan coefficients* give the coupling of two individual isospins to the total isospin (see Section 2.4.3). SU(2) appears as a subalgebra of SU(3) through the relation of isospin to the SU(3) generators

$$\hat{T}_\pm = \frac{1}{2}(\hat{\lambda}_1 \pm \hat{\lambda}_2), \quad \hat{T}_3 = \frac{1}{2}\hat{\lambda}_3. \tag{2.79}$$

Since SU(3) has eight generators, there emerge two other types of operation, *U-spin* ($d \leftrightarrow s$) and *V-spin* ($u \leftrightarrow s$), which appear analogous to isospin (T-spin) [26]

$$\hat{U}_\pm = \frac{1}{2}(\hat{\lambda}_6 \pm i\hat{\lambda}_7), \quad \hat{U}_3 = \frac{1}{4}(-\hat{\lambda}_3 + \sqrt{3}\hat{\lambda}_8), \tag{2.80}$$

$$\hat{V}_\pm = \frac{1}{2}(\hat{\lambda}_4 \pm i\hat{\lambda}_5), \quad \hat{V}_3 = \frac{1}{4}(\hat{\lambda}_3 + \sqrt{3}\hat{\lambda}_8), \tag{2.81}$$

$$[\hat{U}_3, \hat{U}_\pm] = \pm\hat{U}_\pm, \quad [\hat{U}_+, \hat{U}_-] = 2\hat{U}_3, \tag{2.82}$$

$$[\hat{V}_3, \hat{V}_\pm] = \pm\hat{V}_\pm, \quad [\hat{V}_+, \hat{V}_-] = 2\hat{V}_3. \tag{2.83}$$

Hypercharge is often used to characterise states in place of U- and V-spin, being related to them through

$$\hat{Y} = \frac{2}{3}(\hat{U}_3 + \hat{V}_3) = \frac{1}{\sqrt{3}}\hat{\lambda}_8. \tag{2.84}$$

Since the algebra of SU(3) contains the isospin algebra as a subalgebra, the smallest SU(3) representation must contain at least one $T = 1/2$ charge doublet. As a matter of fact, the T-spin, U-spin, and V-spin algebras appear fully symmetric in the algebra of SU(3). Consequently, the SU(3) multiplet we are interested in must contain T, U, and V doublets. Because of the inherent symmetries of the SU(3) multiplets in the $Y - T_3$ plane, we are led to the two equilateral triangles shown in Figure 2.8, denoted by **[3]** and **[$\bar{\mathbf{3}}$]**. As required by general symmetries, they are symmetrically centered around the origin ($Y = 0$, $T_3 = 0$). We see then the link between these states and the three species of light quark (u, d, and

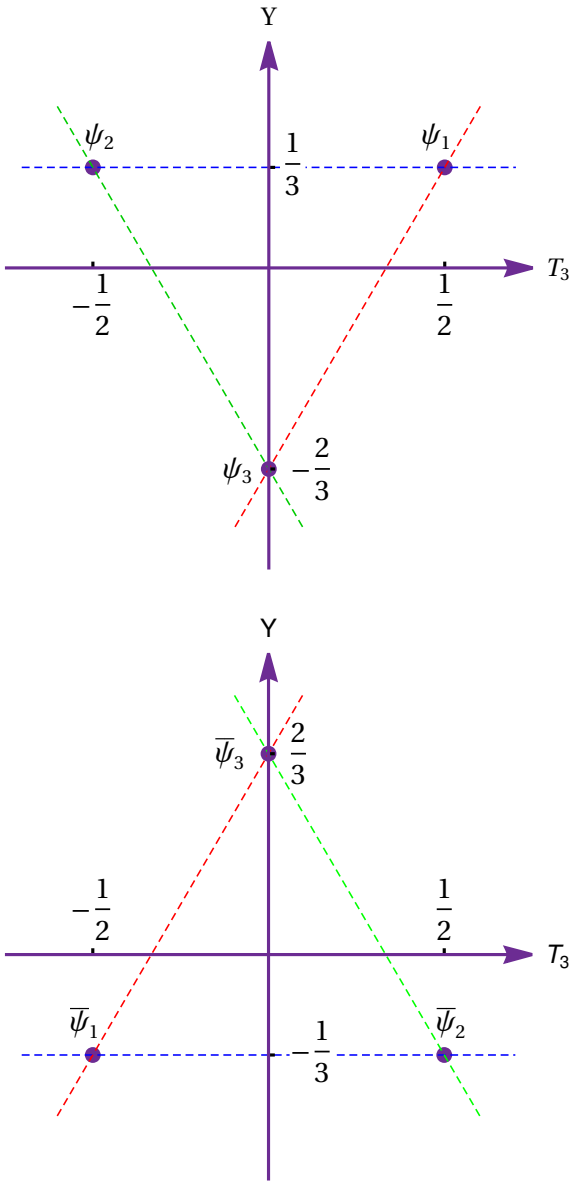

FIGURE 2.8: The lowest order non-trivial representation of SU(3) is the triplet. In both cases there are three SU(2) doublets; isospin (blue), U-spin (green), and V-spin (red).

s), which form such a triangle in the $Y - T_3$ plane with their (Y, T_3) quantum numbers of $\left(\frac{1}{3}, \frac{1}{2}\right)$, $\left(\frac{1}{3}, -\frac{1}{2}\right)$ and $\left(-\frac{2}{3}, 0\right)$, as do the corresponding anti-quarks. Note that in this representation u and d form a left-handed doublet, while s is a singlet under isospin. Just like the notation used in Section 2.1.3, $[\bar{\mathbf{3}}]$ represents the anti-particle equivalents of the particles in $[\mathbf{3}]$, since the state $\bar{\psi}_\nu$ has opposite hypercharge and opposite T_3 component, and so the opposite charge as compared to ψ_ν:

$$\hat{Q}\psi_\nu = Q_\nu \psi_\nu, \quad \hat{Q}\bar{\psi}_\nu = -Q_\nu \bar{\psi}_\nu. \tag{2.85}$$

General n-state representations have $[\mathbf{n}]$ and $[\bar{\mathbf{n}}]$.

2.4.3 Making Predictions

From symmetries to matrix elements

In an approximate SU(3) flavour, or $SU(3)_F$, symmetry (assuming $m_u \approx m_d \approx m_s \ll \Lambda_{QCD}$), decay amplitudes can be expressed in terms of SU(3) matrix elements, with u, d, and s quarks represented by the triplet states $|\mathbf{3}; \frac{1}{2}, \frac{1}{2}, \frac{1}{3}\rangle$, $|\mathbf{3}; \frac{1}{2}, -\frac{1}{2}, \frac{1}{3}\rangle$ and $|\mathbf{3}; 0, 0, -\frac{2}{3}\rangle$ respectively. The numbers after the semi-colon indicate the values of $(T,\ T_3,\ Y)$ [26], the relevant quantum numbers here, and anti-quarks are similarly represented by anti-triplet states $[\bar{\mathbf{3}}]$. The remaining heavy-flavour quarks are all represented by singlets, $|\mathbf{0}\rangle$, meaning that hadrons containing only one light quark have the same group-theoretical representation as that quark, e.g. $B^+(\bar{b}u)$ is represented by $|\mathbf{3}; \frac{1}{2}, \frac{1}{2}, \frac{1}{3}\rangle$. When considering multiple hadrons in the final state, one can make use of the fact that the product of two irreducible representations $[\mathbf{r_1}], [\mathbf{r_2}]$ (with quantum numbers α_1, α_2) can be expressed as the sum over irreducible representations $[\mathbf{R_n}]$ (with quantum numbers A_n) weighted by the Clebsch-Gordan coefficients. This means [80]

$$|\mathbf{r_1}; \alpha_1\rangle\, |\mathbf{r_2}; \alpha_2\rangle = \Sigma_i(\mathbf{R_i}, A_i|\mathbf{r_1}, \alpha_1, \mathbf{r_2}, \alpha_2)\, |\mathbf{R_i}; A_i\rangle\,. \tag{2.86}$$

Thus, the final state of the decay can be expressed as a weighted sum over pure SU(3) states.

The *Wigner-Eckart* theorem[21] states that a matrix element involving an *irreducible* operator, i.e. represented by block-diagonal matrices, is given by the sum of *reduced matrix elements*, with a *reduced* number of quantum numbers, weighted by appropriate Clebsch-Gordan coefficients [26, 81]. To be explicit for the $SU(3)_F$ states, for an interaction from initial state $|\mathbf{r_i}; \alpha_i\rangle$ to final state $|\mathbf{r_f}; \alpha_f\rangle$ via a Hamiltonian $\hat{H}_q^{(\mathbf{k})}$ (in the representation $[\mathbf{k}]$ with quantum numbers q), the matrix element can be decomposed via

$$\langle \mathbf{r_f}; \alpha_f|\, \hat{H}_q^{(\mathbf{k})}\, |\mathbf{r_i}; \alpha_i\rangle = (\mathbf{r_f}, \alpha_f|\mathbf{k}, q, \mathbf{r_i}, \alpha_i)\, \langle \mathbf{r_f}|\, |\hat{H}^{(\mathbf{k})}|\, |\mathbf{r_i}\rangle\,. \tag{2.87}$$

In this way, matrix elements for specific interactions

$$\mathcal{A}(i \to f) = \langle f|\, \mathcal{H}\, |i\rangle \tag{2.88}$$

can be re-expressed in terms of such reduced SU(3) matrix elements.

Combining the triplet and anti-triplet structures seen in Figure 2.8 generates an octet (plus singlet) structure[22]

$$|\mathbf{3}\rangle \otimes |\bar{\mathbf{3}}\rangle = |\mathbf{8}\rangle \oplus |\mathbf{1}\rangle\,,$$

[21] Named after Eugene Wigner and Carl Eckart, with the former being awarded the Nobel Prize in 1963 for his development of symmetry principles applied to subatomic physics [15].

[22] Dubbed *The Noble Eightfold Path* by Gell-Mann as a tongue-in-cheek reference to the Buddhist philosophy [82–84]. Nonetheless, he was awarded the 1969 Nobel Prize for his efforts [15].

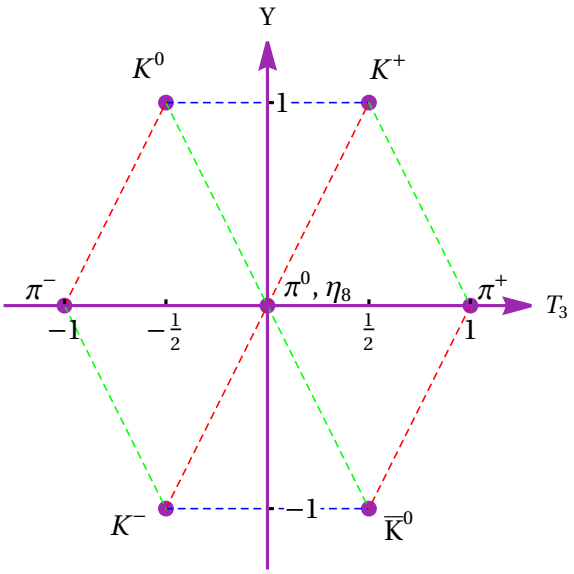

FIGURE 2.9: The octet structure of the lowest-energy pseudoscalar mesons.

with states that correspond to the lowest energy mesons;

$$\pi^+ = |u\bar{d}\rangle\,,\ \pi^- = |d\bar{u}\rangle\,,\ K^+ = |u\bar{s}\rangle\,,\ K^0 = |d\bar{s}\rangle\,,\ K^- = |s\bar{u}\rangle\,,\ \bar{K}^0 = |s\bar{d}\rangle\,,$$
$$\pi^0 = \frac{1}{\sqrt{2}}\left(|u\bar{u}\rangle - |d\bar{d}\rangle\right),\ \text{and}\ \eta_8 = \frac{1}{\sqrt{6}}\left(|u\bar{u}\rangle + |d\bar{d}\rangle - 2\,|s\bar{s}\rangle\right),$$

from the octet (see Figure 2.9), plus the $\eta_1 = \frac{1}{\sqrt{3}}\left(|u\bar{u}\rangle + |d\bar{d}\rangle + |s\bar{s}\rangle\right)$ singlet. The physical η and η' states that come from mixing of η_8 and η_1 will not be considered further here. Quarks and anti-quarks have even- and odd-parities, respectively, resulting in an odd-parity state when combined. These lowest-energy configurations will also have zero spin, as the two spin-1/2 constituents will be anti-aligned. On account of these spin and parity properties, these mesons are *pseudoscalars*. Combining a light anti-quark with a charm quark produces an anti-triplet of D mesons, $D^0(c\bar{u})$, $D^+(c\bar{d})$, $D_s^+(c\bar{s})$, and similar conjugates, while combining with a beauty quark produces an anti-triplet of B mesons, $B^-(b\bar{u})$, $\bar{B}^0(b\bar{d})$, $\bar{B}_s^0(b\bar{s})$, and similar conjugates. All of these states can be excited to the spin-1 states (typically denoted with an asterisk), which are vector particles.

From matrix elements to observables

Section 2.3 shows the relationship between these amplitudes and observable CP asymmetries. The equivalent relation for branching ratios is [85]

$$\mathcal{B}(B \to XX') = |\mathcal{A}(B \to XX')|^2 \mathcal{P}(B, X, X'), \tag{2.89}$$

where $\mathcal{P}(B, X, X')$ is a phase-space factor that is given by

$$\mathcal{P}(B, P, P') = \frac{\tau_B |\mathbf{p}|}{8\pi m_B^2}, \quad |\mathbf{p}| = \frac{m_B}{2}\Phi\left(\frac{m_X}{m_B}, \frac{m_{X'}}{m_B}\right) \tag{2.90}$$

for decays to two pseudoscalar mesons. Here τ_B is the B meson lifetime, m_i denotes the mass of particle i, and Φ is a phase-space function

$$\Phi = [(1-(x+y)^2)(1-(x-y)^2)]^{1/2}. \tag{2.91}$$

For the case of neutral B mesons, which exhibit mixing, Eq. (2.89) only applies in the limit that the difference in decay widths between mass eigenstates, $\Delta\Gamma$, is negligible. This approximation can be made for B^0 mesons, however a small correction is necessary for B_s^0 mesons. Experimentally, time-integrated branching ratios are typically measured, and in this instance [86]

$$\mathcal{B}(\bar{B}_s^0 \to PP') = \frac{1 - A^f_{\Delta\Gamma} y_s}{1 - y_s^2} |\mathcal{A}|^2 \cdot \mathcal{P}(\bar{B}_s^0, P, P')\,, \tag{2.92}$$

where y_s has been experimentally determined to be $2y_s = \Delta\Gamma_s/(\Gamma_s) = 0.128 \pm 0.007$ [87]. In fact, for flavour specific B_s^0 decays, $A^f_{\Delta\Gamma}$ is zero, and the smallness of y_s means that Eq. (2.89) approximately holds in this instance too.

2.4.4 Summary

To summarise, QCD in the SM is expected to exhibit an approximate symmetry under operations exchanging u, d, and s quarks on account of their small masses relative to the QCD scale. This symmetry follows the SU(3) group, and all the participating particles in a reaction may be considered as representations of this group. Known mathematical results of how these can be combined allow the calculation of matrix elements (and thus observables) in terms of a few SU(3) parameters. The degree of breaking of this approximate symmetry is non-negligible $\sim 30\%$, and, as will be seen in Chapters 6 and 7, corrections to this can be included as perturbations. Thus, working in such an approximation provides an effective way to make calculations without the need for in-depth computationally-challenging QCD simulations, and is particularly useful when these alternative methods are not possible at all. QCD factorisation is another approximation that is often made to perform such calculations.

2.5 Expansions of QCD

Theoretical calculations of decays with an all-hadronic final state are generally complicated owing to the related non-trivial QCD dynamics. This section briefly discusses two expansions of QCD that allow such calculations to be simplified and will play a role later. The first approach is *QCD factorisation* (QCDF), which is an expansion in both α_s and Λ_{QCD}/m_b. This is a well-defined framework, based on effective field theories [88], that allows precision predictions for hadronic decays, however its applicability is only given if a considered decay meets certain well-defined conditions. In instances where QCDF cannot be applied, one can turn to an alternative approach, an expansion in powers of the

number of colours, N_c, which is far less precise but allows order of magnitude estimates to be made.

2.5.1 QCD Factorisation

The large size of the b quark mass in comparison to the strong interaction scale (Λ_{QCD}) can simplify calculations for decays involving these particles. In the limit of $\alpha_s \to 0, m_b \to \infty$, the hadronic matrix element for $\bar{B}^0 \to \pi^+\pi^-$, for example, can be represented in the simple form [89]

$$\left\langle \pi^+\pi^- \right| Q \left| \bar{B}^0 \right\rangle = \left\langle \pi^- \right| j_1 \left| \bar{B}^0 \right\rangle \left\langle \pi^+ \right| j_2 \left| 0 \right\rangle, \tag{2.93}$$

where Q is a local operator in the weak effective Hamiltonian and $j_{1,2}$ are quark currents. Through this *naïve factorisation*, the decay is separated into two parts - a transition of $\bar{B}^0 \to \pi^-$ with the emission of a W boson, parameterised by the form factor $F^{B\to\pi}$ dependent on the W momentum transfer, and then the creation of a π^+ meson from the vacuum by said W boson, parameterised by a decay constant f_π.

Introducing higher order terms in α_s breaks the simplicity of naïve factorisation, and a generalised form is required for other modes. Within the formalism of QCDF, the matrix element for the decay of a B meson to a D meson and a light pseudoscalar meson, h, once again factorises into two parts [58, 90]

$$\langle Dh| Q_i |B\rangle = \sum_j F_j^{B\to D}(m_h^2) \int_0^1 du T_{ij}^I(u)\phi_h(u) + \mathcal{O}\left(\frac{\Lambda_{QCD}}{m_b}\right). \tag{2.94}$$

The $F_j^{B\to D}$ are form factors for the $B \to D$ transition, and m_h is the invariant mass of h. The second part itself involves two functions, hard-scattering functions $T_{ij}^I(u)$, which describe dynamics in the limit of large momentum transfer and can be calculated perturbatively, and the light-cone distribution amplitude, $\phi_h(u)$, which describes the momentum distributions of the quark-antiquark pair within h and is non-perturbative. Details of these latter quantities can be found in Ref. [90]. QCDF becomes problematic for heavier final states, such as $B \to DD'$, as the expansion in mass receives more significant corrections at leading order. In fact, this particular set of decays will be examined theoretically in Chapter 6, where a different approach is taken to produce predictions that can be confronted with experimental data to probe for potential BSM effects.

In the limit of $m_b \to \infty$ (though at all orders in α_s), the amplitude for a $B \to Dh$ decay is given as [58]

$$\mathcal{A}(B \to Dh) = i\frac{G_F}{\sqrt{2}} a_1(Dh)\, V_{cb}\, V_{cq}\, (m_B^2 - m_D^2)\, f_h\, F_0^{B\to D}(m_h^2), \tag{2.95}$$

where G_F is the Fermi constant (= $1.17 \times 10^{-5}\,\text{GeV}^{-2}$ [14]), $a_1(Dh)$ is the effective Wilson coefficient, V_{ij} are CKM matrix elements, f_h is the decay constant of h (which can be calculated using lattice QCD), and $F_0^{B\to D}$ is the form factor for pseudoscalar-to-pseudoscalar

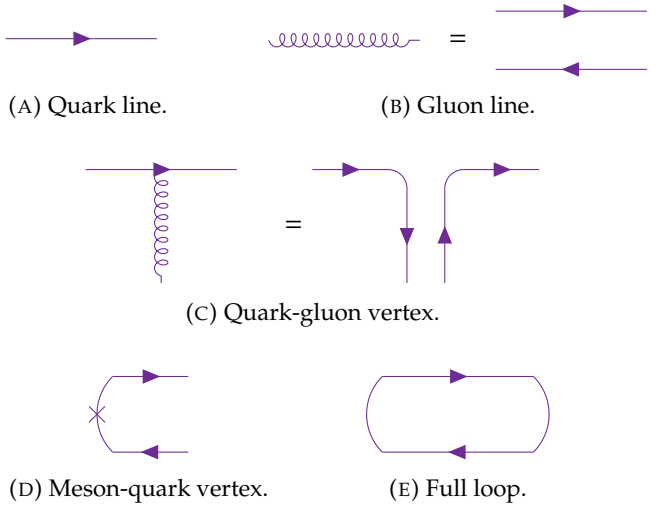

(A) Quark line. (B) Gluon line.

(C) Quark-gluon vertex.

(D) Meson-quark vertex. (E) Full loop.

FIGURE 2.10: $1/N_c$ power counting rules. Adapted from diagrams shown in Ref. [93].

$B \to D$ transitions. This last quantity is expressed in the BGL parameterisation as [91]

$$F_0(z) = \frac{1}{P_0(z)\phi_0(z)} \sum_{n=0}^{N} a_n^0(t_0) z^n, \tag{2.96}$$

where

$$z(q^2, t_0) = \frac{\sqrt{t_+ - q^2} - \sqrt{t_+ - t_0}}{\sqrt{t_+ - q^2} + \sqrt{t_+ - t_0}}, \tag{2.97}$$

with $t_0 = (M_B + M_D)(\sqrt{M_B} - \sqrt{M_D})^2 \simeq 6.19\,\text{GeV}^2$ and $t_+ = (M_B + M_D)^2 \simeq 51.12\,\text{GeV}^2$. The coefficients, a_n^0, are determined from fits to lattice QCD and are provided in documents like Ref. [92]. This approach will be revisited in the context of $B \to DD'$ in Chapter 6.

2.5.2 $1/N_c$ Expansion

The formula of naïve factorization, which can be obtained in the limit $\alpha_s \to \infty$ and $m_b \to 0$ can also be obtained in another limit of QCD, namely the limit of a large number of colours. Figure 2.10 shows the basic procedure for setting up a topology to calculate the N_c suppression power [93]. A quark is represented by a line (A) and a gluon may be replaced by two lines (B). A quark-gluon vertex (as seen in C) carries a factor of $(1/N_c)^{1/2}$. Note that this factor should be included before replacing the gluon with two lines. A meson-quark vertex, represented as shown in D, also carries a factor of $(1/N_c)^{1/2}$. In addition, any closed quark loop (E) carries a factor of N_c. See Figure 2.11 for an example of this procedure applied to estimate the relative suppression between two types of decay. This methodology will become useful to place bounds on different diagrams in Chapter 6. It should be reiterated that this approach is suitable for obtaining order-of-magnitude estimates only.

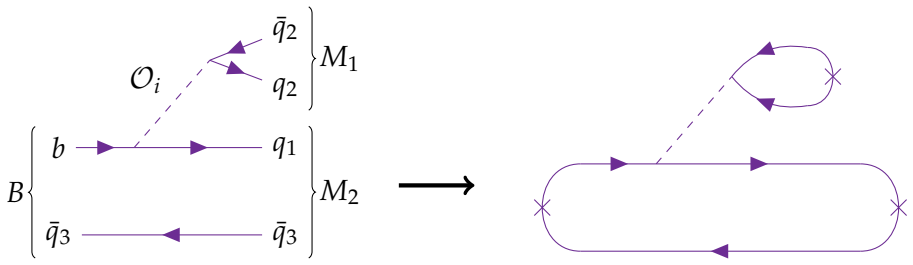

(A) "Tree" Topology

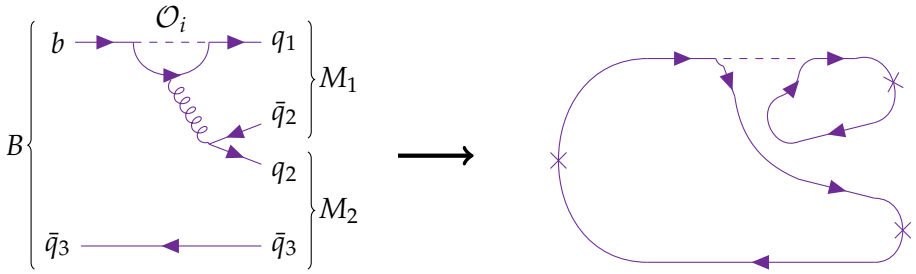

(B) "Penguin" Topology

FIGURE 2.11: Example colour-flow diagrams for two different topologies. Both diagrams have two full loops, carrying a factor of N_c each, and three quark-meson vertices, carrying a factor of $(1/N_c)^{1/2}$ each. In the second diagram there are also two quark-gluon vertices not present in the first, which both come with a factor $(1/N_c)^{1/2}$. The overall suppression of the "penguin" topology, relative to the "tree" topology, based on $1/N_c$ power counting alone is $1/N_c$.

3 The LHCb Experiment

"The show must go on ... inside my heart is breaking, my make-up may be flaking but my smile stays on"

- Queen, *The Show Must Go On*

3.1 History of Heavy-Flavour Physics

The LHCb experiment was by no means the first one to study the interactions of heavy-flavour quarks (i.e. c and b quarks). This story kicked off with the discovery of the J/ψ meson ($c\bar{c}$) independently at Brookhaven National Lab (BNL) [94] and the Stanford Linear Accelerator Center (SLAC) [95] in 1974, which confirmed the quark model, then theorised to have only four flavours [96][1]. In the wake of this, the CLEO detector [98] (recording the collisions from the Cornell Electron-positron Storage Ring or CESR) was commissioned and, from 1979, became the first experiment dedicated to heavy-flavour physics. Operating at around 9-12 GeV, the experiment's early activities involved exploring the three $b\bar{b}$ resonances discovered in 1977-1980 at Fermilab [99, 100], labelled $\Upsilon(1S)$, $\Upsilon(2S)$, and $\Upsilon(3S)$ [101]. It then spent most of its time around the $\Upsilon(4S)$, becoming the first detector to discover this resonance [102] and to study the decays of B mesons [103]. The experiment continued to run for nearly 30 years, shutting down in March 2008 after five significant upgrades in the course of its history and recording many major discoveries, such as that of the B^0 meson [103], D_s meson [104], and $b \to u$ transitions [105].

Already by the early 1980s, it had been proposed that CP violation could, in principle, be measured in the beauty sector, following its discovery in K's, through neutral B meson decays. However, the statistics required appeared to be far beyond the reach of CLEO [106]. Following the measurement of B meson lifetimes at SLAC in 1983 [107, 108]

[1] George Glashow, who co-proposed this fourth quark, is quoted as saying, "We called our construct the 'charmed quark', for we were fascinated and pleased by the symmetry it brought to the subnuclear world." [97]. The J/ψ discovery was awarded the 1976 Nobel Prize [15], which was awarded again in 1990 for another vindication of the quark model (from deep inelastic scattering measurements) by Jerome I. Friedman, Henry Way Kendall, and Richard E. Taylor.

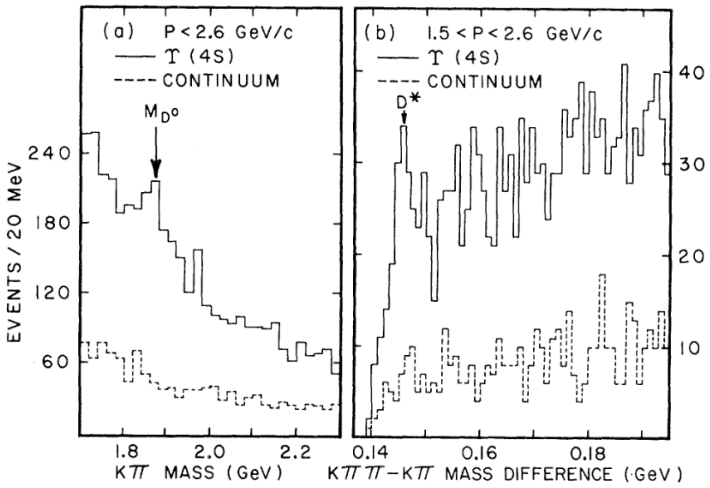

FIGURE 3.1: First observation of B-meson decays to final states consisting of a D or D^* and one or two charged pions. Taken from [103].

and the unexpected discovery of $B^0 - \bar{B}^0$ oscillations [109] by the ARGUS experiment at DESY in 1987, it was concluded that such measurements could indeed be made but only with a thousand-fold increase in the size of the data samples that had previously been collected [106].

To this end, in the late 1990s, the *B-factories* were constructed, so named as they were designed to specifically produce B mesons in significant numbers so as to make precise measurements of these particles. The two primary experiments of this type at that time were BELLE, located at KEK in Japan, and BaBar, located at SLAC in California. They both collided electron-positron pairs at centre-of-mass energies around the $\Upsilon(4S)$ resonance at approximately 10 GeV, and so produced almost exclusively $b\bar{b}$, which would hadronise into pairs of quantum-correlated neutral or charged B mesons. The energies of the colliding beams were asymmetric, meaning that the b meson pairs were highly boosted in the laboratory frame and so had considerable decay lengths that were easy to measure. With integrated luminosities (defined later) of over $1000\,\text{fb}^{-1}$ [110] and over $500\,\text{fb}^{-1}$ [111] respectively, these experiments measured many of the CKM parameters with high precision [110, 112], and discovered CP violation in the decays of neutral B mesons [113].

From the late 1980s, there was also a heavy flavour physics program at the proton-antiproton ($p\bar{p}$) Tevatron collider with the CDF and DØ detectors, which also famously discovered the top quark in 1995 [114]. The main benefit of using hadron collisions over those of leptons was the lack of significant bremsstrahlung effects, allowing operation at a far higher centre-of-mass energy of around 2 TeV [115]. The experiment reached a peak instantaneous luminosity of $4 \times 10^{32}\,\text{cm}^{-2}\text{s}^{-1}$ [116] and took a total integrated luminosity of $\sim 10\,\text{fb}^{-1}$ [117]. The discovery of the B_c meson [118], B_s oscillations [119], and the first measurement of the CKM variable β_s [120] were some of the key successes in beauty physics to come out of these experiments.

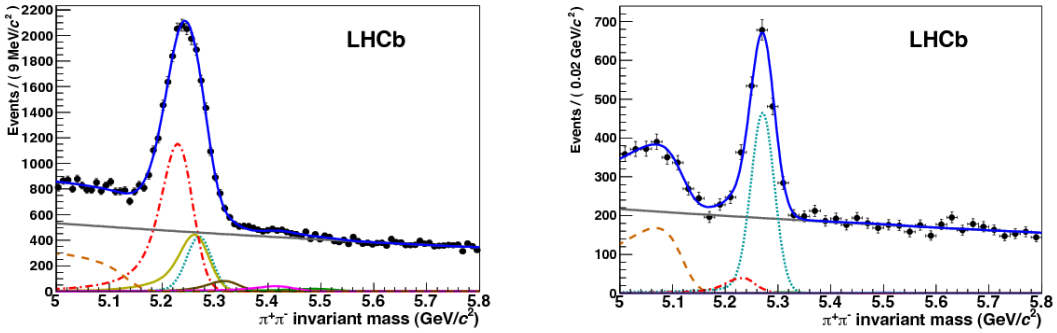

FIGURE 3.2: The invariant mass distribution for reconstructed $B^0 \to \pi^+\pi^-$ decays [126] before (left) and after (right) the application of selections on RICH information to discriminate between pions, kaons, and protons. The signal is shown by the turquoise dotted line with background components designated by other colours; $B^0 \to K\pi$ (red dashed-dotted), $B^0 \to$ three-body (orange dashed-dashed), $B_s^0 \to KK$ (yellow), $B_s^0 \to K\pi$ brown, $\Lambda_b^0 \to pK$ (purple), $\Lambda_b^0 \to p\pi$ (green), and combinatorial (grey). Selections significantly reduce these backgrounds, and so the signal peak can be clearly resolved. Figures taken from Ref. [127].

In 2008, the LHC at CERN became the successor to the Tevatron as the world's highest-energy proton collider, with a design energy of $\sqrt{s} = 14\,\text{TeV}$, and LHCb was designed as its specialist flavour physics experiment. Run 1 operated at 7 TeV, Run 2 at 13 TeV, and Run 3 is currently running at 13.6 TeV. As will be explored further later, the unique design of LHCb has enabled more precise measurements to be made of previously measured quantities as well as making discoveries, including measuring CP violation in charm decays [75], new exotic hadrons (for example X(6900) [121], $P_c(4450)^+$ and $P_c(4380)^+$ [122]), and lepton flavour universality measurements (mentioned earlier) that hint at the presence of new physics [57]. Other LHC experiments (namely ATLAS and CMS) can also make measurements of heavy flavour physics and indeed have presented a number of results in the field, for instance B^+ production cross-sections [123], β_s [124], and, in combination with LHCb, a measurement of $B_s^0 \to \mu^+\mu^-$ [125]. Their higher luminosities offer the possibility of higher statistics, however their instrumentation covering the full 360° around the beam-axis does not favour the reconstruction of B mesons, which are produced predominantly at small angles. By virtue of not being designed exclusively for B physics, their selections are also necessarily less sensitive than more specific experiments like LHCb. Most importantly, they lack detectors, like LHCb's RICH (**R**ing-**I**mage **Ch**erenkov) detectors, that can differentiate between low-momentum pions and kaons, which appear topologically similar. Measuring CPV requires good knowledge of the flavour content of final states, and in order to reduce backgrounds from similar decays one must be able to veto misidentified candidates well. The impact of this can be seen in Figure 3.2.

In recent years, there has been a second incarnation of BELLE in operation, aptly named BELLE-II, which offers complementary measurements to those of LHCb, benefiting from a "cleaner" collision environment and a roughly hermetic coverage, leading to much-improved reconstruction of neutral particles. While bremsstrahlung limits the

centre-of-mass energies of lepton colliders, the fact that BELLE-II operates at the $\Upsilon(4S)$ resonance means that neutral and charged B mesons are produced in abundance. The lack of hadronic effects means that essentially all of the collision energy goes to producing these particles. While some time is spent at the $\Upsilon(5S)$ resonance, to permit the production of B_s^0 mesons, the lengths of these runs are more limited, and so they are not as well-suited to performing measurements with B_s^0 mesons, compared to LHCb. BESIII in China has a similar operating principle, though targets instead resonant production of $c\bar{c}$ pairs, and is therefore specialised towards precision charm measurements.

3.2 The Large Hadron Collider (LHC)

The LHC is the best-known machine at CERN, one of the world's largest and longest-running high-energy physics organisations, located near Geneva on the French-Swiss border. High energies allow for the creation of high-mass particles through $E^2 = p^2c^2 + m^2c^4$, so such a set-up permits the study of the production and decay of all the particles predicted in the Standard Model. This means that it is possible to test the fundamental parameters of the theory.

3.2.1 The Journey to the LHC

There are several steps that must be performed before any protons enter the LHC. The first stage of acceleration involves **Lin**ear **Ac**celerator 4 (Linac4) [128], which uses **r**adio-**f**requency (RF) cavities (i.e. alternating electric fields) to gradually linearly accelerate the input H^- ions in stages to an energy of 160 MeV. The direction of the field switches as the particles reach each successive cavity, such that continued acceleration in a straight line can be achieved without the need for huge potential differences. This can be seen in Figure 3.3.

Quadrupole magnets also focus the ions into a tight beam. The ions are stripped of their two electrons, leaving only protons, and are pulsed by the *chopper* before entry into the Proton Synchrotron Booster [129]. Bending the particles in a circular path with magnetic fields makes the accelerator far more compact. In such a circular accelerator, the momentum and energy of ultra-relativistic particles depend on the bending radius ρ and the average magnetic field B [14]:

$$p = ZeB\rho \quad \text{or} \quad E[\text{GeV}] = 0.3Z(B\rho)[\text{Tm}], \tag{3.1}$$

for a particle of charge Ze. An approximately constant radius of orbit during acceleration can be achieved by tuning the magnetic field with the energy of the protons. Therefore, higher energies may be achieved through larger rings or more powerful magnets (or even both). In the Proton Synchrotron Booster, dipole magnets constrain the protons to a curved path through four 25 m-radius rings, and, using similar RF cavities to Linac4, their energies are increased to 2 GeV [129].

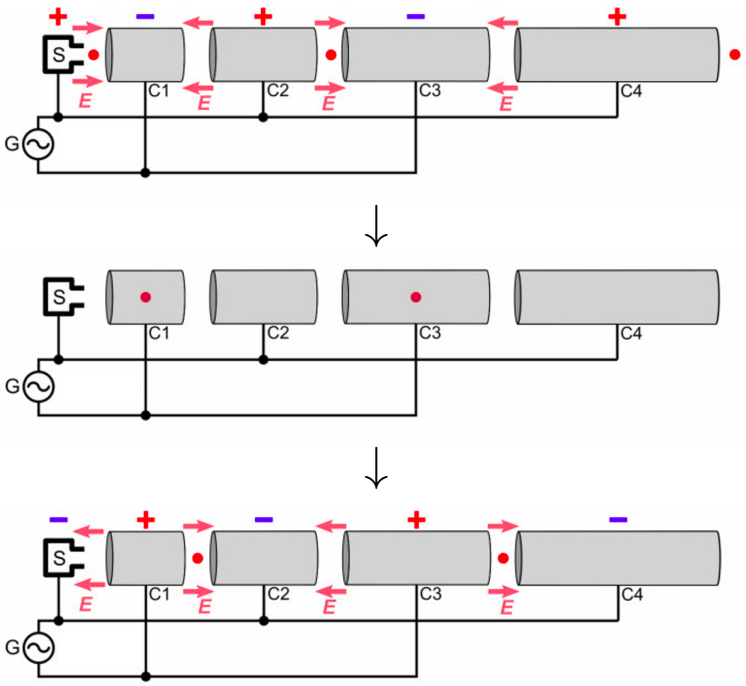

FIGURE 3.3: Operation of a linear accelerator. In the time that a charged particle traverses the length of a cavity, the polarity has flipped. Licensed under Creative Commons.

The next stage, the Proton Synchrotron (PS) [130], is similar to the previous one except with a single ring with a larger radius that increases the energy further to 25 GeV. It is at this stage that the protons are grouped into bunches that are quantised into "buckets" spaced by 25 ns. The Super Proton Synchrotron [131] (an even larger and more sophisticated version of the PS) then boosts the energy to 450 GeV before the protons enter the LHC ring. The LHC uses superconducting (SC) magnets in favour of conventional normal-conducting (NC) magnets that saturate at large field strengths, to avoid the need for unfeasible tunnel lengths or magnet power consumption. The LHC is 26.7 km long ($\rho \approx 2800$ m) with a current beam energy of 6.8 TeV and a maximum magnetic field of 8.3 T (at 1.9 K). The "double-bore" design allows for the acceleration of two counter-rotating beams in the two apertures, which are then collided at given points where experiments can be located.

Talking about a "ring" accelerating to higher energies is, of course, a bit nonsensical. Circular motion requires a force perpendicular to velocity and this does no work[2] therefore no energy gain occurs. To increase a particle's energy one needs linear acceleration. In fact, the LHC has eight long straight sections, each around 500 m in length, where experimental installations can be placed [132], one of which is responsible for linear acceleration. Talking about *the* ring might also give the wrong impression because the counter-rotating beams must be separated to stop them from colliding in the wrong place. Each beam has its own pipe in which it circulates before collision at one of the

[2] I don't mean "does *not* work" here!

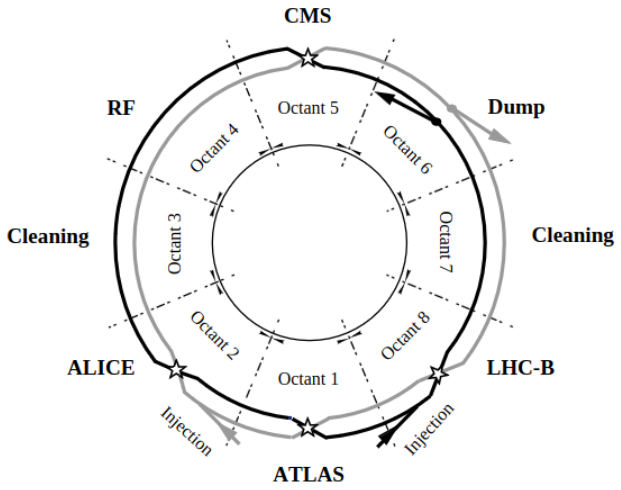

FIGURE 3.4: Diagram of the Large Hadron Collider showing the major experiments and where important operations occur. Taken from [132].

interaction points[3]. The beams can only cross where the pipes open out within the experiments. There are four interaction points and so four major experiments (see Figure 3.4): ATLAS and CMS are diametrically opposite[4] at Points 1 and 5 and have general-purpose detectors; ALICE at Point 2, which studies heavy-ion collisions; and LHCb at Point 8, which is specialised to make precision measurements of the decays of b and c hadrons, and will be the focus of this thesis. Injection of the anti-clockwise beam also takes place at Point 8 [132], while the clockwise beam is injected at Point 2.

The other four points also play an essential role. At Points 3 and 7, the beam is collimated (or "cleaned") to allow for precise collision points with minimal backgrounds from peripheral processes, and to minimise beam loss [132]. These use only NC magnets, which require much lower currents than SC ones, and so the power supplies can be located in surface buildings rather than underground caverns. Point 4 is home to the RF acceleration systems with separate cavities for the two beams. Finally, Point 6 contains the beam-dump, which quickly but safely removes the proton beams from the LHC in the event of loss of control of the beam or at the end of a fill. Here, kicker magnets deflect the beams from their trajectories down 700 m-long transfer tunnels and into massive lead absorbers. Further quadrupole magnets are used to deflect the outgoing beam so that it traces out a spiral shape with time, and dissipates the energy deposition over a wider area.

3.2.2 Proton Collisions

Any claims of discovery rely heavily on statistics and so, particularly for the precision measurements and exploration of the rare processes that are LHCb's forte, achieving

[3] So the LHC is actually two "not-rings". Clear?
[4] Perhaps in more ways than one.

large numbers of detectable interactions of interest is a big priority for high-energy physics experiments. The quantity that determines this is the *luminosity*, $\mathcal{L}$, essentially a measure of the proton density - the number of protons per unit of cross-sectional area in the beams. This generally depends on time, so one can speak both in terms of the *instantaneous* luminosity, $\mathcal{L}(t)$, or the proton density per unit time at a given time, and the time-integral of this quantity over some period of data-taking i.e. the *integrated* luminosity, $\mathcal{L}_{\text{int}}$. Integrated luminosity can be stated in the units of cm^{-2} or often in terms of the *barn*, b = $10^{-24}\,\text{cm}^2$, or multiples thereof e.g. fb = $10^{-39}\,\text{cm}^2$. The number of events of interest, N_{exp}, is proportional to the integrated luminosity [14], with the constant of proportionality defined as the *cross-section* of the reaction of interest, σ_{exp}, which is a proxy for the likelihood of the interaction. To summarise;

$$N_{\text{exp}} = \sigma_{\text{exp}} \cdot \int \mathcal{L}(t)dt = \sigma_{\text{exp}} \cdot \mathcal{L}_{\text{int}}. \tag{3.2}$$

For two relativistic bunches containing N_1 and N_2 particles with a crossing angle ϕ, colliding at a frequency f, the luminosity can be expressed as

$$\mathcal{L} = 2cfN_1N_2\Omega\cos^2\phi, \tag{3.3}$$

where

$$\Omega = \int \rho_1(x,y,z,t)\rho_2(x,y,z,t)dxdydzdt$$

represents the overlap integral of the densities of the two beams, $\rho_{1,2}$, in space (x,y,z) and time t [133]. In reality, the density distributions are non-trivial, and so neither is the integral. One can, however, approximate that for each beam the densities factorise into the product of three Gaussians in x, y, and z. Such an approximation yields

$$\Omega = \frac{e^{-\frac{(\Delta x)^2}{2\Sigma_x^2} - \frac{(\Delta y)^2}{2\Sigma_y^2}}}{2\pi\Sigma_x\Sigma_y}, \tag{3.4}$$

with

$$\Sigma_x^2 = 2\sigma_x^2\cos^2\phi + 2\sigma_z^2\sin^2\phi \quad \text{and} \quad \Sigma_y^2 = 2\sigma_y^2.$$

In the above, the widths $\sigma_{x,y,z}$ are determined from σ_{1i} and σ_{2i}, the widths of the Gaussians for beams 1 and 2,

$$2\sigma_i^2 = \sigma_{i1}^2 + \sigma_{i2}^2 \quad \text{for} \quad i = x,y,z,$$

and $\Delta x, \Delta y$ are equal to the transverse separation of the beams in x and y. Practically, this integral is determined experimentally from scans in x and y of the number of visible interactions per bunch crossing, μ, for a particular process with effective cross-section σ_{eff} [134]

$$\mathcal{L} = f \cdot \frac{\mu}{\sigma_{\text{eff}}}. \tag{3.5}$$

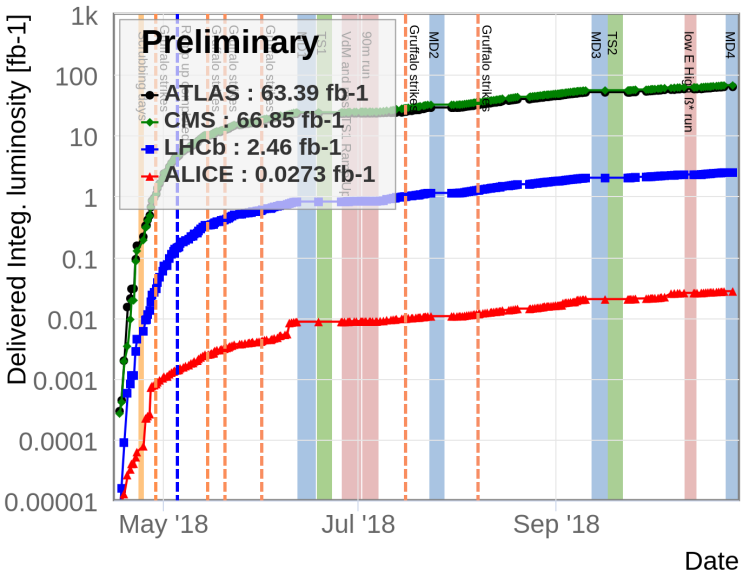

FIGURE 3.5: A comparison of the integrated pp luminosity at the four main LHC experiments as a function of time during 2018. ATLAS and CMS collect similar quantities of data and see significantly higher interaction rates than the one imposed by LHCb's more specialised trigger. ALICE is designed for heavy-ion collisions and so sees an even smaller rate by a couple of orders of magnitude. Figure taken from Ref. [138].

The collision frequency, f, is the product of the number of bunches per beam, n_b, multiplied by the revolution frequency, f_0, the rate at which a single bunch circulates the ring. The luminosity can therefore be maximised by having lots of protons per bunch, with a narrow spread in space, and colliding the bunches often. At the LHC, $f_0 = 11\,245\,\text{Hz}$ [133] and n_b is $\sim$ 2800, with $\sim 10^{11}$ protons in each [135], and thus $f \approx 30\,\text{MHz}$. Over the course of a run, f will naturally decrease as collisions remove protons from the beams. LHCb can maintain an approximately constant luminosity of $\sim 10^{33}\,\text{cm}^{-2}\text{s}^{-1}$ by monitoring μ (~ 2) and compensating any decrease with a reduction in the beam offset [134], which is intentionally introduced to reduce μ to a manageable level. This is in comparison to the far larger interaction rates at ATLAS and CMS with both having $\mu = 60$ and $\mathcal{L} = 2 \times 10^{34}\,\text{cm}^{-2}\text{s}^{-1}$ [136, 137]. The beam crossing-angle is typically very small for LHCb, though the experiment periodically flips the polarity of its magnet, which can cause this angle to change. Taking data in both magnet configurations, called `MagUp` and `MagDown` helps to cancel out charge asymmetries introduced due to detector effects. Figure 3.5 summarises the integrated luminosity over time for the four main LHC experiments.

Compared to leptons, colliding heavier particles like protons benefit from reduced bremsstrahlung, and so are more viable for higher-energy collisions but have other complications due to being composite particles. The fundamental particle interaction takes place at the quark-level, and colliding protons essentially means colliding "bags" of quarks, where the momentum of each individual component is not a-priori known. There is, therefore, the potential for multiple interactions for each proton-proton collision, which

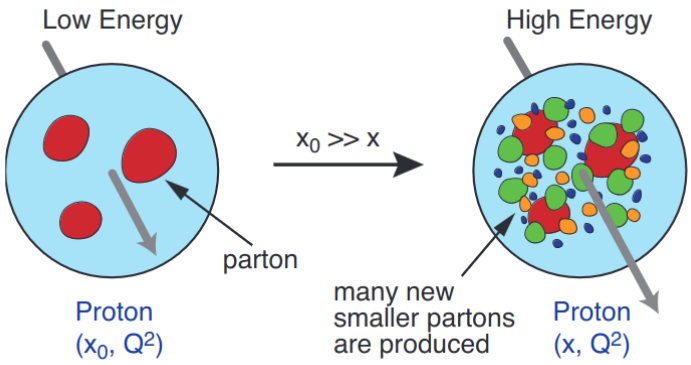

FIGURE 3.6: A more accurate picture of the contents of the proton. Taken from Ref. [139].

makes for a messy experimental environment. What's more is the strong force (as discussed in Section 2.1.1) that binds the quarks together typically cannot be dealt with perturbatively. The existence of gluon self-interactions means that the structure of the proton is actually more complicated than their minimal content of uud (see Figure 3.6), as additional *sea-quarks* can be pair-produced from these gluons. The momentum distributions of all of these components (called *partons*) are non-trivial to determine and in fact the gluons themselves make up a significant fraction of the total proton momentum. Such Parton Distribution Functions (*PDFs*) are shown in Figure 3.7.

It is, therefore, important to note that while the centre-of-mass energy of each proton at the LHC is 6.8 TeV, the collision energies of the quarks in the fundamental interaction are much smaller and in general will be different from each other. Heavy particles (such as b quarks) will be produced with small momenta in the centre-of-mass frame of the colliding partons. Lorentz-transforming into the lab frame (which will be different if the colliding partons have different energies) means applying a significant boost along the beam-axis, and so such particles will appear at small angles θ relative to this axis. The geometry of the LHCb detector, as explained in the following section, was chosen with this fact in mind. One must note the increase in the strong interaction potential with distance that was discussed in Section 2.1.1. This means that as quarks move away from one another, energy builds up in the gluon field, which can stimulate pair production processes (like the reverse of the first diagram in Figure 2.2), which create more $q\bar{q}$ pairs from the vacuum. Consequently, there is an abundance of quarks produced immediately following collision.

The confinement properties of QCD then mean that any b quarks that have been produced will quickly *hadronise* i.e. bind with other quarks to form the composite particles that become the measured objects. This is a highly non-perturbative process but the probability, f_i, that a b quark will hadronise with quark i (or *into* composite particle i) as a function of p_T can be experimentally measured. Typically, such *fragmentation fractions* for u and d quarks are assumed to be equal, due to isospin symmetry, i.e. $f_u = f_d$. The

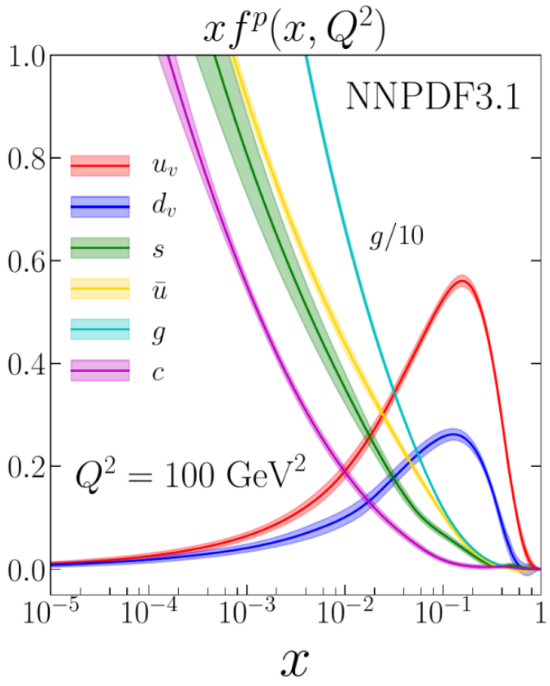

FIGURE 3.7: The coloured lines show the relative probabilities of different types of parton carrying a fraction x of the total momentum of the proton i.e. Parton Distribution Functions (PDFs). As expected, the large values of x are dominated by u and d valence quarks (with roughly a factor of 2 between them). The fact that exact parton collision energies are unknown for proton-colliders makes for a more complex environment that is more challenging to model than for lepton colliders. Figure taken from [140].

newly-created b hadrons then travel some small distance before decaying further. The lifetimes, τ, and so flight distances of each of the hadrons are known precisely and, as will be seen, measuring them allows for good selection of b hadron candidates.

The LHCb detector has recently undergone a significant upgrade ahead of Run 3 of the LHC. The original detector, as used during Runs 1 and 2, and most pertinent to the LHCb analyses discussed in Chapters 4 and 6, is explored in the next section. The differences between this and the upgraded detector that recently replaced it, relevant to Chapter 5, are then detailed in the subsequent section.

3.3 The Run 1 and 2 LHCb Detector

LHCb primarily studies the behaviour of beauty and charm quarks, particles which typically travel at small angles with respect to the beam-axis (see Figure 3.8). Hence, the detector takes the form of a forward-spectrometer, covering angles between 15 and 300 (250) mrad in the horizontal (vertical) direction. The conventional coordinate system has z along the beam-axis, with the $x-z$ and $y-z$ planes being perpendicular and parallel, respectively, to the magnetic field. Consequently, it is in the horizontal $x-z$ plane that particle trajectories are bent. The geometry of the collision often means that cylindrical (r,ϕ,z) or spherical (r,θ,ϕ) polar coordinates are, however, often more convenient.

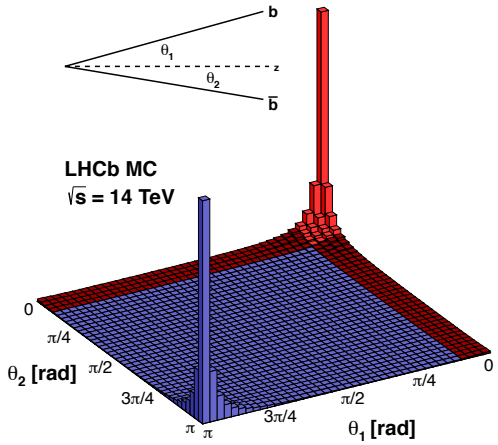

FIGURE 3.8: Angular distribution of $\bar{b}b$ pairs in LHCb. The red region marks the LHCb acceptance. Figure taken from Ref. [141].

Furthermore, the *pseudorapidity*, η, is often used in place of the angle θ, where

$$\eta = -\ln\left[\tan\left(\frac{\theta}{2}\right)\right], \tag{3.6}$$

and the LHCb acceptance is given as $2 < \eta < 5$. This quantity is so named since, for large energies, it approximates to *rapidity*, y, which parameterises Lorentz boosts (through $\cosh y = \gamma$, $\sinh y = \beta\gamma$). This is a convenient quantity since it is additive for translations to longitudinally-boosted frames. It is, though, practically difficult to measure as it relies on measuring the total momentum vector, which is not always possible. Hence, for hadron colliders η is a useful quantity to consider. The cylindrical geometry around the beam-axis also motivates the use of the momentum transverse to the beam-axis, p_T, in favour of total momentum, $p = p_T \cosh\eta$.

The LHCb detector composition used during Runs 1 and 2 is shown in Figure 3.9. One can imagine the collisions occurring on the left of the diagram with b hadrons and their decay products produced within a small angle about the beam axis, travelling in equal amounts both forwards (to the right) and backwards (to the left), as seen in Figure 3.8. The latter set of particles is undetected, though this halving of statistics is more than compensated for by LHCb's investment in cutting-edge technology for its subdetectors in the forward direction. As the resolved particles propagate forwards, they pass successively through each of the subdetectors; VELO, RICH detector, tracking stations, calorimeters, and muon stations. Each of these is specialised to provide different pieces of information that are ultimately combined to reconstruct the particle interactions that occurred. The following section explains the operation of these subdetectors, with performance data taken from Ref. [142].

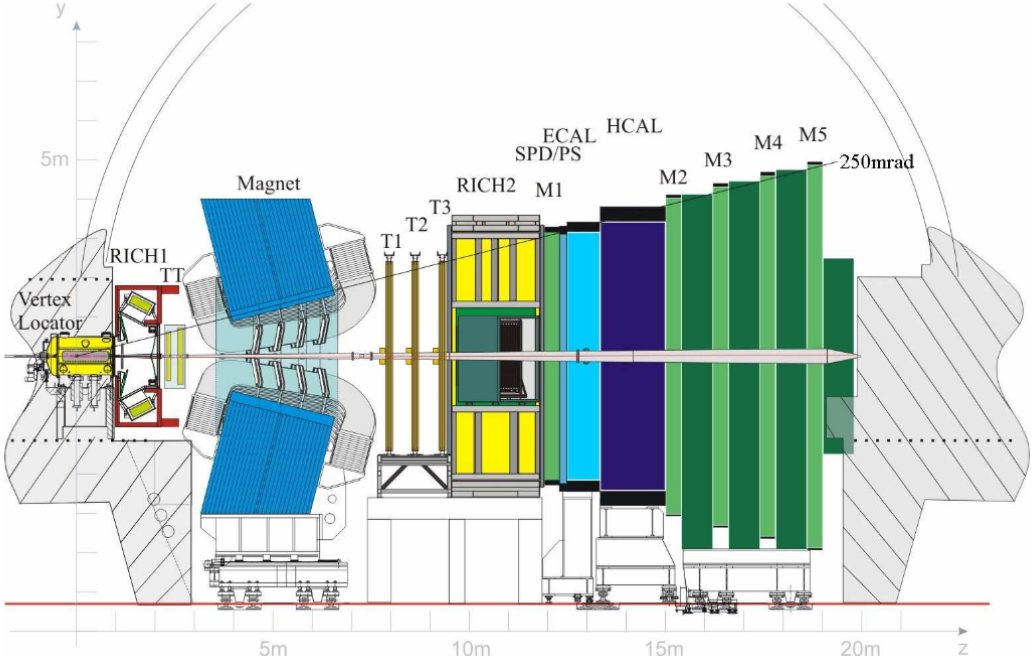

FIGURE 3.9: Schematic of the original LHCb detector, used during Runs 1 and 2. Taken from Ref. [143].

3.3.1 Vertex Locator (VELO)

The protons collide within the **Ve**rtex **Lo**cator (or *VELO*) [144]. The main function of this component is to measure, with high precision, the positions of the collision point or *primary vertex* (PV) and decay (*secondary*) vertex of candidate B hadrons, from which one can measure the distance of flight as well as the *impact parameter* (IP) of nearby tracks. The impact parameter is the closest distance between a track and a vertex, and requirements on both of these quantities play a key role in the identification of the B hadrons in the detector, alongside the lifetimes inferred from the distance of flight.

Since B hadrons travel within a small angular acceptance ($\sim 200\,\text{mrad}$), their decay products, relative to those from the PV, have an appreciable IP parallel to the beam axis (the $r-z$ plane) but a more moderate displacement perpendicular to the axis ($r-\phi$ plane) that is similar to that of the tracks emerging from the PV [142, 144]. The *trigger* system, which rapidly filters events, uses this information by first selecting events with significant $r-z$ projections and reconstructs ϕ information later. This approach motivated the design of the VELO modules (see Figure 3.10), half of which have silicon strips at constant radius (to deduce displacements in r), the other half having silicon radial-strip sensors pitched by an angle of $10^\circ - 20^\circ$. These latter sensors predominantly measure ϕ coordinates, but this finite pitch permits some discrimination in radial coordinates to allow the combination of information from the two halves. The two types of submodule swap sides with each successive VELO module. The pitch also provides a means to spread occupancy, i.e. the number of hits per sensor, across the subdetector, with small strip pitches (and the best hit resolution) used close to the beam axis and large pitches

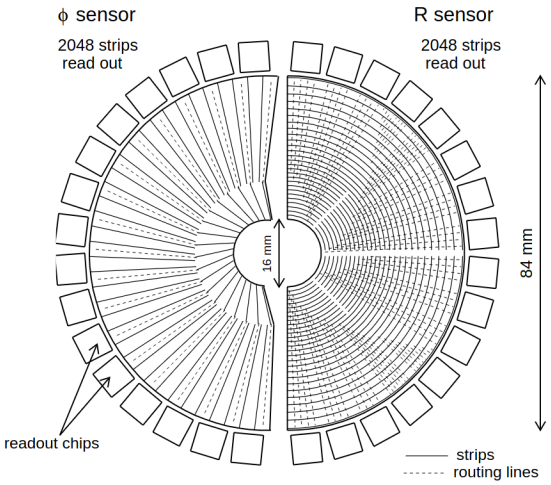

FIGURE 3.10: VELO module design from Runs 1 and 2. The two halves are separated from each other during beam fills and only closed together once proton beams are stable. Figure taken from Ref. [145].

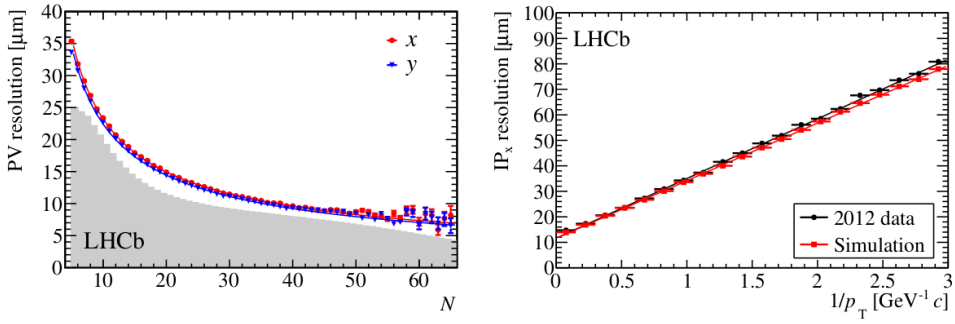

FIGURE 3.11: PV and IP resolution for Run 1/2 VELO, dependent on track multiplicity, N, and transverse momentum, p_T, respectively. Taken from Ref. [142].

used further away.

Since LHCb is primarily specialised towards processes with displaced decay vertices, having accurate and precise information on the IP, and the χ^2 on the charged-track fit to determine it, is crucial to be able to suppress backgrounds and reduce uncertainties. The IP resolution mainly depends on three factors: the position resolution of the individual hits that make up the track, the distance of flight of particles between primary vertex and first detection point, and the amount that particles scatter off the material of the detector itself [142]. The design of the VELO is such that all three of these effects are mitigated.

Firstly, the individual modules provide high-resolution hit position information, e.g. $\sim 5\,\mu$m at a pitch of $40\,\mu$m to $\sim 25\,\mu$m at $100\,\mu$m. The resolution of the PV depends heavily on the number of tracks making the vertex (*track multiplicity*). At a benchmark multiplicity of 25, the resolution is $13\,\mu$m in x and y, and $71\,\mu$m in z, with the full multiplicity dependence (for x and y) as shown in Figure 3.11. To address the second factor, the sensors are placed as close to the beams as is feasible, with the closest strips being found just 8 mm away during physics data-taking. This means, of course, that there is a danger

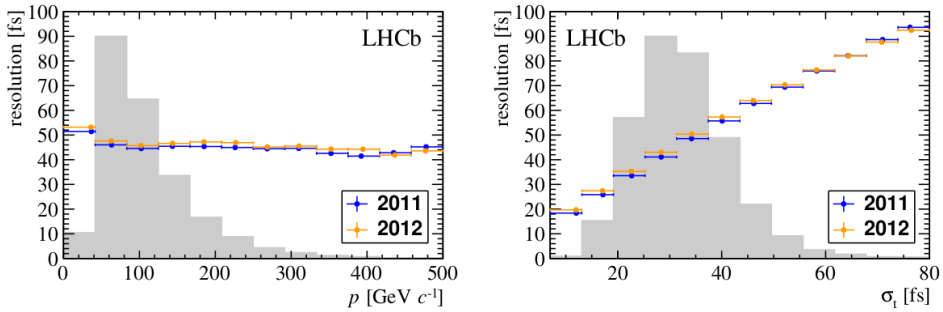

FIGURE 3.12: Time-resolution for Run 1/2 VELO as a functions of momentum (left) and decay-time uncertainty (right). The grey histograms represent distributions of these quantities on an arbitrary scale. Taken from Ref. [142].

of radiation damage to the modules. Unless the LHC has stable beams, the two halves of the detector are separated from the beam aperture by 30 mm [145], and only when the stability of the proton beams is assured are the two halves closed together to achieve this minimum distance. There is also a sheet of aluminium RF foil between the modules and the vacuum to reduce noise from the charge-flow of the beam and separate the beam vacuum from the VELO vacuum. This RF foil is incredibly thin, with a thickness of 0.3 mm, so as to optimise IP resolution.

Some of LHCb's headline measurements have been of time-dependent CP violation effects. Such measurements require resolving the oscillation of mesons, some of which can occur at more than $1\,\text{ps}^{-1}$. Therefore, a fine decay-time resolution (~ 40 fs) without bias is essential to support these programmes of activity. Indeed, the amplitude of such oscillations is diluted relative to the time-resolution; for a recent measurement of B_s^0 oscillations [77], which have a mixing frequency of $17.7\,\text{ps}^{-1}$, the CP asymmetry was diluted by a factor ~ 0.7, on account of the decay-time resolution. The performance from Run 1 for this quantity is shown in Figure 3.12.

3.3.2 Ring-Imaging Cherenkov (RICH) Detectors

As previously introduced, the **R**ing-**I**maging **Ch**erenkov (*RICH*) detectors are another specialisation of LHCb to precision flavour physics, since these allow for accurate **p**article **id**entification (PID) of light particles. Particles travelling faster than the speed of light in a given medium emit photons known as Cherenkov radiation[5], which appears as a ring of light when viewed front-on. This results from the bunching up of wavefronts in front of the particle in an equivalent process to the production of a "sonic boom" by a supersonic jet. The angle at which this radiation is emitted, the Cherenkov angle (θ_C), and thus the radius of the ring, depends on the velocity of the particle, β, and the refractive index, n, of the medium [146]:

$$\cos\theta_C = \frac{1}{n\beta}, \tag{3.7}$$

[5]Named after Pavel Cherenkov, who, alongside Ilya Frank and Igor Tamm, won the 1958 Nobel Prize for the discovery and interpretation of this effect [15].

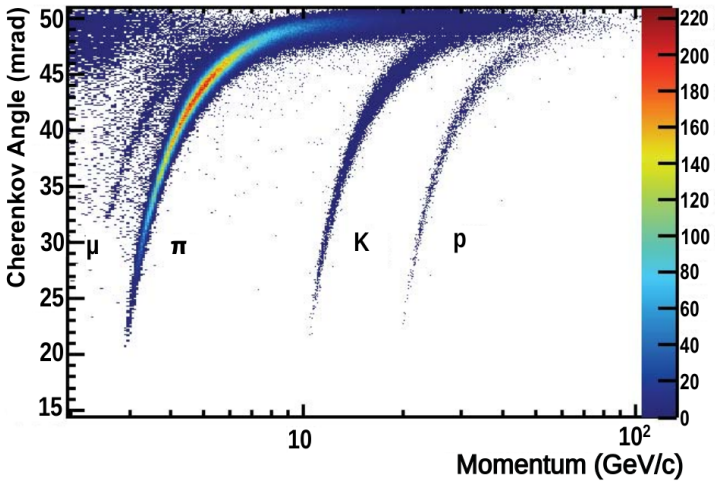

FIGURE 3.13: Cherenkov angle versus momentum shows great discrimination between different particle IDs. Taken from Ref. [142].

which is clearly only valid for $|n\beta| > 1 \implies \beta > 1/|n|$, with no radiation being produced for particles below this threshold. This can, therefore, be used to provide excellent discrimination between different types of particles (see Figure 3.13) that would otherwise appear similar. This first detector was specialised to detect low momentum particles, which typically come out at larger angles (θ not θ_C), covering an angular acceptance of 25-300 mrad with C_4F_{10}, and in Run 1 also a silica aerogel, as a medium [147]. A second RICH detector specialised to detect the high momentum particles (at small angles), using CF_4, was found after the tracking stations and covered an angular acceptance of 15-120 mrad. Since the Cherenkov angle was the primary discriminator between particle identities in this subdetector, its performance depended mainly on the resolution of this angle, $\sigma(\theta_C)$, which was 1.618 ± 0.002 mrad and 0.68 ± 0.02 mrad for the first and second RICH detectors, respectively [142]. The photoelectron yield (N_{pe}), the average number of photons that can be detected for a single track, was another parameter that was optimised.

When PID information from the RICH detectors is used, particles are identified (as electrons, muons, pions, kaons, protons, etc.) by evaluating the relative (log) likelihoods for each hypothesis. When performing selection cuts with this information, one must reach a compromise between the misidentification rates and efficiencies. When averaging over the momentum range 2 - 100 GeV, with a cut on the relative log-likelihood of the kaon and pion hypotheses, PIDK=$\Delta \log \mathrm{L}(K - \pi) > 0$, one finds the kaon efficiency to be $\sim$ 95% with a pion misidentification rate of $\sim$ 10%. Tightening the PID requirement to PIDK$>$ 5 reduces the pion misidentification rate to $\sim$ 3% at the cost of an approximate 10% decrease in kaon efficiency, on average [142]. The detection efficiency versus misidentification rate, as a function of momentum, for the RICH is shown in Figure 3.14.

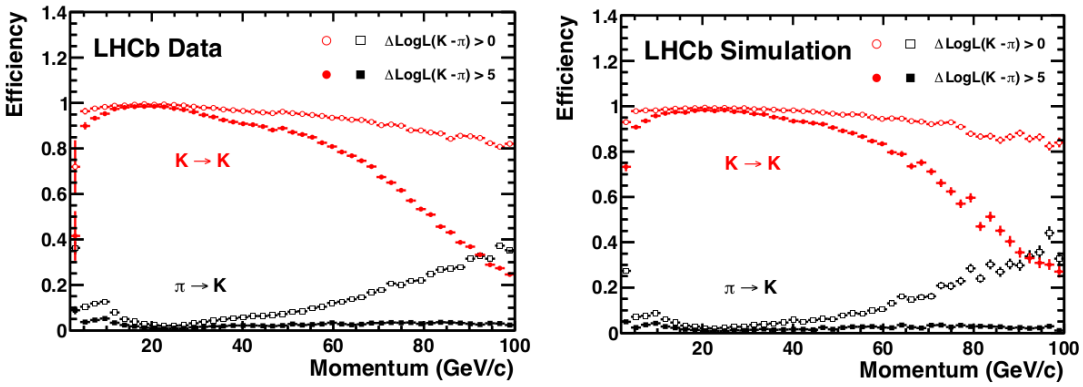

FIGURE 3.14: Detection efficiencies and misidentification rates in Run 1/2 RICH subdetectors. Taken from Ref. [142].

3.3.3 Tracking Stations

In addition to the VELO, the tracking system was formed by four planes of tracking stations: the Tracker Turicensis (*TT*)[6] before the magnet, and tracking stations T1-T3 after [142]. These subdetectors "track" the trajectories of charged particles traversing the detector and determine their momenta from bending radii, as in Eq. (3.1). Such momentum information allows particles to be selected according to their invariant mass, $E^2 - p^2c^2$, a Lorentz invariant quantity that permits the reconstruction of short-lived particles from their decay products. Information on track trajectories is necessary for effective reconstruction in the subsequent RICH detector. The triggers also rely heavily on cuts involving tracking information.

The tracking stations T1-3 are themselves composed of four layers of modules, as seen in Figure 3.15. In order to give some sensitivity in the y direction, there is a relative pitch between the four layers, forming an $x - u - v - x$ geometry. In the x layers, the modules point vertically, while the u and v layers are tilted by $+5°$ and $-5°$ respectively. The priority for the x direction is because it is the direction of track-bending, where good resolution is especially needed. There are two halves to each station, which are further split into Inner (*IT*) and Outer trackers (*OT*) on account of the difference in occupancies close to the beam pipe compared to the periphery of the detector acceptance.

The OT is made up of gaseous straw-tube drift cells, covering an area of around 5 m $\times$ 6 m, with 12 double layers of straw tubes. Each straw tube is 2.4 m long with 4.9 mm inner diameter and is filled with a mixture of Argon, Carbon Dioxide, and Oxygen. A positively-charged gold-plated tungsten wire runs through the centre along the length of the tube, set to +1550V. Charged particles will ionise the gas mixture, triggering a cascade of electrons onto the anode wire, which can be read out to indicate the presence of a particle in that part of the detector. The particle flux in the cross-shaped inner tracking

[6] On looking up the meaning of this unusual word, I found that it refers to Zürich through its Roman name of Turicum. It also appears that TT originally stood for Trigger Tracker, but when the focus of this subdetector changed, another name with the same acronym needed to be found. Conveniently the Zürich group had played a key role in the development of this subdetector.

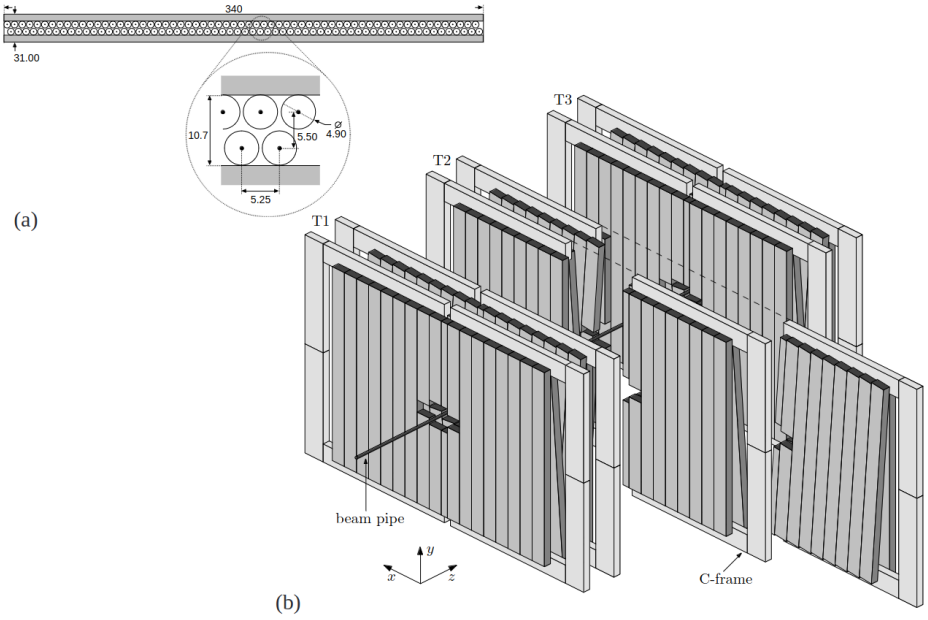

FIGURE 3.15: Layout of the LHCb tracking stations in Runs 1 and 2. Taken from Ref. [148].

region, however, is too high for conventional drift chambers. The TT and the IT rely instead on silicon micro-strips, with the dimensions of the sensors differing between these two subdetectors both in terms of area and thickness. Like in other subdetectors, the TT system has higher granularity closest to the beam-pipe, with the highest flux, achieved using a higher pixel density closest to the beam pipe.

Tracking efficiency is the probability that the path of a charged particle through the tracking stations will, in fact, be identified as a track, assuming that particles do not interact with the detector material, do not decay in the tracking volume, and do not exit the detector acceptance. Across the whole phase-space of LHCb, i.e. $p \in [5, 200]$ GeV and $\eta \in [2, 5]$, the average efficiency is at least 96%, excluding high multiplicity events of 200 tracks or more. For momenta below 20 GeV, the momentum resolution is around 0.5%, rising to around 0.8% around 100 GeV, with an approximate systematic uncertainty of 0.03% (see Figure 3.16). The tracking alignment must not change considerably with time, and re-alignment is necessary whenever detectors are moved during maintenance and when the direction of the magnetic field is reversed, which usually occurs around once every fortnight. Even with this procedure, there can still be some small misalignments in the relative position of neighbouring detector modules that remain, and these are estimated from the scatter of hits around the fitted tracks to be approximately 10 μm in the IT and 30 μm in the TT.

3.3.4 Calorimeters

The calorimeter system follows the tracking system, providing information on particle energies and being invaluable for the reconstruction of neutral particles that do not leave

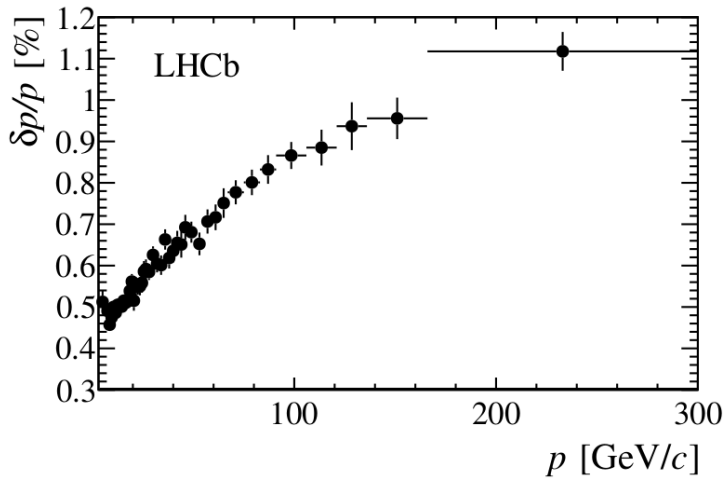

FIGURE 3.16: Momentum resolution of the Run 1 and 2 tracking system. Taken from Ref. [142].

a signal in other subdetectors. There are two varieties of calorimeter present, which follow two other complementary subdetectors that will be explored in the next subsection.

The first of the calorimeters is the **E**lectromagnetic **Cal**orimeter or *ECAL* [149]. This allows for the detection of electrons, positrons, or high-energy photons. Electrons and positrons may emit bremsstrahlung (as photons), and photons themselves may yield pair-production of electrons and positrons. Electrons and positrons may also annihilate to produce photons. The combination of these processes means that any one of these entering the ECAL will cause a cascade of such particles to be produced, and energy is deposited in a cluster. The longitudinal extent of this cascade is typically expressed in terms of the radiation length, X_0, i.e. the distance over which the energy of an incoming particle is reduced by a factor of Euler's constant, e [14]. The subdetector is composed of alternating layers of 2 mm-thick lead sheets and 4 mm-thick scintillator plates connected to wavelength-shifting (WLS) fibres. Its total thickness is chosen to be large ($25X_0$) to maximise the energy resolution for high-energy photon showers. A similar process can happen for hadrons in the second calorimeter - the **H**adronic **Cal**orimeter or *HCAL* [149]. The HCAL design is similar, with the 4 mm-thick scintillator plates instead being interspersed with 16 mm-thick iron sheets. The energy resolution of the ECAL is $10\%/\sqrt{E[\text{GeV}]} + 1.5\%$, while for the HCAL it is $80\%\sqrt{E[\text{GeV}]} + 10\%$.

The detector covers 300 mrad horizontally and 250 mrad vertically, the region covered by charged particles. Close to the beam axis, the effects of background are considerable, and for this reason, as well as on grounds of radiation protection, there is a central hole of 30 mrad in both directions. The hit density does, though, vary by two orders of magnitude over the calorimeter surface, so it makes sense to divide the calorimeter into regions with different cell-sizes, optimised in order to equalise occupancy, given a fixed number of channels. The ECAL has three such regions, while the HCAL has only two and generally has larger cell sizes. The need to be able to resolve the two separate showers from high-energy $\pi^0 \to \gamma\gamma$ puts certain requirements on the ECAL. In the most active region,

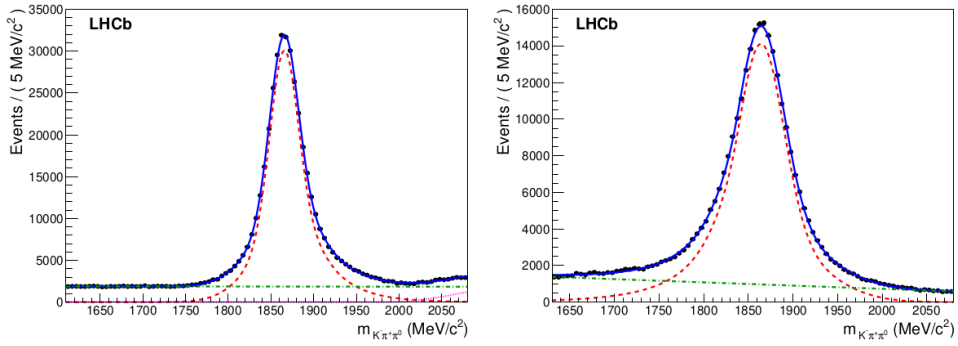

(A)

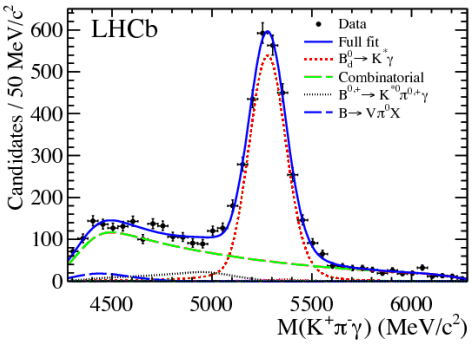

(B)

FIGURE 3.17: Invariant mass fits, using 2011 LHCb data, for final states containing a charged kaon and pion plus a neutral particle; a π^0 (A) or a photon (B). For the first case, mass fits for $D^0 \to K^-\pi^+\pi^0$ are shown separately for resolved (left) and merged (right) π^0 candidates, and for the second a mass fit for $B^0 \to (K^* \to K^+\pi^-)\gamma$ is shown below. The full fit model is shown in solid blue, comprised mainly of signal (red dashed) and combinatorial (green dashed) components. Further background components are designated by additional colours/patterns. Figures adapted from Ref. [142].

closest to the beam axis, the cell size corresponds to approximately the *Molière radius*, $\left(\approx \frac{21.2\text{MeV}}{E_c} X_0\right)$ [14] such that the majority of the energy of a single isolated shower is distributed across just four adjacent cells. π^0 candidates where the two photons fall within a single ECAL cluster are termed "merged", while candidates with two separate clusters are termed "resolved".

The mass resolution with which neutral pion candidates can be reconstructed is an obvious key indicator of performance, impacting the efficiencies of any selection made on this quantity. As a benchmark, Figure 3.17 shows the distribution for $D^0 \to K^-\pi^+\pi^0$ candidates for resolved and merged π^0 candidates, with the numerical values being 30 MeV for the merged π^0 candidates and 20 MeV for the resolved ones. A similar case can be made for high-energy photon reconstruction, shown in the same figure for the example of $B^0 \to K^{*0}\gamma$. The mass resolution comes primarily from that of the ECAL energy deposition, and in this example is 93 MeV.

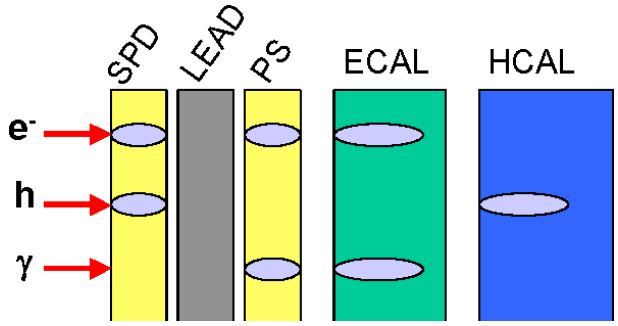

FIGURE 3.18: Discrimination on calorimeter response provided by SPD and PS subdetectors. Figure taken from Ref. [150].

3.3.5 SPD/PS Detector

The response of the ECAL to incoming electrons and photons converted in the material after the magnet is very similar, and it is necessary to use additional technology to discriminate between the two cases [142, 149]. One such technology utilised at LHCb involved scintillators which emit photons when interacting with charged particles. The inventively-named Scintillator Pad Detector (*SPD*) preceded the ECAL and transmitted the scintillation light via fibres to photomultiplier tubes (PMTs), which amplify the signal to around 25 photoelectrons, on average. The efficiency of the PMT is optimised through the use of WLS fibres to transmit the scintillation light. As with other subdetectors, PMTs with higher granularity are used closer to the beam axis. As seen in Figure 3.18, the presence or absence of such a signal serves to resolve the ambiguity of the ECAL. The precision of the evaluation of the energies of positions of candidates in the ECAL, as well as the accuracy of the identification of these candidates, can be further improved through measurements of energy losses in the material before this subdetector. To this end, a second set of scintillating pads, the **Pre**shower (*PS*) detector, follows 2.5 radiation lengths (15 mm) of lead and placed ahead of the ECAL. Furthermore, backgrounds from charged pions can be reduced using information from this subdetector. Information from this subdetector is used in the calculation, in simulation, of the signal and background probability density functions for *non-converted* photons that pair-produce within the ECAL. The resulting photon hypothesis likelihoods when applied to data are used to identify such particles. This is in contrast to *converted* photons that pair-produce before the ECAL, which are reconstructed from the resulting electron and positron tracks, and the purity vs efficiency performance from Runs 1 and 2 are shown in Figure 3.19. This figure also shows the performance of the calorimeter system in discriminating between a γ candidate and a $\pi^0 \to \gamma\gamma$ candidate achieved using a neural network classifier, again trained on simulation.

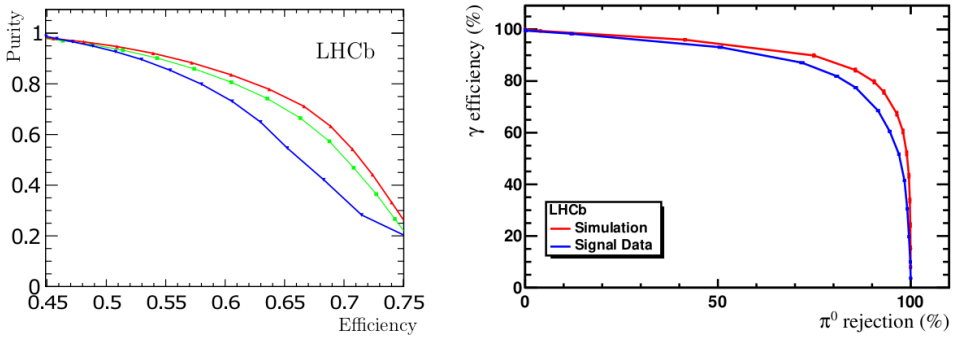

FIGURE 3.19: Run 1/2 performance for photon identification. On the left, the effect of selection efficiency on sample purity is shown for non-converted candidates (red), converted candidates (blue), and for a combined sample (green). On the right, the discriminating power between photons and neutral pions is shown in terms of pion selection efficiency compared to the efficiency of π^0 rejection for simulation (red) and data (blue). Taken from Ref. [142].

3.3.6 Muon Chambers

Following the calorimeters, which see the destruction of the vast majority of types of particle that traverse the detector, the only variety of measurable particle (excluding neutrinos) that is expected to remain is the muon. Charged particles, hypothesised as being muons, are detected at this point in four tracking stations (M2-M5), which utilise Multi Wire Projection Chamber (MWPC) technology[7], with a fifth (M1) placed ahead of the calorimeters on grounds of space [151]. In a similar way to the straw-tube detectors, here there are grids of wires within each station, and the motion of a muon near any one of these will induce a small current in the wires, benefiting also from electron multiplication, that allows the muon position to be pinpointed.

LHCb targets a muon trigger efficiency greater than 95%, meaning that each muon station must have an average efficiency in excess of 99%. The efficiency performance of the stations is summarised in Figure 3.20. This efficiency can be affected by misalignments in the first two stations, where the muon momentum is estimated, and also introduce a charge asymmetry. To remove such an asymmetry in the trigger efficiencies and to keep the momentum uncertainty below 0.1%, requires an alignment precision of $\sim$ 1 mm, which is indeed achieved at LHCb. A lower spatial resolution is necessary for M3-5, which do not contribute to the momentum estimation. The timing of muon detector hits is also measured precisely, with a resolution between 2.5 and 4 ns, though this can depend on phase-space.

[7]Development of this technology won Georges Charpak the Nobel prize in 1992, the last time a single person was awarded it in Physics and the most recent occasion recognising development in particle detector technology, following the awards of 1948, 1950, 1960, and 1968 [15].

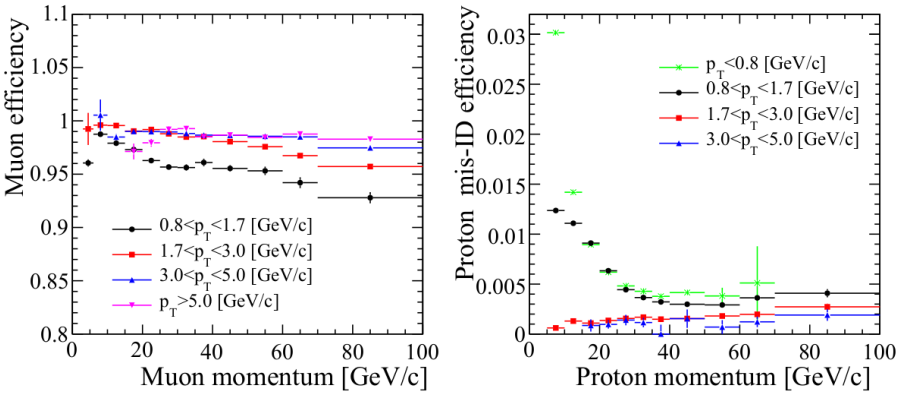

FIGURE 3.20: LHCb muon station performance in Runs 1 and 2, in terms of the momentum dependence of reconstruction efficiency for true muons (left) and of misidentification probability for protons (right). Figure taken from Ref. [142].

3.3.7 Software

In addition to hardware, there are a number of key software packages that are central to LHCb's analyses. As will be detailed in the next subsection, raw data is rapidly filtered through the trigger system after detection, saving a small subset and discarding the majority. *Moore* [152] performs the software portion of this process. Objects like tracks and clusters that are required for further selection are reconstructed from subdetector signals here, outputting files in the *DST* format, which are ROOT [153] files containing both the raw data and reconstructed objects. To minimise data storage, the raw data can be discarded by saving a μDST file instead. The *Brunel* [154] application, in Runs 1 and 2, then applied more detailed and precise reconstruction, following the quick and rough one performed by Moore.

Though the DST files at this point are technically suitable for analysis, typical users do not have access to them. This is because the raw data is stored on physical tape, which is time-consuming to read out, and users are typically only interested in channels that make up a fraction of the total dataset. It therefore makes more sense to further filter these DST's by a set of selections known as the *stripping*, which again outputs a DST or µDST. This allows data to be grouped together in *streams* that contain similar decay topologies, reducing the amount of data needed to be accessed at one time and making for a more robust system. The *DaVinci* [155] application permits such further filtering and selection of samples, and users may also run their own offline analysis, which outputs ROOT files called *ntuples*.

As well as experimental data, it is often useful to also have access to simulated data. *Gauss* [156] is an example application that simulates (*Monte Carlo*) proton-proton collisions as well as the subsequent hadronisation and decays. This itself calls upon different Monte Carlo event generators, including Pythia [157] and POWHEG [158], as well as EvtGen [159] (which describes the decays of the simulated particles) and GEANT4 [160] (which models the detector response to the different particles). The application *Boole* [161]

can convert such simulated detector response into digitised signals akin to real detector output. The output of this can then be fed through the same software applications as real data, from Moore onwards.

3.3.8 Trigger

The rate at which proton collisions occur in the LHCb detector means that the majority of raw data cannot be saved to disk, with regard to the cost of maintaining such a storage space. There is, therefore, a *trigger* system, the function of which is to enrich the output of the detector by keeping more signals of interest than background. Figure 3.21 summarises this process. In Runs 1 and 2, the first stage of this process (*L0*) involved a hardware trigger that removed events with small momentum transverse to the beam axis, p_T, and large numbers of hits in the SPD [149]. It also selected events with high p_T muons and rejected those with multiple interactions per bunch crossing [162]. This reduced the data rate from around 40 MHz to around 1 MHz. The second and third stages of the process were termed High Level Trigger (*HLT*) 1 and 2, which were software triggers.

HLT1 used tracking information and performed some inclusive selections to make decisions. The second stage, HLT2, performed a full reconstruction suitable for offline analysis, including both inclusive and exclusive selections to reduce the data rate further. In Run 2, this stage outputted at around 12.5 kHz. There was also a disk buffer of ~ 10 PB, which allowed for calibration and alignment to be performed in real-time. It also allowed data to be processed during LHC downtime. During Run 1, this was placed between L0 and HLT1, which permitted slightly more data to be processed by the software trigger during accelerator downtime. For Run 2, this was moved to be between HLT1 and HLT2, benefiting from the lower input rate, which resulted in a larger number of events that could be stored in the buffer. The calorimeter triggers selected on particles that left a significant transverse energy (E_T) in the calorimeters and includes information from the SPD and PS. This helped to identify the presence of electrons, photons, neutral pions, or hadrons. When associating calorimeter clusters with the particles that generated them, a compromise had to be found between using a large number of cells to ensure that most of the energy of the shower is accounted for, and using a small number of cells to minimise overlap and reduce the rate at which two neighbouring showers are resolved as a single cluster. Showers tend to be narrow, so a zone of 2×2 cells was used. At each stage, only the highest E_T candidate was kept to mitigate the required processing power.

The selection was performed in three successive steps. Firstly, high E_T deposits were identified in the ECAL and HCAL. The information from the SPD and PS was combined to discriminate the source of the electromagnetic shower (e, γ, π^0). Finally, for each type, the highest E_T candidate was selected, and information on the total E_T in the HCAL and SPD multiplicity was persisted. Again, processing time was reduced by cutting out events with high SPD multiplicity. In a similar way to the calorimeter trigger, the muon trigger selected tracks in the muon stations with large p_T, searching for hits consistent

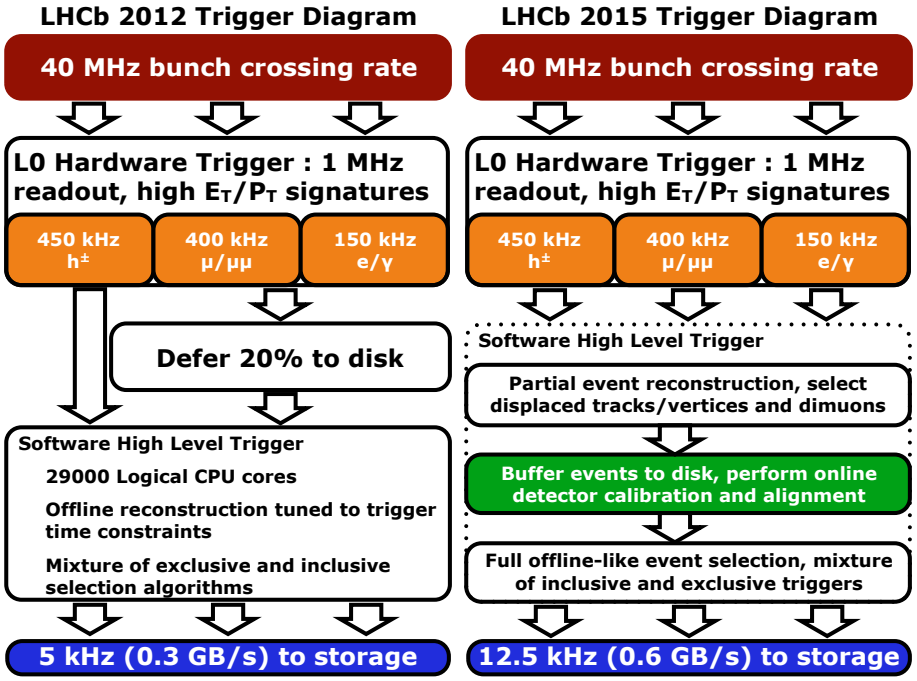

FIGURE 3.21: A summary of the main stages of the LHCb trigger during Runs 1 and 2 [163].

with a straight line track from the interaction point. The p_T was determined from the track hits in the first two stations. The pile-up system, composed of silicon strips and located upstream of the VELO, allowed the determination of the number of primary interactions per bunch crossing. The detectors of this system were specially designed to have fast readout such that pile-up information could be made available at L0. LHCb regularly operated with an instantaneous luminosity of $4 \times 10^{32}\,\mathrm{cm}^{-2}\mathrm{s}^{-1}$ [142], so this required all sub-detectors to have the capacity to manage luminosities at least this high.

Crossings with multiple interactions, which tend to be dominated by combinatorial background rather than genuine b decay candidates, take up a disproportionally large share of the event-building bandwidth and the available processing power. Removing these crossings freed up bandwidth, which could be used to loosen trigger cuts on other variables and boost the number of signal events collected. Note that the pile-up system only detected backward tracks, so there was no overlap between pile-up interactions and B decays within LHCb. The pile-up system also offered information on the luminosity at LHCb since the rate of crossings with zero, one, and multiple interactions is expected to follow Poisson statistics. Information from the calorimeter, muon, and pile-up triggers were combined at the L0 Decision Unit in order to make overall decisions as to which events were kept. The trigger received information at 40 MHz and had a latency of 500ns. Trigger efficiencies are often evaluated via *TISTOS* variables [164], which divide triggered events into three categories:

1. Triggered On Signal (TOS): the signal part of the event alone (removing all non-signal) was enough to cause the trigger line to fire.

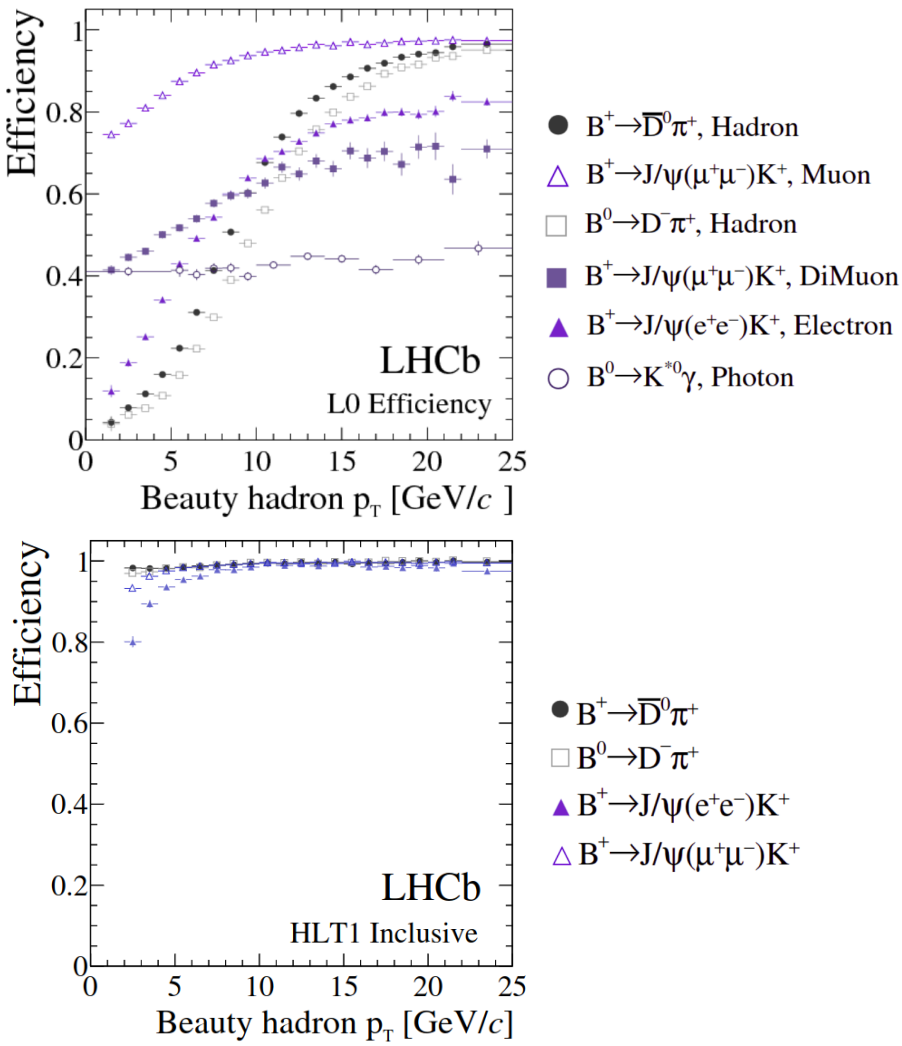

FIGURE 3.22: Trigger efficiencies as a function of beauty hadron p_T for both L0 (top) and HLT1 (bottom). Figures adapted from Ref. [165].

2. Triggered Independent of Signal (TIS): the part of the event not including signal (the "rest") passes the trigger selection on its own.

3. Triggered On Both (TOB): neither the signal nor the rest of the event alone would pass the trigger line, but both are required to pass.

3.3.9 Limitations

L0 performed poorly for hadronic final states (see Figure 3.22). For the B2OC modes of $B^+ \to \bar{D}^0\pi^+$ and $B^0 \to D^-\pi^+$, for a characteristic value of $p_T(B)$ of 10 GeV, the efficiencies are below 50% and this is then further compounded with similar inefficiencies for the D decays. This was a limiting factor for hadronic analyses, which included extractions of the weak phase, γ. By comparison, the HLT1 efficiencies for these same modes were in excess of $\sim$ 95%, even for low p_T values. This motivated the removal of the L0 trigger ahead of Run 3.

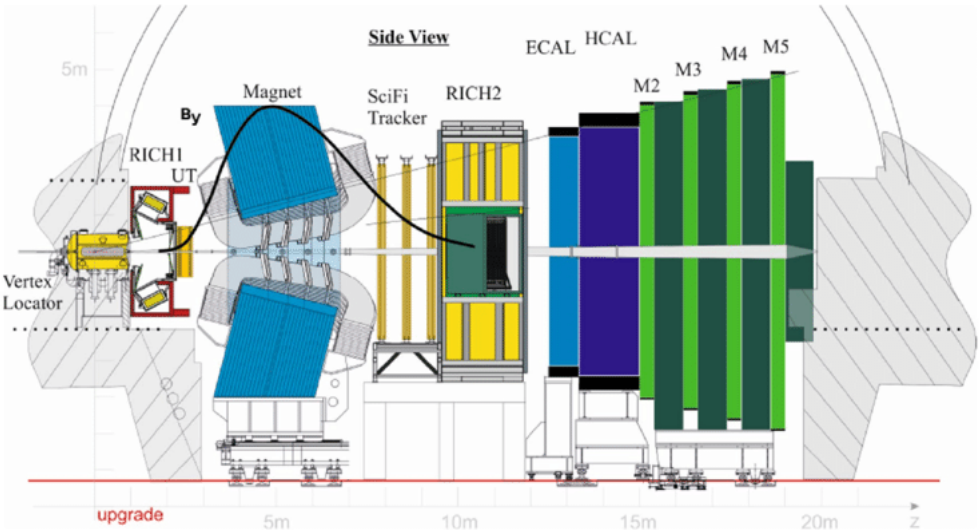

FIGURE 3.23: Schematic of the Upgrade I LHCb detector. Taken from Ref. [166].

3.4 LHCb Upgrade I Detector

For Run 3, the baseline instantaneous luminosity has increased to $10^{33}\,\mathrm{cm}^{-2}\mathrm{s}^{-1}$ [144], which offers better statistics across the board. In addition, the L0 hardware trigger has been removed, meaning that online selections are almost entirely software-based. This greatly improves prospects for measurements with hadronic final states but also means that sensors have to read out at a much higher rate (40 MHz in comparison to 1 MHz). Correspondingly, many of the LHCb subdetectors were upgraded in one shape or form during Long Shutdown 2 (LS2), as shown in Figure 3.23. One may note, for instance, the removal of the muon station M1, which previously had high occupancy with high background. While the general philosophy of the LHCb detector did not change between Run 2 and Run 3, some of the more significant changes will be discussed in the following.

3.4.1 VELO

While the Run 3 VELO reused much of the mechanical infrastructure of the old VELO (including the vacuum tank and much of the cooling system), the modules themselves changed significantly. The geometry shifted from a semi-circular geometry with individual sensors for r and ϕ to roughly L-shaped silicon pixel-based modules (see Figure 3.24), which fit together to form a diamond shape with small aperture in the centre for the beam to travel through. The distribution in z of the modules is also different to that of the old detector, with 24 pairs of modules [144]. This is to optimise the resolution of impact parameters, considering the smaller module sizes and smaller distance from the beam. Each of the modules is composed of 12 VeloPix **a**pplication-**s**pecific **i**ntegrated **c**ircuits (ASICs), which themselves are made up of 256x256 radiation-hard square pixels, and are capable of 40 MHz readout. Three chips arranged in a row make up a sensor, and four such sensors are combined to form a module with two sensors on either side.

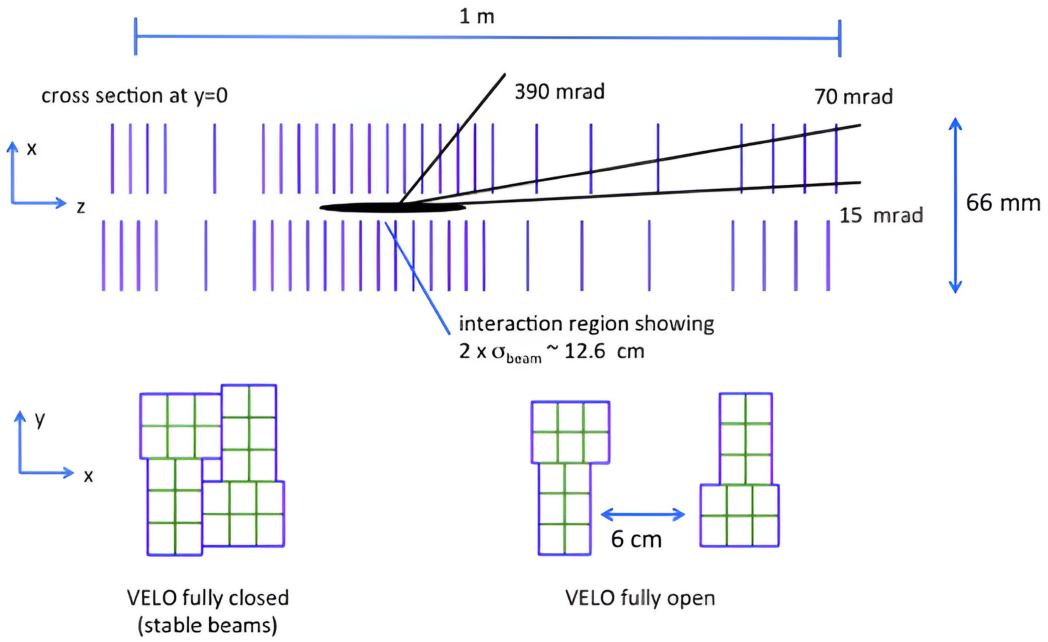

FIGURE 3.24: Sensor arrangement in the upgraded VELO detector. Figure taken from Ref. [144].

3.4.2 RICH

For RICH1, silica aerogel has been removed as a medium, and the size of the ring image was increased to reduce occupancy. In both detectors, the photon sensors were also changed from Hybrid Photon Detectors (HPDs), which have readout electronics integrated into the chips, to Multi-anode PMTs, which are available commercially and have external readout electronics.

3.4.3 Upstream Tracker (UT)

The Upstream Tracker (*UT*) supersedes the Tracker Turicensis (TT), having a broadly similar geometry ($x-u-v-x$) and composition (silicon strips), however with thinner sensors, larger coverage (with a smaller gap between the beam-pipe and the sensors) and finer granularity [167]. The last point is especially important as the larger expected occupancies would have overwhelmed the previous subdetector. Signals are also read out at the sensors rather than being transported away in order to reduce noise. An update to the readout was also necessary in order to operate at 40 MHz, which is required during Run 3.

3.4.4 Scintillating Fibre (SciFi) Detector

Very much "science fact", the *SciFi* (**Sci**ntillating **Fi**bre) Detector, as the name suggests, is composed of mats of six layers of fibres, which are then combined together to form modules [167]. The modules make up the layers of the detector, of which there are four, in a similar configuration to the UT ($x-u-v-x$). Charged particles traversing the

subdetector cause the emission of photons from the scintillator, which can be wavelength-shifted and then photo-multiplied to boost the signal. There are three Sci-Fi stations, superseding the tracking stations of Runs 1 and 2.

3.4.5 Software and Trigger

In Run 2, HLT1 outputted at around 1 MHz, and this will not change in Run 3, so this stage has to work 40 times as fast as in Run 2 to compensate for the missing L0 trigger. In Run 2, this stage outputted at around 12.5 kHz, but this is expected to be an order of magnitude larger for Run 3, with a data rate of 10 GB/s and average event size of 70 kB. The signal rates facing the upgraded detector are considerable, potentially as much as 27 GB/s of just $\bar{b}b$ events using an inclusive trigger, and three times as many $\bar{c}c$ events. Such conditions could necessitate applying a pre-scale to many trigger lines just to fit within the bandwidth available. This has motivated a move to save more of the data in a reduced format, according to the *Turbo* model, making use of more complete real-time reconstruction and saving only reconstructed, rather than raw, information. This means that the HLT2 selection is roughly equivalent to offline selections and what would have been done in Brunel. Brunel's presence now simply allows users to re-run the reconstruction with a different parameterisation without the need to redo the trigger selection. Like the stripping in Runs 1 and 2, data in Run 3 is run offline through *sprucing* for sorting into streams and further selecting to improve signal quality and reduce data size.

Global Event Cuts (GECs) remove events with the largest multiplicities, which typically have the worst signal purities and are more computationally expensive, and free up bandwidth to allow the reconstruction of the remaining events to be brought closer to that of the offline algorithms. The event multiplicity can be considered in terms of a number of metrics, e.g. the number of PVs, the number of tracks reconstructed, or simply the hit multiplicity of a subdetector, all of which are well correlated. Many of these measures are, in fact, correlated with each other, as shown in Figure 3.25, where a GEC based on the sum of the ECAL and HCAL multiplicities (GEC = N_{ECAL} + N_{HCAL}) is compared to other possible measures of the event multiplicity.

The effect of making a cut on calorimeter multiplicity was studied using $B_s^0 \to \phi\phi$ simulation for expected upgrade conditions, and it was found that the most complex events could be sufficiently removed with a cut on events with multiplicities above 1200, while maintaining a 90% signal efficiency, as shown in Figure 3.26.

3.4.6 Commissioning

Since much of the infrastructure of the LHCb detector is brand-new for Run 3, great effort is required to ensure that the projected performance is realised and the operations of each part are validated. Much work has already been done by subdetector experts to commission each individual aspect under the pressure of a number of setbacks. In order to commission the entire detector as a whole, analysis of the data is a key objective,

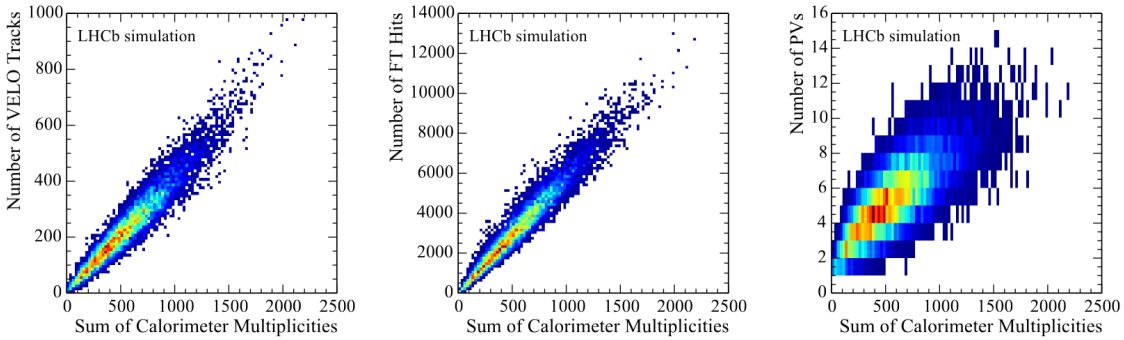

FIGURE 3.25: Correlation of the sum of the calorimeter multiplicities (GEC) with other measures of event complexity: (left) number of VELO tracks, (middle) number of SciFi (or Fibre Tracker, FT) hits, and (right) number of reconstructed primary vertices. Figure taken from Ref. [168].

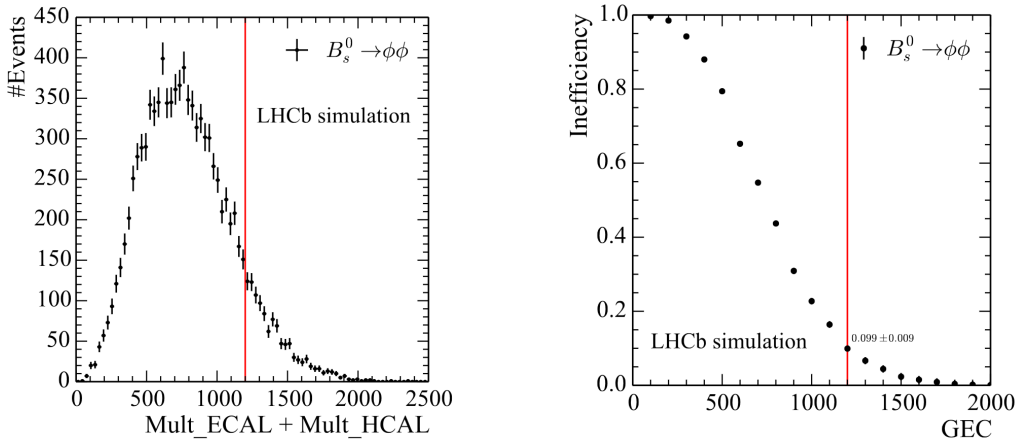

(A) (B)

FIGURE 3.26: Studies of the efficiencies of GEC selections. (A) shows the distribution of events with GEC. (B) shows the integrated inefficiency as a function of GEC value. Figure taken from Ref. [168]

and I have been responsible for *Early Measurements* involving b hadrons as part of this commissioning task. These are described in Chapter 5.

4

CP Violation in $\bar{B}_s^0 \to D_s^+ \pi^-$ at LHCb

"You, the people, have the power to make this life free and beautiful, to make this life a wonderful adventure ... Let us fight for a world of reason, a world where science and progress will lead to all men's happiness ... in the name of democracy, let us all unite!"

- Charlie Chaplin, *The Great Dictator*

4.1 Introduction

At the time of writing, one of the most significant suggestions of deviations between the predictions of the SM and experimental data comes from branching ratios of decays of the form $\bar{B}^0_{(s)} \to D^{(*)+}_{(s)} h^-$, where $h = \{\pi, K, \rho, K^*\}$, which are in significant tension with the predictions of QCD Factorisation (QCDF), a technique introduced in Section 2.5. In particular disagreement are the branching ratios of $\bar{B}^0_s \to D^+_s \pi^-$, $\bar{B}^0 \to D^+ \pi^-$ and $\bar{B}^0 \to D^+ K^-$, though the exact value depends on which prediction is used. As will be seen in Chapter 7, the first and last of these decays are dominated by tree-level $b \to c\bar{u}q$ diagrams, with theoretical uncertainties that are well-controlled, and are two of the most reliable SM predictions for non-leptonic branching ratios [58]. $\bar{B}^0 \to D^+ \pi^-$ also has contributions from annihilation topologies, which spoil this somewhat. Explicitly, the tensions for $\bar{B}^0_s \to D^+_s \pi^-$ and $\bar{B}^0 \to D^+ K^-$ are 5.8σ and 7.1σ, respectively, compared with Ref. [58], and 4.5σ and 6.1σ, respectively, compared with Ref. [59]. These channels being tree-dominated means that they would be expected to be reasonably well-described by QCDF, underlining the significance of these tensions, though it is important to verify that QCD is well-understood with further theoretical analyses. This provides the context for what is discussed in Chapter 7. There is, nonetheless, the tantalising prospect that BSM effects are at play. Since CP asymmetries are also sensitive to such new physics, measurements of these quantities for the tree-dominated modes are excellent potential probes for BSM effects [169].

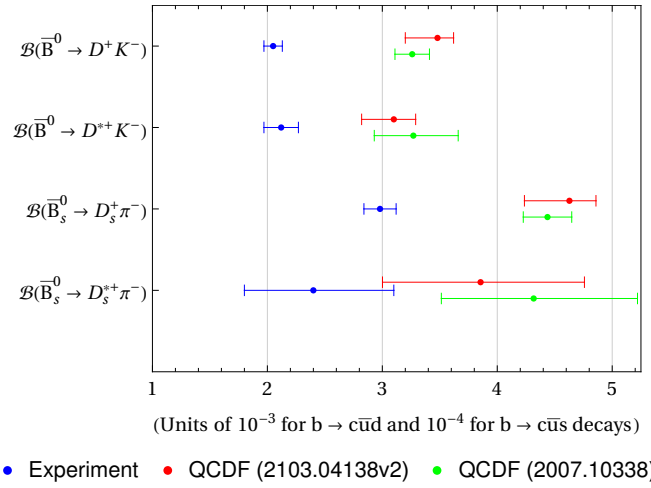

(A) Tree-dominated modes. Experimental values (in blue) are compared with two sets of QCDF predictions (in red and green) from Refs. [58, 59]

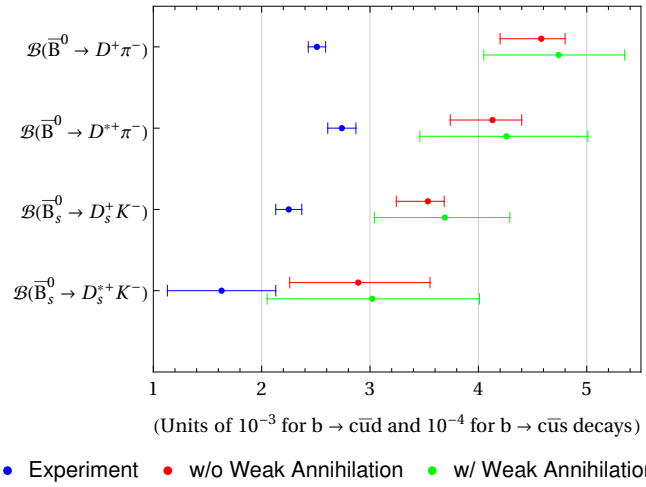

(B) Modes not dominated solely by tree diagrams, for which QCDF is expected to hold less well. Experimental values (in blue) are compared with predictions from Ref. [59], both with (green) and without (red) weak annihilation diagrams.

FIGURE 4.1: Current tensions in $B \to Dh$ modes between experiment and QCDF predictions. Significant tensions are seen for $\bar{B}^0 \to D^+K^-$, $\bar{B}^0_s \to D^+_s\pi^-$, and $\bar{B}^0 \to D^+\pi^-$.

4.1.1 Theoretical Background

In the SM, $\bar{B}^0 \to D^+K^-$ and $\bar{B}^0_s \to D^+_s\pi^-$ are both flavour specific and CP-conserving at amplitude-level, category 2 in Section 2.3.2, where the only contribution to the total CP asymmetry, A^q_{fs}, can be from CP violation in meson mixing, a^q_{fs}. Therefore we have

$$A^q_{\text{fs}} = \frac{\Gamma\left(\bar{B}^0_q(t) \to D^+_q h^-\right) - \Gamma\left(B^0_q(t) \to D^-_q h^+\right)}{\Gamma\left(\bar{B}^0_q(t) \to D^+_q h^-\right) + \Gamma\left(B^0_q(t) \to D^-_q h^+\right)} = a^q_{\text{fs}}. \tag{4.1}$$

Here, the complex amplitude $\mathcal{A}_f$ for $\bar{B}^0_q \to D^+_q h^-$ has a single contribution, which can be denoted as $\mathcal{A}^{SM}_f$ with separate strong and weak phases of ϕ^{SM} and φ^{SM}, respectively.

There is no interference, and so no direct CP violation.

Generally, any additional New Physics contribution will change this, as the amplitude becomes

$$\mathcal{A}_f = \left|\mathcal{A}_f^{\mathrm{SM}}\right| e^{i\phi^{\mathrm{SM}}} e^{i\varphi^{\mathrm{SM}}} + \left|\mathcal{A}_f^{\mathrm{BSM}}\right| e^{i\phi^{\mathrm{BSM}}} e^{i\varphi^{\mathrm{BSM}}} \equiv \left|\mathcal{A}_f^{\mathrm{SM}}\right| e^{i\phi^{\mathrm{SM}}} e^{i\varphi^{\mathrm{SM}}} \left(1 + r e^{i\phi} e^{i\varphi}\right), \tag{4.2}$$

where r, ϕ, and φ are, respectively, the *relative* magnitude, strong phase, and weak phase of the BSM contribution compared to the SM. A similar definition may be made for the conjugate decay amplitude, $\bar{\mathcal{A}}_{\bar{f}}$, for $B_q^0 \to D_q^- h^+$. The presence of interference in these amplitudes then allows for direct CP violation [169]. The amplitudes themselves are not physical, but the squares of their magnitudes

$$\left|\mathcal{A}_f\right|^2 = \left|\mathcal{A}_f^{\mathrm{SM}}\right|^2 \left|1 + r e^{i\phi} e^{i\varphi}\right|^2 = \left|\mathcal{A}_f^{\mathrm{SM}}\right|^2 \left(1 + 2r\cos(\phi + \varphi)\right) + \mathcal{O}(r^2) \tag{4.3a}$$

$$\left|\bar{\mathcal{A}}_{\bar{f}}\right|^2 = \left|\bar{\mathcal{A}}_{\bar{f}}^{\mathrm{SM}}\right|^2 \left|1 + r e^{i\phi} e^{-i\varphi}\right|^2 = \left|\mathcal{A}_f^{\mathrm{SM}}\right|^2 \left(1 + 2r\cos(\phi - \varphi)\right) + \mathcal{O}(r^2), \tag{4.3b}$$

are proportional to the appropriate partial widths:

$$\Gamma\left[\bar{B}_q(t) \to f\right] = \frac{1}{2} N_f \left|\mathcal{A}_f\right|^2 (1 + a_{\mathrm{fs}}^q) e^{-\Gamma_q t} X_q^-(t), \tag{4.4a}$$

$$\Gamma\left[B_q(t) \to \bar{f}\right] = \frac{1}{2} N_f \left|\bar{\mathcal{A}}_{\bar{f}}\right|^2 (1 - a_{\mathrm{fs}}^q) e^{-\Gamma_q t} X_q^-(t), \tag{4.4b}$$

$$\Gamma\left[B_q(t) \to f\right] = \frac{1}{2} N_f \left|\mathcal{A}_f\right|^2 e^{-\Gamma_q t} X_q^+(t), \tag{4.4c}$$

$$\Gamma\left[\bar{B}_q(t) \to \bar{f}\right] = \frac{1}{2} N_f \left|\bar{\mathcal{A}}_{\bar{f}}\right|^2 e^{-\Gamma_q t} X_q^+(t), \tag{4.4d}$$

where the notation $X_q^{\pm}(t)$ denotes a function dependent on the mass and width differences, ΔM_q and $\Delta\Gamma_q$, between the two flavour states

$$X_q^{\pm}(t) \equiv \cosh\left(\frac{\Delta\Gamma_q t}{2}\right) \pm \cos\left(\Delta M_q t\right). \tag{4.5}$$

Here, we used the fact that $\left|\mathcal{A}_f^{\mathrm{SM}}\right| = \left|\bar{\mathcal{A}}_{\bar{f}}^{\mathrm{SM}}\right|$ and $\left|\bar{\mathcal{A}}_f^{\mathrm{SM}}\right| = \left|\mathcal{A}_{\bar{f}}^{\mathrm{SM}}\right| = 0$. Eq. (4.1) then becomes [169]

$$\begin{aligned}
A_{\mathrm{fs}}^q &= \frac{\Gamma\left(\bar{B}_q(t) \to D_q^- h^+\right) - \Gamma\left(B_q(t) \to D_q^+ h^-\right)}{\Gamma\left(\bar{B}_q(t) \to D_q^- h^+\right) + \Gamma\left(B_q(t) \to D_q^+ h^-\right)} \\
&\approx \frac{(1 + a_{\mathrm{fs}}^q) - (1 - a_{\mathrm{fs}}^q)}{(1 + a_{\mathrm{fs}}^q) + (1 - a_{\mathrm{fs}}^q)} - 2r \frac{(1 + a_{\mathrm{fs}}^q)\cos(\phi - \varphi) - (1 - a_{\mathrm{fs}}^q)\cos(\phi + \varphi)}{(1 + a_{\mathrm{fs}}^q) + (1 - a_{\mathrm{fs}}^q)} \\
&\approx a_{\mathrm{fs}}^q - 2r\left[\frac{1}{2}\left(\cos\phi\cos\varphi + \sin\phi\sin\varphi\right) - \frac{1}{2}\left(\cos\phi\cos\varphi - \sin\phi\sin\varphi\right)\right] \\
A_{\mathrm{fs}}^q &= a_{\mathrm{fs}}^q - 2r\sin\phi\sin\varphi = a_{\mathrm{fs}}^q - A_{\mathrm{dir}}^q,
\end{aligned} \tag{4.6}$$

where $A^q_{\text{dir}} \approx 2r \sin\phi \sin\varphi$, and a^q_{fs} is assumed to be small. Measurements of a^q_{fs} (predominantly from semi-leptonic decays) confirm that this is the case and are currently consistent with the SM [170]:

$$A^s_{\text{fs}} = a^s_{\text{fs}} (= a^s_{\text{sl}}) = (-60 \pm 280) \times 10^{-5},$$
$$A^d_{\text{fs}} = a^d_{\text{fs}} (= a^d_{\text{sl}}) = (-21 \pm 17) \times 10^{-4}.$$

A^q_{fs} is, however, yet to be explicitly measured for $\bar{B}^0_s \to D^+_s \pi^-$ or $\bar{B}^0 \to D^+ K^-$. Here, measurements of A^q_{fs} could give access to A^q_{dir}, which may be as large as 10^{-2} [169], and can probe BSM effects in tree-level hadronic decays independent of theoretical assumptions. On account of the rapid oscillation, governed by ΔM_q, of $\bar{B}^0_s$ compared to $\bar{B}^0$, the production asymmetry effects present in the latter are "washed out" in the former case when time-integrated. I was a proponent of an analysis that made such a measurement for $\bar{B}^0_s \to D^+_s \pi^-$ in Run 2. This is, at the time of writing, in the review process, and the following chapter follows the analysis note (Ref. [1]), with an emphasis on my particular contributions; the determination of detection asymmetries and misidentified (misID) background fractions. Titles of sections where I had limited personal involvement will be italicised.

4.1.2 Experimental Considerations

The effective flavour tagging efficiency (i.e. to tag a neutral B meson as $B^0_{(s)}$ or $\bar{B}^0_{(s)}$) in a hadron collider like the LHC, taking into account mistagging probabilities, is generally low. At LHCb, this is in the region of 6% [77] and counteracts the sensitivity improvement of a factor of two that would be gained from performing a tagged analysis rather than an untagged one, and so it is experimentally advantageous to make an untagged measurement [169]

$$\begin{aligned} A^q_{\text{untag.}} &= \frac{\left[\Gamma\left(\bar{B}_q(t) \to \bar{f}\right) + \Gamma\left(B_q(t) \to \bar{f}\right)\right] - \left[\Gamma\left(\bar{B}_q(t) \to f\right) + \Gamma\left(B_q(t) \to f\right)\right]}{\left[\Gamma\left(\bar{B}_q(t) \to \bar{f}\right) + \Gamma\left(B_q(t) \to \bar{f}\right)\right] + \left[\Gamma\left(\bar{B}_q(t) \to f\right) + \Gamma\left(B_q(t) \to f\right)\right]} \\ &= \frac{\left|\bar{\mathcal{A}}_f\right|^2 \left[X^+_q(t) + \left(1 - a^q_{\text{fs}}\right) X^-_q(t)\right] - \left|\bar{\mathcal{A}}_f\right|^2 \left[X^+_q(t) + \left(1 + a^q_{\text{fs}}\right) X^-_q(t)\right]}{\left|\bar{\mathcal{A}}_f\right|^2 \left[X^+_q(t) + \left(1 - a^q_{\text{fs}}\right) X^-_q(t)\right] + \left|\bar{\mathcal{A}}_f\right|^2 \left[X^+_q(t) + \left(1 + a^q_{\text{fs}}\right) X^-_q(t)\right]} \\ &= \frac{2r \sin\phi \sin\varphi - a^q_{\text{fs}} \left(1 + 2r \cos\phi \cos\varphi + r^2\right) Y(t)}{1 + 2r \cos\phi \cos\varphi + r^2 - 2a^q_{\text{fs}} r \sin\phi \sin\varphi Y(t)} \\ &\approx \frac{2r \sin\phi \sin\varphi}{1 + 2r \cos\phi \cos\varphi + r^2} - a^q_{\text{fs}} Y(t), \end{aligned} \tag{4.7}$$

with

$$Y(t) = \frac{X^-_q(t)}{X^+_q(t) + X^-_q(t)} = \frac{1}{2}\left[1 - \frac{\cos\left(\Delta M_q t\right)}{\cosh\left(\frac{\Delta\Gamma_q t}{2}\right)}\right].$$

Time-integrating, we find a modification to Eq. (4.6)

$$\left\langle A^q_{\text{untag.}} \right\rangle \approx A^q_{\text{dir}} - \frac{a^q_{\text{fs}}}{2}(1-\rho_q), \tag{4.8}$$

where

$$1-\rho_q = \frac{\Gamma_q^2 - \frac{\Delta\Gamma_q^2}{4}}{\Gamma_q^2 + \Delta M_q^2},$$

and

$$A^q_{\text{dir}} = A^q_{\text{untag.}}(a^q_{\text{fs}} = 0) = \frac{2r\sin\phi\sin\varphi}{1+2r\cos\phi\cos\varphi+r^2}.$$

Since ρ_s is very small (~ 0.001), for $\bar{B}_s^0 \to D_s^+\pi^-$, we have

$$\left\langle A^s_{\text{untag.}} \right\rangle \approx A^s_{\text{dir}} - \frac{a^s_{\text{fs}}}{2}. \tag{4.9}$$

It should be noted that the conventions for defining A^q_{fs} and $\left\langle A^q_{\text{untag.}} \right\rangle$ introduces a relative sign difference between the two. Practically-speaking, there are several contributions to the total asymmetry to consider

$$\left\langle A^s_{\text{untag.}} \right\rangle = A_{\text{raw}} - A_{\text{det}} - A_{\text{prod}} \frac{\int e^{-\Gamma_s t}\cos(\Delta M_s t)\epsilon(t)dt}{\int e^{-\Gamma_s t}\cosh\left(\frac{\Delta\Gamma_s t}{2}\right)\epsilon(t)dt}, \tag{4.10}$$

where A_{raw} is simply the normalised asymmetry of reconstructed decays, A_{det} is the detection asymmetry, A_{prod} is the production asymmetry, and $\epsilon(t)$ is an acceptance function. Each of these contributions will need to be measured to give access to the untagged, time-integrated asymmetry, and so to potential BSM effects via Eq. (4.9).

4.2 Data Samples

Having devised an analysis strategy, the first thing to do is to get a sample of $\bar{B}_s^0 \to D_s^+\pi^-$ events, ideally with as little contamination from background modes as possible. LHCb collected around 6 fb^{-1} of data during Run 2, and we make use of events reconstructed through one of two final states, $D_s^+ \to K^+K^-\pi^+$ and $D_s^+ \to \pi^+\pi^-\pi^+$. These come from the output of the `StrippingB02DPiD2HHHBeauty2CharmLine` stripping line, as also used in Ref. [77]. This line applies loose requirements on the decay kinematics and geometry, with the rate further reduced using a bagged boosted decision tree (BDT) classifier [171] trained on simulation. A pre-requisite of the stripping is that the event was `TOS` or `TIS` on the HLT2 topological lines, which ultimately select events with significant displacement from the PV and/or high p_T [172], or the line that selects inclusive ϕ decays. The event must also have less than 500 long tracks.

All charged particles making up the B meson candidate have to obey several requirements. Firstly, the fit for the associated track must be of decent quality, with a maximum value of 4.0 for the χ^2 per degree of freedom. Conversely, the total χ^2 for the impact parameter to any primary vertex must exceed 4.0, so as to reject tracks coming from here. The probability that the particle is a "ghost", a signal that doesn't correspond to a particle at truth-level, can be no more than 40%. While generically all charged particles are required to have $p_T > 100\,\text{MeV}$ and $p > 1\,\text{GeV}$, candidates for the bachelor particle (in this case the π^- directly from the $\bar{B}^0_s$) have stricter requirements placed on them; $p_T > 500\,\text{MeV}$ and $p > 5\,\text{GeV}$. A D candidate, can then be constructed from three charged particles with a total p_T greater than 1.8 GeV, a maximum distance of closest approach (DOCA) between any two of 0.5 mm, and a combined invariant mass within 100 MeV of the D mass. One of these three must also satisfy the same stricter requirements as the bachelor. The combined vertex must also have a reasonable quality (χ^2 per degree of freedom < 10) and be sufficiently well-separated from all primary vertices (vertex separation $\chi^2 > 16$).

Similarly, the bachelor and the D may be associated to a B meson decay vertex with an equivalent χ^2, that is displaced from the PV. The resulting B candidate must have a momentum consistent with having been produced at the primary vertex with an IPχ^2 to this vertex of less than 25. The BDT selects on further properties of the B candidate, namely its p_T, vertex separation χ^2 from the nearest PV, and the sum of the B- and D-vertex χ^2 divided by the sum of their numbers of degrees of freedom. The requirement of a BDT response larger than 0.05 is ∼100% efficient for signal decays.

It is also useful, as will be seen later, to have access to MC simulated samples, which were run through these same stripping lines. A number of different channels are simulated, including the two signal modes reconstructed in data and several background samples: $\bar{B}^0 \to (D^+ \to K^-\pi^+\pi^+)\pi^-$, $\bar{B}^0 \to (D_s^+ \to K^+K^-\pi^+)\pi^-$, $\bar{B}^0_s \to (D_s^+ \to K^+K^-\pi^+)K^-$, and $\bar{B}^0_s \to [D_s^{*+} \to (D_s^+ \to K^+K^-\pi^+)\pi^0/\gamma)]\pi^-$. At the generation level there are equal numbers of $\bar{B}^0_s \to D_s^+\pi^-$ and $B^0_s \to D_s^-\pi^+$ and the acceptance and stripping line cuts are found not to induce a significant asymmetry ($\lesssim 0.7\%$). For each sample, truth-level requirements are applied to remove non-physical contributions. Table 4.1 summarises these requirements on the *background category*, which classify the source of each contribution, for both B candidates (`lab0`) and D candidates (`lab2`). This procedure is detailed in Ref. [173]. In the appropriate backgrounds, particle misidentification is included by modifying the reconstructed ID to match the intended final state, for example the misidentified proton in $\Lambda^0_b \to (\Lambda_c^+ \to pK^-\pi^+)\pi^-$ had a true identity matching a p but a reconstructed identity matching a K.

4.3 Offline Selection

On top of the stripping lines, further selection criteria are applied to data and MC, as displayed in Table 4.2, in order to improve purity. At the most basic level, the B^0_s is distinguished by both its lifetime and its mass, so cuts on these quantities, as well as on

Decay channel	Background category requirements	
	`lab0`	`lab2`
$\bar{B}^0 \to D^+ \pi^-$	< 60	$= 30$
$\bar{B}^0 \to D^+_s \pi^-$	< 30 or $= 50$	< 30 or $= 50$
$\bar{B}^0_s \to D^+_s \pi^-$	≤ 30	≤ 30
$\bar{B}^0_s \to D^+_s K^-$	< 60	< 30 or $= 50$
$\bar{B}^0_s \to D^{*+}_s \pi^-$	< 60	< 30 or $= 50$
$\Lambda^0_b \to \Lambda^+_c \pi^-$	< 60	$= 30$

Background Type	Category
Signal	0
Fully reconstructed physics background	20
Reflection (Misidentification)	30
Partially reconstructed physics background	40
Low mass background	50
Technical and combinatoric backgrounds	60-130

TABLE 4.1: Requirements on background category applied to MC samples and summary of the physical interpretation of each category. Adapted from Refs. [1, 173]

Decay Modes	Cut	Cut applied
Both D^-_s modes	B^0_s lifetime	$0.25 < \tau < 15$ ps
	B^0_s mass	$5300\ \text{MeV}/c^2 < M(\bar{B}^0_s) < 6000\ \text{MeV}/c^2$
	D^-_s mass	$1930\ \text{MeV}/c^2 < M(D^+_s) < 2010\ \text{MeV}/c^2$
	K^- global PID	$P_K > 0.6, P_\pi < 0.4, P_\mu < 0.95$
	K^- strict PID	$P_K > 0.8, P_\pi < 0.2, P_\mu < 0.95$
	π^- global PID	$P_K < 0.4, P_\pi > 0.6, P_\mu < 0.8$
	π^- strict PID	$P_K < 0.2, P_\pi > 0.8, P_\mu < 0.8$
	L0 trigger	`L0HadronDecision_TOS` on any track
	HLT1 trigger	`Hlt1TrackMVADecision_TOS` and/or `Hlt1TwoTrackMVADecision_TOS`
	HCAL separation	$d_{\text{HCAL}} > 1000$mm on all final-state tracks
$D^-_s \to K^- K^+ \pi^-$	D^0 from $D^*(2010)$	$1830\ \text{MeV}/c^2 < M(KK) < 1890\ \text{MeV}/c^2$
	Λ^+_c peak	$2265\ \text{MeV}/c^2 < M(\hat{p}_K K\pi) < 2310\ \text{MeV}/c^2$ $P_p < 0.5$
$D^-_s \to \pi^- \pi^+ \pi^-$	D^0 from $D^*(2010)$	$1845\ \text{MeV}/c^2 < M(\pi\pi)_{\text{high, low}} < 1867.5\ \text{MeV}/c^2$

TABLE 4.2: Summary of the selection cuts applied to Run 2 data to obtain $B^0_s \to D^+_s \pi^-$ signal candidate samples. As discussed in Sections 4.3.1 and 4.3.3, stricter PID selections were applied to events lying outside of resonance regions. The PID variable `ProbNNX` is abbreviated as P_X.

the mass of the D^+_s for the same reason, are the absolute bare minimum that one should apply. The D^+_s, being a short-lived particle, is reconstructed from its decay products and two dominant decay modes were used, $D^+_s \to K^+K^-\pi^+$ and $D^+_s \to \pi^+\pi^-\pi^+$. It is clearly also important to verify that the PID of the final state pions and kaons match these particular final states. One should also ensure that the trigger lines that initially selected the events make sense. At L0, the event should have been selected due to it containing at least one hadronic track i.e. a `TOS` outcome for the line `L0HadronDecision`,

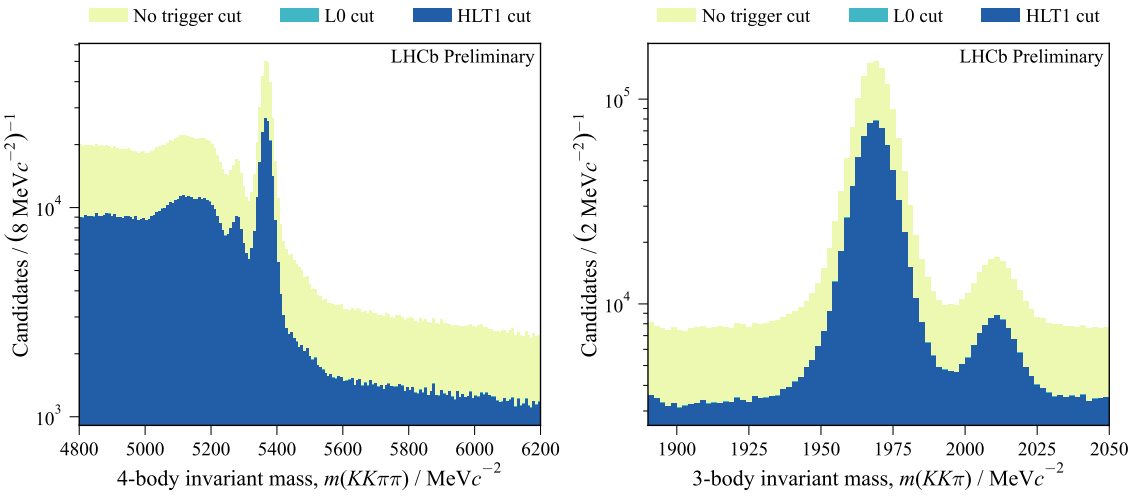

(A) four-body invariant mass spectrum.

(B) three-body invariant mass spectrum.

FIGURE 4.2: Comparison of the effect of trigger selections on invariant mass distributions.

while at HLT1 the event should be `TOS` on either `Hlt1TrackMVADecision` or `Hlt1TwoTrackMVADecision`, which select interesting one- or two-track events based on a multivariate algorithm (MVA). Figure 4.2 demonstrates the impact of these cuts. For the remaining selections, an explanation of how and why these particular choices were made can be found in the following sections.

4.3.1 *Global PID Cut*

Charged final state particles, particularly pions and kaons, all tend to leave similar experimental traces, and one of LHCb's assets is its PID system, which provides additional information that many other experiments do not possess, such that the particle identities can be accurately deduced. Having this discriminating power is essential in analyses such as this one, since there are a number of background modes that come from particle misidentification that must be removed to allow for precision measurements to be made. The same goes for distinguishing between the two signal modes used to reconstruct the D_s^-. A specialised MVA trained on inputs from the PID system, principally from the RICH detectors, can assign probabilities (`ProbNN`) to a reconstructed final state particle, for a variety of mass hypotheses. To give an example, `ProbNNpi` gives the probability that the reconstructed particle was a $\pi^\pm$. One assigns a particular identity to a final state particle by requiring these probabilities to be above or below a certain cutoff for the different hypotheses. Note that the exact cutoff values will vary from one analysis to another, according to the specific requirements. In this instance, to choose the most appropriate cut values, visual comparisons are made of the invariant mass distributions with a range of different values applied, and the optimal set found from the one that gives the best compromise of background suppression vs signal efficiency, as can be seen in Figure 4.3.

Muons misidentified as pions can be rejected by vetoing particles with a positive result for the boolean `isMuon`, which is related to the presence of hits in the muon chambers

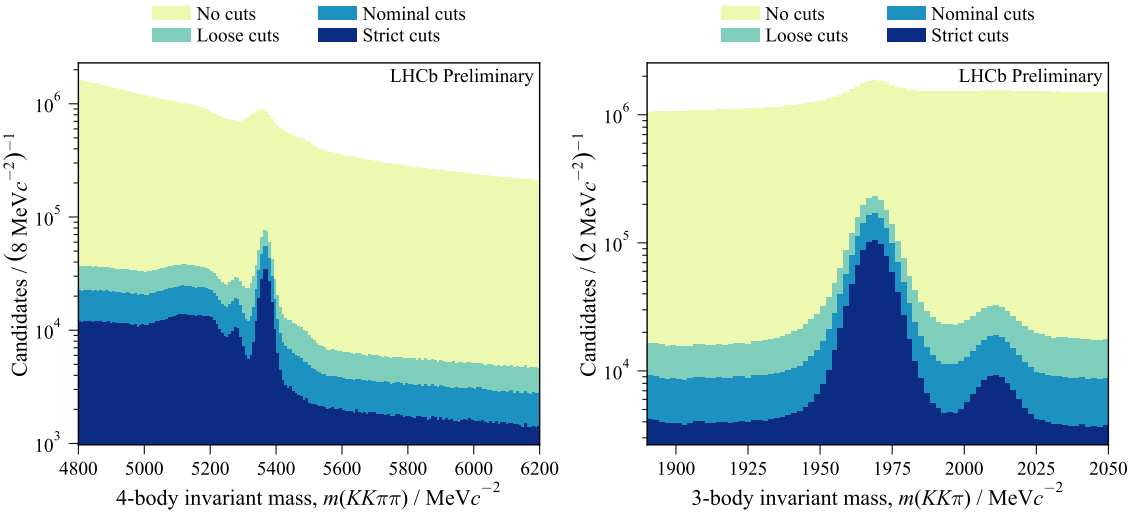

(A) Four-body invariant mass spectrum.

(B) Three-body invariant mass spectrum.

Scenario	Particle	ProbNNk	ProbNNpi	ProbNNmu
None	K^+	–	–	–
	π^+	–	–	–
Loose	K^+	> 0.4	< 0.6	< 0.99
	π^+	< 0.6	> 0.4	< 0.9
Nominal	K^+	> 0.6	< 0.4	< 0.95
	π^+	< 0.4	< 0.6	< 0.8
Strict	K^+	> 0.8	< 0.2	< 0.8
	π^+	< 0.2	> 0.8	< 0.6

FIGURE 4.3: Comparison of the impact of varying severity of ProbNN selection cuts on the signal purity of the full data sample with $K^+K^-\pi^+\pi^-$ final states. Pre-selections were mass window and PID assignment. The corresponding cut values for each of these scenarios are shown in the table.

associated with the particle. The improvement in signal purity due to such cuts is made clear in Figure 4.4. It is also required that each final state particle must be above the Cherenkov threshold in one of the RICH detectors, which will be necessary when PID efficiencies are determined later.

4.3.2 *HCAL separation*

It is often the case, particularly considering the considerable pseudorapidities of the particles involved, that HCAL showers from multiple tracks overlap and are reconstructed within the same energy cluster. Information from the HCAL forms part of the input to the L0 trigger, and in circumstances like these, the efficiency is harder to determine. To avoid this, it is necessary to impose a cut on the separation of projected tracks (inferred from other subdetectors) within the HCAL, which was chosen to be defined as

$$d = \sqrt{(x_K - x_\pi)^2 + (y_K - y_\pi)^2}, \tag{4.11}$$

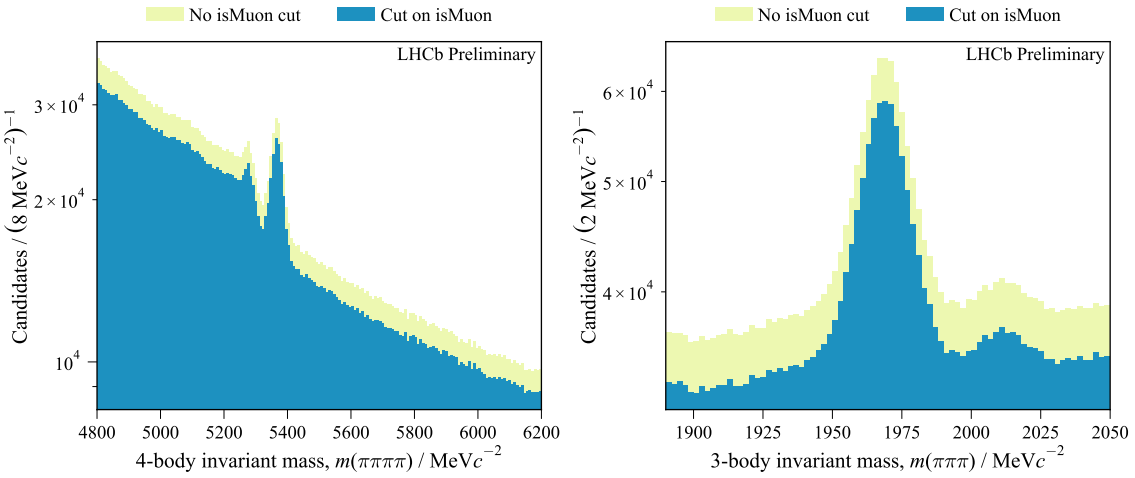

(A) Four-body invariant mass spectrum.

(B) Three-body invariant mass spectrum.

FIGURE 4.4: Comparison of invariant mass distributions for selections with (blue) and without (yellow) a veto on final state pions passing `isMuon` for the $D_s^+ \to \pi^+\pi^-\pi^+$ channel.

Year	Efficiency / %		
	HCAL separation	L0 separation	L0+HCAL separation
2015	29.63(32)	60.30(51)	22.09(27)
2016	29.83(14)	60.75(22)	22.48(12)
2017	30.36(13)	60.64(21)	22.85(11)
2018	29.96(12)	60.38(20)	22.53(10)
Run 2	30.019(74)	60.56(12)	22.586(62)

TABLE 4.3: Efficiencies for the two selections on HCAL separation.

where x_h and y_h are the x and y coordinates of h in the HCAL. This separation is related to the Molière radius introduced in Section 3.3.4. The efficiencies associated with this selection are given in Table 4.3. There is another possible method to enforce such a separation, which requires TOS on `L0Hadron` for the bachelor π^-, or TOS on `L0Hadron` for the h^+ and TIS on `L0Hadron` for the same-sign pion, π^+. Efficiencies from these two separate methods, as well as both together, are shown in Table 4.3, with the overlap between the two characterised by the conditional probabilities

$$P\left(\texttt{L0}|\texttt{HCAL}\right) = 75.24(28)\,\%, \quad \text{and} \quad P\left(\texttt{HCAL}|\texttt{L0}\right) = 37.30(13)\,\%.$$

4.3.3 *Local PID Selection*

What can be hidden within the simple notation for a three-body decay, for example $D \to h_1h_2h_3$, is that there is often an intermediate state H such that the decay can be thought of as two sequential two-body decays, i.e. $D \to Hh_1, H \to h_2h_3$. Identifying such resonant processes requires the study of the invariant masses of pairs of final state particles, typically shown graphically through a two-dimensional *Dalitz* plot. These

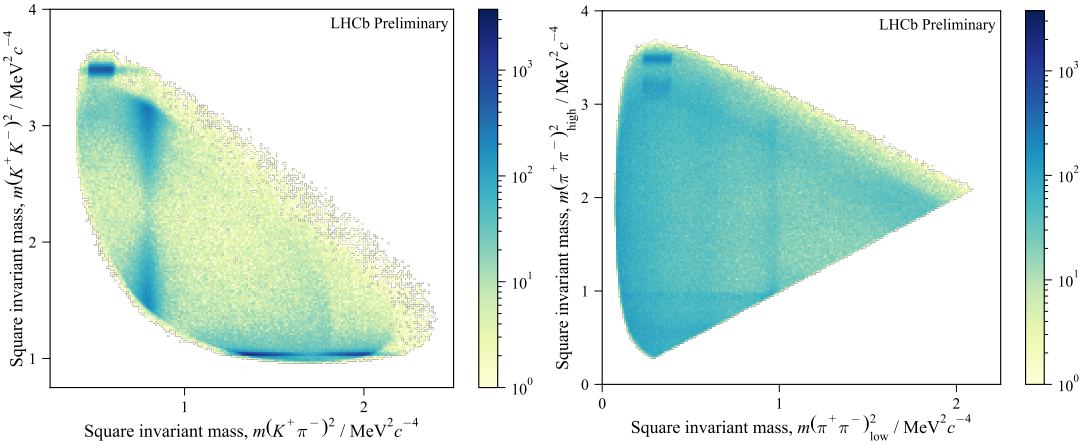

(A) $D^+_s \to K^+K^-\pi^+$. (B) $D^+_s \to \pi^+\pi^-\pi^+$ (with bins flipped).

FIGURE 4.5: Two-dimensional (Dalitz) plots of invariant mass for pairs of daughters in the three-body final state of D^+_s. Resonances can be seen from dark bands. The bin flip method [174] was utilised for the 3π final state, to recast the axes as the higher and lower mass pairings of opposite-sign pions.

have two such pairings on the $x-$ and $y-$axes (the third pair is related to both of these by energy conservation). Resonances will appear as highly-populated bands in this two-dimensional space. Figure 4.5 shows such a plot for the full Run 2 dataset. The spectra for the $D^+_s \to K^+K^-\pi^+$ channel indicates $D^+_s \to \phi(1020)\pi^+$ resonance for 980 MeV $< M(K^\pm K^\mp) <$ 1080 MeV and $K^*(892) \to K^-\pi^+$ for 825 MeV $< M(K^\pm\pi^\mp) <$ 950 MeV. The triple-pion final state has two possible pairings of oppositely-charged pions, which can be distinguished from one another by their invariant mass, with the higher mass pair labelled "high" and the lower mass pair labelled "low". Using such a labelling in a Dalitz plot enhances intermediate resonances, and two $f_0(980) \to \pi^\pm\pi^\mp$ resonance bands can be seen, due to the symmetry of the final state, for 930 MeV $< M(\pi^\pm\pi^\mp)_{\text{low, high}} <$ 1010 MeV. The resonances improve signal purity and, as seen in Table 4.2, a stricter PID requirement is applied outside of these resonant regions. The choice of `ProbNN` cut values is made in a similar way to in Section 4.3.1. The improvement in background reduction relative to signal can be clearly seen in Figure 4.6.

4.3.4 *Misidentified Backgrounds*

Despite the PID cuts outlined in the previous section, there can still be a small number of events, misidentified in reconstruction, that pollute the data. One can focus on the key sources of such backgrounds in order to mitigate this effect, and the treatment of two such sources is detailed in this section, where the samples contained both charge conjugates combined.

Figure 4.5 shows for both decay modes a clear resonance structure around $m^2(K^+K^-) \simeq 3.4\,\text{GeV}^2$ or $m^2(\pi^+\pi^-)_{\text{high}} \simeq 3.4\,\text{GeV}^2$. This can be attributed to the $D^*(2010)^+$ resonance, decaying into $(D^0 \to hh')\pi^+$, where $h, h' \in \{K, \pi\}$, which is reconstructed as a $D^+_s \to h^+h^-\pi^+$ decay. Plotting the 1-dimensional invariant mass spectrum (Figure 4.7,

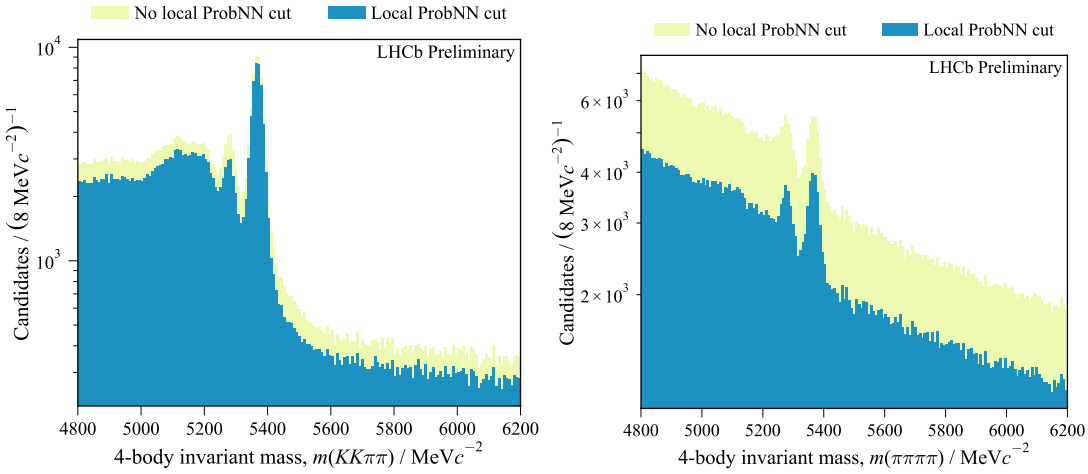

(A) $D_s^+ \to K^+K^-\pi^+$. (B) $D_s^+ \to \pi^+\pi^-\pi^+$.

FIGURE 4.6: Comparison of the impact of imposing variable PID selections, with tighter cuts outside resonance regions, on the four-body invariant mass spectra for the two D_s^+ decay channels.

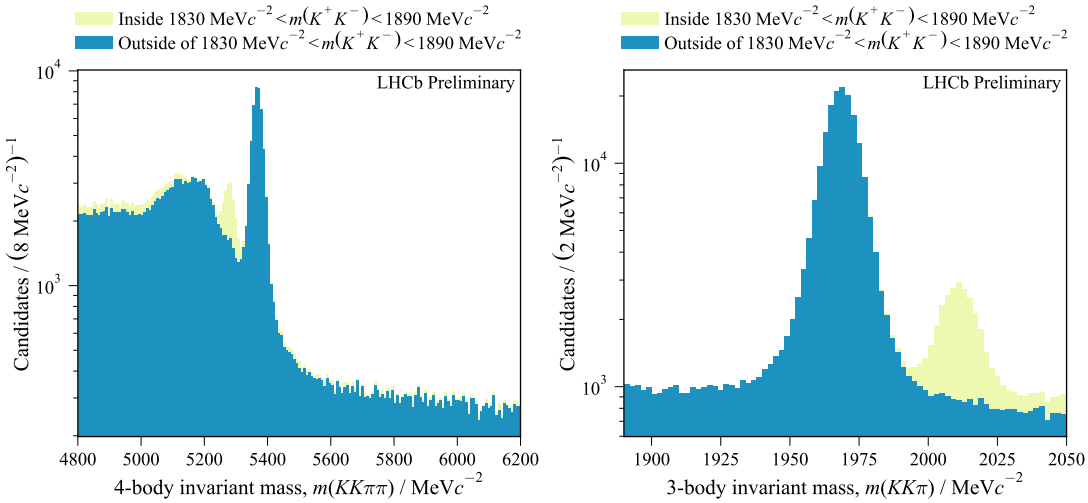

(A) $K^+K^-\pi^+\pi^-$ invariant mass spectrum. (B) $K^+K^-\pi^+$ invariant mass spectrum.

FIGURE 4.7: Comparisons of invariant mass distributions for events within (yellow) and outside (blue) of the region 1830 MeV $< K^+K^- <$ 1890 MeV. The additional peaks seen can be understood as coming from $D^*(2010)^+ \to D^0(K^+K^-)\pi^+$.

right) for the reconstructed D_s^+ shows the presence of a second peak at a slightly higher mass and with a slightly larger width. This peak also appears in the four-body spectrum shown on the left of Figure 4.7. The signal contribution is reasonably low in this region, and so this background is removed with simple vetoes for 1830 MeV $< m(K^+K^-) <$ 1890 MeV and 1845 MeV $< m(\pi^+\pi^-)_{\text{high}} <$ 1890 MeV.

The other dominant misidentified background is $\Lambda_b^0 \to (\Lambda_c^+ \to pK^-\pi^+)\pi^-$, where the proton is reconstructed as a kaon. Thus, a cut on `ProbNNp` is imposed within this resonance region, [2265, 2310] MeV, as seen in Table 4.2. The effect of such a veto can be seen in Figure 4.8.

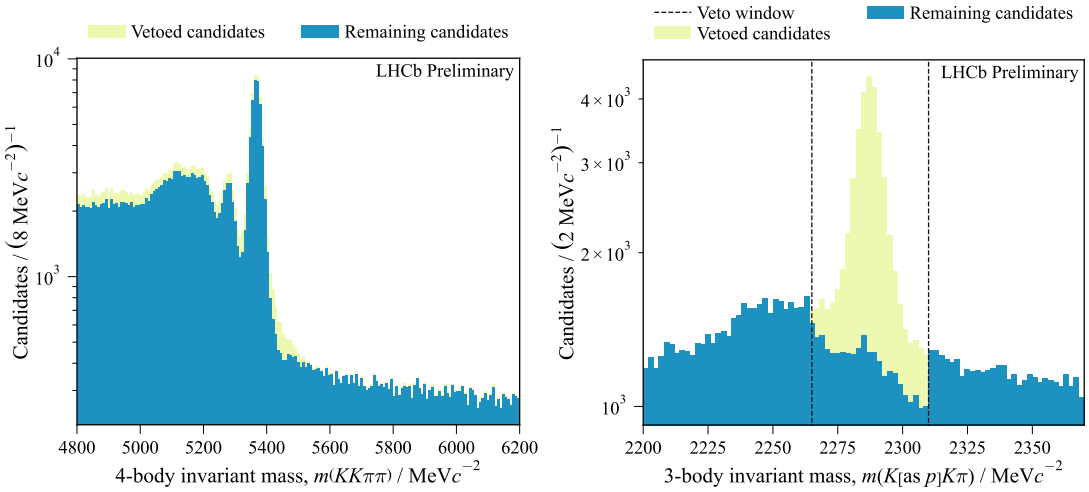

(A) $K^+K^-\pi^+\pi^-$ invariant mass spectrum. (B) K^+ [as p] $K^-\pi^+$ invariant mass spectrum.

FIGURE 4.8: The effect of the Λ_b^0 veto on four-body (left) and three-body (right) invariant mass distributions, with the events remaining after such a selection shown in blue. The latter case is reconstructed in the scenario that the positive kaon was, in fact, a proton. The events that were removed by this selection are shown in yellow, and for the three-body case, it can be seen that the veto removes a peak of events lying around the Λ_c^+ mass, with the bounds of the veto range shown in dashed black.

4.3.5 *Multiple Candidates*

The same event could potentially be reconstructed under both final state hypotheses, meaning the corresponding event number would appear in samples of both $K^+K^-\pi^+\pi^-$ and $\pi^+\pi^-\pi^+\pi^-$ final states. If untreated, this could result in double-counting of events. In cases such as these, we keep the candidate with a $K^+K^-\pi^+\pi^-$ final state and remove the $\pi^+\pi^-\pi^+\pi^-$ candidate, since the former has the greater branching ratio and also the greater signal purity. When there were multiple candidates for a single final state, one candidate is randomly chosen to be persisted, and the others are removed.

4.4 Raw Asymmetry

The raw asymmetry is the normalised difference between the number of $D_s^+\pi^-$ and $D_s^-\pi^+$

$$A_{\text{raw}} = \frac{N\left(D_s^+\pi^-\right) - N\left(D_s^-\pi^+\right)}{N\left(D_s^+\pi^-\right) + N\left(D_s^-\pi^+\right)}, \tag{4.12}$$

where $N\left(D_s^+\pi^-\right)$ and $N\left(D_s^-\pi^+\right)$ can be obtained in a simultaneous unbinned 1D log-likelihood fit to $m(D_s\pi)$. Such fits are performed in a mass window between 5280 MeV and 6000 MeV, also constraining the D_s mass to lie in the range 1930 MeV to 2010 MeV. Through this, the contribution of the partially-reconstructed background $\bar{B}_s^0 \to D_s^+\rho^-$ that lies principally below this window is reduced to a negligible level. This is true also for the $\bar{B}^0 \to D^+\pi^-$ component, though only for the $\pi^+\pi^-\pi^+\pi^-$ final state; as seen in Figure 4.9, a large proportion of this component remains for the $K^+K^-\pi^+\pi^-$ final

Process category	Decay channel
Signal	$\bar{B}^0_s \to D^+_s \pi^-$
Combinatorial	Combinatorial $h^+h^-\pi^+\pi^-$
Misidentified	$\bar{B}^0 \to D^+(K^+\pi^-\pi^+)\pi^{-\dagger}$
	$\bar{B}^0 \to D^-_s(h^-h^+\pi^-)\pi^+$
	$\bar{B}^0_s \to D^+_s(h^+h^-\pi^+)K^-$
Part.-reco.	$\bar{B}^0_s \to D^{*+}_s(D^+_s(h^+h^-\pi^+)\pi^0/\gamma)\pi^-$

TABLE 4.4: Summary of the components included in the invariant mass fits. † The $\bar{B}^0 \to D^+\pi^-$ component was included only for the $K^+K^-\pi^+\pi^-$ final state.

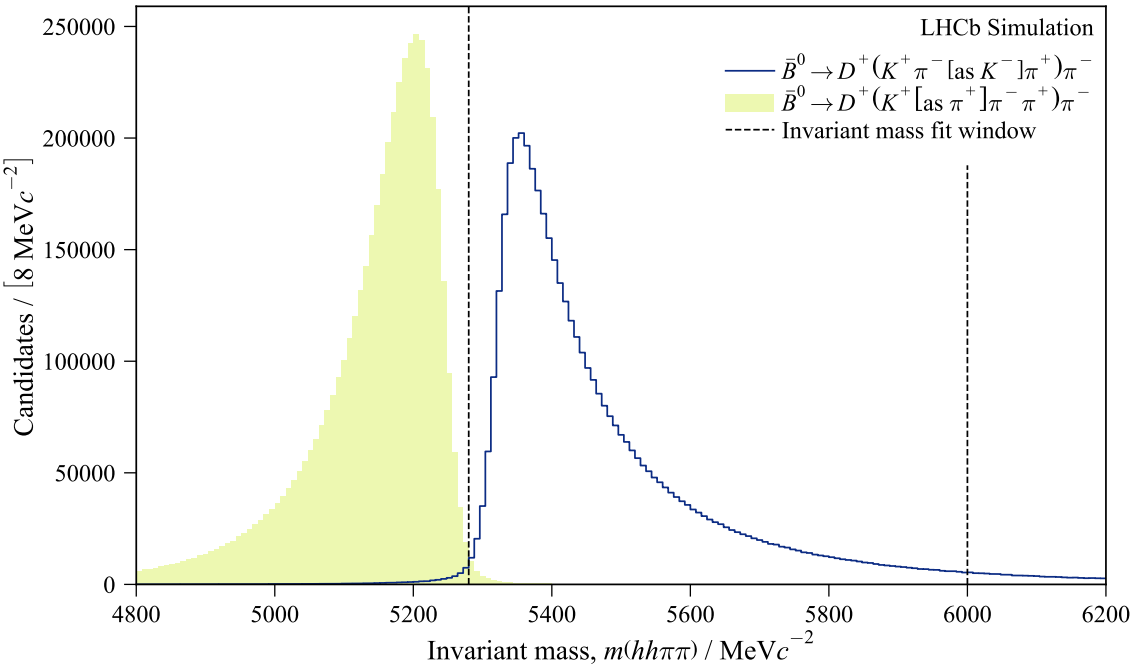

FIGURE 4.9: Invariant mass distributions of simulated $\bar{B}^0 \to (D^+ \to K^+\pi^-\pi^+)\pi^-$ where one of the D^+ daughters is misidentified to give the same $K^+K^-\pi^+\pi^-$ (blue) and $\pi^+\pi^-\pi^+\pi^-$ (yellow) final states as the $\bar{B}^0_s \to D^+_s\pi^-$ signal considered in this analysis [1]. The window where the fit is performed is shown in black.

state and so must be modelled. The Λ^+_c veto described in Section 4.3.4 means that the contribution from misidentified $\Lambda^0_b \to \Lambda^+_c\pi^-$ background is expected to be small too. Table 4.4 summarises the components that are modelled in the mass fits, and the full fit function is the sum of these, weighted by their respective yields:

$$F(m) = \sum_i N_i f_i(m). \tag{4.13}$$

4.4.1 *Signal Model*

To model the signal, we make use of the Extended Cruijff (EC) function [175], defined as

$$f_{\mathrm{EC}}(m|\mu,\beta,\sigma_L,\sigma_R,\alpha_L,\alpha_R) = \begin{cases} C_L\left(m|\mu,\beta,\sigma_L,\alpha_L\right) & m \leq \mu \\ C_R\left(m|\mu,\beta,\sigma_R,\alpha_R\right) & m > \mu \end{cases}, \tag{4.14}$$

and

$$C_{L,R}\left(m|\mu,\sigma_{L,R},\alpha_{L,R},\beta\right) = A\exp\left(\frac{-\left(m-\mu\right)^2\left(1+\beta\left(m-\mu\right)^2\right)}{2\sigma_{L,R}^2+\alpha_{L,R}\left(x-\mu\right)^2}\right), \tag{4.15}$$

where μ represents the mean, β parameterises some asymmetry around this mean, $\sigma_{L,R}$ are the Gaussian widths to the left and right of the mean, $\alpha_{L,R}$ parameterises the tails either side, and A is a normalisation factor. We determine that most suitable signal model for this analysis is the sum of an EC distribution and a Gaussian, f_{G} (mean μ^{G}, width σ^{G}) that makes up a fraction c of the total signal, i.e.

$$f_{\mathrm{EC+G}}(m|c,\boldsymbol{t}^{\mathbf{G}},\boldsymbol{t}^{\mathbf{EC}}) = A\left(cf_{\mathrm{G}}(\boldsymbol{t}^{\mathbf{G}}) + (1-c)f_{\mathrm{EC}}(\boldsymbol{t}^{\mathbf{EC}})\right), \tag{4.16}$$

where $\boldsymbol{t}^{\mathbf{G,EC}}$ are the parameters of the Gaussian and Extended Cruijff terms, respectively. Throughout the rest of this chapter, the abbreviation EC+G will be used to denote this distribution.

4.4.2 Background Components

Misidentified Backgrounds

The misidentified background components are $\bar{B}_s^0 \to D_s^+ K^-$ and, for the $K^+K^-\pi^+\pi^-$ final state, $\bar{B}^0 \to D^+\pi^-$. These follow similar distributions and thus are strongly correlated, and overlap significantly with signal. It is, therefore, necessary to estimate the relative yields of each component to aid the fitting process and ensure that the fit is representative. We find that the time-integrated CP-asymmetry of misidentified background is negligible in comparison to our statistical sensitivity (which will be evaluated later). The background yields can be expressed as fractions of total signal yield. These fractions can be deduced from the branching fractions, $\mathcal{B}_{\mathrm{sig.}}$ and $\mathcal{B}^i_{\mathrm{bkg.}}$, and selection efficiencies, $\varepsilon_{\mathrm{sig.}}$ and $\varepsilon^i_{\mathrm{bkg.}}$, for signal and background:

$$N^i_{\mathrm{bkg.}} = \frac{\mathcal{B}^i_{\mathrm{bkg}}}{\mathcal{B}_{\mathrm{sig.}}} \times \frac{\varepsilon^i_{\mathrm{bkg.}}}{\varepsilon_{\mathrm{sig.}}} N_{\mathrm{sig.}}. \tag{4.17}$$

The branching ratios for signal and background can be taken from the existing literature. The selection efficiencies factorise into those from kinematic selection and those from PID, both determined using MC. The kinematic efficiencies are determined simply from the fraction of MC signal events that lie within the fit range. The *PIDCalib2* package [176] is designed for estimating the efficiencies of PID selections. Since PID is

Channel	Quantity	Value
$\bar{B}_s^0 \to D_s^+ K^-$	Kinematic efficiency ratio, $\varepsilon^{\text{kin.}}_{\bar{B}_s^0 \to D_s^+ K^-} / \varepsilon^{\text{kin.}}_{\text{sig.}}$	0.982 78(66)
	Branching fraction ratio, $\frac{\mathcal{B}(\bar{B}_s^0 \to D_s^+ K^-)}{\mathcal{B}(\bar{B}_s^0 \to D_s^+ \pi^-)}$	0.0755(54)
	PID efficiency ratio, $\varepsilon^{\text{PID}}_{\bar{B}_s^0 \to D_s^+ K^-} / \varepsilon^{\text{PID}}_{\text{sig.}}$	0.057 79(15)
	Yield factor	0.004 29(31)
$\bar{B}^0 \to D_s^+ \pi^-$	Kinematic efficiency ratio, $\varepsilon^{\text{kin.}}_{\bar{B}^0 \to D_s^+ \pi^-} / \varepsilon^{\text{kin.}}_{\text{sig.}}$	0.9995(28)
	Branching fraction ratio, $\frac{\mathcal{B}(\bar{B}^0 \to D_s^+ \pi^-)}{\mathcal{B}(\bar{B}_s^0 \to D_s^+ \pi^-)} \frac{f_s}{f_d}$	0.0268(28)
	PID efficiency ratio, $\varepsilon^{\text{PID}}_{\bar{B}^0 \to D_s^+ \pi^-} / \varepsilon^{\text{PID}}_{\text{sig.}}$	–
	Yield factor	0.0268(28)
$\bar{B}^0 \to D^+ \pi^-$	Kinematic efficiency ratio, $\varepsilon^{\text{kin.}}_{\bar{B}^0 \to D^+ \pi^-} / \varepsilon^{\text{kin.}}_{\text{sig.}}$	0.802 33(62)
	Branching fraction ratio, $\frac{\mathcal{B}(\bar{B}^0 \to D^+ \pi^-)}{\mathcal{B}(\bar{B}_s^0 \to D_s^+ \pi^-)} \frac{f_s}{f_d}$	3.32(21)
	PID efficiency ratio, $\varepsilon^{\text{PID}}_{\bar{B}^0 \to D^+ \pi^-} / \varepsilon^{\text{PID}}_{\text{sig.}}$	0.004 234(59)
	Yield factor	0.011 27(75)

TABLE 4.5: Contributions to the background fractions for the three misidentified components, evaluated for the $K^+K^-\pi^+\pi^-$ final state in a combined Run 2 sample of both magnet polarities [1].

not well-modelled in MC, this tool uses reference samples from data to produce binned efficiency tables that can then be applied to the kinematics of a user's MC sample. Comparing the resulting total efficiency for the misidentified sample to that of the signal will give an estimate of the misidentified fraction. It is, of course, also necessary to scale the B^0 modes with a factor of f_s/f_d. The numerical results from this process are given in Table 4.5.

Low-Mass Background

The background from partially-reconstructed $\bar{B}_s^0 \to D_s^{*+}\pi^-$ decays, as well as misidentified $\bar{B}^0 \to D_s^+\pi^-$, is only significant on the low-mass side of the signal region and as such only the high-mass sides of these components required fitting. The low-mass sides are instead fixed with parameters that have a limited effect on the signal peak. Using this one-sided fit model means that the Gaussian part would add unnecessary complexity and is not included for these components.

Combinatorial Background

Finally, the combinatorial background component in the invariant mass distribution is assumed to follow an exponential distribution

$$f_{\text{Comb.}}(m) = \ell e^{-\ell m}, \tag{4.18}$$

with decay constant ℓ. A characteristic value of ℓ can be estimated through a pre-fit of this function to the upper mass sideband $m\,(h^+h^-\pi^+\pi^-) \in [5600, 5800]\,\text{MeV}$. The central value and associated error obtained from this are then used to place an appropriate

Function	Parameter	Final state	
		$K^+K^-\pi^-\pi^+$	$\pi^+\pi^-\pi^-\pi^+$
Extended Cruijff	Mean, μ^{EC}	5368.500(38) MeV	5369.30(24) MeV
	Beta parameter, β^{EC}	0.0003472(33) MeV^{-2}	0.000284(96) MeV^{-2}
	Left width, σ^{EC}_L	16.187(66) MeV	16.166(88) MeV
	Right width, σ^{EC}_R	15.833(50) MeV	15.646(51) MeV
	Left tail parameter, α^{EC}_L	0.13511(32)	0.1348(21)
	Right tail parameter, α^{EC}_R	0.14289(27)	0.13206(71)
Gaussian	Mean difference, $\Delta\mu^{\text{EC+G}}$	0.323(85)	-4.3(1.7)
	Width, σ^G	13.851(24)	15.98(55)
	Fraction, c	0.7089(65)	0.920(17)

TABLE 4.6: The results of the fit to simulated signal for both types of final state. $\Delta\mu^{\text{EC+G}}$ characterises the difference in means of the Extended Cruijff and Gaussian components.

Gaussian constraint on ℓ in the nominal fit.

4.4.3 *Nominal Mass Fit*

The stability of the fit to experimental data can be improved by first applying the fit model to simulated data for both decay modes. The signal MC sample is chosen to contain both charges of D_s, as the parameters of the signal fit are assumed to be common to both conjugate final states. The model fits the MC samples well. A similar approach is taken for the background components, however MC is only available for $K^+K^-\pi^+\pi^-$, so the resulting fit parameters are assumed to also apply to the $\pi^+\pi^-\pi^+\pi^-$ final state. This assumption is not unjustified due to the experimental similarity of kaons and pions. In instances of misidentified background, appropriate identity replacements and truth-matching are applied to these MC samples. The results from these fits, shown in Table 4.6, were used to constrain the nominal fit to data to ensure good stability.

The results from the MC fits are used as input parameters to fits to the full B^0_s invariant mass spectrum, allowing for small deviations common to all other similar parameters. A common shift, $\delta\mu$, applies to all mean-like parameters (μ^{EC} and μ^{G}) across all components:

$$\mu^{\alpha}_{\text{MC}} \to \mu^{\alpha}_{\text{data}} = \mu^{\alpha}_{\text{MC}} + \delta\mu. \tag{4.19}$$

In a similar way, a common multiplicative factor, s_σ, applies to width-like parameters ($\sigma^{\text{EC}}_{L,R}$ and σ^{G}):

$$\sigma^{\alpha}_{\text{MC}} \to \sigma^{\alpha}_{\text{data}} = s_\sigma \cdot \sigma^{\alpha}_{\text{MC}}. \tag{4.20}$$

The numerical results of the nominal fits to experimental data are provided in Table 4.7.

At the time of writing, this analysis is under review, so the central value of A_{raw} and any information that might enable this to be determined remains concealed from human eyes; it is *blinded*. This is done to avoid any bias that might come from the analysts themselves, and the blinding will only be removed in the final stages of review. The nominal fit is performed separately for both D_s charges but, for illustration prior to unblinding,

Parameter	Final state	
	$K^+K^-\pi^-\pi^+$	$\pi^+\pi^-\pi^-\pi^+$
ℓ	(-4.0 ± 4.1) $\times 10^{-4}$	(-7.09 ± 0.21) $\times 10^{-4}$
$\delta\mu$	-1.13 ± 0.10 MeV	-1.94 ± 0.33 MeV
s_σ	1.0388 ± 0.0057	1.054 ± 0.021
$N_{\text{Comb.}}$ $(D_s^+\pi^-)$	BLINDED	BLINDED
$N_{\text{Comb.}}$ $(D_s^-\pi^+)$	BLINDED	BLINDED
$N_{\text{Comb.}}$ (total)	21850 ± 190	81940 ± 360
$N_{B_s\to D_s^*\pi}$ $(D_s^+\pi^-)$	BLINDED	BLINDED
$N_{B_s\to D_s^*\pi}$ $(D_s^-\pi^+)$	BLINDED	BLINDED
$N_{B_s\to D_s^*\pi}$ (total)	1454 ± 78	1300 ± 100
$N_{B_s\to D_s\pi}$ $(D_s^+\pi^-)$	BLINDED	BLINDED
$N_{B_s\to D_s\pi}$ $(D_s^-\pi^+)$	BLINDED	BLINDED
$N_{B_s\to D_s\pi}$ (total)	42218 ± 230	10450 ± 200
A_{raw}	BLINDED	BLINDED

TABLE 4.7: Numerical results for the floating parameters of the nominal fit plotted in Figure 4.10. These include the decay constant from the fit to the combinatorial background, ℓ, and the deviations compared to the fit to MC, characterised by the common shift of mean-like parameters, $\delta\mu$, and common scaling, s_σ, of width-like parameters. The individual yields for the charge conjugate decays are currently blinded, though their sum is shown.

Figure 4.10 shows the results of a combined fit where the yields for each component are calculated from the sum of yields of the two charge conjugates. All these fits are of good quality, and Figure 4.11 shows the correlations between the floating parameters, which are as expected. None of the floated parameters appear to be strongly correlated, i.e. more than 50%, with the largest effect being between the slope of the combinatorial background, and the yield and width of the signal. Furthermore, these correlations are not significantly different for the two charge conjugates, which suggests that the fits performed similarly for each.

4.4.4 Fit Validation

To validate the fit, 1000 toy MC samples are generated with the value of each of the fit parameters sampled from a Gaussian with mean and width equal to the central value and error, respectively, of its result in the nominal fit. An invariant-mass fit is then applied to each of these toys, 97% of which successfully converge. For each toy, $\mathcal{P}_{A_{\text{raw}}}$, the *pull* on A_{raw}, is calculated by comparing the toy value, $A_{\text{raw}}^{\text{toy}}$, with that from the nominal fit, $A_{\text{raw}}^{\text{data}}$:

$$\mathcal{P}_{A_{\text{raw}}} = \frac{A_{\text{raw}}^{\text{toy}} - A_{\text{raw}}^{\text{data}}}{\sigma_{A_{\text{raw}}}^{\text{toy}}}, \tag{4.21}$$

where $\sigma_{A_{\text{raw}}}^{\text{toy}}$ is the error on $A_{\text{raw}}^{\text{toy}}$. In the ideal case of no bias, the pulls should follow a Gaussian distribution centred on zero, with a width of one, though with N toys the error on these should be $1/\sqrt{N}$ and $1/\sqrt{2N}$, respectively. The toy asymmetry errors

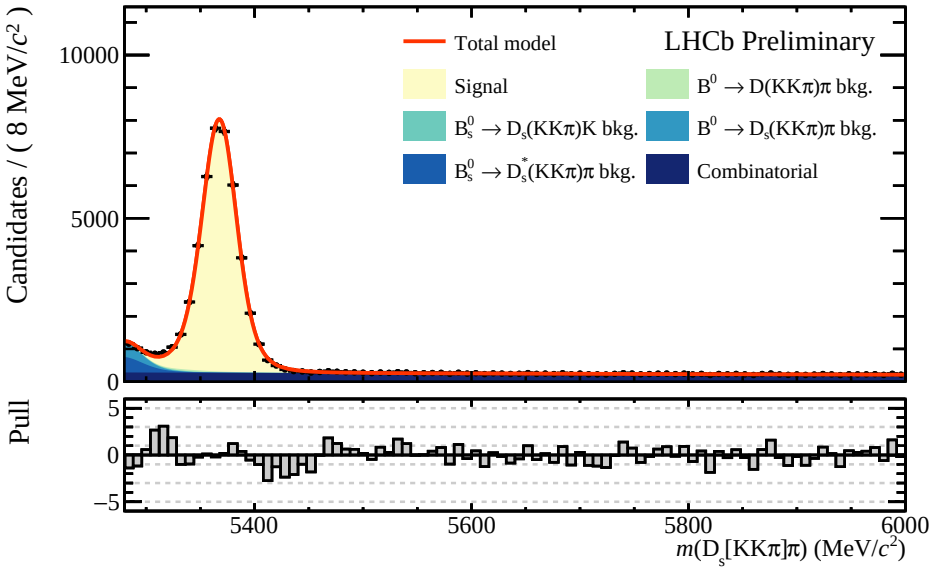

(A) $K^+K^-\pi^+\pi^-$ final state.

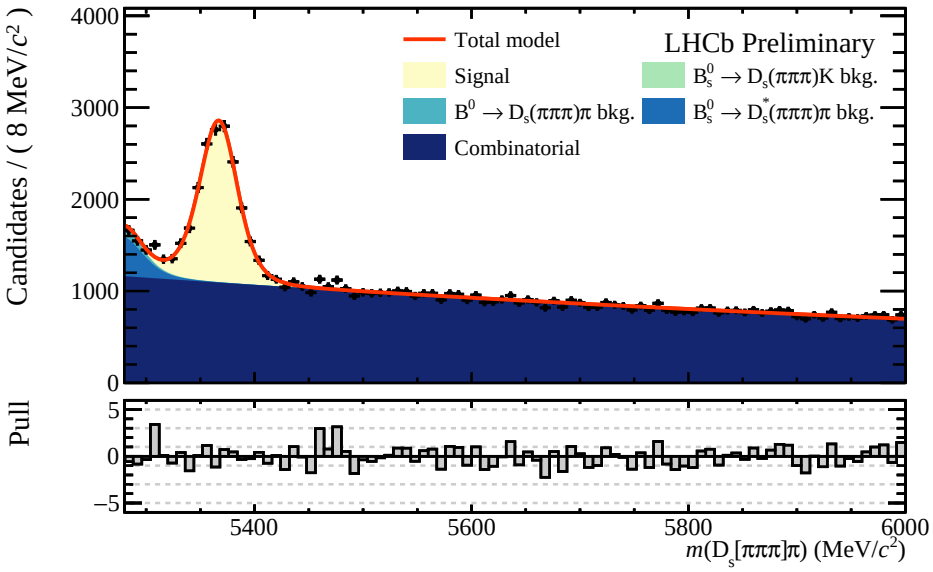

(B) $\pi^+\pi^-\pi^+\pi^-$ final state.

FIGURE 4.10: Nominal fits to the full sample of 6fb^{-1} collected in Run 2.

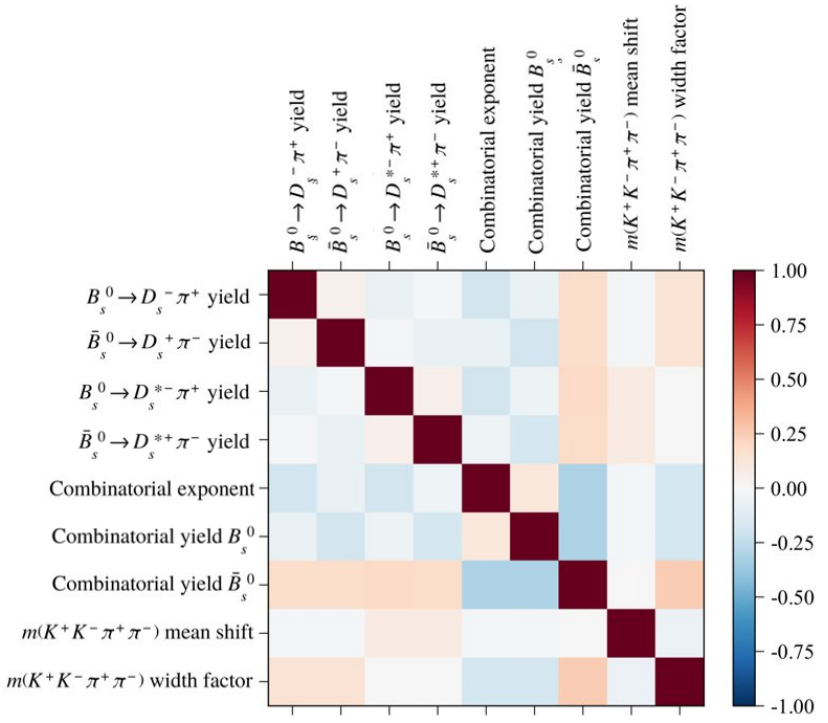

(A) $K^+K^-\pi^+\pi^-$ final state.

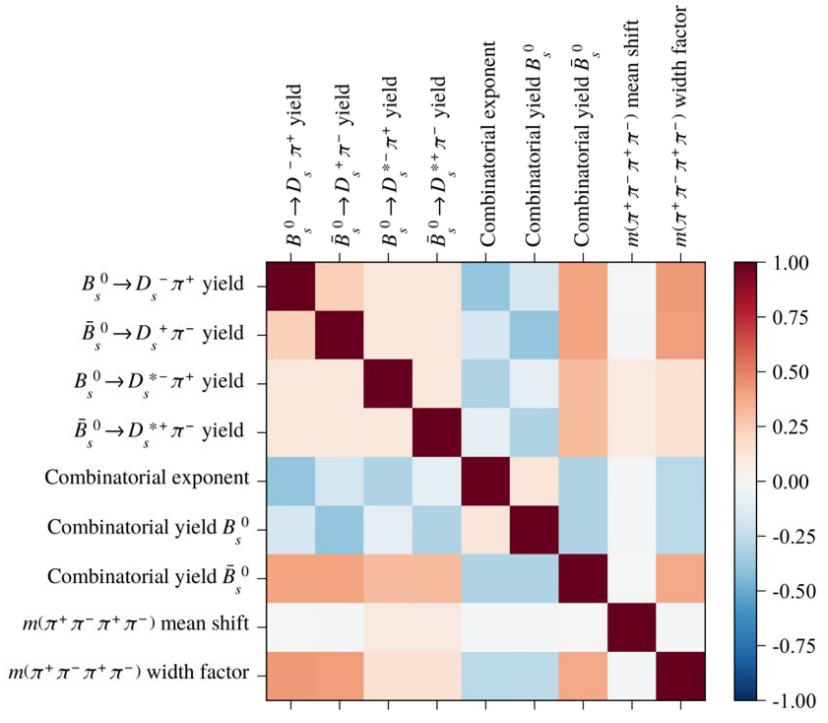

(B) $\pi^+\pi^-\pi^+\pi^-$ final state.

FIGURE 4.11: Correlations between the floating parameters listed in Table 4.7 from the nominal fits shown in Figure 4.10.

Final state	Parameter	Mean, μ	Width, σ	χ^2_R
$K^+K^-\pi^+\pi^-$	Asymmetry pull	$(-1.0 \pm 3.2) \times 10^{-2}$	1.017 ± 0.023	0.636
	Toy asymmetry error	$(5.163 \pm 0.001) \times 10^{-3}$	$(1.682 \pm 0.038) \times 10^{-5}$	0.694
$\pi^+\pi^-\pi^+\pi^-$	Asymmetry pull	$(2.6 \pm 3.2) \times 10^{-2}$	1.007 ± 0.023	0.659
	Toy asymmetry error	$(1.494 \pm 0.001) \times 10^{-2}$	$(2.223 \pm 0.050) \times 10^{-2}$	1.304

TABLE 4.8: Results of Gaussian fits to the distribution of pulls on A_{raw} and of the errors on A_{raw} from toy MC samples.

themselves should also be Gaussian-distributed and the mean and width of this would give the statistical precision and associated error. The fit parameters resulting from these Gaussian fits are given in Table 4.8 for both final states. The fit-quality is good for the distribution of pulls, with means, widths, and their associated errors being consistent with an unbiased fit. Likewise for the toy errors, where the fitted means indicate a statistical sensitivity of 5.16×10^{-3} and 14.9×10^{-3} for $D_s^+ \to K^+K^-\pi^+$ and $D_s^+ \to \pi^+\pi^-\pi^+$, respectively.

Two additional fit scenarios are also considered to validate the extraction of the component yields for both conjugate final states. The first is a fit to a combined sample containing both conjugate states, where the expectation is that the resulting yields should match the sum of the yields for the two D_s charges obtained from the nominal fit. This uses the same inputs from MC fits as the nominal fit. An extension of this scenario performs a two-dimensional fit to both the four-body final state from the B_s and the three-body final state from the D_s. The purpose of this is to check for the presence of non-resonant $h^+h^-\pi^+$ backgrounds. Explicitly, each component of the total distribution is the product of a three-body component and a four-body component, both obtained from fits to the D_s and B_s invariant-mass distributions, respectively. The four-body fit uses the same MC inputs as the nominal fit but the three-body components requires separate MC fits. Each peaking background component in the four-body spectrum is multiplied by an appropriate peaking component from the three-body spectrum; D_s signal for those proceeding via this particle, or peaking background otherwise. The four-body signal component is multiplied by a sum of two three-body components; one from true D_s signal and another from combinatorial three-body background, where all of the hadrons in the final state come directly from the $\bar{B}_s^0$. A similar situation applies to the four-body combinatorial background, which in the three-body spectrum is composed of two components; a true combinatorial component and a peaking component for the case that the D_s^+ is real but is mis-associated with a π^- that did not originate from the B_s.

Figure 4.12 compares the fit results for the floating parameters in the nominal, combined, and 2D scenarios, and close agreement is seen between the combined and nominal fits. The 2D fit, however, does not agree well with the nominal fit for the majority of the parameters, and it is believed that this is due to some mis-modelling. As the analysis remains blinded to the value of A_{raw}, it is also blinded to the separate signal yields for the two charges of D_s.

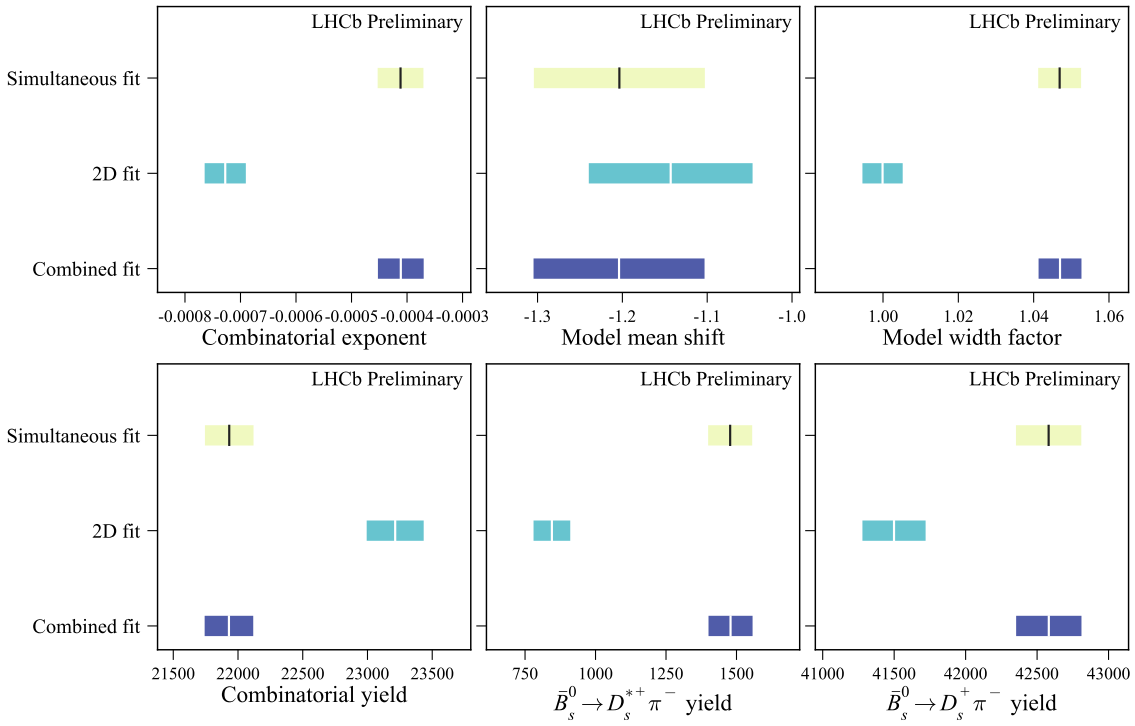

(A) $K^+K^-\pi^+\pi^-$ final state.

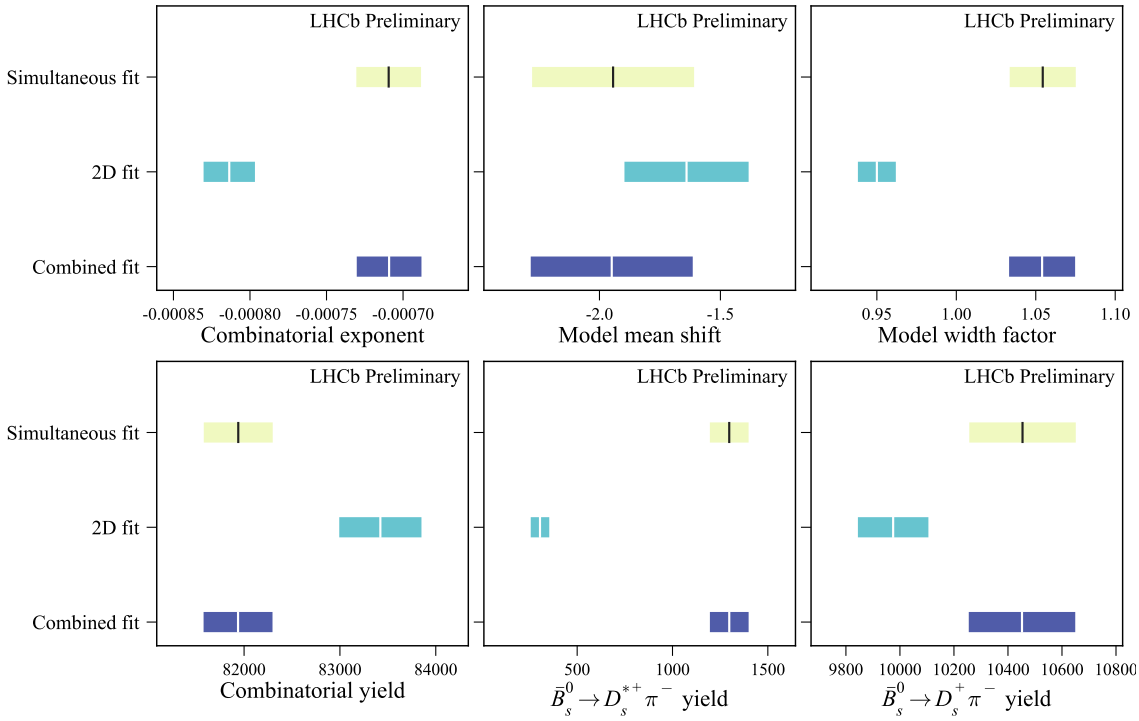

(B) $\pi^+\pi^-\pi^+\pi^-$ final state.

FIGURE 4.12: Comparisons of the consistency of the three different fit scenarios in terms of the resulting values of the floating parameters. Results of the nominal (or simultaneous) fit are shown in yellow, while those of the combined and 2D fits are shown in light- and dark-blue, respectively.

4.5 Production Asymmetry

4.5.1 Definition

Allowing for a production asymmetry, i.e. $N \neq \bar{N}$, the untagged time-dependent decay rates obey modified versions of Eqs. (4.4a)-(4.4d), as [177]

$$\begin{aligned}\Gamma[f,t] &= \Gamma\left(B_s^0(t) \to f\right) + \Gamma\left(\bar{B}_s^0(t) \to f\right) \\ &= \frac{|A_f|^2}{2} e^{-\Gamma_s t}\left[\{N + \bar{N}(1 + a_{\text{fs}}^s)\}\cosh\left(\frac{\Delta\Gamma_s t}{2}\right)\right. \\ &\qquad \left. + \{N - \bar{N}\,(1 + a_{\text{fs}}^s)\}\cos\left(\Delta M_s t\right)\right]\end{aligned} \tag{4.22a}$$

and

$$\begin{aligned}\Gamma\left[\bar{f},t\right] &= \Gamma\left(B_s^0(t) \to \bar{f}\right) + \Gamma\left(\bar{B}_s^0(t) \to \bar{f}\right) \\ &= \frac{\left|\bar{A}_{\bar{f}}\right|^2}{2} e^{-\Gamma_s t}\left[\{\bar{N} + N\,(1 - a_{\text{fs}}^s)\}\cosh\left(\frac{\Delta\Gamma_s t}{2}\right)\right. \\ &\qquad \left. + \{\bar{N} - N\,(1 - a_{\text{fs}}^s)\}\cos\left(\Delta M_s t\right)\right].\end{aligned} \tag{4.22b}$$

From these relations, assuming $|A_f| = |\bar{A}_{\bar{f}}|$, introducing a time-dependent experimental acceptance function $\epsilon(t)$ and integrating, the raw untagged asymmetry is written as

$$\begin{aligned}A_{\text{raw}} &= \frac{\int\left(\Gamma\left[\bar{f},t\right] - \Gamma\left[f,t\right]\right)dt}{\int\left(\Gamma\left[\bar{f},t\right] + \Gamma\left[f,t\right]\right)dt} \\ &= -\frac{a_{\text{fs}}^s}{2} + \left(\frac{\bar{N} - N}{\bar{N} + N} + \frac{a_{\text{fs}}^s}{2}\right)\frac{\int e^{-\Gamma_s t}\cos\left(\Delta M_s t\right)\epsilon(t)dt}{\int e^{-\Gamma_s t}\cosh\left(\frac{\Delta\Gamma_s t}{2}\right)\epsilon(t)dt}.\end{aligned} \tag{4.23}$$

Defining the production asymmetry as

$$A_{\text{prod}} = \frac{\bar{N} - N}{\bar{N} + N}, \tag{4.24}$$

which is much larger than a_{fs}^s, and using Eq. (4.10) with no NP we find

$$\left\langle A_{\text{untagged}}^s \right\rangle = A_{\text{raw}} - A'_{\text{prod}}, \tag{4.25}$$

with an effective production asymmetry A'_{prod}

$$A'_{\text{prod}} = A_{\text{prod}}\frac{\int_0^\infty e^{-\Gamma_s t}\cos\left(\Delta M_s t\right)\epsilon(t)dt}{\int_0^\infty e^{-\Gamma_s t}\cosh\left(\frac{\Delta\Gamma_s t}{2}\right)\epsilon(t)dt}. \tag{4.26}$$

4.5.2 *Determination*

Γ_s, $\Delta\Gamma_s$, and ΔM_s are known, fixed values (shown in Table 4.9) and thus A'_{prod} depends on the decay time acceptance $\epsilon(t)$. The integrating factor that multiplies A_{prod} can then

Parameter	Value
Γ_s	$0.6573(23)\,\text{ps}^{-1}$
$\Delta\Gamma_s$	$0.090(5)\,\text{ps}^{-1}$
$\Delta M_s/\hbar$	$17.765(6)\,\text{ps}^{-1}$

TABLE 4.9: Summary of input parameters used to calculate the production asymmetry factor through numerical integration. Values taken from Ref. [14].

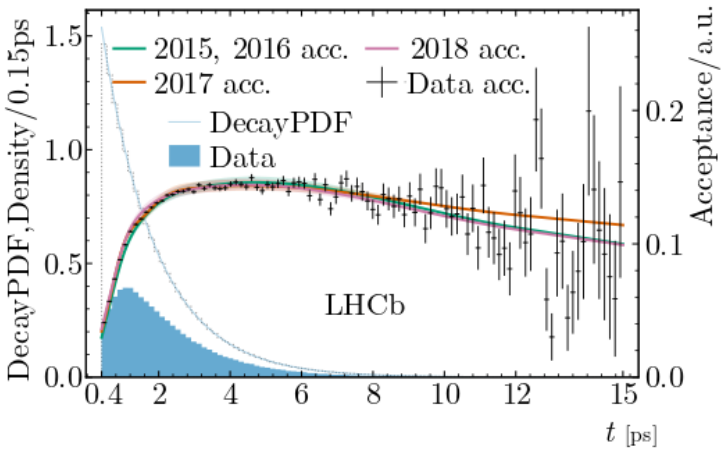

FIGURE 4.13: Decay-time acceptance for Run 2 $\bar{B}^0_s \to D^+_s\pi^-$ data fitted with a cubic spline. Adapted from Ref. [77].

be evaluated for a range of choices of $\epsilon(t)$. Figure 4.13 shows the decay-time acceptance found in the LHCb measurement of ΔM_s [77], where a cubic spline was fitted to MC simulated 2018 signal events and was the nominal choice of acceptance function used here. The function rapidly rises with time for $\approx 3\,\text{ps}$, after which it plateaus. To evaluate the systematics on this choice of acceptance, two extreme scenarios are also considered: a uniform complete acceptance, and a step-function acceptance. Table 4.10 summarises the calculated integration factor for each case. Numerical integration is performed by splitting the domain of $t \in (0.25\,\text{ps}, 15\,\text{ps})$ into 10^8 pieces. It can be seen that this factor is $\mathcal{O}(1\%)$ for all cases. Furthermore, A_{prod} itself was measured by the recent ΔM_s analysis as $A_{\text{prod}} = (-0.0031 \pm 0.0032)$ [77]. Thus, assuming this as an indicative value for this analysis would predict an overall A'_{prod} factor of $\mathcal{O}\left(10^{-4}\right)$. When compared to the statistical sensitivity of the analysis ($\mathcal{O}(10^{-3})$) seen earlier, this is negligible, and so any production asymmetry can be comfortably ignored going forward, aside from assigning a systematic error of $\mathcal{O}\left(10^{-4}\right)$, as was done also in the LHCb measurement of a^s_{sl} [177]. In the event of future measurements, where the sensitivity is greater, accuracy could be improved by using an acceptance function more specific to the sample, obtained from a fit to a combined sample containing both conjugate final states, but for our case this would be unnecessary.

Acceptance function	Integration factor
Uniform	3.5×10^{-2}
Step (> 3ps)	-6.34×10^{-3}
Spline	1.12×10^{-2}

TABLE 4.10: Integration factors for different acceptance functions. The effect appears to be generally $\sim 1\%$

4.6 Detection Asymmetry

There is also an asymmetry due to different efficiencies for conjugate final states to be reconstructed by the LHCb detector. If this asymmetry is small, it can simply be added to the other asymmetries previously discussed when evaluating the total measured asymmetry. For example, with an existing asymmetry between $\bar{\mathcal{N}}$ $\bar{B}_s^0$ decays and $\mathcal{N}$ B_s^0 decays at truth-level, the presence of differing detection efficiencies of, respectively, ϵ_1 and ϵ_2, will modify this asymmetry:

$$\frac{\bar{\mathcal{N}} - \mathcal{N}}{\bar{\mathcal{N}} + \mathcal{N}} \to \frac{\epsilon_1\bar{\mathcal{N}} - \epsilon_2\mathcal{N}}{\epsilon_1\bar{\mathcal{N}} + \epsilon_2\mathcal{N}}.$$

Defining $\epsilon = (\epsilon_1 + \epsilon_2)/2$ and $\Delta = (\epsilon_1 - \epsilon_2)/2$, then this becomes

$$\begin{aligned}\frac{\epsilon(\bar{\mathcal{N}} - \mathcal{N}) + \Delta(\bar{\mathcal{N}} + \mathcal{N})}{\epsilon(\bar{\mathcal{N}} + \mathcal{N}) + \Delta(\bar{\mathcal{N}} - \mathcal{N})} &= \left(\epsilon\frac{\bar{\mathcal{N}} - \mathcal{N}}{\bar{\mathcal{N}} + \mathcal{N}} + \Delta\right) \Big/ \left(\epsilon + \Delta\frac{\bar{\mathcal{N}} - \mathcal{N}}{\bar{\mathcal{N}} + \mathcal{N}}\right) \\ &\approx \frac{\bar{\mathcal{N}} - \mathcal{N}}{\bar{\mathcal{N}} + \mathcal{N}} + \frac{\Delta}{\epsilon} \\ &= \frac{\bar{\mathcal{N}} - \mathcal{N}}{\bar{\mathcal{N}} + \mathcal{N}} + A_{\text{det}},\end{aligned}$$

where

$$A_{\text{det}} = \frac{\epsilon_1 - \epsilon_2}{\epsilon_1 + \epsilon_2} = \frac{\epsilon(D_s^+\pi^-) - \epsilon(D_s^-\pi^+)}{\epsilon(D_s^+\pi^-) + \epsilon(D_s^-\pi^+)}, \tag{4.27}$$

and is assumed to be small. By the same logic, it can be seen that multiple sources of detection asymmetry are additive, and several dominant asymmetries are considered in this section, the sum of which is the total detection asymmetry as in Eq. (4.10), having now shown where this comes from.

4.6.1 $K - \pi$ Tracking Efficiency Asymmetry

The nuclear cross-sections of kaons have been found to be charge-asymmetric, a phenomenon that can shift CP asymmetry measurements by as much as a 10^{-2} [178, 179]. This can be understood from the net charge of the collision environment. To estimate the asymmetry in tracking efficiencies for oppositely-charged final-state kaons in the $D_s^+ \to K^+K^-\pi^+$ mode, we make use of a pre-existing LHCb tool, `KPiTwoTrackAsymmetry`, which was proposed and explained in Ref. [178]. This tool evaluates the charge asymmetry for $K^\pm\pi^\mp$ pairs since this is experimentally simpler to determine than a single kaon

asymmetry. Under the assumption that the Cabibbo-favoured charm decays are not CP-violating, this two-track $K-\pi$ asymmetry can be determined from the raw asymmetries of $D^{\pm} \to K^{\mp}\pi^{\pm}\pi^{\pm}$ and $D^{\pm} \to K^0_S\pi^{\pm}$ decays:

$$A^{\text{track}}(K^-\pi^+) = \frac{N(D^+ \to K^-\pi^+\pi^+) - N(D^- \to K^+\pi^-\pi^-)}{N(D^+ \to K^-\pi^+\pi^+) + N(D^- \to K^+\pi^-\pi^-)} - \frac{N(D^+ \to K^0_S\pi^+) - N(D^- \to K^0_S\pi^-)}{N(D^+ \to K^0_S\pi^+) + N(D^- \to K^0_S\pi^-)} - A(K^0). \quad (4.28)$$

This receives a correction from the asymmetry of $K^0 \to \pi^+\pi^-$, $A(K^0) = (0.054 \pm 0.014)\%$, which is an external input to the tool, having been determined from specialised simulation in Ref. [180]. The tool evaluates this expression using calibration samples of Run 2 data. The $D^+ \to K^-\pi^+\pi^+$ sample was selected in the HLT2 trigger by `Hlt2CharmHadDpToKmPipPipTurbo` in 2015, and subsequently by the more specialised `Hlt2CharmHadDpToKmPipPip_ForKPiAsymTurbo` line, which increases the overlap with the $D^+ \to K^{0,LL}_S\pi^+$ channel. "LL" requires that the two charged pions from K^0_S are reconstructed as long tracks, which limits its flight distance. The $D^+ \to K^{0,LL}_S\pi^+$ sample comes from data selected by `Hlt2CharmHadDp2KS0Pip_KS0LLTurbo`.

To be applicable to the particular sample under study, in this case $\bar{B}^0_s \to (D^+_s \to K^+K^-\pi^+)\pi^-$, the calibration samples must be weighted such that the kinematic distributions match. The $D^+ \to K^-\pi^+\pi^+$ sample is weighted first since it has the higher selection efficiency, and the full weighting strategy is as follows:

1. The calibration $D^+ \to K^-\pi^+\pi^+$ sample is weighted such that the binned distributions of $(p, \eta)_{K^-}$ and $(p_T, \eta)_{\pi^+}$ match. Figure 4.14 illustrates such a procedure.

2. Similarly to step 1, the calibration $D^+ \to K^0_S\pi^+$ sample is reweighted in $(p_T)_{\pi^+}$ and $(p_T, \eta)_{D^+}$ to match the weighted calibration $D^+ \to K^-\pi^+\pi^+$ (from step 1).

3. A further weighting is applied to the $D^+ \to K^0_S\pi^+$ sample in $(\phi)_{\pi^+}$ to match the weighted calibration $D^+ \to K^-\pi^+\pi^+$.

In the final state of the signal mode under study, i.e. $K^+\pi^-K^-\pi^+$, there are clearly two oppositely-charged $K-\pi$ pairs, and so the above procedure must be performed for both of these, and the combined effect is then determined from the sum. Table 4.11 summarises the numerical results of this methodology.

4.6.2 Single π Tracking Asymmetry

For the $D^+_s \to \pi^+\pi^-\pi^+$ final state, since it lacks kaons, a slightly different approach to that explained in the previous subsection is required, though the general concept remains the same. The calibration samples in this instance come from previous determinations of the tracking asymmetry for single pions, $A^{\text{track}}(\pi)$, using semi-leptonic decays. The Run 2 analysis of this quantity [181] presented only measurements integrated over phase-space and so one can refer to the similar analysis on 2011/2012 data [182], which gives

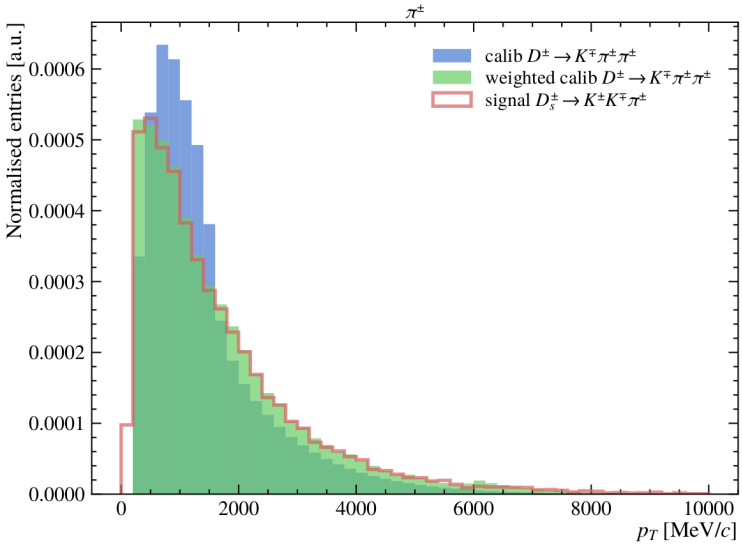

FIGURE 4.14: Example weighting of calibration $D^\pm \to K^\mp\pi^\pm\pi^\pm$ to match signal $D_s^\pm \to K^\pm K^\mp\pi^\pm$, as used by the `KPiTwoTrackAsymmetry` tool to determine $K-\pi$ tracking asymmetries

Year	Magnet	Asymmetry (%)
2015	Up	-1.2 ± 0.9
	Down	0.0 ± 1.1
	Combined	-0.77 ± 0.70
2016	Up	-0.2 ± 0.9
	Down	0.1 ± 0.9
	Combined	-0.05 ± 0.64
2017	Up	0.6 ± 0.9
	Down	-0.7 ± 0.8
	Combined	-0.04 ± 0.60
2018	Up	0.4 ± 0.9
	Down	1.2 ± 0.9
	Combined	0.82 ± 0.64
Run 2	Up	0.2 ± 0.5
	Down	0.3 ± 0.5
	Combined	0.24 ± 0.35

TABLE 4.11: Tracking asymmetries for oppositely-charged $K\pi$ pairs.

results in bins of p, to perform the "reweighting". The approach to determine the Run 2 tracking asymmetry for each final state pion in $\bar{B}_s^0 \to (D_s^+ \to \pi^+\pi^-\pi^+)\pi^-$ is then as follows:

1. Use the distribution of charge-summed yields in $p(\pi^\pm)$ from simulated $\bar{B}_s \to (D_s^+ \to \pi^+\pi^-\pi^+)\pi^-$ to perform a weighted average of the binned asymmetries from 2012 data.

2. Determine the difference between this new integrated asymmetry and the one given in Ref. [182] for 2012, i.e. an estimate of the shift in integrated asymmetry between the semi-leptonic channel and $\bar{B}_s \to (D_s^+ \to \pi^+\pi^-\pi^+)\pi^-$.

Year	Magnet	Asymmetry (%)
2016	Up	-0.33 ± 0.11
	Down	0.29 ± 0.11
	Combined	-0.01 ± 0.08
2017	Up	-0.33 ± 0.11
	Down	0.29 ± 0.11
	Combined	-0.01 ± 0.08
2018	Up	-0.33 ± 0.11
	Down	0.29 ± 0.11
	Combined	-0.04 ± 0.08
Run 2	Up	-0.33 ± 0.06
	Down	0.29 ± 0.06
	Combined	-0.02 ± 0.04

TABLE 4.12: Summary of detection asymmetries associated with tracking of single pions. The uncertainties are statistical while the systematic components are negligible.

3. Use this shift value to correct the integrated Run 2 asymmetry for each year given in Ref. [181].

Steps 1-3 are performed for each of the four final state pions and the total value of $A^{\text{track}}(\pi)$ calculated as the sum over these individual asymmetries, accounting for differences in sign. Table 4.12 shows the asymmetries resulting from this method for each individual polarity and for a polarity-average, for years 2016-2018. Though no corresponding information is available for 2015, from inspection of the results for the other years one can estimate an indicative asymmetry of 0.00 ± 0.08 for this year.

4.6.3 *Charge asymmetry of kinematic cuts*

Selections made on particle kinematics, in this instance the mass constraints on B_s and D_s candidates and veto on $B^0 \to D^*(2010)^+(D^0\pi^+)\pi^-$ background, may also introduce a small asymmetry between the conjugate final states. This effect is studied from the cut efficiencies for simulated truth-matched candidates, and the calculated asymmetries are given in Table 4.13. These are significantly smaller than the statistical sensitivity of their respective final state, coming out below $\sim \mathcal{O}(10^{-4})$. The charge asymmetry of the kinematic cuts thus has a negligible impact on the total detection asymmetry.

4.6.4 Charge asymmetry of PID cuts

In addition to the cuts on kinematics, there are also PID selections that may contribute to the detection asymmetry. The `PIDCalib2` tool [176] was thus used to evaluate these efficiencies for positively- and negatively-charged final state particles. It is important here to note that different PID selections are applied in different regions of phase-space, so this approach must take these regions into account. As introduced in Section 4.3, stricter PID requirements are applied to events lying outside of the "resonant" region,

Year	Decay	Asymmetry ($\times 10^{-4}$)
2015	$K^+K^-\pi^+$	1.8 ± 1.2
	$\pi^+\pi^-\pi^+$	-2.5 ± 2.9
2016	$K^+K^-\pi^+$	-0.18 ± 0.19
	$\pi^+\pi^-\pi^+$	-0.16 ± 0.08
2017	$K^+K^-\pi^+$	0.19 ± 0.21
	$\pi^+\pi^-\pi^+$	-0.48 ± 0.78
2018	$K^+K^-\pi^+$	0.07 ± 0.19
	$\pi^+\pi^-\pi^+$	-0.73 ± 0.81
Run 2	$K^+K^-\pi^+$	0.03 ± 0.11
	$\pi^+\pi^-\pi^+$	-0.98 ± 0.45

TABLE 4.13: Kinematic selection asymmetries averaged over magnet polarity.

so one can speak of "strong-" and "weak-" PID regions. This necessitates a separate evaluation of the charge asymmetry of the PID selections in each phase-space region. The steps involved in determining the PID asymmetries are as follows:

1. Use `PIDCalib2` to generate reference tables for both charges of π and K.
2. Apply appropriate reference tables to unweighted MC samples, divided into phase-space regions and D_s charge, to determine the PID efficiency for individual particles.
3. Multiply efficiencies for each final state particle to find the total PID efficiency for both charge conjugates:

$$\varepsilon(D_s^{\pm}\pi^{\mp}) = \varepsilon(K^{\pm}) \times \varepsilon(K^{\mp}) \times \varepsilon(\pi^{\pm}) \times \varepsilon(\pi^{\mp}_{\text{bach.}})$$

4. Calculate the asymmetry using Eq. (4.27)

This asymmetry is determined separately for both resonant and non-resonant regions in both $D_s \to K^+K^-\pi^+$ and $D_s^+ \to \pi^+\pi^-\pi^+$. Tables 4.14 and 4.15 summarise the results of this procedure with a more detailed breakdown given in Section A.2. The uncertainty is dominated by systematics, which principally comes from the choice of binning used in `PIDCalib2`. The nominal binning is the default one used by the tool, chosen to optimise uncertainties. The systematic uncertainty associated with this choice of binning is estimated by observing the shift in asymmetries when each of the nominal bins was split into two.

4.6.5 *Contribution from L0 trigger efficiencies*

Finally, the L0 trigger may have differing responses for the two charge conjugate final states. For the hadronic mode considered here, the relevant aspect is `L0Hadron` trigger, which selects predominantly on HCAL information. To calculate the corresponding L0 efficiencies, we make use of the `L0HadronTables` tool [183]. In a similar way to

Year	PID cut asymmetry / % $D_s^+(\pi_1^+\pi_2^-\pi_3^+)\pi^-$		
	Strong	**Weak**	**Average**
2015	-0.13 ± 0.22	-0.41 ± 0.04	-0.29 ± 0.07
2016	0.00 ± 0.02	0.02 ± 0.01	0.01 ± 0.02
2017	0.03 ± 0.01	-0.05 ± 0.01	-0.01 ± 0.01
2018	0.00 ± 0.02	0.12 ± 0.02	0.07 ± 0.00
Run 2	0.00 ± 0.02	0.01 ± 0.01	0.01 ± 0.01

TABLE 4.14: Charge asymmetries in PID cut efficiency for $D_s^+ \to \pi^+\pi^-\pi^+$, with uncertainties coming from varying the binning scheme. The asymmetries were determined separately for the "weak" and "strong" PID regions corresponding to events inside and outside of the resonant region. The uncertainties are dominated by systematics and are estimated from the shift observed when varying the binning scheme.

Year	PID cut asymmetry / % $D_s^+(K^+K^-\pi_1^+)\pi^-$				
	Strong In	**Strong Out**	**Weak In**	**Weak Out**	**Average**
2015	0.27 ± 0.18	0.11 ± 0.00	0.86 ± 0.46	-0.37 ± 0.02	0.10 ± 0.01
2016	0.01 ± 0.02	-0.03 ± 0.01	-0.26 ± 0.13	-0.07 ± 0.02	-0.03 ± 0.01
2017	-0.06 ± 0.03	0.01 ± 0.01	-0.16 ± 0.24	-0.09 ± 0.01	0.00 ± 0.01
2018	0.02 ± 0.04	0.02 ± 0.01	0.04 ± 0.04	-0.05 ± 0.06	0.02 ± 0.00
Run 2	0.01 ± 0.02	0.01 ± 0.01	-0.06 ± 0.09	-0.08 ± 0.02	0.00 ± 0.00

TABLE 4.15: Charge asymmetries in PID cut efficiency for $D_s^+ \to K^+K^-\pi^+$, with uncertainties coming from varying the binning scheme. The asymmetries were determined separately for four regions: with "weak-" and "strong-" PID selections, corresponding to inside and outside of the $\phi(1020) \to K^+K^-$ resonance, and "in" and "out" of the Λ_c^+ mass region. The uncertainties are dominated by systematics and are estimated from the shift observed when varying the binning scheme.

`PIDCalib2`, this tool uses reference efficiency tables for a range of hadron types evaluated in both the inner and outer regions of the calorimeter to compute total per-event efficiencies. This tool is applied to charge-split signal MC, and the results are summarised in Table 4.16. Such reference tables do not exist for 2015 and we have to assume a similar behaviour to the rest of Run 2.

4.6.6 Summary

The different contributions to the total detection asymmetry explained in this section are summarised in Table 4.17.

4.7 Conclusions

To conclude, in search of experimental phenomena that are inconsistent with Standard Model predictions, promising signs have been noted in the branching ratios of the decays of neutral B mesons to an open charm meson and a light meson. Two of the most

Year	Decay	Asymmetry ($\times 10^{-3}$)
2016	$K^+K^-\pi^+$	-0.03 $\pm$ 0.46
	$\pi+\pi^-\pi^+$	0.4 $\pm$ 1.7
2017	$K^+K^-\pi^+$	-0.72 $\pm$ 0.51
	$\pi+\pi^-\pi^+$	1.6 $\pm$ 1.7
2018	$K^+K^-\pi^+$	-0.72 $\pm$ 0.45
	$\pi+\pi^-\pi^+$	-2.0 $\pm$ 1.8
Run 2	$K^+K^-\pi^+$	-0.48 $\pm$ 0.27
	$\pi+\pi^-\pi^+$	0.1 $\pm$ 1.0

TABLE 4.16: L0 trigger asymmetries by year averaged over magnet polarity.

significant tensions with the expectations of QCD Factorisation (QCDF) come from the $\bar{B}^0 \to D^+K^-$ and $\bar{B}^0_s \to D^+_s\pi^-$ channels, both of which are dominated by tree-diagrams and are thus expected to be well-described by theory. Indeed, these are related to the "golden" modes used in the direct extraction of the CKM phase γ, which is a "benchmark" of the SM, to which other measurements are compared. CP asymmetries are observables with particular sensitivity to the possible presence of New Physics, and the suggestion that such effects may be at play motivates an examination of CPV in the modes showing tension. The SM predicts that CPV in these two modes can only come from meson-mixing, and thus BSM effects could be clearly exhibited if an additional direct contribution was found.

The latter mode, i.e. $\bar{B}^0_s \to D^+_s\pi^-$ has the added experimental advantage that the rapid oscillation of B_s mesons greatly dilutes the effect of asymmetry in their production, which would contaminate a measured CP asymmetry. This is the channel under study here, and the data that is used comprises the full $6\,\text{pb}^{-1}$ sample collected during Run 2 at LHCb. Indeed, the production asymmetry is found to be negligible here, and numerous sources of charge asymmetry in detector response are estimated, with a combined uncertainty of $\mathcal{O}(10^{-3})$. The raw asymmetry, i.e. the normalised imbalance of the $\bar{B}^0_s \to D^+_s\pi^-$ yield compared to its conjugate, can be extracted from invariant-mass fits to samples split by D_s charge. At the time of writing, the central value of the raw asymmetry remains blinded, though the fits have been validated through a number of approaches, from which the statistical sensitivity is expected to be $\mathcal{O}(10^{-3})$. The current estimate of the systematic contribution to a^s_{fs} is very small, however additional sources are under investigation. These additional sources include the choice of PID selections introduced in Section 4.3 and accounting for the the non-factorisability of the individual particle PID efficiencies in Section 4.6.4. This means that large BSM effects at the upper end of their expected size may be visible with the current data. The analysis is currently in working group review and we look forward to unblinding, which will indicate whether or not this is the case. It is, though, possible that the size of New Physics is more moderate, which would require the greater statistics of Run 3 to uncover. In fact, measuring A^s_{fs} was one of the selected physics goals stated in the Letter of Intent for the Upgrade I detector [184].

The next chapter will explore my work on validating LHCb in Run 3, where the advantages of the new detector for Beauty to Open Charm measurements will be shown. It will be seen that a combined sample from Runs 2 and 3 would mean an increase in the number of signal events by a factor of ~ 5.7, leading to statistical and systematic uncertainties a factor 2-3 smaller. A theoretical investigation of the puzzle introduced in this chapter will be analysed in Chapter 7, after the methodology is motivated with $B \to DD'$ modes in Chapter 6.

Year	**Decay**	$A_{\text{track+kin.}}(\%)$	$A_{\text{PID}}(\%)$	$A_{\text{L0}}(\%)$	**Total** $(\%)$
2015	$D^+_s(K^+K^-\pi^+)\pi^-$	-0.75 $\pm$ 0.70 $\pm$ XX	0.10 $\pm$ 0.00 $\pm$ 0.01	0.00 $\pm$ 0.05 $\pm$ XX	-0.65 $\pm$ 0.70 $\pm$ XX
	$D^+_s(\pi^+\pi^-\pi^+)\pi^-$	-0.03 $\pm$ 0.09 $\pm$ XX	-0.29 $\pm$ 0.00 $\pm$ 0.07	0.00 $\pm$ 0.18 $\pm$ XX	-0.32 $\pm$ 0.20 $\pm$ XX
2016	$D^+_s(K^+K^-\pi^+)\pi^-$	-0.05 $\pm$ 0.64 $\pm$ XX	-0.03 $\pm$ 0.00 $\pm$ 0.01	0.00 $\pm$ 0.05 $\pm$ XX	-0.08 $\pm$ 0.64 $\pm$ XX
	$D^+_s(\pi^+\pi^-\pi^+)\pi^-$	-0.01 $\pm$ 0.08 $\pm$ XX	0.01 $\pm$ 0.00 $\pm$ 0.02	0.04 $\pm$ 0.17 $\pm$ XX	0.04 $\pm$ 0.19 $\pm$ XX
2017	$D^+_s(K^+K^-\pi^+)\pi^-$	-0.04 $\pm$ 0.60 $\pm$ XX	0.00 $\pm$ 0.00 $\pm$ 0.01	-0.07 $\pm$ 0.05 $\pm$ XX	-0.11 $\pm$ 0.60 $\pm$ XX
	$D^+_s(\pi^+\pi^-\pi^+)\pi^-$	-0.01 $\pm$ 0.08 $\pm$ XX	-0.01 $\pm$ 0.00 $\pm$ 0.01	0.16 $\pm$ 0.17 $\pm$ XX	0.14 $\pm$ 0.19 $\pm$ XX
2018	$D^+_s(K^+K^-\pi^+)\pi^-$	0.82 $\pm$ 0.64 $\pm$ XX	0.02 $\pm$ 0.00 $\pm$ 0.00	-0.07 $\pm$ 0.05 $\pm$ XX	0.77 $\pm$ 0.64 $\pm$ XX
	$D^+_s(\pi^+\pi^-\pi^+)\pi^-$	-0.05 $\pm$ 0.08 $\pm$ XX	0.07 $\pm$ 0.00 $\pm$ 0.00	-0.20 $\pm$ 0.18 $\pm$ XX	-0.18 $\pm$ 0.20 $\pm$ XX
Run 2	$D^+_s(K^+K^-\pi^+)\pi^-$	0.24 $\pm$ 0.35 $\pm$ XX	0.00 $\pm$ 0.00 $\pm$ 0.00	-0.05 $\pm$ 0.03 $\pm$ XX	0.19 $\pm$ 0.35 $\pm$ XX
	$D^+_s(\pi^+\pi^-\pi^+)\pi^-$	-0.03 $\pm$ 0.04 $\pm$ XX	0.01 $\pm$ 0.00 $\pm$ 0.01	0.01 $\pm$ -0.10 $\pm$ XX	-0.03 $\pm$ 0.11 $\pm$ XX

TABLE 4.17: A summary of the contributions to the total detection asymmetry. The small kinematic contributions are included with the more substantial tracking asymmetries. The first uncertainty is statistical, and the second is systematic. "XX" indicates uncertainties to be determined.

5 Run 3 Early Measurements at LHCb

"The key to success is failure."

- Michael Jordan

5.1 Introduction

When first using an upgraded detector that differs significantly from the previous one, such as the one that LHCb enters Run 3 with, it is essential to ensure that its behaviour is as expected, or at least is understood. In the early months of data-taking, the individual aspects of the hardware and software of the new apparatus were studied and fine-tuned with this pursuit in mind. However, it is also sensible to take a more holistic approach and test the full reconstruction and analysis chain as a whole. Such "Early Measurements" should satisfy a few key criteria:

- They should be of quantities that are already known with a relatively high degree of precision.
- They should be possible with a small amount of data. These checks should be performed quickly if they are to be of any use to the collaboration.
- If there is some aspect of the measurements that is in some way "novel" then this provides more motivation, since they have a use beyond that of simply a cross-check.

I performed preliminary work for such early measurements of the production cross-sections, $\sigma(pp \to H_b X)$, of a few beauty hadrons, $H_b = \{B^+, B^0, B_s^0, \Lambda_b^0\ (udb)\}$. The conjugates of each of these particles are also implicit in H_b for the remainder of this chapter. As will be seen, cross-section measurements don't require a lot of data and do not rely as heavily on factors such as impact parameter resolution, which can take time to be properly calibrated. To take advantage of the greatly improved hadronic performance in Run 3 without the hardware trigger, the production of these particles is reconstructed through

Mode	Branching Ratio (%)	Product ($\times 10^{-4}$)
$\mathcal{B}(B^+ \to \bar{D}^0\pi^+)$	0.468 ± 0.013	1.85 ± 0.05
$\mathcal{B}(\bar{D}^0 \to K^+\pi^-)$	3.95 ± 0.03	
$\mathcal{B}(B^0 \to D^-\pi^+)$	0.252 ± 0.013	2.36 ± 0.13
$\mathcal{B}(D^- \to K^+\pi^-\pi^-)$	9.38 ± 0.16	
$\mathcal{B}(B_s^0 \to D_s^-\pi^+)$	0.300 ± 0.023	1.62 ± 0.13
$\mathcal{B}(D_s^- \to K^+K^-\pi^-)$	5.39 ± 0.15	
$\mathcal{B}(\bar{\Lambda}_b^0 \to \bar{\Lambda}_c^-\pi^+)$	0.490 ± 0.040	3.08 ± 0.30
$\mathcal{B}(\bar{\Lambda}_c^- \to \bar{p}K^+\pi^-)$	6.28 ± 0.32	

TABLE 5.1: A summary of the decay modes of interest for cross-section measurements, with branching ratios and products of relevant pairs of branching ratios shown. Data taken from Ref. [14].

their decays to hadrons, more specifically to a pion and an open-charm hadron (as is the theme of this thesis), which subsequently decays via a dominant hadronic channel (see Table 5.1). Measurements of these quantities have been made previously only using semi-leptonic final states [185], so our determination will be novel in that regard, and the increase in efficiencies means that one can be competitive with these measurements using a small amount of data (see Section. 5.2.1). In addition to the cross-sections, our early measurements will include an experimental determination of f_s/f_d, using $B_s^0 \to D_s^-\pi^+$ and $B^0 \to D^-K^+$ decays.

Numerous factors have negatively affected the quantity and quality of data being collected by the time of writing, and this data has been insufficient to produce competitive measurements. However, a preliminary analysis of 2023 and early 2024 data has been performed, and these measurements are expected to be completed by the end of 2024. In this chapter, I detail this preliminary work, including the estimation of required data-size for competitive measurements (Section 5.2), estimation of detection efficiencies (Sections 5.3.1 and 5.3.3), development of trigger selections (Section 5.3.2), and finally fits to invariant mass distributions using 2023 and 2024 data (Section 5.6), from which cross-sections can then be extracted when sufficient data is available. This work was also summarised as part of an internal note on the activities of the Early Measurements Taskforce [2].

5.2 Estimating Data Requirements

5.2.1 Cross-Section Luminosity

Part of the motivation for selecting these measurements is that they require only a small amount of data to be competitive, so it makes sense to first check that this is indeed the case. The cross-sections relate integrated luminosity, $\mathcal{L}$, to the number of H_b's produced in pp collisions. Practically, these hadrons are reconstructed through their decay and the interaction of its products with the detector, and so this total number will be diluted, relative to the number of reconstructed signal events, N_{sig}, by the appropriate branching

Efficiency	Value (%)	Uncertainty (%)
ϵ_{acc}	89.0	0.09
$\epsilon_{\text{reco+sel}}$	40.9	0.49
ϵ_{PID}	82.2	0.08
ϵ_{track}	98.1	2.55
$\epsilon_{\text{trigger}}$	51.5	1.34
ϵ_{GEC}	99.3	0.10

TABLE 5.2: Summary of the values of the different efficiencies quoted for the previous $\sigma(pp \to B^{\pm}X)$ measurement [185].

fractions, $\mathcal{B}$, and detection efficiency, ϵ_{det}:

$$\sigma(pp \to H_b X) = \frac{N_{\text{sig}}}{\mathcal{L} \times \mathcal{B}_{\text{B}} \times \mathcal{B}_{\text{C}} \times \epsilon_{\text{det}}}, \tag{5.1}$$

where $\mathcal{B}_{\text{B}}, \mathcal{B}_{\text{C}}$ refer to the branching ratios of the appropriate beauty and charm decays, respectively. The total detection efficiency itself has many contributions:

$$\epsilon_{\text{det}} = \epsilon_{\text{acc}} \times R_{\text{PID}} \times R_{\text{track+reco}} \times \epsilon_{\text{HLT1}} \times \epsilon_{\text{HLT2}} \times \epsilon_{\text{sel}} \times \epsilon_{\text{GEC}}, \tag{5.2}$$

where ϵ_{acc} is the fraction of signal with all final-state particles within the fiducial region of the detector acceptance, $R_{\text{PID/track+reco}}$ is the ratio of PID/tracking efficiency of data compared to MC, $\epsilon_{\text{HLT1/2}}$ is the efficiency of the trigger stages HLT1/2, ϵ_{sel} is the efficiency of the offline selection, and ϵ_{GEC} is the GEC efficiency (see Section 3.4.5).

The pre-existing LHCb measurement of $\sigma(pp \to B^{\pm}X)$, which used the "golden" decay mode $B^{\pm} \to (J/\psi \to \mu^+\mu^-)K^{\pm}$ found a value of $86.6 \pm 0.5(\text{stat}) \pm 5.4(\text{syst}) \pm 3.4(\text{BR})\,\mu\text{b}$ [185], where the uncertainties are given separately for statistical, systematic, and branching ratio contributions. This leptonic analysis used a fiducial region of $2.0 < \eta < 4.5$ and $p_T < 40\,\text{GeV}$, and we consider this same region. The acceptance in η is defined by that of the RICH since we require hadronic PID from this subdetector. The efficiencies quoted in this analysis provide a starting point for estimating the efficiencies and their uncertainties, summarised in Table 5.2. In this prior semi-leptonic measurement, the largest source of uncertainty was the luminosity systematic, at 3.9% [185].

One would expect the values from the previous $B^{\pm} \to J/\psi K^{\pm}$ analysis to be roughly indicative for this Early Measurements analysis except for the trigger and reconstruction/selection efficiencies, which are specific to each decay mode. These efficiencies are estimated considering recent B2OC analyses that explicitly provide such inputs: $B^0 \to D^-\pi^+$ in Refs. [186–188], $B_s^0 \to D_s^-\pi^+$ in Ref. [188], and $\bar{\Lambda}_b^0 \to \bar{\Lambda}_c^-\pi^+$ in Ref. [186]. Table 5.3 summarises the final efficiencies that were used for the luminosity estimation for *all* modes, after consideration of all the pre-existing literature. The trigger efficiency is grouped with the reconstruction/selection efficiency since the three are difficult to disentangle. As seen in Section 3.3, for indicative p_T values for hadronic b decays, the L0 efficiency was a little below 50% [165], and so with this removed, and also taking into account slightly tighter HLT selections, we estimate that this combined efficiency should

Variable	Value (%)	Uncertainty (%)
ϵ_{acc}	80.0	0.08
$\epsilon_{reco+sel+trigger}$	10.0	0.29
ϵ_{PID}	80.0	0.08
ϵ_{track}	98.0	2.55
ϵ_{GEC}	99.0	0.10

TABLE 5.3: Summary of the central values and their uncertainties that were assumed for the efficiencies to be used in the rough estimation. These values were chosen to be roughly in line with efficiencies used in previous analyses that used the same decay modes. The exception to this is the combined reconstruction, selection, and trigger efficiency, which is expected to increase from Run 2 to Run 3, so this value is twice the value suggested in the previous literature.

approximately double.

In addition to the explicit measurement of $\sigma(pp \to B^{\pm}X)$ from Ref. [185], the cross-sections for the remaining modes can also be inferred from the *b quark* production cross-section $\sigma(pp \to b\bar{b}X) = 144 \pm 1 \pm 21\,\mu b$ [189] (note the presence of two b-type quarks) and the production fractions for a b quark to hadronise into a B^0, B_s^0, and Λ_b^0 (f_d, f_s, and $f_{\Lambda_b^0}$, respectively). The production fraction for B^0, i.e. f_d, equal to 0.34 ± 0.021 [190] is assumed to be the same as for B^+ (f_u). This is based on isospin-symmetry, i.e. that the masses of the u and d quarks are sufficiently similar compared to the scale of the hadronic interaction that they are essentially indistinguishable. Though Ref. [185] would imply a different central value, this assumption of $f_d/f_u = 1$ holds within 1σ. This assumption of isospin-symmetry will, however, be challenged in Chapter 6. The production fractions for B_s^0 and Λ_b, normalised to $f_d + f_u \approx 2f_d$, are given in Ref. [191] as 0.122 ± 0.006 and 0.259 ± 0.018, respectively. Combining this information, one obtains:

- $\sigma(pp \to B^0X) = 97.92 \pm 0.68 \pm 15.5\,\mu b$,
- $\sigma(pp \to B_s^0X) = 23.9 \pm 0.61 \pm 3.78\,\mu b$,
- $\sigma(pp \to \Lambda_bX) = 50.7 \pm 1.73 \pm 8.31\,\mu b$.

The central value of N_{sig} can be estimated as a function of $\mathcal{L}$ using Eq. (5.1), the inputs for the branching ratios and efficiencies previously discussed, and assuming the same extrapolated cross-sections presented above. The statistical uncertainty on this is estimated as $\sigma_N = \sqrt{N} \times 1.5$, where scaling of 1.5 was to account for the fact that, in reality, the error on the number of events comes from a fit to data. This additional factor is roughly in line with the discrepancy between the uncertainties shown in the previous B^+ analysis [185] and those that would be obtained by naïvely taking the square root of the number of events.

With these estimated inputs and Eq. (5.1), one can estimate the production cross-section for each hadron as a function of luminosity. By construction, the central values of the cross-sections will be the same as what was calculated earlier, so it is really the

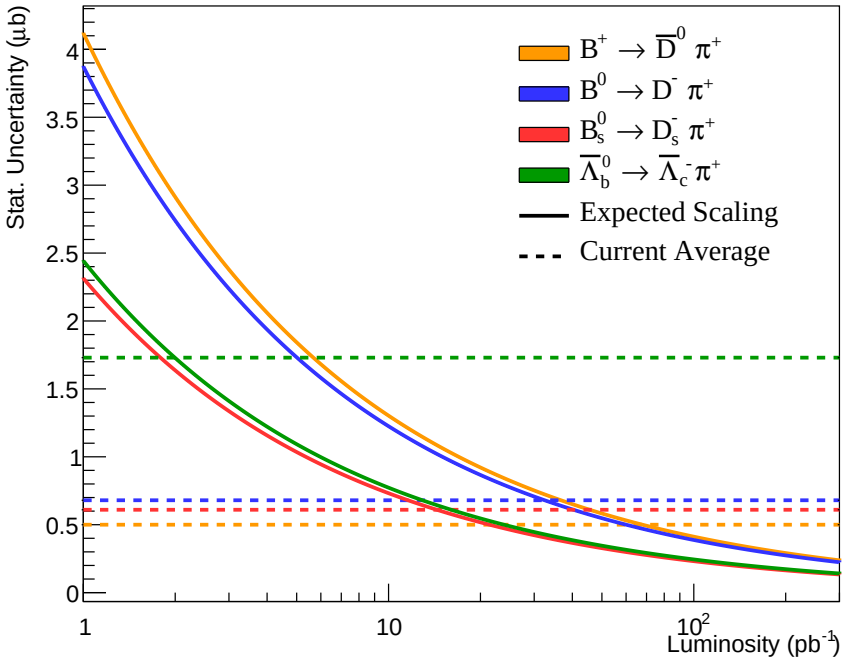

FIGURE 5.1: Predicted statistical uncertainty scaling of Run 3 B meson production cross-section measurements with luminosity (solid lines) compared to those of existing measurements (dashed lines), using a range of decay modes.

Particle	**Stat. Error** (μb)	$\mathcal{L}_{\text{min.}}$ (pb^{-1})	$N_{\text{fid}}(\times 10^6)$	$N_{4\pi}(\times 10^6)$
B^+	0.5	69	1.58 ± 0.08	9.88 ± 0.50
B^0	0.7	32	2.31 ± 0.09	14.4 ± 0.6
B_s^0	0.6	14	0.39 ± 0.02	2.41 ± 0.10
$\bar{\Lambda}_b^0$	1.7	2	1.56 ± 0.06	9.75 ± 0.38

TABLE 5.4: Summary of the estimated luminosities required to produce competitive cross-section measurements. Also, statistical errors on the corresponding cross-sections and the expected yields within the detector acceptance and in the full 4π region.

uncertainties on these values that are of interest. As stated before, the luminosity is expected to be the largest source of uncertainty. One can then perform scans of uncertainty as a function of luminosity, as shown in Figure 5.1, and aim to obtain a similar statistical uncertainty to previous papers, as these were all systematics limited. The resulting luminosity estimates are shown in Table 5.4 alongside estimates for the signal yields both in the fiducial region, N_{fid}, and in the full 4π region (assuming a 16% acceptance efficiency). This latter number is relevant when considering simulated events. From these results, it is clear that, to achieve a competitive statistical uncertainty in all modes, a luminosity of approximately $100\,\text{pb}^{-1}$ is required. The yield estimates also inform the size of MC production samples necessary for the evaluation of the various efficiencies involved in this measurement.

Decay	$N_{\text{fid}}(\times 10^5)$	$N_{4\pi}(\times 10^6)$
$B^0 \to D^- K^+$	1.63 ± 0.07	1.02 ± 0.04
$B_s^0 \to D_s^- \pi^+$	6.24 ± 0.25	3.90 ± 0.16

TABLE 5.5: Expected yields within the detector acceptance and in the full 4π region required for competitive measurement of f_s/f_d, i.e. with a luminosity of $161\,\text{pb}^{-1}$.

5.2.2 Relative B_s^0/B^0 production fraction (f_s/f_d)

The relative production fraction of B_s^0 and B^0 mesons, f_s/f_d, is a key input for many analyses, including those discussed in Chapter 6. It is also crucial for the $B_s^0 \to \mu^+\mu^-$ branching fraction measurement [192], where the current systematic uncertainties are dominated by the uncertainty on this quantity. In principle, this can be determined from the ratio of the production cross-sections for B^0 and B_s^0 using the channels described above, but many detection efficiencies (and their associated uncertainties) can be cancelled by ensuring that the final state particles are the same. Indeed, the current global average used comparisons of $B_s^0 \to D_s^- \pi^+$ to $B^0 \to D^- K^+$, as well as measurements using semi-leptonic final states, using the expression [193]:

$$\frac{f_s}{f_d} = \Phi_{PS} \left|\frac{V_{us}}{V_{ud}}\right| \left(\frac{f_K}{f_\pi}\right)^2 \left(\frac{\tau_{B^0}}{\tau_{B_s^0}}\right)^2 \frac{1}{\mathcal{N}_a \mathcal{N}_F} \frac{\mathcal{B}(D^- \to K^+\pi^-\pi^-)}{\mathcal{B}(D_s^- \to K^+K^-\pi^-)} \frac{\epsilon_{DK}}{\epsilon_{D_s\pi}} \frac{N_{D_s\pi}}{N_{DK}}, \tag{5.3}$$

which uses the same quantities as Eq. (5.1), namely branching ratios, $\mathcal{B}$, signal yields, N, and total efficiencies, ϵ. It should be noted, though, that these are the very same modes that currently display significant tensions with SM predictions, as was introduced in the previous chapter and will be further explored in Chapter 7. The factors $\mathcal{N}_a$, $\mathcal{N}_F$, Φ_{PS}, and f_K/f_π are ratios of, respectively, non-factorisable corrections, $B_{(s)}^0 \to D_{(s)}^-$ form factors, phase space factors, and decay constants, as seen in Section 2.5. External inputs can be used for these latter set of factors, as in Ref. [194], though they all approximately evaluate to unity. $B_s^0 \to D_s^- \pi^+$ is already a mode of interest for cross-section studies, and $B^0 \to D^- K^+$ is very closely related to another, i.e. $B^0 \to D^- \pi^+$, via K/π misidentification. It therefore makes sense to try to measure this quantity as well, as an extension of the analysis proposed in the previous subsection.

The most recent contribution to the world average used $1\,\text{fb}^{-1}$ of hadronic data at $\sqrt{s} = 7\,\text{TeV}$ to give $f_s/f_d = 0.238 \pm 0.004(\text{stat}) \pm 0.015(\text{syst}) \pm 0.021(\text{theo})$ [193], where the uncertainties are due to statistical, systematic, and theoretical effects, respectively. The theoretical uncertainty comes predominantly from the uncertainties on $\mathcal{N}_a$ and $\mathcal{N}_F$. Assuming the efficiencies calculated above and proceeding similar to before, one would need $161\,\text{pb}^{-1}$ of early data to compete with this result. Using such a luminosity, the estimated number of required events of $B^0 \to D^- K^+$ and $B_s^0 \to D_s^- \pi^+$ in the fiducial region are shown in Table 5.5.

Mode	$\epsilon_{\text{acc}}(\%)$
$B_s^0 \to D_s^-(\to K^+K^-\pi^-)\pi^+$	36.3 ± 0.1
$B^0 \to D^-(\to K^+\pi^-\pi^-)\pi^+$	34.7 ± 0.1
$B^0 \to D^-(\to K^+\pi^-\pi^-)K^+$	35.4 ± 0.1
$B^+ \to \bar{D}^0(\to K^+\pi^-)\pi^+$	36.0 ± 0.1
$\bar{\Lambda}_b^0 \to \bar{\Lambda}_c^-(\to \bar{p}^-K^+\pi^-)\pi^+$	36.6 ± 0.1

TABLE 5.6: A summary of the total acceptance efficiencies for each mode of interest. Binned efficiencies are shown in the appendix.

5.3 Efficiencies

In this section, two contributions to the total detection efficiency are determined for each of the modes, using simulated Run 3 data with 100,000 events per polarity. The numerical values are summarised in Tables 5.6 and 5.7, and are described in the following subsections. The remaining contributions to the detection efficiency will be determined from experimental data at such a time that sufficient statistics are collected.

5.3.1 Acceptance Efficiencies

In order to estimate the acceptance efficiencies, i.e. the fraction of events that lie within the acceptance of the LHCb detector, one can perform a simple simulation of the decay modes of interest using the Gauss package introduced in Section 3.3.7. By default, when simulating events, the so-called *Daughters in LHCb* requirement is applied, which requires all daughter particles to be forward-travelling and within an angular range of $0.01\ (0.05) < \theta < 0.4$ rad for charged (neutral) particles. For the purposes of estimating the acceptance efficiency, this requirement is removed to generate the events, and then these additional requirements added later to remove events. The total acceptance efficiency is then

$$\epsilon_{\text{acc}} = \frac{\#\text{ events after cut}}{\#\text{ events before cut}}. \tag{5.4}$$

This is run using 500,000 simulated events, and these total acceptance efficiencies are shown in Table 5.6. These efficiencies were also determined for a nominal binning in p_T and η, which are shown in Appendix B.

5.3.2 Trigger Lines

HLT1 makes use of a few minimal selections, largely using information from the tracking-type subdetectors, in order to reduce the data rate by a factor of ~ 30 [195]. Events with a single track, or double track from a common vertex, with significant displacement and large p_T are retained. This stage has separate requirements for muon events and selects those with a single high-p_T muon or a di-muon vertex, more moderate in p_T, that is either displaced or with a mass in excess of the J/ψ. These selections account for around 95% of the output of HLT1. HLT2 then makes use of a full reconstruction of each incoming event in order to select those belonging to a particular decay. As an example, consider how the selection process works for the $B^0 \to D^-K^+$ HLT2 line that I wrote. The *bachelor*

K^+, i.e. coming directly from the B^0, is selected as a long track with a RICH response and the following criteria:

- PIDK > 0
- 500 MeV < p_T < 5 GeV.

The D^- is reconstructed from 3 long tracks with a RICH response and satisfying the following:

- Tracks have $p > 2$ GeV and $p_T > 250$ MeV.
- Pions and kaons satisfy PIDK < 5 and PIDK > -5, respectively.
- Any pair of tracks must have a maximum distance of closest approach of 0.2 mm, a combined mass between 1830 and 1910 MeV, and a total p_T greater than 1800 MeV.
- The D^- vertex quality must be good, with a χ^2 per degree of freedom less than 10.
- Must not be consistent with coming from the PV- it must increase the χ^2 of the PV fit, and its flight distance must be significant (with a χ^2 with respect to the PV > 36).
- The D^- must be forward-travelling with respect to the displacement vector from primary to secondary vertex.

The D^- and the K^+ are then combined to form a B^0 with the following requirements:

- Combined mass between 4950 MeV and 6000 MeV and a total $p_T > 5$ GeV.
- Candidate lifetime must exceed 0.2 ps, and must have good vertex quality (χ^2 per degrees of freedom less than 20).
- Must be consistent with originating at the PV (IP χ^2 with respect to the PV < 25) and have a momentum parallel to the vector from primary to secondary vertex.
- Loose MVA cut at a value of 0.1.

5.3.3 Trigger Efficiencies

Some care is needed when thinking about what is meant by the terms ϵ_{HLT1} and ϵ_{HLT2} shown in Eq. (5.2). The most intuitive definition would consider the order in which the two trigger stages occur and define ϵ_{HLT1} as the number of events that pass at least one HLT1 line divided by the total number of events entering the HLT system, i.e. "raw" events. Correspondingly, ϵ_{HLT2} would be the number of events that passed at least one HLT2 line divided by the total number of events that passed HLT1 i.e. the efficiency of HLT2 *given HLT1*. This would be more appropriately notated as $\epsilon_{\text{HLT2}||\text{HLT1}}$. The product of these two efficiencies is the total efficiency of the trigger system. Bayes' theorem, however, shows that this total trigger efficiency could be equivalently factorised as $\epsilon_{\text{HLT1}||\text{HLT2}} \times \epsilon_{\text{HLT2}}$, where here $\epsilon_{\text{HLT1}||\text{HLT2}}$ is the efficiency of HLT1 *given HLT2* and ϵ_{HLT2}

Mode	$\epsilon_{\text{HLT1\|HLT2}}(\%)$	$\epsilon_{\text{HLT2}}(\%)$
$B_s^0 \to D_s^-(\to K^+K^-\pi^-)\pi^+$	63.08 ± 0.50	11.2 ± 0.1
$B^0 \to D^-(\to K^+\pi^-\pi^-)\pi^+$	60.95 ± 0.51	10.8 ± 0.1
$B^0 \to D^-(\to K^+\pi^-\pi^-)K^+$	61.54 ± 0.50	10.6 ± 0.1
$B^+ \to \bar{D}^0(\to K^+\pi^-)\pi^+$	61.27 ± 0.58	7.77 ± 0.07
$\bar{\Lambda}_b^0 \to \bar{\Lambda}_c^-(\to \bar{p}^-K^+\pi^-)\pi^+$	58.71 ± 0.58	9.80 ± 0.09

TABLE 5.7: Summary of the trigger efficiencies for each of the modes of interest. Binned efficiencies are shown in the appendix.

is the efficiency of HLT2 on "raw" data. This first efficiency seems peculiar at first glance, however one may think of it as the percentage of the events that are passed by HLT2 that would also have been passed by HLT1. It turns out that this second method of factorisation is the more straightforward approach since events are not fully reconstructed before HLT2 , so there is no "signal" to determine the efficiency at HLT1.

We make use of the MC samples in which the reconstruction is not applied. "Raw" data samples may be produced by directly writing the generator level quantities to ntuple, i.e. no trigger is applied. "Signal" data samples can be produced by running the simulated data through HLT1 in passthrough mode (no cuts are made, but decisions are noted) followed by HLT2. The binned HLT1 efficiencies can then be determined, taking as the denominator the number of events in the "signal" sample for each bin, and the numerator the number of events in that same bin of the "signal" sample that also passed at least one HLT1 line. The binned HLT2 efficiencies can be similarly determined, with the number of events in the "signal" sample in each bin in the numerator and the corresponding number of events for that bin from the "raw" sample in the denominator. Tables showing these binned efficiencies are given in Appendix B, however Table 5.7 shows the total HLT1 and HLT2 efficiencies for each mode of interest.

5.4 Continuous Integration Pipeline

To simultaneously automate the main analysis steps and allow for regular automatic checks that background software updates do not generate errors when running these steps, I set up a Continuous Integration (CI) pipeline using Snakemake [196], a workflow management tool designed to create reproducible and scalable data analyses. This culminates in performing mass fits, as is explored in the next section. The stages involved here are calculating the bin edges from the number of bins required, creating a new configuration for each bin with appropriate constraints put on p_T and η, and running the fitting routine for each of the individual bins (see Figure 5.2).

Raw data or simulation comes in the form of `XDIGI` files, from which tracks and vertices are reconstructed in HLT1, the output of which is in `dst` format. This is followed by full reconstruction in HLT2, which also outputs a `dst` file. HLT processing is performed as data is collected by the experiment, but the pipeline allows this process to be re-run. Data selected by the trigger passes through DaVinci, which produces a `root` file suitable

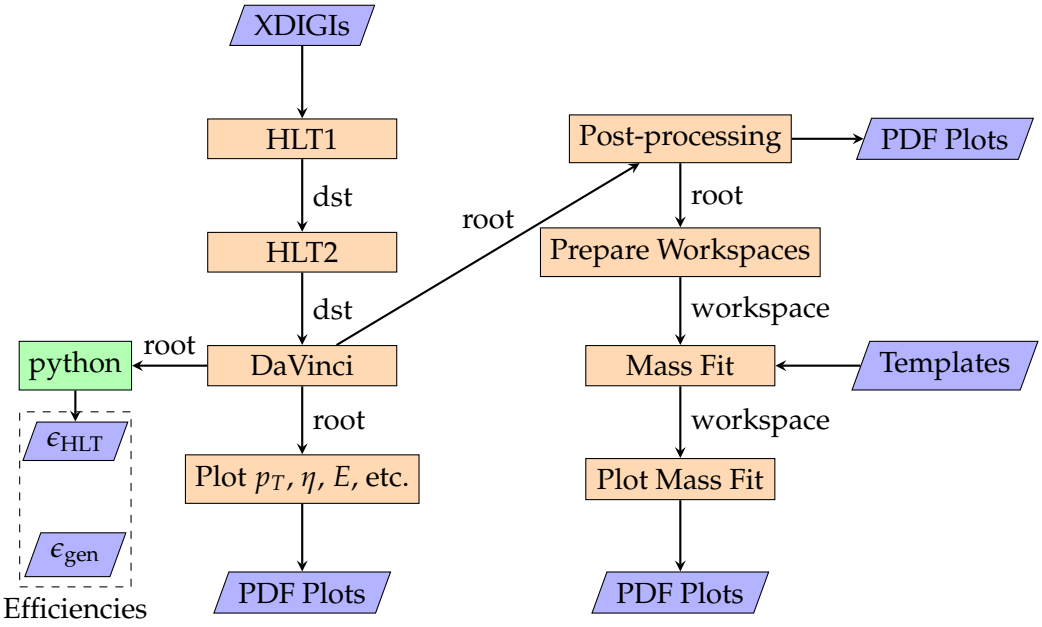

FIGURE 5.2: The stages of the continuous integration pipeline. See main text for details.

for analysis, and trigger efficiencies can be determined using this. PDF plots of data distributions can also be made using this information. The process to produce mass fit plots then happens in three stages. The first step prepares a workspace, declaring the variables contained in the DaVinci output that will be used in the fit, according to a configuration provided by the user. Following this, the fit itself is performed, with the resulting fit parameters being passed through a workspace file to the plotting stage, which visualises the fit. The mass fit requires external input of templates for each of the fit components.

5.5 Mass Fitting and Selection

In order to extract signal yields, fits to invariant mass distributions must be performed. Fit models are defined using MC samples prior to running on 2023 data, with each consisting of signal and background components, described in the following sections. This discussion is applicable to all modes. Table 5.8 summarises the components that are present in the fits for each mode of interest.

5.5.1 Signal

The signal components for all modes are modelled using a sum of two components.

Component	Mode			
	$B^0 \to D^-\pi^+$	$B_s^0 \to D_s^-\pi^+$	$B^+ \to \bar{D}^0\pi^+$	$\bar{\Lambda}_b^0 \to \bar{\Lambda}_c^-\pi^+$
$B^0 \to D^-\pi^+$	✓ (Signal)	✓	✗	✓
$B_s^0 \to D_s^-\pi^+$	✓	✓ (Signal)	✗	✓
$B^+ \to \bar{D}^0\pi^+$	✗	✗	✓ (Signal)	✗
$\bar{\Lambda}_b^0 \to \bar{\Lambda}_c^-\pi^+$	✓	✓	✗	✓ (Signal)
$\pi_{\text{bach}} \to K$	✓	✓	✓	✓
$\pi_{\text{bach}} \to \rho$	✓	✓	✗	✓
Excited Charm	✓	✓	✓ †	✓
$B^0 \to D^{*-}\pi^+$	✓	✗	✓	✗
$B^0 \to D_s^{(*)-}\pi^+$	✗	✓	✗	✗
$B_s^0 \to D^{*-}\rho^+$	✗	✓	✗	✗
$B^+ \to D^{(*)-}\pi^+\pi^+$	✗	✗	✓	✗
Combinatorial	✓	✓	✓	✓

TABLE 5.8: Summary of the components present in the fits for each of the modes of interest. † There are separate components for D^{*0} decaying with the emission of a γ or a π^0.

- **Double-Sided Hypatia Function** [197] - this is related to the general hyperbolic function

$$G(m,\mu,\sigma,\lambda,\zeta,\beta) \propto [(m-\mu)^2 + A_\lambda^2(\zeta)\sigma^2]^{\frac{1}{2}\lambda-\frac{1}{4}}\, e^{\beta(m-\mu)}\, K_{\lambda-\frac{1}{2}}\left(\zeta\sqrt{1+\left(\frac{m\mu}{A_\lambda(\zeta)\sigma}\right)^2}\right), \tag{5.5}$$

where K_λ are the cylindrical harmonics or special Bessel functions of third kind, and $A_\lambda^2(\zeta) = \frac{\zeta K_\lambda(\zeta)}{K_{\lambda+1}(\zeta)}$. The double-sided Hypatia function is defined as follows

$$I(m,\mu,\sigma,\lambda,\zeta,\beta,a,n) \propto \begin{cases} G(m,\mu,\sigma,\lambda,\zeta,\beta) & \text{if } \frac{m-\mu}{\sigma} > -a \\ \mathcal{N}\cdot G(\mu - a\sigma,\mu,\sigma,\lambda,\zeta,\beta) & \text{otherwise,} \end{cases}, \tag{5.6}$$

where $\mathcal{N} = \mathcal{N}(m,\mu,\sigma,\lambda,\zeta,\beta)$ relates G to its derivative with respect to m, G';

$$\frac{G(\mu - a\sigma,\mu,\sigma,\lambda,\zeta,\beta)}{G'(\mu - a\sigma,\mu,\sigma,\lambda,\zeta,\beta)} = \frac{1}{n}\left(\frac{m}{1-\mathcal{N}^{1/n}} + a\sigma\right). \tag{5.7}$$

This modifies the *Crystal Ball* (CB) function that is also commonly used to parameterise signal distributions. The CB consists of a Gaussian core, which models the detector resolution, and a tail on the left-hand side, which accounts for energy losses due to radiative emissions from particles like photons or pions. The variation of mass resolution may vary from event to event, distorting the CB core and causing it to be non-Gaussian. The exact distribution, named the Double-Side Hypatia function, is determined empirically from previous analyses and has a hyperbolic core.

- **Johnson SU Function** [198]- the applicability of this distribution in the signal model is an empirical fact, shown in Ref. [199], for example. The distribution is given by

$$J(m,\mu,\sigma,\nu,\tau) \propto \frac{1}{2\pi c(\nu,\tau)\sigma} \frac{\exp\left(-r(m,\mu,\sigma,\nu,\tau)^2/2\right)}{\tau\sqrt{z(m,\mu,\sigma,\nu,\tau)^2+1}}, \tag{5.8}$$

where

$$c = \left[\frac{1}{2}(e^{\tau^2}-1)(e^{\tau^2}\cosh(2\nu\tau))\right]^{-1/2}, \quad z = \frac{m-(\mu+c-\sigma e^{\tau^2/2}\sinh(\nu\tau))}{c\sigma},$$
$$r = -\nu + \frac{\sinh^{-1} z}{r}.$$

5.5.2 Background

Partially-reconstructed backgrounds can result from decays with a vector particle, such as $B \to D^* h$ where the D^* subsequently decays to a D and an unreconstructed particle, typically either a π^0 (spin-0) or a photon (spin-1). These two cases are respectively parameterised by `HORNSdini` and `HILLdini` functions [200]. These functions come from different distributions in the helicity angle θ, i.e. the angle between the daughter particle momentum vector in the D^* rest frame and the D^* boost vector in the B rest frame. The B and h are pseudoscalars with zero spin, therefore zero helicity, so the D^* must also have zero helicity, as this is a conserved quantity. This means it must be longitudinally-polarised, i.e. its spin is perpendicular to its momentum. With such a polarisation, an emitted π^0 would follow a $\cos^2\theta$ distribution [201], being preferentially produced at $\theta = 0°$ or $\theta = 180°$. Missing particles produced at larger angles take a larger fraction of the total momentum, decreasing the reconstructed B mass, and so the double-peaked structure in θ also translates into the invariant-mass spectrum. The corresponding mass values for $\theta = 0°$ or $\theta = 180°$ that will designate the positions of the peaks, say a and b, will be determined by the masses of the particles involved in the decay. The resulting probability distribution for $m(D\pi^\pm)$ can then be approximately modelled by a parabola $p(m)$, defined between a and b

$$p_{\text{HORNS}}(m) = \left(m - \frac{a+b}{2}\right)^2, \; a < m < b. \tag{5.9}$$

A photon, being massless, can only have transverse polarisation when on-shell [28], and as such its spin must be parallel to its momentum. This spin, and so also momentum, will align preferentially parallel to the spin of the D^*. The momentum of the D^*, being perpendicular to its spin, is thus also perpendicular to the momentum of the photon, and so the angular distribution of the unreconstructed particle is maximal for $\theta = 90°, 270°$. For both of these angles, the fraction of momentum carried by the photon is the same, so a double-peaked structure is not seen. The resulting $m(D\pi^\pm)$ distribution is once more a parabola defined between the kinematic endpoints a and b, however this time with

negative curvature:

$$p_{\text{HILL}}(m) = -(m-a)(m-b),\ a < m < b. \tag{5.10}$$

To account for multiple resolution effects, the parabola is convolved with a sum of two Gaussian functions, G, with a common mean, μ, i.e.

$$DG(x|m,\sigma,f_G,R_\sigma) = f_G G(x|\mu,\sigma) + (1-f_G)G(x|\mu,R_\sigma\sigma), \tag{5.11}$$

where σ is the width of the first Gaussian, f_G is the fraction contained by the first Gaussian, and R_σ is the relative width of the two components. Furthermore, if there is a mass dependence in the selection, this can distort the shape of the `HORNSdini` such that the right-hand peak is higher than the left. This is taken into account by introducing a linear polynomial with a slope of $1-\xi$, where $0 < \xi < 1$. As $\xi \to 0$, the left-hand peak decreases in size relative to the right-hand peak. The resulting `HORNS/HILL` functions are obtained using $p(m)$ from Eqs. (5.9) and (5.10), through

$$\int_a^b dx\ p(x)\ DG(x|m,\sigma,f_G,R_\sigma)\ \left(\frac{1-\xi}{b-a}x + \frac{b\xi - a}{b-a}\right), \tag{5.12}$$

where ξ is generally different for the two distributions.

In the $B_s^0 \to D_s^-\pi^+$ fit, the $B_{(s)}^0 \to D_s^{*-}\pi^+$ components are parameterised by a sum of the two distributions, while for $B_{(s)}^0 \to D_s^-\rho^+$ and $B_{(s)}^0 \to D_s^{*-}\rho^+$ there is only a contribution from the `HORNSdini` distribution. In the $B^+ \to \bar{D}^0\pi^+$ fit, a similar line of reasoning applies, with $B^0 \to D^{*-}\pi^+$ modelled by a `HORNSdini`, while the $B^+ \to D^{*0}\pi^+$ component is split and modelled differently according to the missing particle from the decay of the D^{*0}; `HORNSdini` for a missing π^0 and `HILLdini` for a missing γ. $B^+ \to D^{(*)-}\pi^+\pi^+$ is modelled by a `DoubleHORNSdini`, i.e. a sum of two `HORNSdini` distributions. In all of these cases, the distribution is chosen to be no more complicated than is needed to fit the data well.

Some of the misidentified backgrounds are modelled in different ways; misidentification of a K as a π in $B^+ \to \bar{D}^0\pi^+$ is modelled by a `DoubleCrystalBall`, while misidentification of a B^0 as a B_s^0 in $B_s^0 \to D_s^-\pi^+$ is modelled by a shifted `Hypathia+JohnsonSU`. The combinatorial background is parameterised using an exponential function where the slope is allowed to vary freely in the fit to data. For the remaining background components not explicitly mentioned, numerical shapes from Refs. [77] and [202] were used.

5.5.3 Selection

PID selections are applied to the final state daughter particles; PIDK$>$ 5 for kaons, and PIDK$<$ 0 for pions. There is also a cut on the HLT2 B2OC Neural Net at 0.9 (0.75) for the B meson ($\bar{\Lambda}_b^0$) decays. The $\bar{\Lambda}_b^0$ has further requirements of $m(\Lambda_b^0) < 6000$ MeV/c^2, $\Delta\log L(K-p) < -5$, and $\Delta\log L(p-\pi) > 0$. These minimal selections were chosen as these would be robust against the lack of calibration needed for more performant ones,

Mode	HLT2 Line
$B^0 \to (D^- \to \pi^-\pi^-K^+)\pi^+$	`Hlt2B2OC_BdToDmPi_DmToPimPimKp`
$B_s^0 \to (D_s^- \to K^-K^+\pi^-)\pi^+$	`Hlt2B2OC_BdToDsmPi_DsmToKpKmPim`
$B^+ \to (\bar{D}^0 \to K^+\pi^-)\pi^+$	`Hlt2B2OC_BuToD0Pi_D0ToHH`
$\Lambda_b^0 \to (\Lambda_c^+ \to pK^-\pi^+)\pi^-$	`Hlt2B2OC_LbToLcpPi_LcpToPKPi`

TABLE 5.9: HLT2 lines for modes of interest.

and were used to estimate signal yields at an early stage. Note that these selections may be subject to change.

5.6 2023 Data

For data-taking in 2023, the VELO was in an open position, and with half the UT still to be installed, reconstruction also did not make use of this subdetector. "Commissioning" data was that in which the subdetectors were still in the process of being calibrated and aligned. There then followed a period of "collision" data, where the quality was deemed suitably high as to be appropriate for use in physics analyses. Data recorded by the experiment is stored according to the data-taking conditions and configuration.

5.6.1 Mass Fits

The invariant mass distributions obtained from the `Commissioning23` and `Collisions23` datasets for the four modes of interest are shown in Figures 5.3, 5.4, 5.5, and 5.6. Here, all yields are allowed to float freely.

In all cases, a clear signal peak is visible. The data are fitted using a signal component, several partially reconstructed background components, peaking at small invariant mass, and a small combinatorial background component, spanning all the mass range shown. The signal component is shown by the dashed line. For $B^+ \to \bar{D}^0\pi^+$, the partially reconstructed background components are described using numerical functions. For this mode, even if the modelling of the low invariant mass region is still rough, the fit reasonably describes the data in the full mass range. The performance is also similarly good for selections with the $B^0 \to D^-\pi^+$ sprucing line `SpruceB2OC_BdToDmPi_DmToPimPimKp`, which is very similar to the corresponding HLT2 line. The yields in the signal region for the selected `Commissioning23` sample are shown in Table 5.10.

5.6.2 Comparison with Run 2

The signal component is parameterised by a `Hypatia+JohnsonSU` function depending on several parameters that are fixed from simulation or kept free in the fit. Two of these parameters, σ_I and σ_J, are related to the width of the distribution. The "narrow width", σ_J, is floated and can be used as a signal width estimator. The σ_J values obtained from fits without or with D mass constraint to the `Commissioning23` and `Collision23` data

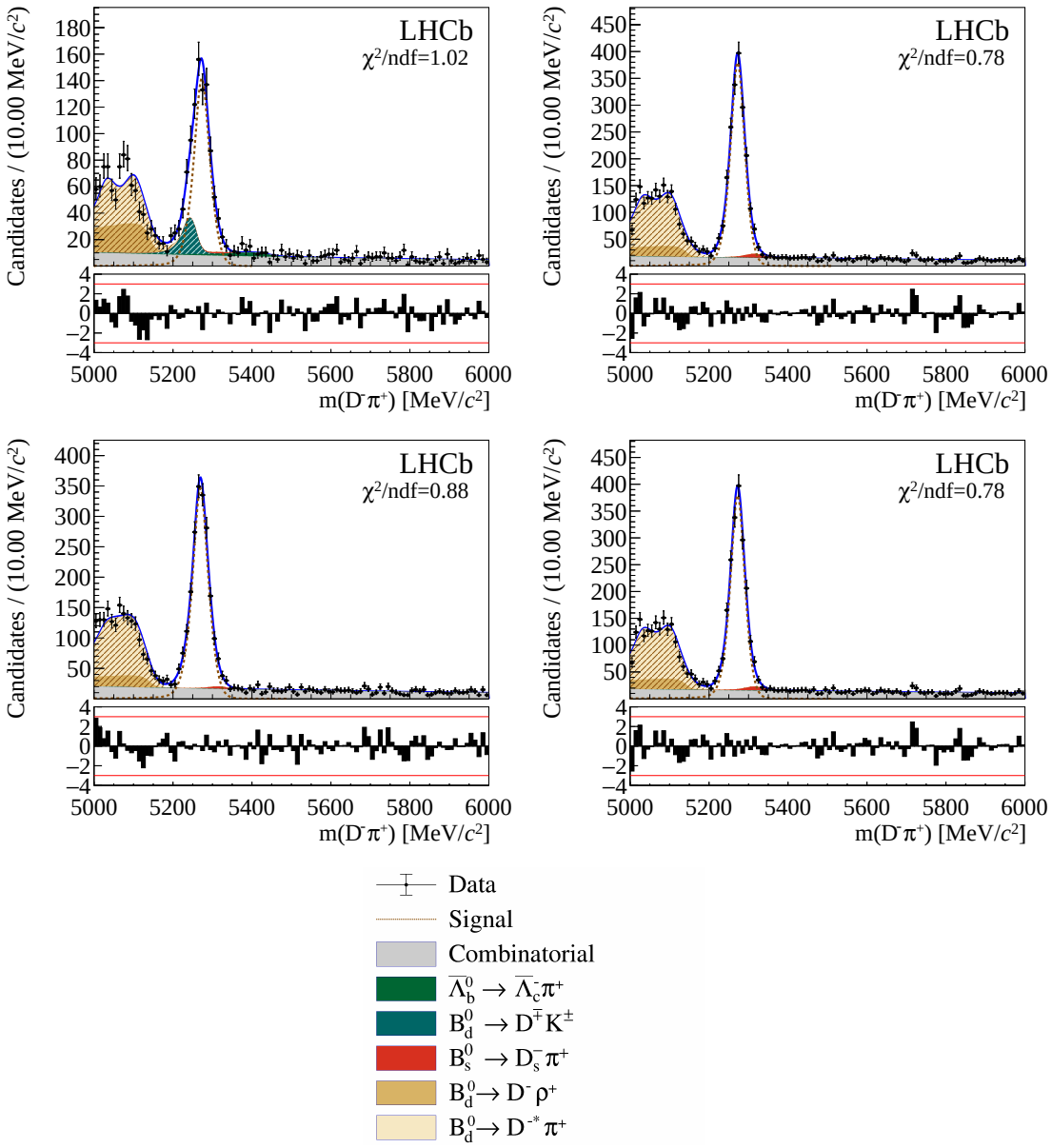

FIGURE 5.3: B^0 invariant mass distribution from the $B^0 \to D^-\pi^+$ decay. The D^- is reconstructed in the $D^- \to K^-\pi^+\pi^+$ mode. On the left (right) without (with) D^- mass constraint. The upper (lower) plots show the fits for commissioning (collision) data. A colour legend is provided below the mass plots.

samples are summarised in Table 5.11. In the larger statistic `Collision23` data sample, the width reduction due to the D mass constraint is very visible.

Decay-time efficiency check

The decay-time efficiency can also be checked in a binned manner for simplicity, though an unbinned determination would be possible. We examine the distribution in decay-time for events lying in the signal region (5229.63 MeV $< m(D^-\pi^+) <$ 5329.63 MeV). To

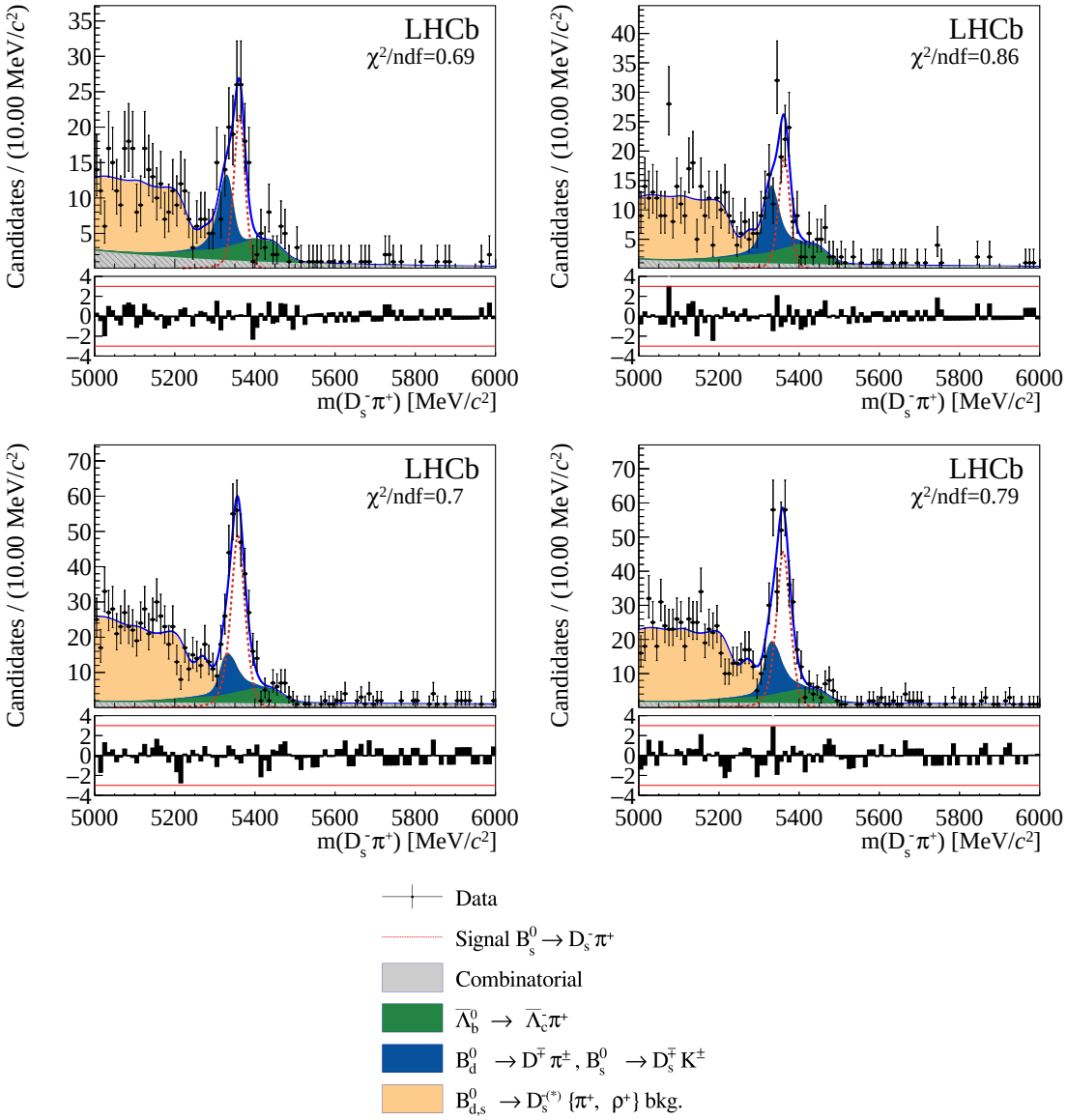

FIGURE 5.4: B_s^0 invariant mass distribution from the $B^0 \to D_s^- \pi^+$ decay. The D_s^- is reconstructed in the $D_s^- \to K^- K^+ \pi^-$ mode. On the left (right) without (with) D_s^- mass constraint. The upper (lower) plots show the fits for the commissioning (collision) data. A colour legend is provided below the mass plots.

find the efficiencies as a function of decay-time, these distributions can be compared with the expectation from a perfect detector, i.e. $\Delta_i \exp(-t_i/\tau)$, where t_i is the bin centre, τ the B^0 lifetime and Δ_i the bin width. In Figure 5.7, a comparison in these distributions is made between the 2023 collision data and Run 3 MC. The MC distribution is as expected; a monotonically increasing function with a sharp initial rise. The distribution for data is indeed monotonically increasing but lacks the sharp rise in the first three bins. The bin widths for these low decay-times is $\delta = 0.3\,\text{ps}$, which is equivalent to a distance $c \cdot \delta = 90\,\mu\text{m}$. A number of possible causes may explain this effect:

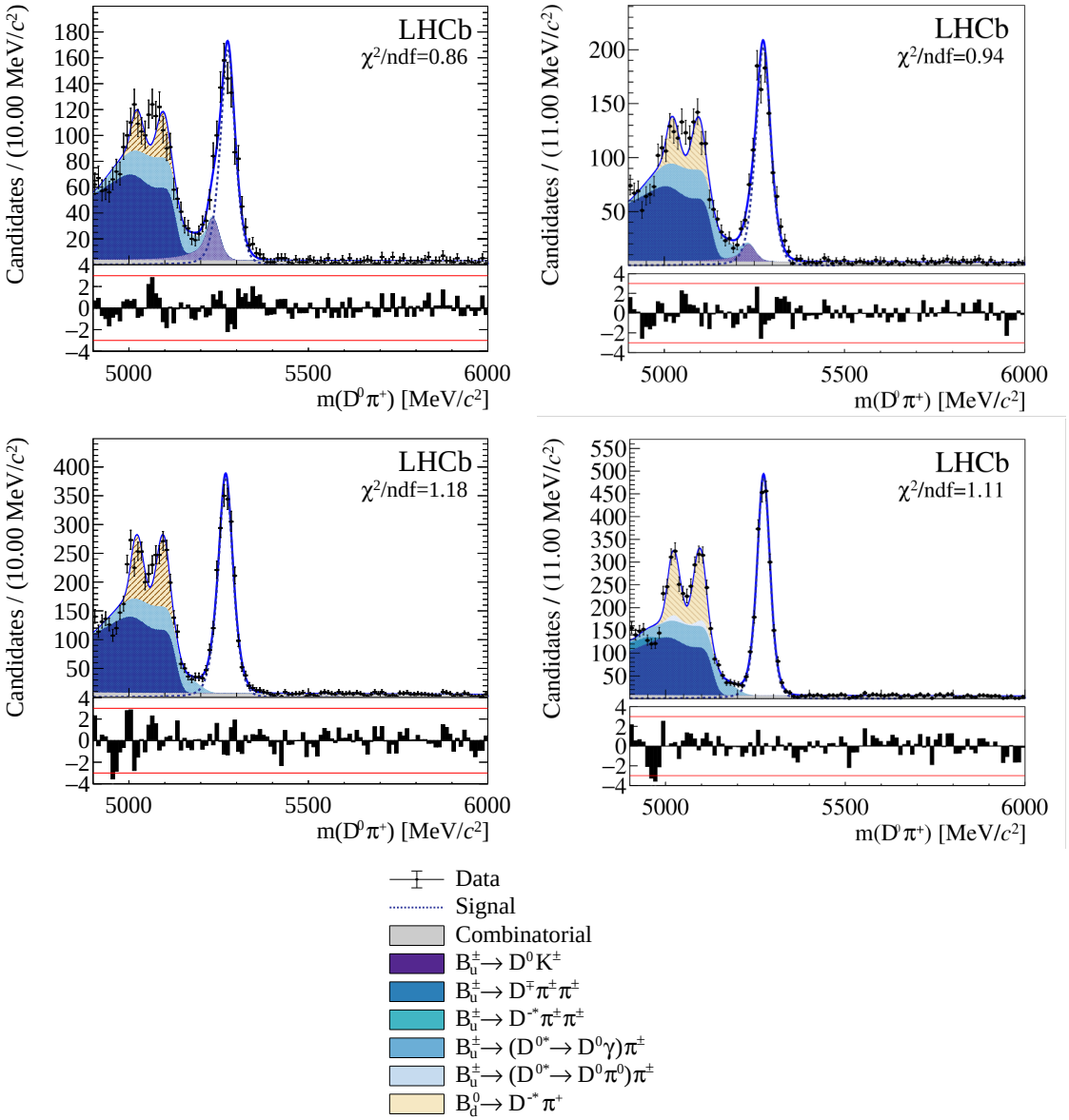

FIGURE 5.5: B^+ invariant mass distribution from the $B^+ \to \bar{D}^0\pi^+$ decay without (with) the charm mass constraint on the left (right). The $\bar{D}^0$ is reconstructed in the $\bar{D}^0 \to K^+\pi^-$ mode. The upper (lower) plots show the fits for commissioning (collision) data. A colour legend is also shown below.

- Since the number of events in the sample is relatively small, this may simply be a statistical fluctuation.
- There may be an influence from the small number of background events in the signal region.
- The Run 3 MC sample was produced with the VELO in the (nominal) closed position, while the 2023 data was taken when the subdetector was in the open position.
- The detector may have been misaligned by $\sim 90\,\mu$m.

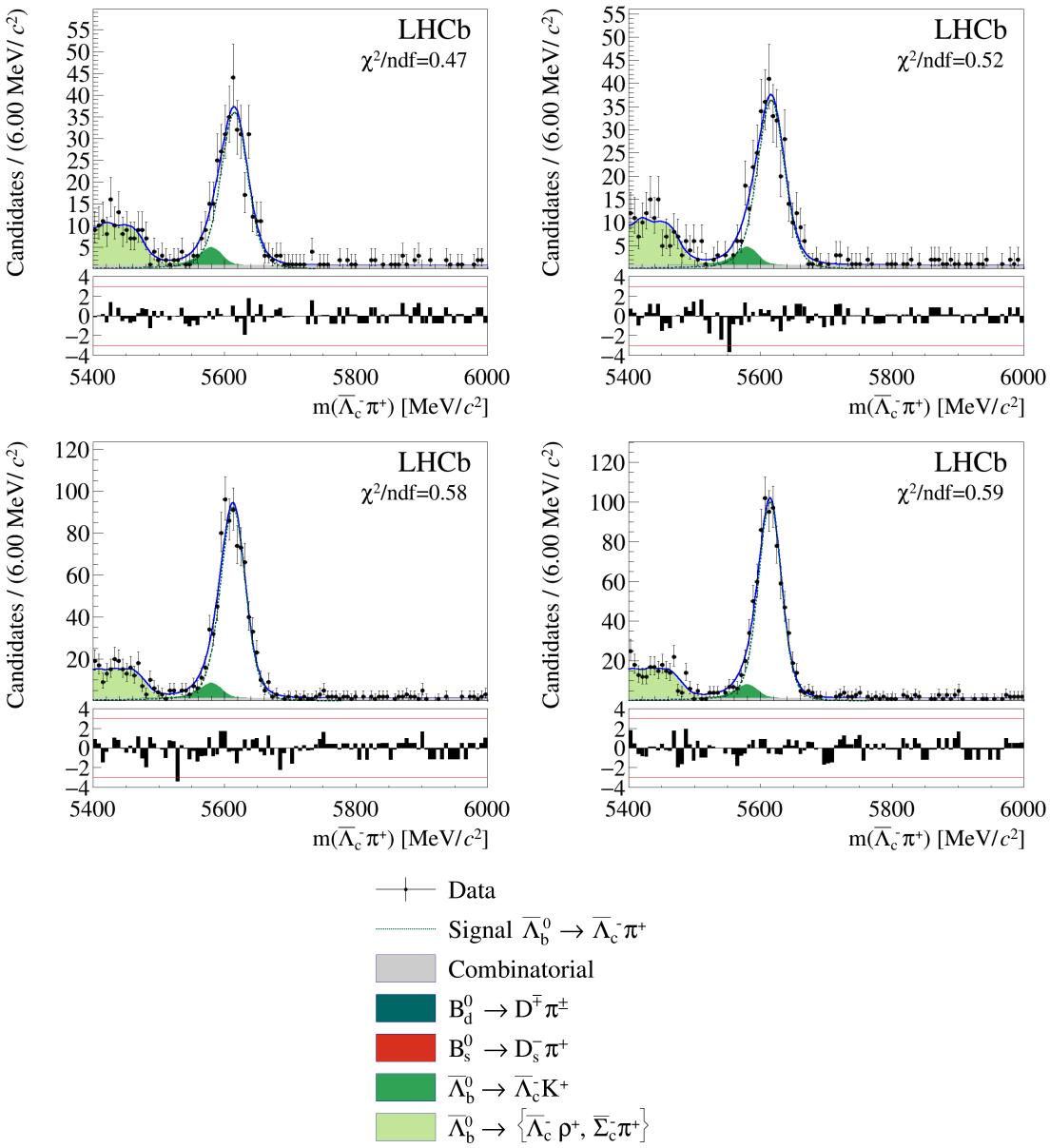

FIGURE 5.6: Λ_b^0 invariant mass distribution from the $\Lambda_b^0 \to \Lambda_c^+ \pi^-$ decay for the `Commissioning23` dataset. The Λ_c^+ is reconstructed in the $\Lambda_c^+ \to pK^-\pi^+$ mode. On the left (right) without (with) Λ_c^+ mass constraint. The upper (lower) plots show the fits for commissioning (collision) data. A legend is shown below.

This check will be repeated with early 2024 data, or if an improved alignment is later applied to the `Collision23` data.

Signal Quality

In total, with a D mass constraint applied, the signal yields for `Commissioning23` and `Collision23` were 793 and 1848, respectively, and with integrated luminosities of 34 pb^{-1} and 47 pb^{-1}, this means yields per unit luminosity of 23.3 and 39.3 pb, respectively. These

Decay	Component	no constraint	charm constraint
$B^0 \to D^- \pi^+$	Signal	1833	1883
	Background	174	171
$B_s^0 \to D_s^- \pi^+$	Signal	250	277
	Background	103	78
$B^+ \to \bar{D}^0 \pi^+$	Signal	1969	2060
	Background	68	63
$\bar{\Lambda}_b^0 \to \bar{\Lambda}_c^- \pi^+$	Signal	753	763
	Background	43	42

TABLE 5.10: Yields in signal region for `Collision23` data

Decay	Sample	no constraint	charm constraint	Run 2
$B^0 \to D^- \pi^+$	`Commissioning23`	25.2 ± 2.2	25.2 ± 2.4	15.73 ± 0.16 [77]
	`Collision23`	24.8 ± 1.6	21.5 ± 0.8	
$B_s^0 \to D_s^- \pi^+$	`Commissioning23`	20.4 ± 6.1	20.7 ± 5.4	15.12 ± 0.07 [77]
	`Collision23`	23.4 ± 3.0	24.1 ± 2.7	
$B^+ \to \bar{D}^0 \pi^+$	`Commissioning23`	26.4 ± 1.7	26.4 ± 0.2	14.66 ± 0.08 [203]
	`Collision23`	26.4 ± 1.2	22.0 ± 0.4	
$\bar{\Lambda}_b^0 \to \bar{\Lambda}_c^- \pi^+$	`Commissioning23`	21.3 ± 1.5	21.4 ± 1.4	15.16 ± 0.04 [204]
	`Collision23`	19.6 ± 0.8	18.2 ± 0.8	

TABLE 5.11: The σ_J values (in MeV) obtained from fits with and without the charm meson mass constraint.

Decay	Sample	no constraint	charm constraint	PDG
$B^0 \to D^- \pi^+$	`Commissioning23`	5273.1 ± 1.6	5274.2 ± 0.6	5279.7 ± 0.1
	`Collision23`	5269.3 ± 0.7	5272.3 ± 0.5	
$B_s^0 \to D_s^- \pi^+$	`Commissioning23`	5362.0 ± 5.8	5361.5 ± 5.9	5366.9 ± 0.1
	`Collision23`	5359.9 ± 3.5	5359.5 ± 2.8	
$B^+ \to \bar{D}^0 \pi^+$	`Commissioning23`	5274.5 ± 1.2	5274.5 ± 1.2	5279.3 ± 0.1
	`Collision23`	5269.4 ± 0.7	5272.5 ± 0.3	
$\bar{\Lambda}_b^0 \to \bar{\Lambda}_c^- \pi^+$	`Commissioning23`	5614.2 ± 1.5	5615.5 ± 1.5	5619.6 ± 0.2
	`Collision23`	5611.5 ± 0.8	5613.3 ± 0.8	

TABLE 5.12: The mean mass values (in MeV) obtained from fits with and without the charm meson mass constraint.

are to be compared with 343.3 pb for 2018 data [77]. The large difference between the `Commissioning23` and `Collision23` yields is not understood at the time this document is being written but the difference with respect to the 2018 yield is due to the open-VELO position in 2023. The D^+ and D^- invariant mass distributions are compared in Figure 5.8. A shift between the mean values, shown by the red and black dashed vertical lines, is observed. This shift is more pronounced in the `Commissioning23` data sample. Plots such as these helped to inform the Run 3 detector alignment.

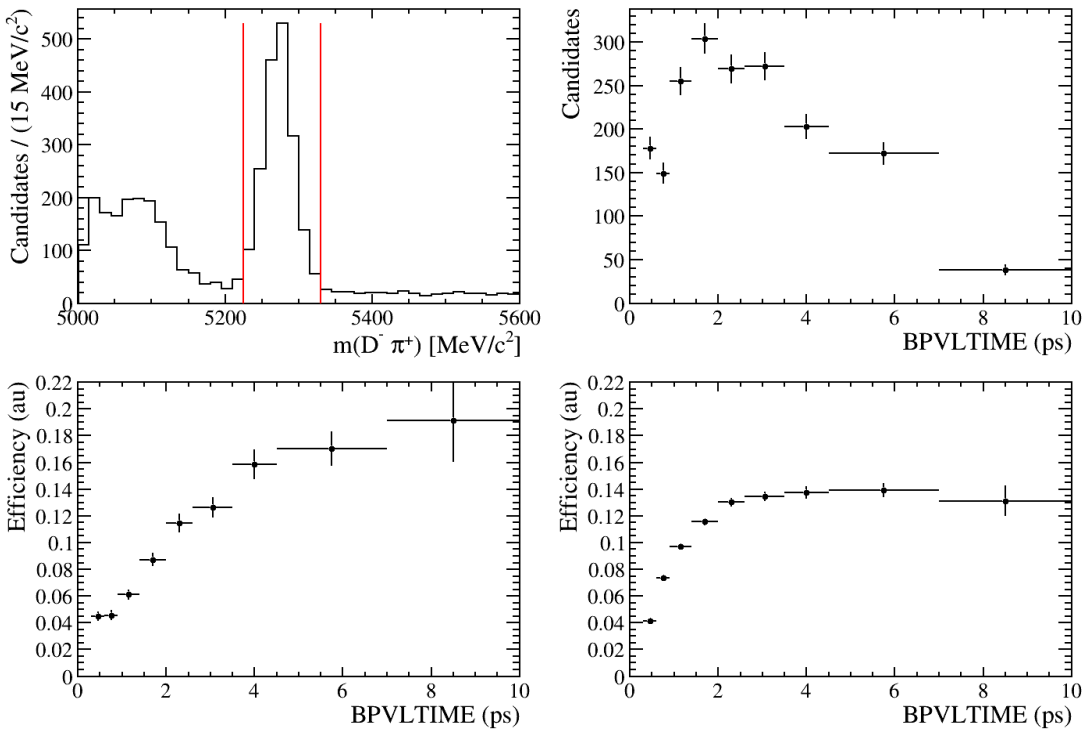

FIGURE 5.7: B^0 invariant mass distribution, top left plot, for the `Collision23` data sample used to check the decay-time efficiency. Only the events in the signal region, given by the red vertical lines, are retained. Number of candidates in each decay-time (BPVLTIME) bin, top right plot. Binned decay-time efficiency as obtained from the `Collision23` data, bottom left plot, and from a B^0 Upgrade MC sample, bottom right plot.

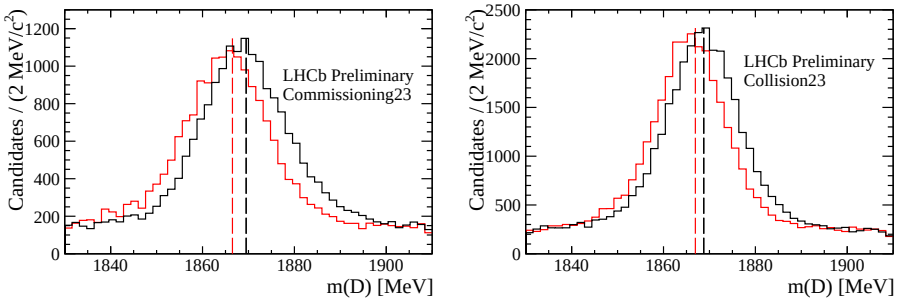

FIGURE 5.8: D^- invariant mass distribution from the $B^0 \to D^-\pi^+$ decay. The D^- is reconstructed in the $D^- \to K^-\pi^+\pi^+$ mode. On the left (right) the `Commissioning23` (`Collision23`) data, D^+ (D^-) in red (black). The mass shift is more pronounced in the `Commissioning23` data sample.

5.7 Conclusions

Numerous external factors contributed to an insufficient amount of data being collected by LHCb for use in completing these early measurements at the time of writing, though it has been possible to work on in-depth preparatory studies. These efforts have meant that we are in a strong position to complete this analysis with the further Run 3 data

that is expected to become available during the remainder of 2024. Our analysis of Run 3 performance with the small amount of data that was taken in 2023 played a part in informing the overall commissioning of the new detector and associated software. The signal yield per luminosity for $B^0 \to D^-\pi^+$ of 39.3 events/pb^{-1} found for `Collision23` events, fell well below the corresponding value from 2018. Signal widths were also significantly increased, and shifts in mean masses were observed, the latter being used to optimise alignment. The 2023 data was, though, taken using sub-optimal conditions, particularly an open VELO subdetector, and so the expected tracking efficiency of 95% per particle was significantly reduced to around 50%. For the four-particle final states considered here, the total reduction in tracking efficiency is compounded to a factor of $(0.95/0.5)^4 \sim 13$. With data-taking in 2024 and 2025, the tracking efficiencies are expected to return to their nominal values, and hence significant improvements in data quality associated with this are expected.

Indeed analysis of early 2024 data has shown this to be true. In a sample with an integrated luminosity of $20.3 \pm 0.1\,\text{pb}^{-1}$, 12287 ± 178 signal $B^0 \to D^-\pi^+$ events were identified after selections. This would suggest a signal yield per luminosity now around ~ 600 events/pb^{-1}, a significant improvement upon the Run 2 values, and even more so on the 2023 value. This is shown graphically in Figure 5.9. The improvement in efficiencies is driven mainly by that of the trigger, thanks to the removal of the L0 hardware stage, which is shown in Figure 5.10 to have improved by the approximate factor of two estimated earlier. This efficiency appears far less dependent on decay time, an encouraging prospect for future time-dependent analyses. The combined integrated luminosity expected for the remainder of Run 3 is $14\,\text{fb}^{-1}$, which, based on the earlier yield per luminosity estimate, would mean a yield of $\sim 8 \times 10^6$ in total, after selection. The modes considered in this chapter match several of those that will be considered in the phenomenological analysis in Chapter 7, though it is not expected that LHCb could challenge the inputs used there.

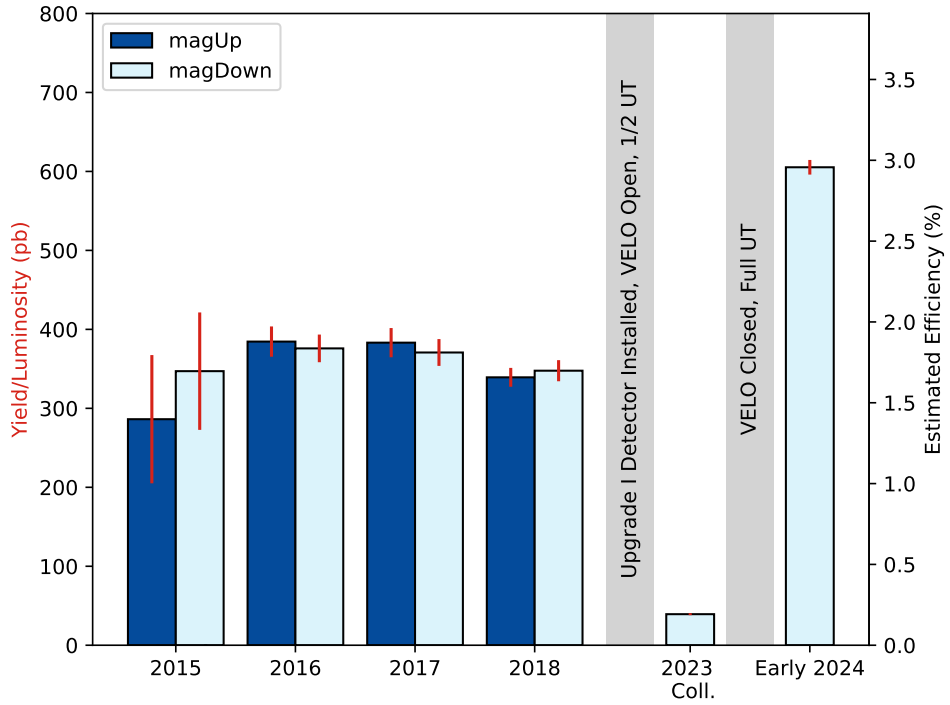

FIGURE 5.9: Number of events per luminosity for $B^0 \to D^-\pi^+$ for Run 2, compared to `Collision23` and early 2024 data.

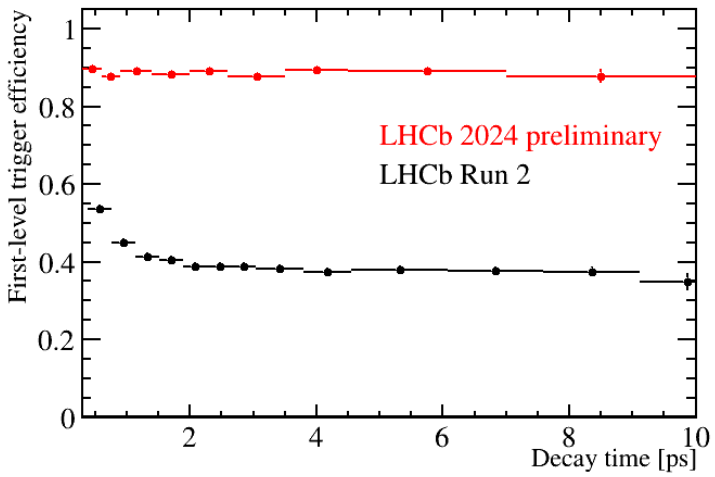

FIGURE 5.10: Trigger efficiency for $B^0 \to D^-\pi^+$ as a function of decay time for Run 2, and for the early 2024 data evaluated as part of the beauty hadron cross-section early measurements [205]. An approximate doubling in total efficiency can be seen, as well as much-reduced dependence on decay-time.

6 $B \to DD'$ Phenomenology

"You are braver than you believe, stronger than you seem, smarter than you think"

- A. A. Milne, *The House at Pooh Corner*

6.1 Introduction

To be sensitive to the effects of new physics, precise experimental measurements must be complemented by precise theoretical predictions. Measurements of hadronic beauty decays are key inputs for understanding CP violation, the SM flavour sector in general, and sensitivity to possible BSM physics. Their impact on the CKM triangle was introduced in Section 2.1.4. Indeed, we have already discussed related non-leptonic B decays that show hints of possible new physics [58,59,206–217] in Chapter 4. Making precise predictions in such a fully hadronic environment is, however, a significant challenge due to the non-perturbative nature of QCD. The presence of such heavy quarks can, though, present opportunities to simplify the calculations through appropriate assumptions based on the symmetries introduced in Section 2.4. The next chapter details how this approach can be applied to make predictions for the $B \to Dh, h \in \{K, \pi\}$ variety of modes that display tensions. However, the technique will be first introduced in the context of $B \to DD'$ decays, which are particularly rich in terms of both experimental measurements and phenomenology. This chapter closely follows the work I performed towards Ref. [3]. Unlike $B \to Dh$, $B \to DD'$ decays do not factorise in the heavy-quark limit, and so one cannot currently precisely calculate the relevant hadronic matrix elements from first principles.

Significant contributions from loop diagrams here provide precisely the environment where New Physics may live, and many of these modes are theoretically well-controlled thanks to similar structures to those present in the golden modes $B \to J/\psi K$ and $B_s \to J/\psi\phi$. Several modes are also dominated by $b \to c\bar{c}s$ transitions, which benefit from a clear hierarchy in the CKM matrix (as seen in Section 2.1.4), with the subleading hadronic

matrix elements coming from "penguins" that are suppressed, as will be explained in Section 6.2.5. Time-dependent CP asymmetries of these modes then make for excellent precision measurements of the $B^0_{(s)}$ mixing phases, which may include BSM contributions. One could search for New Physics through simple relations based on the CKM hierarchy, though such a method would be unable to disentangle subleading SM contributions to CP violation ("penguin pollution") from genuine BSM signals. This necessitates a more sophisticated treatment.

Ref. [3] was an update of the earlier analysis of Ref. [9] and there was good reason for performing this update. For a start, several measurements of $B \to DD'$ have been made since the original publication, including the first-time measurement of $A_{CP}(B^- \to D_s^- D^0)$, and more precise determinations of $A_{CP}(B^- \to D^- D^0)$, $A_{CP}(B^0 \to D^- D^+)$, $S_{CP}(B^0 \to D^- D^+)$. The new analysis was, however, much more than a simple update of inputs. It included a more comprehensive array of subleading contributions, a more sophisticated treatment of correlations between inputs, and allowances for isospin breaking in the production of charged and neutral B mesons, i.e. $f_d/f_u \neq 1$. A departure of this latter quantity from unity could have substantial consequences for branching fraction measurements at LHCb, such as $B^0_s \to \mu^+\mu^-$. A complementary phenomenological analysis was made in Ref. [218].

6.2 Theoretical parameterisation

As explained in Section 2.4.2, the SM exhibits an approximate SU(3) flavour symmetry, relating decays with u, d, and s quarks interchanged. Since these three light quarks have masses much smaller than that of the QCD scale, Λ_{QCD}, they can be approximated to have the same mass, and thus observables for decays related by this symmetry can be given a common parameterisation according to group theoretical arguments, namely through SU(3) matrix elements. In particular, such approximate relations allow $b \to c\bar{c}d$ observables, which are less favoured in the CKM hierarchy, to be inferred from $b \to c\bar{c}s$ ones, thus sensitivity can be greatly improved. This baseline assumption is known as the SU(3)$_F$ limit and acts as a way of obtaining first-order predictions, which we expect to be accurate to within around $\sim 30\%$. This estimated accuracy conservatively allows for additional symmetry breaking in excess of the 20% breaking effect seen from comparing pion and kaon decay constants [92] and also conveniently, though coincidentally, brings this in line with suppression by the number of colours, i.e. three. Ref. [219] showed that this first set of SU(3)$_F$-breaking terms are significant and impact the extraction of contributions from loop-level diagrams, particularly "penguin"-type diagrams. One could include corrections at higher orders to further improve accuracy, at the cost of greater complexity of the parameterisation. Through the common parameterisation, this method can become predictive through fits to experimental data that allow the unknown matrix elements, which cannot be calculated from first-principles, to be extracted.

6.2.1 SU(3) matrix elements

Observables for the $B \to DD'$ decays can be expressed in terms of SU(3) matrix elements, as in Section 2.4.3 and Ref. [26], with the u, d, and s quarks represented by the triplet states $\left|\mathbf{3}; \frac{1}{2}, \frac{1}{2}, \frac{1}{3}\right\rangle$, $\left|\mathbf{3}; \frac{1}{2}, -\frac{1}{2}, \frac{1}{3}\right\rangle$ and $\left|\mathbf{3}; 0, 0, -\frac{2}{3}\right\rangle$, the anti-quarks by the equivalent states in the anti-triplet representation, and the heavy flavours represented by singlets, $|\mathbf{0}\rangle$. Note that decays of $B_c^+(\bar{b}c)$ involve singlet matrix elements that are linearly independent of the other $B \to DD'$ decays, and so these will not be considered in this analysis.

The effective Hamiltonian responsible for the decays can be decomposed into two parts that are governed by different CKM matrix elements [219]

$$\mathcal{H}_{\text{eff}}^{b\to d,s} = \mathcal{H}_c^{b\to d,s} + \mathcal{H}_u^{b\to d,s}, \tag{6.1}$$

where one can express these parts in terms of SU(3) representations $\mathbf{k}$ with quantum numbers q, denoted by $(\mathbf{k})_q$

$$\mathcal{H}_c^{b\to d} \sim (3)_{\frac{1}{2},-\frac{1}{2},\frac{1}{3}}, \tag{6.2a}$$

$$\mathcal{H}_u^{b\to d} \sim \sqrt{\frac{3}{8}}(3)_{\frac{1}{2},-\frac{1}{2},\frac{1}{3}} - \frac{1}{2}(\bar{6})_{\frac{1}{2},-\frac{1}{2},\frac{1}{3}} + \sqrt{\frac{1}{24}}(15)_{\frac{1}{2},-\frac{1}{2},\frac{1}{3}} + \sqrt{\frac{1}{3}}(15)_{\frac{3}{2},-\frac{1}{2},\frac{1}{3}}, \tag{6.2b}$$

$$\mathcal{H}_c^{b\to s} \sim (3)_{0,0,-\frac{2}{3}}, \tag{6.2c}$$

$$\mathcal{H}_u^{b\to s} \sim \sqrt{\frac{3}{8}}(3)_{0,0,-\frac{2}{3}} + \frac{1}{2}(\bar{6})_{1,0,-\frac{2}{3}} + \sqrt{\frac{1}{8}}(15)_{0,0,-\frac{2}{3}} + \frac{1}{2}(15)_{1,0,-\frac{2}{3}}. \tag{6.2d}$$

Sandwiching these expressions between initial and final states and considering Eq. (2.87) produces a sum of terms of the form

$$\left(\mathbf{r_f}, \alpha_f | \mathbf{k}, q, \mathbf{r_i}, \alpha_i\right) \langle \mathbf{r_f}| \left(\mathbf{k}\right) |\mathbf{r_i}\rangle_U ,$$

where the appropriate Clebsch-Gordan coefficients, $\left(\mathbf{r_f}, \alpha_f | \mathbf{k}, q, \mathbf{r_i}, \alpha_i\right)$, can be looked up, and the label for the relevant up-type quark, U, is retained [80]. The results of this are summarised in Table 6.1.

6.2.2 Topological amplitudes

An alternative parameterisation is possible. The effective Hamiltonian above ultimately comes from an operator product expansion [220],

$$\mathcal{H}_{\text{eff}}^{b\to d,s} = \frac{4G_F}{\sqrt{2}} \sum_{U=c,u} \sum_{D=d,s} \lambda_{UD} \left(\sum_{i=1}^{2} C_i \mathcal{O}_i^U + \sum_{i=3}^{10} C_i \mathcal{O}_i \right) , \tag{6.3}$$

where $\lambda_{UD} = V_{Ub}V_{UD}^*$ denotes a product of CKM-matrix elements ($U = t$ has been eliminated using the unitarity of the CKM matrix), $\mathcal{O}_{1,2}^U$ are tree operators, $\mathcal{O}_{3-6}$ penguin[1]

[1]The oft-quoted legend of this name regards a bet on a lost game of darts by renowned theorist John Ellis in 1977 [221]. He had to include the word "penguin" in his next paper, and this topology (if one squints) looks a bit like the animal. Then-student Melissa Franklin cites the inspiration behind the bet as this joke:

Decay	$\langle 8\vert\,(3)\,\vert\bar{3}\rangle_c$	$\langle 1\vert\,(3)\,\vert\bar{3}\rangle_c$	$\langle 8\vert\,(15)\,\vert\bar{3}\rangle_u$	$\langle 8\vert\,(\bar{6})\,\vert\bar{3}\rangle_u$	$\langle 8\vert\,(3)\,\vert\bar{3}\rangle_u$	$\langle 1\vert\,(3)\,\vert\bar{3}\rangle_u$
$B^- \to D^- D^0$	1	0	$-\sqrt{\frac{3}{40}}$	$-\sqrt{\frac{1}{12}}$	$\sqrt{\frac{3}{8}}$	0
$B^- \to D_s^- D^0$	1	0	$-\sqrt{\frac{3}{40}}$	$-\sqrt{\frac{1}{12}}$	$\sqrt{\frac{3}{8}}$	0
$\bar{B}^0 \to D_s^- D^+$	1	0	$\sqrt{\frac{1}{120}}$	$\sqrt{\frac{1}{12}}$	$\sqrt{\frac{3}{8}}$	0
$\bar{B}_s^0 \to D^- D_s^+$	1	0	$\sqrt{\frac{1}{120}}$	$\sqrt{\frac{1}{12}}$	$\sqrt{\frac{3}{8}}$	0
$\bar{B}^0 \to D^- D^+$	$\frac{2}{3}$	$-\frac{1}{3}$	$-\sqrt{\frac{1}{30}}$	0	$\sqrt{\frac{1}{6}}$	$-\sqrt{\frac{1}{24}}$
$\bar{B}_s^0 \to D_s^- D_s^+$	$\frac{2}{3}$	$-\frac{1}{3}$	$-\sqrt{\frac{1}{30}}$	0	$\sqrt{\frac{1}{6}}$	$-\sqrt{\frac{1}{24}}$
$\bar{B}^0 \to D_s^- D_s^+$	$-\frac{1}{3}$	$-\frac{1}{3}$	$\sqrt{\frac{1}{120}}$	$-\sqrt{\frac{1}{12}}$	$-\sqrt{\frac{1}{24}}$	$-\sqrt{\frac{1}{24}}$
$\bar{B}_s^0 \to D^- D^+$	$-\frac{1}{3}$	$-\frac{1}{3}$	$\sqrt{\frac{1}{120}}$	$-\sqrt{\frac{1}{12}}$	$-\sqrt{\frac{1}{24}}$	$-\sqrt{\frac{1}{24}}$
$\bar{B}^0 \to \bar{D}^0 D^0$	$\frac{1}{3}$	$\frac{1}{3}$	$\sqrt{\frac{3}{40}}$	$-\sqrt{\frac{1}{12}}$	$\sqrt{\frac{1}{24}}$	$\sqrt{\frac{1}{24}}$
$\bar{B}_s^0 \to \bar{D}^0 D^0$	$\frac{1}{3}$	$\frac{1}{3}$	$\sqrt{\frac{3}{40}}$	$-\sqrt{\frac{1}{12}}$	$\sqrt{\frac{1}{24}}$	$\sqrt{\frac{1}{24}}$

TABLE 6.1: The decomposition of each of the $B \to DD'$ modes of interest (i.e. all $B \to DD'$ decays that are related under SU(3) symmetry) into relevant SU(3) matrix elements. Entries are as in Ref. [9].

operators, and $\mathcal{O}_{7-10}$ electroweak penguin operators. These operators are defined in this instance as [222]:

$$\mathcal{O}_1 = (\bar{U}b)_{V-A}(\bar{D}U)_{V-A} \qquad \text{(A)} \tag{6.4a}$$

$$\mathcal{O}_2 = (\bar{D}b)_{V-A}(\bar{U}U)_{V-A} \qquad \text{(A)} \tag{6.4b}$$

$$\mathcal{O}_{3,5} = \sum_q (\bar{D}b)_{V-A}(\bar{q}q)_{V\mp A} \qquad \text{(B)} \tag{6.4c}$$

$$\mathcal{O}_{4,6} = \sum_q (\bar{q}b)_{V-A}(\bar{D}q)_{V\mp A} \qquad \text{(B)} \tag{6.4d}$$

$$\mathcal{O}_{7,9} = \sum_q (\bar{D}b)_{V-A} e_q (\bar{q}q)_{V\mp A} \qquad \text{(C)} \tag{6.4e}$$

$$\mathcal{O}_{8,10} = \sum_q e_q (\bar{q}b)_{V-A}(\bar{D}q)_{V\mp A} \qquad \text{(C)}, \tag{6.4f}$$

where U denotes $\{u, c\}$ and D denotes $\{d, s\}$. The notation $(\bar{q}q')_{V\pm A}$ is a shorthand for $\bar{q}\gamma_\mu(1 \pm \gamma_5)q'$. The labels "A", "B", and "C" correspond to the diagrams shown in Figure 6.1, which represent example diagrams in the full theory corresponding to the operators [220]. The corresponding Wilson coefficients display a hierarchy in sizes; $C_1 \sim C_2/N_c \gg C_{3-6} \gg C_{7-10}$.

Again, the resulting hadronic matrix elements cannot be reliably determined from first principles, but can be parameterised in terms of *topological amplitudes*, which are

'A truck driver is delivering two penguins to a new zoo when he runs over a nail in the road. He flags down a passing motorist- "I've got a flat, but I need to get these penguins to the zoo ASAP. Can you take them while I fix this problem?" "Of course!" says the motorist. The two penguins get in, and off they go. Later on, the truck driver gets his tyre fixed and heads for the zoo, but when he passes by the cinema he sees the motorist and penguins walking out. "Hey!" he calls out. "I thought I asked you to take them to the zoo!" "Yes, you did," says the motorist. "But we had a bit of change left over, so we decided to see a movie too!"'

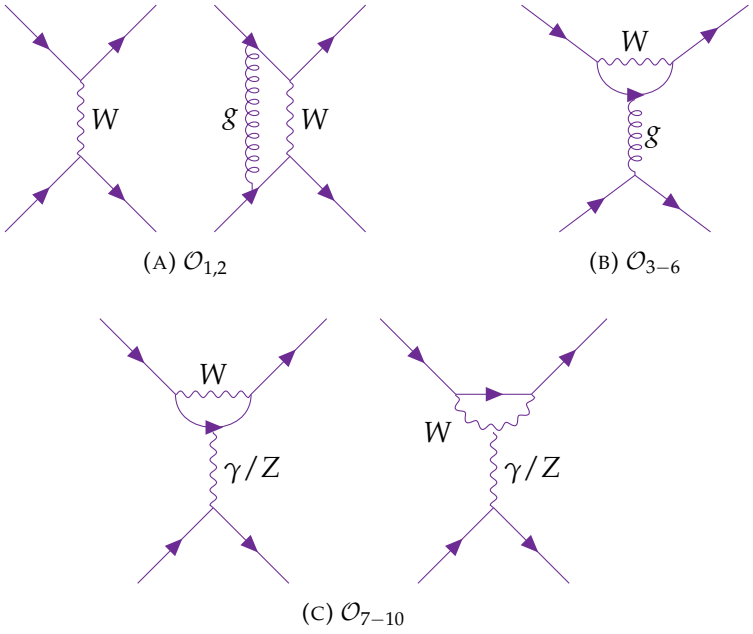

(A) $\mathcal{O}_{1,2}$ (B) $\mathcal{O}_{3-6}$ (C) $\mathcal{O}_{7-10}$

FIGURE 6.1: Typical diagrams in the full theory from which the operators $\mathcal{O}_i$ result. Adapted from diagrams shown in Ref. [220].

independent of energy-scale and renormalisation-scheme. This parameterisation was introduced in Ref. [222]. The decay amplitude for decay $\mathcal{D}$ can thus be decomposed as

$$\begin{aligned}\mathcal{A}(\mathcal{D}) &= \mathcal{A}_c(\mathcal{D}) + \mathcal{A}_u(\mathcal{D}) \\ &= \frac{\lambda_{cD}}{\lambda_{cs}} \sum_i C_c^i(\mathcal{D}) \mathcal{T}_c^i + \frac{\lambda_{uD}}{R_u \lambda_{cs}} \sum_i C_u^i(\mathcal{D}) \mathcal{T}_u^i ,\end{aligned} \tag{6.5}$$

where $\mathcal{T}_{c,u}^i$ are topological amplitudes (with partially absorbed CKM factors), which are defined below, and the corresponding coefficients $C_{c,u}^i(\mathcal{D})$ are shown in Table 6.3. Topological amplitudes are non-perturbative objects representing infinite sums of Feynman diagrams (i.e. any number of low-energy gluons can be added to such a diagram), which show the colour and flavour flow of particular processes. To understand these, it is first necessary to introduce a few types of topology, which are shown in Figure 6.2, following Ref. [222]. Given these, one can define the amplitudes $\{E_1,\ A_{1,2},\ P_{1,3},\ P_{1,3}^{GIM}\}$ given in Table 6.2, from which one can finally arrive at six independent topological amplitudes, defined as [9]:

- $T = E_1 + P_1$
- $A_1^U = A_1$ with $V_{UD},\ U \in \{u, c\}$
- $A_2^U = A_2$ with $V_{UD},\ U \in \{u, c\}$
- $A^c = A_2^c + P_3$
- $\tilde{P}_1 = P_1^{GIM} - P_1$

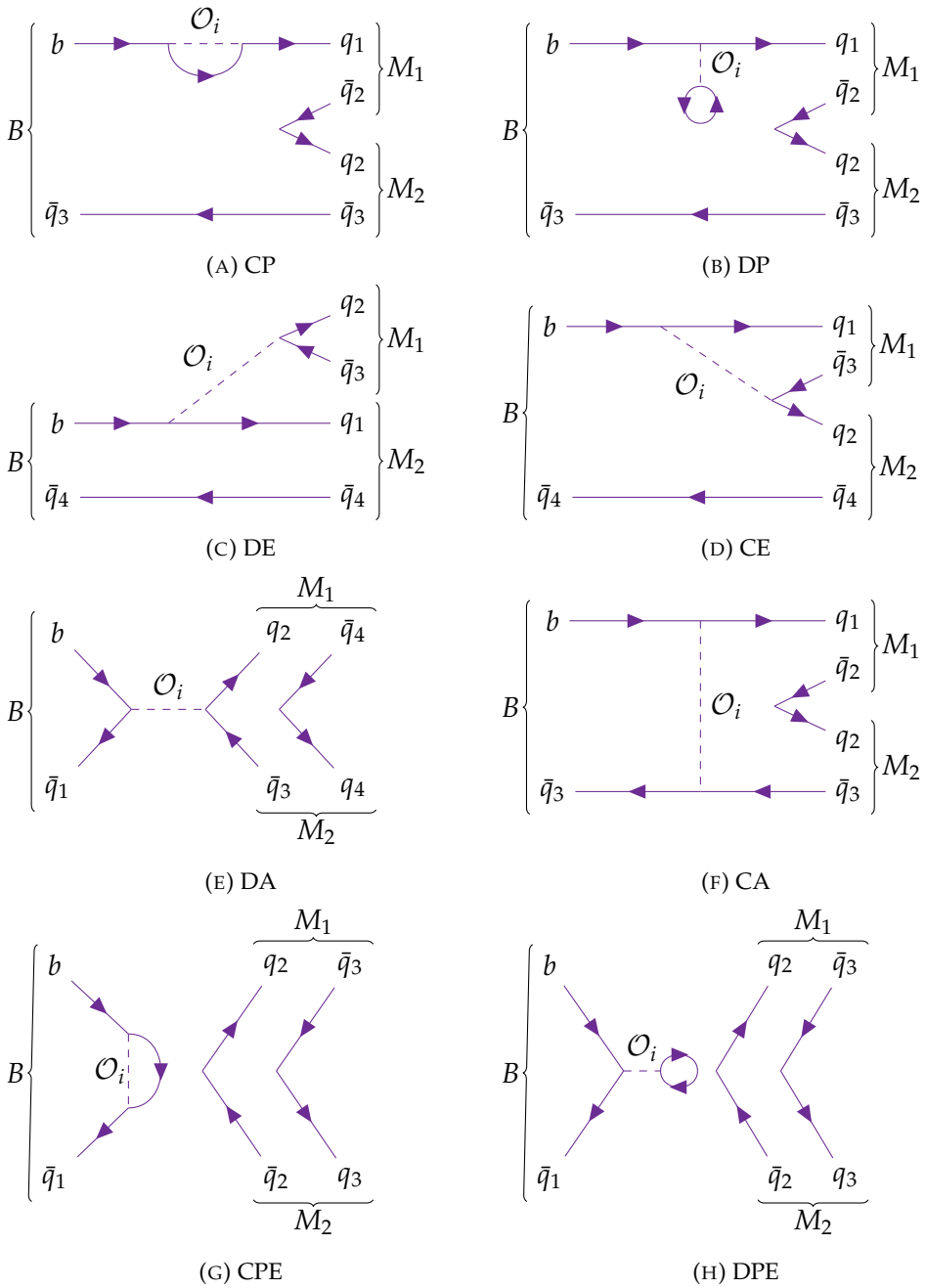

(A) CP (B) DP

(C) DE (D) CE

(E) DA (F) CA

(G) CPE (H) DPE

FIGURE 6.2: The eight independent types of topological diagram. Adapted from diagrams shown in Ref. [222].

- $\tilde{P}_3 = P_3^{GIM} - P_3$

The naming system, $\{T, A, P\}$, is a shorthand for tree, annihilation and penguin topologies. The task is then to note which topologies contribute to each of the modes of interest and the corresponding decomposition table is shown in Table 6.3. The convention used was to add a minus sign wherever a $\bar{u}$ is present in a meson state. The reasoning for this is so that the anti-quark doublet transforms in the same way as the quark doublet.

This new parameterisation is equivalent to the group theoretical one and does not

Amplitude	Decomposition
E_1	$C_1 \langle \mathcal{O}_1 \rangle_{DE} + C_2 \langle \mathcal{O}_2 \rangle_{CE}$
A_1	$C_1 \langle \mathcal{O}_1 \rangle_{DA} + C_2 \langle \mathcal{O}_2 \rangle_{CA}$
A_2	$C_1 \langle \mathcal{O}_1 \rangle_{CA} + C_2 \langle \mathcal{O}_2 \rangle_{DA}$
P_1^{GIM}	$C_1(\langle \mathcal{O}_1 \rangle^c_{CP} - \langle \mathcal{O}_1 \rangle^u_{CP}) + C_2(\langle \mathcal{O}_1 \rangle^c_{DP} - \langle \mathcal{O}_1 \rangle^u_{DP})$
P_3^{GIM}	$C_1(\langle \mathcal{O}_1 \rangle^c_{CPA} - \langle \mathcal{O}_1 \rangle^u_{CPA}) + C_2(\langle \mathcal{O}_1 \rangle^c_{DPA} - \langle \mathcal{O}_1 \rangle^u_{DPA})$
P_1	$C_1 \langle \mathcal{O}_1 \rangle^c_{CP} + C_2 \langle \mathcal{O}_2 \rangle^c_{DP} + \sum_{i=2}^{5}(C_{2i-1} \langle \mathcal{O}_{2i-1} \rangle_{CE} + C_{2i} \langle \mathcal{O}_{2i} \rangle_{DE})$ $+ \sum_{i=2}^{5}(C_{2i-1} \langle \mathcal{O}_{2i-1} \rangle_{CA} + C_{2i} \langle \mathcal{O}_{2i} \rangle_{DA}) + \sum_{i=3}^{10}(C_i \langle \mathcal{O}_i \rangle_{CP} + C_i \langle \mathcal{O}_i \rangle_{DP})$
P_3	$C_1 \langle \mathcal{O}_1 \rangle^c_{CP} + C_2 \langle \mathcal{O}_2 \rangle^c_{DP} + \sum_{i=2}^{5}(C_{2i-1} \langle \mathcal{O}_{2i-1} \rangle_{CA} + C_{2i} \langle \mathcal{O}_{2i} \rangle_{DA})$ $+ \sum_{i=3}^{10}(C_i \langle \mathcal{O}_i \rangle_{CPA} + C_i \langle \mathcal{O}_i \rangle_{DPA})$

TABLE 6.2: Operator product expansions for different topological amplitudes [222]. The notation $\langle \mathcal{O}_i \rangle_A$ means the operator $\mathcal{O}_i$ inserted in the topology A and a superscript c or u means that only a c or u quark is included in any quark loops.

Mode	T	A^c	$\tilde{P}_1$	$\tilde{P}_3$	A_1^u	A_2^u
Counting	1	$\epsilon^{1.5}$	$\epsilon^{2.5}$	$\epsilon^{3.5}$	$\epsilon^{2.5}$	$\epsilon^{3.5}$
$B^- \to D^- D^0$	1	0	- 1	0	1	0
$B^- \to D_s^- D^0$	1	0	-1	0	1	0
$\bar{B}^0 \to D_s^- D^+$	1	0	-1	0	0	0
$\bar{B}_s^0 \to D^- D_s^+$	1	0	-1	0	0	0
$\bar{B}^0 \to D^- D^+$	1	1	-1	-1	0	0
$\bar{B}_s^0 \to D_s^- D_s^+$	1	1	-1	-1	0	0
$\bar{B}^0 \to D_s^- D_s^+$	0	1	0	-1	0	0
$\bar{B}_s^0 \to D^- D^+$	0	1	0	-1	0	0
$\bar{B}^0 \to \bar{D}^0 D^0$	0	-1	0	1	0	-1
$\bar{B}_s^0 \to \bar{D}^0 D^0$	0	-1	0	1	0	-1

TABLE 6.3: Decomposition of $B \to DD'$ decay modes into topological amplitudes with power counting for each indicated. Entries are as in Ref. [9].

reduce the number of unknown parameters. However, with this setup it is more straightforward to deduce the relative sizes of each of the amplitudes, based on the topological structure of each. These power-counting arguments were adapted from Ref. [9], though were modified to be even more conservative, with details given in Section 6.2.5. The relative suppression factors were expressed in terms of powers of some generic factor, ϵ, assumed to be $\sim 30\%$.

6.2.3 Linking SU(3) to Topologies

Given Tables 6.1 and 6.3, it is straightforward to find the correspondence between the $SU(3)_F$ matrix elements and the topological amplitudes, since there are six of each. At

first glance, this does not seem possible as, considering the U-spin symmetry ($d \leftrightarrow s$) seen in both tables, there are essentially only five equations for six unknowns. Furthermore, only four of these equations are independent. This fact can be dealt with by noting that, for instance, the topological decomposition of $\bar{B}^0 \to D_s^- D^+$ consists of T, weighted by λ_{cD}, and $\tilde{P}_1$, weighted by λ_{uD}. Comparing with Table 6.1, it is clear that T can only involve SU(3)$_F$ matrix elements involving the c quark and $\tilde{P}_1$ can only involve SU(3)$_F$ matrix elements involving the u quark. From this, one finds that

$$T = \langle 8| (3) |\bar{3}\rangle_c, \tag{6.6}$$

$$\tilde{P}_1 = -\frac{1}{\sqrt{120}}(\sqrt{45}\langle 8| (3) |\bar{3}\rangle_u + \sqrt{10}\langle 8| (\bar{6}) |\bar{3}\rangle_u + \langle 8| (15) |\bar{3}\rangle_u). \tag{6.7}$$

Similarly, $\bar{B}^0 \to D^- D^+$ consists only of A^c and $\tilde{P}_3$ so, by the same logic, one obtains

$$A^c = -\frac{1}{3}(\langle 8| (3) |\bar{3}\rangle_c + \langle 1| (3) |\bar{3}\rangle_c), \tag{6.8}$$

$$\tilde{P}_3 = \frac{1}{\sqrt{120}}(\sqrt{5}(\langle 1| (3) |\bar{3}\rangle_u + \langle 8| (3) |\bar{3}\rangle_u) + \sqrt{10}\langle 8| (\bar{6}) |\bar{3}\rangle_u - \langle 8| (15) |\bar{3}\rangle_u). \tag{6.9}$$

Then, comparing the first and third lines and then the seventh and ninth lines of the two tables, one sees

$$A_1^u = -\frac{\sqrt{30}}{15}\langle 8| (15) |\bar{3}\rangle_u - \frac{1}{\sqrt{3}}\langle 8| (\bar{6}) |\bar{3}\rangle_u, \tag{6.10}$$

$$A_2^u = -\frac{\sqrt{30}}{15}\langle 8| (15) |\bar{3}\rangle_u + \frac{1}{\sqrt{3}}\langle 8| (\bar{6}) |\bar{3}\rangle_u, \tag{6.11}$$

as presented in Ref. [9]. The same result may be seen by using matrices, again considering the independent sum rules and separating parameters involving u and c quarks.

6.2.4 SU(3) Breaking

Next-to-leading order SU(3)$_F$-breaking effects can be calculated by accounting for $m_s \neq m_u, m_d$. Quarks come associated with appropriate masses, i.e. a q quark enters the Hamiltonian as $m_q q\bar{q}$. This was not relevant in the SU(3)$_F$ limit, where a single mass value, say m_d, was assumed for all three light quarks. Correcting this assumption, for diagrams involving s quarks, requires the addition of a term [85]

$$\mathcal{H}_{\cancel{SU(3)}} \sim (m_s - m_d) s\bar{s}. \tag{6.12}$$

Note that we still assume $m_u = m_d$ so the above can be written equally with m_u. To reinforce the point, if $m_s = m_d$, this term is zero. In group-theoretical language, this means taking the product with $(\mathbf{8})_{0,0,0}$, while for the diagrammatic approach this means inserting a cross wherever there is an s quark line. Figure 6.3 shows the example of this applied to a T topology, where two SU(3)$_F$-breaking diagrams result, $\delta T_{1,2}$. Similarly, there are two SU(3)$_F$-breaking contributions to A^c, notated as $\delta A^c_{1,2}$. The remaining parameters

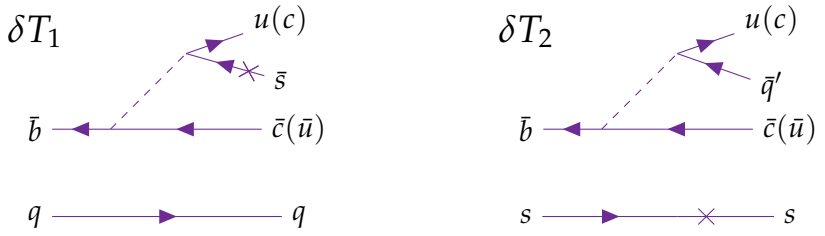

FIGURE 6.3: The two types of $SU(3)_F$-breaking contributions to the T topology.

	Mode	δT_1	δT_2	δA_1^c	δA_2^c
	Counting	$\varepsilon^{1(2)}$	$\varepsilon^{1(2)}$	$\varepsilon^{2.5}$	$\varepsilon^{2.5}$
1	$B^- \to D^- D^0$	0	$-\frac{1}{2}$	0	0
2	$B^- \to D_s^- D^0$	1	0	0	0
3	$\bar{B}^0 \to D_s^- D^+$	1	0	0	0
4	$\bar{B}_s^0 \to D^- D_s^+$	-1	$\frac{1}{2}$	0	0
5	$\bar{B}^0 \to D^- D^+$	0	$-\frac{1}{2}$	$\frac{1}{2}$	$-\frac{1}{2}$
6	$\bar{B}_s^0 \to D_s^- D_s^+$	0	1	-1	1
7	$\bar{B}^0 \to D_s^- D_s^+$	0	0	$\frac{1}{2}$	$\frac{1}{2}$
8	$\bar{B}_s^0 \to D^- D^+$	0	0	-1	0
9	$\bar{B}^0 \to \bar{D}^0 D^0$	0	0	$-\frac{1}{2}$	$\frac{1}{2}$
10	$\bar{B}_s^0 \to \bar{D}^0 D^0$	0	0	1	0

TABLE 6.4: Parameterisation of $SU(3)_F$-breaking contributions to the $B \to DD$ system and corresponding power counting. Numbers in parentheses indicate the suppression of the imaginary parts of the tree amplitudes, in contrast to the suppression of the real parts and absolute values. Table adapted from Ref. [9].

are already suppressed in the $SU(3)_F$ limit and so the breaking terms corresponding to each of these are expected to be sufficiently small that they can be reasonably left out of the model. Such a procedure yields Table 6.4, containing additional terms to be added to those in Table 6.3 to allow for this symmetry breaking and improve the accuracy of our method.

6.2.5 Power Counting

The relative sizes of each topology can be estimated using a little physical intuition, with the tree amplitude, T, expected to be leading and the other diagrams suppressed accordingly, which we parameterise by powers of a generic factor $\epsilon \sim 30\%$ [3, 9], as motivated at the start of this section. Please note that this power counting is a theoretical assumption. This suppression, shown in Tables 6.3 and 6.4 for each of the topologies, can come from a variety of sources. $SU(3)_F$-breaking contributions, for example, are expected to be suppressed by an additional factor of $\mathcal{O}(\epsilon)$. The remaining sources are explained in the following and summarised in Table 6.5.

CKM Structure

Diagrams can be suppressed relative to one another according to their associated CKM factors, which cannot always be separated from the hadronic amplitude. The relative suppression can be best seen by expressing all factors in terms of λ_{cs} and using the Wolfenstein parameterisation in λ:

$$\lambda_{cd} \approx -\bar{\lambda}\lambda_{cs}\,, \quad \lambda_{ud} \equiv -R_u e^{-i\gamma}\lambda_{cd} \approx R_u\bar{\lambda}e^{-i\gamma}\lambda_{cs}\,, \quad \lambda_{us} \approx \bar{\lambda}^2 R_u e^{-i\gamma}\lambda_{cs}\,, \tag{6.13}$$

where $R_u \left(= \left|\frac{\lambda_{cd}}{\lambda_{ud}}\right| \approx 0.35\right)$ represents one of the sides of the unitarity triangle in Figure 2.6, and $\bar{\lambda} = \lambda(1+\lambda^2/2)$ [3,9]. As seen in Eq. (6.5), this common factor is absorbed into the amplitudes as is the factor R_u for those governed by λ_{ud}, denoted as $\mathcal{A}_u$. Hence, such $\mathcal{A}_u$ topologies carry a counting factor $R_u \sim \epsilon$.

Colour Suppression

As detailed in Section 2.5, each topology has an associated scaling with N_c, the number of colours, following approaches taken in Refs. [9,93,222,223]. Relative to the scaling for the T topology, these are; $\{T, A_1^u\} \sim 1$, $\{\tilde{P}_1\,,\, A_2^u\,,\, A^c\} \sim 1/N_c$ and $\tilde{P}_3 \sim 1/{N_c}^2$. In the limit $N_c \to \infty$ (the large-N_c limit), naïve factorisation provides an accurate description of T amplitudes, even allowing SU(3)$_F$ breaking. These methods give only real amplitudes and so for the SU(3)$_F$-breaking corrections, the imaginary parts are expected to be subdominant with respect to the real part. We do not use factorisation in our approach but we make use of this argument by conservatively adding an additional suppression factor (on top of the generic suppression of SU(3)$_F$ breaking) to the imaginary parts of the SU(3)$_F$-breaking parameters, i.e.

$$|\delta T_{1,2}| \sim \mathcal{O}(\varepsilon)\,, \qquad \mathrm{Re}(\delta T_{1,2}) \sim \mathcal{O}(\varepsilon)\,, \qquad \mathrm{Im}(\delta T_{1,2}) \sim \mathcal{O}(\varepsilon^2)\,. \tag{6.14}$$

Penguin Suppression

The parameters $\tilde{P}_{1,3}$ have two dominant contributions. The first comes from tree topologies with QCD penguin operators ($\mathcal{O}_{3-6}$) inserted, which are suppressed relative to the tree diagram by their Wilson coefficients $\sim \mathcal{O}(\epsilon^2)$. The other contribution comes from QCD penguin topologies with tree operators inserted, where the expected relative suppression is less clear since the suppression comes from long-distance physics. While there are no significant indications of large penguin amplitudes in $B \to DD'$ decays, the central values of the CP asymmetries in $B \to D^+D^-$ are especially sizeable. To be conservative, we assign a corresponding suppression factor of

$$\varepsilon^{1/2} \sim 55\%$$

to this effect. This counting lies between the two scenarios of "Standard Counting" and "Enhanced Penguins" in Ref. [9] and was chosen such that any substantial disagreement

Topology	CKM	Colour	Annihilation	Penguin	~~SU(3)$_F$~~	Total
$\lvert T\rvert$	1	1	1	1	1	1
$\lvert A^c\rvert$	1	ϵ	$\epsilon^{0.5}$	1	1	$\epsilon^{1.5}$
$\lvert \tilde{P}_1\rvert$	ϵ	ϵ	1	$\epsilon^{0.5}$	1	$\epsilon^{2.5}$
$\lvert \tilde{P}_3\rvert$	ϵ	ϵ^2	1	$\epsilon^{0.5}$	1	$\epsilon^{3.5}$
$\lvert A_1^u\rvert$	ϵ	1	$\epsilon^{1.5}$	1	1	$\epsilon^{2.5}$
$\lvert A_2^u\rvert$	ϵ	ϵ	$\epsilon^{1.5}$	1	1	$\epsilon^{3.5}$
$\lvert \delta T_{1,2}\rvert$	1	1 (ϵ)	1	1	ϵ	$\epsilon\,(\epsilon^2)$
$\lvert \delta A^c_{1,2}\rvert$	1	ϵ	$\epsilon^{0.5}$	1	ϵ	$\epsilon^{2.5}$

TABLE 6.5: Summary of sources of suppression that apply to each of the topological amplitudes [3]. As explained in the text (see Eq. (6.14)), the imaginary part of the SU(3)$_F$-breaking amplitudes $\delta T_{1,2}$ are further suppressed (relative to the real part), hence the parenthesised values. The overall effect of all contributions is simply the product of the individual suppression factors. An entry of "1" denotes that no suppression is applied to this effect.

would be a clear sign of BSM physics. There are also contributions from electroweak penguin topologies, though these involve photon interactions $\mathcal{O}(\alpha) \sim \mathcal{O}(\epsilon^4)$ so the associated matrix elements are sufficiently suppressed that they can be safely neglected (see also Ref. [9]).

Annihilation

Annihilation diagrams, A_i^U, involve the spectator quark in the interaction, which introduces another source of suppression [89]. In QCDF, as in Eq. (2.93), this naïvely introduces a suppression of $\mathcal{O}(\Lambda_{\rm QCD}/m_b)$, but having heavy mesons in the final state breaks the validity of this estimate. Consequently, we assume a conservative suppression of

$$\epsilon^{1/2} \sim 55\%$$

for annihilation topologies in general, assuming $\epsilon \sim 30\%$. Since diagrams, like A_1^u and A_2^u, that involve $c\bar{c}$ pair-production are not permitted in the heavy-quark limit, these topologies are given an extra suppression factor of ϵ.

6.3 Experimental Inputs

In order to be predictive, our theoretical parameterisation must be confronted with experimental data, both branching ratios and CP asymmetries. These are related to the amplitudes through the expressions in Section 2.3 for CP asymmetries and via Eq. (2.89) for branching ratios, with the correction in Eq. (2.92) applying to non-flavour specific B_s^0 branching ratios. For DD' final states, since ϕ_s is small, $A_{\Delta\Gamma}^{b\to s}(\mathcal{D}) \approx \cos\phi_s \approx \pm 1$, with the sign determined by the CP eigenvalue of the final state (c.f. Eq. (2.74)). In this case

the eigenvalue is positive and so such non-flavour-specific $\bar{B}^0_s$ branching ratios approximately follow

$$\mathcal{B}(\bar{B}^0_s, D, D') = (1 - y_s) \cdot |\mathcal{A}|^2 \cdot \mathcal{P}(\bar{B}^0_s, D, D') \,. \tag{6.15}$$

For the numerical inputs, we use the full set of measurements from a range of different experiments, taken over many years. All of these required careful consideration for them to be reliably combined and to give the best sensitivity. These numerical inputs are summarised in Tables C.1, C.2, and 6.6, and detailed further in the following section.

6.3.1 Branching Ratios

A summary of the numerical values is given in Tables C.1 and C.2. In practice, for most experimental analyses, the final quantity that is reported is, in fact, not the quantity that was directly measured. Typically, these also involve external inputs or assumptions, from which we would like to be disentangled. For a start, it is often a ratio of branching ratios that is measured, since many uncertainties cancel in the determination. This means that there are non-trivial correlations involving all of the modes. Secondly, the D mesons themselves are reconstructed through their decays, so there is also some dependence on the relevant D branching ratio(s). Many of these will have since been measured with greater precision, especially for the older analyses, so we improve sensitivity by making these dependences explicit. The D branching ratios can then be updated and one can account for the further correlations induced by these inputs being shared by multiple measurements. Measuring branching ratios also relies on good knowledge of the number of each type of B meson that was produced in the first place, so there is also a dependence on production fractions. As will be seen later, the correlations due to all of these effects are non-negligible, with some as large as 60%. Though some of the above considerations may have been made by the PDG [14] in their determinations, to be sure that we have correctly accounted for these effects, we instead extract the branching ratios from a fit to the available measurements. This averaging procedure is shown in Section 6.4.

Production Fractions

As seen in Chapter 5, f_s/f_d is the production fraction of B_s mesons relative to that of B_d mesons, and hadronic decays, like the ones considered there, are typically used in the extraction of this quantity [224]. However, as discussed in Chapter 4, the $B \to Dh$ modes used in such extractions have recently displayed tensions between theory and experiment [58]. Hence, for LHCb measurements we instead take the value of f_s/f_d extracted from semi-leptonic decays [58, 225, 226]. This quantity, as well as f_{Λ_b}/f_d, appears to depend strongly on transverse momentum [191, 194, 227], and so a separate and independent production fraction, $(f_s/f_d)_{\text{Tev}}$, was used for measurements from the Tevatron, using the measured ratio of branching fractions [228] as an experimental determination.

Many branching ratio measurements assume isospin symmetry, i.e. that hadrons related by the interchange of u and d quarks are produced in equal quantities, and consequently that the fractions of decays to $B^{\pm}$ and B^0 mesons obey $f_{+-} = f_{00}$, or equivalently $f_d = f_u$. The two different notations refer to B-factory and hadron collider experiments respectively. Isospin symmetry is not an unreasonable assumption considering the similar masses of the two flavours, particularly in comparison to collision energies. There is, however, good reason to believe that this assumption may not hold in either collision environment. For B-factories, since $\Upsilon(4S)$ lies so close to the $b\bar{b}$ threshold, it has be shown to experience enhanced isospin breaking ($\sim 5\%$) in its decay [229, 230]. At hadron colliders also, the non-trivial isospin structure of both the initial and final states [231] calls into question the validity of arguments based on this symmetry. As has been observed for f_s/f_d, the production fraction f_d/f_u may also be expected to depend on p_T and the production mechanism.

Theoretical estimates of these quantities for B-factories differ significantly, and so we would like to use the available experimental information to restrict it [219, 231]. We use $f_{00} = 0.484 \pm 0.007$, to cover the interval determined in Ref. [231]. To simplify the situation, given the large uncertainties in the $B^- \to \bar{D}D$ branching fractions, we assume $f_{+-} + f_{00} = 1$. This assumption should be relaxed once higher precision is achieved but right now the additional uncertainty related to this assumption is negligible [215, 231]. This ratio is yet to be measured at LHCb, and we wish to determine its size from our fit instead of making assumptions, allowing conservatively for

$$f_d/f_u \in [0.5, 1.5]\,.$$

Allowing this to vary leads to additional systematic uncertainties for the branching ratios whose inputs are reliant on this variable.

LHCb

The LHCb analysis in Ref. [232] conveniently gives an explicit breakdown of how the branching ratios that it presents were measured, and the observables used in the fit closely follow the expressions presented there:

$$R_1 = \frac{f_s}{f_d}\frac{\mathcal{B}(\bar{B}^0_s \to D^+D^-)}{\mathcal{B}(\bar{B}^0 \to D^+D^-)} = \epsilon_{\text{rel}}\kappa\frac{N_{\bar{B}^0_s\to D^+D^-}}{N_{\bar{B}^0\to D^+D^-}}\,, \tag{6.16}$$

$$R_2 = \frac{f_s}{f_d}\frac{f_d}{f_u}\frac{1}{\epsilon'_{\text{rel}}}\frac{\mathcal{B}(\bar{B}^0_s \to D^0\bar{D}^0)}{\mathcal{B}(B^- \to D^0D^-_s)} = \kappa\frac{N_{\bar{B}^0_s\to \bar{D}^0D^0}}{N_{B^-\to \bar{D}^0D^-_s}}, \tag{6.17}$$

$$R_3 = \frac{f_d}{f_u}\frac{1}{\epsilon'_{\text{rel}}}\frac{\mathcal{B}(\bar{B}^0 \to \bar{D}^0D^0)}{\mathcal{B}(B^- \to D^0D^-_s)} = \frac{N_{\bar{B}^0\to \bar{D}^0D^0}}{N_{B^-\to \bar{D}^0D^-_s}}\,, \tag{6.18}$$

$$\begin{aligned} R_4 &= \frac{f_s}{f_d}\frac{\mathcal{B}(D^+_s \to K^+K^-\pi^+)}{\mathcal{B}(D^+ \to K^-\pi^+\pi^+)}\frac{\mathcal{B}(\bar{B}^0_s \to D^+_sD^-_s)}{\mathcal{B}(\bar{B}^0 \to D^+D^-_s)} \\ &= \epsilon^{B_0/B_s}_{\text{rel}}\kappa\frac{N_{\bar{B}^0_s\to D^-_sD^+_s}}{N_{\bar{B}^0\to D^+D^-_s}}\,, \end{aligned} \tag{6.19}$$

$$R_5 = \frac{f_u}{f_d}\frac{\mathcal{B}(D^0 \to K^-\pi^+)}{\mathcal{B}(D^+ \to K^-\pi^+\pi^+)}\frac{\mathcal{B}(B^- \to D^0 D_s^-)}{\mathcal{B}(\bar{B}^0 \to D^+ D_s^-)}$$
$$= \epsilon_{\rm rel}^{B^-/B^0}\kappa\frac{N_{B^-\to D^0 D_s^-}}{N_{\bar{B}^0\to D^+ D_s^-}}, \tag{6.20}$$
$$R_6 = \frac{f_s}{f_d}\frac{\mathcal{B}(\bar{B}_s^0 \to D_s^- D^+)}{\mathcal{B}(\bar{B}^0 \to D^+ D_s^-)} = \epsilon_{\rm rel}\frac{N_{\bar{B}_s^0\to D_s^- D^+}}{N_{\bar{B}^0\to D^+ D_s^-}}. \tag{6.21}$$

Ref. [233] also measured the ratio

$$R_7 = \frac{\mathcal{B}(B^- \to D^- D^0)\mathcal{B}(D^- \to K^+\pi^-\pi^-)}{\mathcal{B}(B^- \to D_s^- D^0)\mathcal{B}(D_s^- \to K^+K^-\pi^-)}. \tag{6.22}$$

The relevant D branching ratios and production fractions assumed in the experimental analyses are explicit in these observables. Unlike in previous analyses, we allowed for a non-unity value of f_d/f_u. Values for the other quantities in these ratios, namely efficiencies and counting rates, were also given in the paper, with appropriate systematic uncertainties and correlations[2]. The factor $\epsilon'_{\rm rel}$ includes appropriate D branching fractions for the relevant modes. An updated measurement of the ratio R_6 was made by Ref. [234], which was simply used in place of the one from Ref. [232], as this result was essentially independent of the other ratios.

CDF

The CDF collaboration measured a variant of R_4 defined above, where one of the D_s mesons from the $\bar{B}_s^0$ is reconstructed by the same decay mode as the one from the $\bar{B}^0$ is, while the second one decays via $D_s^+ \to \phi(\to K^+K^-)\pi^+$ [228]. We define this observable as

$$R_4^{\rm CDF} = \left.\frac{f_s}{f_d}\right|_{\rm Tev}\frac{\mathcal{B}(D_s^+ \to \phi(\to K^+K^-)\pi^+)}{\mathcal{B}(D^+ \to K^-\pi^+\pi^+)}\frac{\mathcal{B}(\bar{B}_s^0 \to D_s^+ D_s^-)}{\mathcal{B}(\bar{B}^0 \to D^+ D_s^-)}. \tag{6.23}$$

An update of this observable was possible using relevant information provided in the paper, as well as global averages from the PDG review corresponding to the year the paper was published.

CLEO II

Appropriate branching ratio measurements were made by CLEO II in Ref. [235]. While it was possible to update the inputs for the predominant D branching fractions, which were made explicit in the analysis, we were unable to account for some other subdominant D decay modes, which could not be easily reconstructed from the information provided.

[2] We found a mismatch of $\sim$ 2% compared to Ref. [232], when reproducing the numerical results for Eq. (6.20) from information provided in the paper. To account for this, we applied a corresponding correction factor. There were also misprints noticed in the table of systematic uncertainties for $\bar{B}^0 \to \bar{D}^0 D^0$.

For these inputs, we used the observables

$$\mathcal{B}_1^{\text{CLEO}} = 2f_{+-}\mathcal{B}(B^- \to D^0 D_s^-)\mathcal{B}(D^0 \to K^-\pi^+)\mathcal{B}(D_s^- \to \phi\pi^-)\,, \tag{6.24}$$
$$\mathcal{B}_2^{\text{CLEO}} = 2f_{00}\mathcal{B}(\bar{B}^0 \to D^+ D_s^-)\mathcal{B}(D^+ \to K^-\pi^+\pi^+)\mathcal{B}(D_s^- \to \phi\pi^-)\,, \tag{6.25}$$

making use of all available information given in the paper.

BaBar

The two relevant analyses by BaBar are given in Refs. [236,237]. The analysis Ref. [236] is special in that it uses a double-tagging technique such that its results do not depend on the Y branching fractions, thereby providing absolute branching fraction measurements. Of the D branching fractions, only that of the $D_s^+ \to \phi\pi^+$ mode was made explicit, as the largest source of systematic uncertainty, so it was again only possible to perform a partial update using this mode alone. In this analysis, only one of the two final-state D mesons was reconstructed, so for each of the measured modes ($B^- \to D^0 D_s^-$ and $\bar{B}^0 \to D^+ D_s^-$) we used two separate observables: direct measurements where the $D^{(0,+)}$ was reconstructed and there is no update of D branching fractions (labelled $\mathcal{B}_{1,2}^{\text{BaBar,dir}}$), and measurements where the D_s was reconstructed that we rescale by a factor $k = 3.6\%/\mathcal{B}(D_s^+ \to \phi\pi^+)$ (labelled $\mathcal{B}_{1,2}^{\text{BaBar,re}}$):

$$\mathcal{B}_1^{\text{BaBar,dir}} = \mathcal{B}(B^- \to D^0 D_s^-)\,, \tag{6.26}$$
$$\mathcal{B}_2^{\text{BaBar,dir}} = \mathcal{B}(\bar{B}^0 \to D^+ D_s^-)\,, \tag{6.27}$$
$$\mathcal{B}_1^{\text{BaBar,re}} = \mathcal{B}(B^- \to D^0 D_s^-)/k\,, \tag{6.28}$$
$$\mathcal{B}_2^{\text{BaBar,re}} = \mathcal{B}(\bar{B}^0 \to D^+ D_s^-)/k\,. \tag{6.29}$$

For Ref. [237], it was only possible to update the branching fractions for charged D decay, since several D^0 decays were considered that could not be easily updated based on the information provided. Hence, we considered the observables

$$\mathcal{B}_3^{\text{BaBar}} = 2f_{00}\mathcal{B}(D^+ \to K^-\pi^+\pi^+)^2(\bar{B}^0 \to D^+ D^-)\,, \tag{6.30}$$
$$\mathcal{B}_4^{\text{BaBar}} = 2f_{+-}\mathcal{B}(D^+ \to K^-\pi^+\pi^+)\mathcal{B}(B^- \to D^0 D^-)\,. \tag{6.31}$$

Belle

The Belle experiment provides four separate relevant analyses, in Refs. [238–241]. Once again, it was not possible to update the D branching fractions for the analysis in Ref. [239], however in this instance they do not represent dominant uncertainties. Consequently, we scale only by the production fraction f_{+-}:

$$\mathcal{B}_1^{\text{Belle}} = 2f_{+-}\mathcal{B}(B^- \to D^0 D^-)\,. \tag{6.32}$$

Ref. [238] gives explicit measurements of $\mathcal{B}(\bar{B}^0 \to D^+ D_s^-)$ for three separate D decay channels, all of which could be updated through the observables

$$\mathcal{B}_{2a}^{\text{Belle}} = 2 f_{00} \mathcal{B}(\bar{B}^0 \to D^+ D_s^-) \mathcal{B}(D_s^- \to \phi(\to K^+ K^-)\pi^-)\,, \tag{6.33}$$

$$\mathcal{B}_{2b}^{\text{Belle}} = 2 f_{00} \mathcal{B}(\bar{B}^0 \to D^+ D_s^-) \mathcal{B}(D_s^- \to K^{*0}(\to K^- \pi^+) K^-)\,, \tag{6.34}$$

$$\mathcal{B}_{2c}^{\text{Belle}} = 2 f_{00} \mathcal{B}(\bar{B}^0 \to D^+ D_s^-) \mathcal{B}(D_s^- \to K_S(\to \pi^+ \pi^-) K^-)\,. \tag{6.35}$$

The three measurements shared many significant systematic uncertainties so we constructed a correlation matrix from the information in the paper. We verified that this procedure reproduces the average given in the paper. Ref. [240] supersedes the analysis of Ref. [242] for $\mathcal{B}(\bar{B}^0 \to D^+ D^-)$, and here it was possible to perform an approximate rescaling of the D branching ratio, since in $\sim 75\%$ of cases the $D^\pm$ was reconstructed from the dominant mode. Rescaling also with the production fraction, we used the observable

$$\mathcal{B}_3^{\text{Belle}} = 2 f_{00} \mathcal{B}(\bar{B}^0 \to D^+ D^-) \mathcal{B}(D^+ \to K^- \pi^+ \pi^+)^2\,. \tag{6.36}$$

Finally, Ref. [241] provides an absolute $B_s^0 \to D_s^+ D_s^-$ branching fraction, in which we were unable to update the D_s branching fractions. We therefore used the value as in the paper;

$$\mathcal{B}_4^{\text{Belle}} = \mathcal{B}(\bar{B}_s^0 \to D_s^+ D_s^-)\,. \tag{6.37}$$

This particular measurement was limited by a significant uncertainty in the number of $\bar{B}_s^0$ mesons.

6.3.2 CP Asymmetries

The notation for CP asymmetries here is the same as that introduced in Section 2.3, and the available inputs are summarised in Table 6.6. It can also be useful to consider the quantity ΔS, defined as

$$\Delta S = -\eta_{CP}^f S_{CP} - \sin\phi_D\,, \tag{6.38}$$

since (when it can be defined) this quantity has the same power counting as A_{CP}, unlike S_{CP}.

Charged B Decays

For the measurements of $A_{CP}(B^- \to D_{(s)}^- D^0)$, the 2022 PDG average [14] includes LHCb measurements from Ref. [246] that has since been superseded by Ref. [233], and one must take care to avoid double-counting. We thus took an average of the 2022 PDG inputs, with the exception of the LHCb results, and then averaged this with the updated correlated LHCb measurements.

Observables	Value/%	Comment	Ref.
$A_{CP}(B^- \to D^- D^0)$	-3.3 ± 7.1	Average excluding LHCb result.	[237, 239]
$A_{CP}(B^- \to D^- D^0)$	2.5 ± 1.1	Only LHCb.	[233]
$A_{CP}(B^- \to D_s^- D^0)$	0.5 ± 0.6	$\text{corr}(D^- D^0, D_s^- D^0) = 0.386$	
$A_{CP}(\bar{B}^0 \to D^- D^+)$	13 ± 17	Our average (see text for details).	[14, 240, 243, 244]
$S_{CP}(\bar{B}^0 \to D^- D^+)$	-81 ± 20	$\text{corr}(S_{CP}, A_{CP}) = -19.6\%$	
$A_{CP}(\bar{B}_s^0 \to D_s^- D_s^+)$	-7.8 ± 17.9	From $\lvert\lambda\rvert$ and ϕ_s^{eff}.	[245]
$S_{CP}(\bar{B}_s^0 \to D_s^- D_s^+)$	-2.0 ± 17.1	$\text{corr}(S_{CP}, A_{CP}) = -3.2\%$	

TABLE 6.6: Available experimental CP asymmetries that were used as input [3]. Ref. [240] also presented a value of $A_{CP}(\bar{B}^0 \to D_s^- D^+) = -0.01 \pm 0.02$, though this was in the context of a simple cross-check, which was not as rigourous as the other results presented therein. Consequently, this result was not used as input.

PDG Averaging for $\bar{B}^0 \to D^- D^+$

The measurements of $A_{CP}(\bar{B}^0 \to D^- D^+)$ and $S_{CP}(\bar{B}^0 \to D^- D^+)$ made by Belle [240] and BaBar [244] display a tension. These measurements are known to be significantly correlated and here it was necessary to calculate our own average. The reasons for this and the methodology are outlined below. Correlations between the other CP asymmetry inputs were not taken into account, since the effect of shared inputs in the calculation of production and detection asymmetries was assumed to be small.

When averaging N experimental measurements of the same quantity, the following relationship is expected [14]:

$$\chi^2 \equiv \sum_i \left(\frac{x_i - \bar{x}}{\sigma_i} \right) \approx N - 1, \tag{6.39}$$

where x_i and σ_i are the respective central values and uncertainties of the individual results, $\bar{x}$ is the average, and $N - 1$ is the number of degrees of freedom. If χ^2 is far larger than this value, it is indicative that some of the uncertainties may have been underestimated. In such a case, the PDG [14] recommends a modified averaging procedure where the individual errors are scaled by

$$S = \sqrt{\chi^2 / (N - 1)}\,. \tag{6.40}$$

For averaging with multiple correlated quantities, as is the case here with $A_{CP}(\bar{B}^0 \to D^- D^+)$ and $S_{CP}(\bar{B}^0 \to D^- D^+)$, a multi-dimensional weighted average must be performed. Ref. [247] provides the formula for such an average, $\bar{\mathbf{x}}$, as

$$\bar{\mathbf{x}} = \left(\sum_i (\mathbf{V_i})^{-1} \right)^{-1} \cdot \left(\sum_i (\mathbf{V_i})^{-1} \cdot \mathbf{x_i} \right), \tag{6.41}$$

where $\mathbf{V_i}$ and $\mathbf{x_i}$ are the covariance matrices and central values for $A_{CP}(\bar{B}^0 \to D^- D^+)$

and $S_{CP}(\bar{B}^0 \to D^- D^+)$ from the individual experiments. In this multi-dimensional scenario, the χ^2 is then expressed as [247]

$$\chi^2 \equiv \sum_i (\mathbf{x_i} - \bar{\mathbf{x}})^T \cdot (\mathbf{V_i})^{-1} \cdot (\mathbf{x_i} - \bar{\mathbf{x}}) \,, \tag{6.42}$$

and for the two-dimensional average one expects

$$\chi^2 \approx N - 2 \,,$$

where N is the total number of measurements (of both quantities), and therefore $N-2$ is the number of degrees of freedom.

The correlations for the systematic uncertainties were taken from Ref. [14] and the statistical ones were assumed to be uncorrelated. Constructing a χ^2 as outlined above for the three sets of A_{CP} and S_{CP} from Refs. [240, 243, 244], one would expect that

$$\chi^2 \approx 4 \,,$$

since here $N = 6$. However, using those experimental inputs, one finds

$$\chi^2 = 10.7 > 4 \,.$$

We were, therefore, justified to apply Eq. (6.42) and to scale the errors of the individual experiments by a factor of

$$S = \sqrt{10.7/4} \approx 1.6 \,. \tag{6.43}$$

The averages in Table 6.6 result from the application of Eq. (6.41), following this scaling of the errors. This procedure is visualised in Figure 6.4 and results in the uncertainties given in Table 6.6.

Indirect Determinations for $\bar{B}^0_s \to D^-_s D^+_s$

$A_{CP}, S_{CP}(\bar{B}^0_s \to D^-_s D^+_s)$ have not yet been measured directly, but they can be inferred from measurements of the magnitude and phase of $\lambda(\bar{B}^0_s \to D^-_s D^+_s)$ [245], defined as in Eq. (2.70). The phase is sometimes referred to as ϕ_s^{eff}, as it would equal ϕ_s in the case of no CPV in decay. $\bar{B}^0_s \to D^-_s D^+_s$ is an excellent mode to extract ϕ_s from, though at the time of writing it can be determined indirectly from global fits [37, 40] or directly measured from $B_s \to J/\psi\phi$ [248] at a precision far greater than what could currently be achieved from our fit. For this reason, we included ϕ_s as an external input in this work. Deviations from this value could then, in principle be probed in the fit. In future, when the precision of $B \to DD'$ determinations improve, this input should be removed and ϕ_s extracted from the fit.

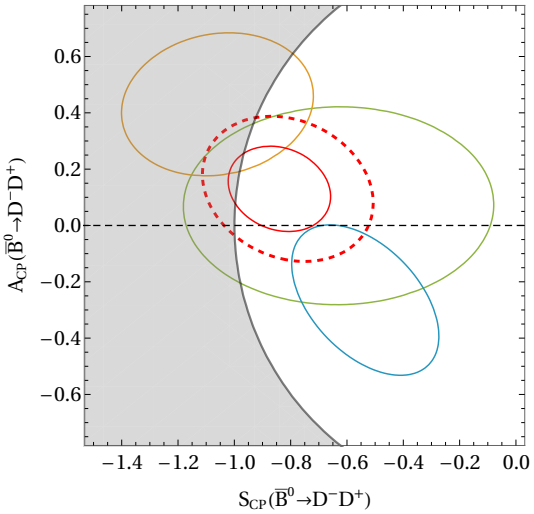

FIGURE 6.4: 68% CL regions for the time-dependent CP asymmetry measurements of $\bar{B}^0 \to D^- D^+$ from Belle [240] (yellow), BaBar [244] (green) and LHCb [243] (blue), as well as their correlated average, as given in HFLAV [56] (red solid). As described in the text, we instead use the average (red dashed) where the uncertainties of each have been symmetrically enlarged to produce a more representative χ^2. The limit of the physical parameter space, defined by $A_{CP}(\bar{B}^0 \to D^- D^+)^2 + S_{CP}(\bar{B}^0 \to D^- D^+)^2 \leq 1$ is marked by the black solid line, with the unphysical region shaded.

Input	Value
λ	0.22500
γ	1.143
$\phi_d \equiv 2\beta$	0.787 ± 0.018
$\phi_s \equiv -2\beta_s$	-2×0.01841
$y_s \equiv \Delta\Gamma_s/(2\Gamma_s)$	0.062

TABLE 6.7: Additional input data from the global CKM fit [37].

CKM Inputs

Table 6.7 gives relevant inputs from the global CKM fit of Ref. [37], which will be needed for the global fit. Values shown without uncertainties are included as constants in the fit. The uncertainties on y_s and ϕ_s are far smaller than those of other observables or assumptions in the fit, so they are neglected. ϕ_d has been determined experimentally, and so this parameter is floated in the fit. As already discussed in Ref. [9], the CKM phase γ is impacted by an effect known as *reparameterisation invariance* [249–251]. The key point is that in $B \to DD'$ a change in the apparent phase γ can be compensated by a corresponding shift in the topological amplitudes and hence, without additional assumptions about at least one of them, analysis of these modes cannot be sensitive to this phase. These additional assumptions were discussed in Refs. [9] and [252]. Our power counting strategy allows for large variations in the topological amplitudes, and so any uncertainty of γ has no real impact and would only matter if one were to wish to interpret the fitted topological amplitudes physically or calculate them from first principles.

6.4 Combining Branching Ratio Inputs

Before using our theoretical parameterisation, we first perform our own average of the numerous branching ratio inputs through a fit where the branching ratios themselves are the floated parameters. This allows a comparison with the values presented in the PDG, shown in Table 6.8. Since the CP asymmetry measurements would have little impact on the fit without theoretical parameterisation, these are left out at this point. The fit performs well and the results appear consistent within themselves, and with the Gaussian approximation, i.e. that the covariance matrix, V, is given by [14]

$$\left(V^{-1}\right)_{ij} = \frac{1}{2}\frac{\partial^2\chi^2}{\partial\theta_i\partial\theta_j}\bigg|_{\boldsymbol{\theta}=\hat{\boldsymbol{\theta}}}, \tag{6.44}$$

where $\boldsymbol{\theta}$ are the fit parameters, and $\hat{\boldsymbol{\theta}}$ are the coordinates of the global minimum. The correlation matrix, crucial for a meaningful interpretation of the available data, resulting from this approach is also shown in Table 6.8 but is not provided by the PDG.

While we generally allow f_d/f_u to float, we also examine the effect of explicitly setting it to unity, which is assumed in most other analyses. As shown in the table, both scenarios generally see reduced uncertainties relative to the PDG [14], an impressive result since varying the production fractions f_d/f_u and $f_{+-,00}$ would, in principle, allow for larger uncertainties. The observed improvement can, though, be understood for the use of updated lifetimes and D meson branching fractions, as well as the inclusion of a recent LHCb analysis [233].

The extracted values of the production fraction f_s/f_d at LHCb, as well as $f_{+-,00}$, do not change significantly relative to the input values, however the corresponding value at the Tevatron

$$(f_s/f_d)_{\text{Tev}} = 0.34^{+0.06}_{-0.05}, \tag{6.45}$$

is competitive but consistent with the current HFLAV average Ref. [254]. This value is greater than that for LHCb by around one standard deviation, which supports the claim of a p_T dependence in the quantity. In this scenario, we find agreement with the isospin assumption of $f_d/f_u = 1$ at LHCb,

$$(f_d/f_u)^{\text{LHCb, 7 TeV}} = 0.99^{+0.15}_{-0.13}, \tag{6.46}$$

though this also permits relatively large deviations. This result should, in principle, be model-independent, but it should be noted that this specific determination uses a large amount of information external to LHCb. Nonetheless, this appears to be the first determination of such a quantity at LHCb, though this has been done for CMS in Ref. [227]. The additional input of theoretical assumptions will improve upon this extraction, as will be seen below.

	Observable	Fit result	Fit result ($f_d/f_u = 1$)	PDG [14]
1	$\mathcal{B}(B^- \to D^- D^0)$	0.383 ± 0.034	0.385 ± 0.028	0.38 ± 0.04
2	$\mathcal{B}(B^- \to D_s^- D^0)$	9.2 ± 0.8	9.3 ± 0.7	9.0 ± 0.9
3	$\mathcal{B}(\bar{B}^0 \to D_s^- D^+)$	7.6 ± 0.7	7.5 ± 0.6	7.2 ± 0.8
4	$\mathcal{B}(\bar{B}_s^0 \to D^- D_s^+)$	0.280 ± 0.044	0.278 ± 0.040	0.28 ± 0.05
5	$\mathcal{B}(\bar{B}^0 \to D^- D^+)$	0.231 ± 0.023	0.231 ± 0.023	$0.211 \pm 0.018^\dagger$
6	$\mathcal{B}(\bar{B}_s^0 \to D_s^- D_s^+)$	4.3 ± 0.6	4.3 ± 0.6	4.4 ± 0.5
7	$\mathcal{B}(\bar{B}^0 \to D_s^- D_s^+)$			≤ 0.036 [238]
8	$\mathcal{B}(\bar{B}_s^0 \to D^- D^+)$	0.24 ± 0.05	0.24 ± 0.05	0.22 ± 0.06
9	$\mathcal{B}(\bar{B}^0 \to \bar{D}^0 D^0)$	0.012 ± 0.006	0.012 ± 0.006	0.014 ± 0.007
10	$\mathcal{B}(\bar{B}_s^0 \to \bar{D}^0 D^0)$	0.166 ± 0.039	0.165 ± 0.036	0.19 ± 0.05

	$BR(B^- \to D^- D^0)$	$BR(B^- \to D_s^- D^0)$	$BR(\bar{B}^0 \to D_s^- D^+)$	$BR(\bar{B}_s \to D^- D_s^+)$	$BR(\bar{B}^0 \to D^- D^+)$	$BR(\bar{B}_s \to D_s^- D_s^+)$	$BR(\bar{B}_s \to D^- D^+)$	$BR(\bar{B}^0 \to \bar{D}^0 D^0)$	$BR(\bar{B}_s \to \bar{D}^0 D^0)$
$BR(B^- \to D^- D^0)$	100.0	91.7	6.3	5.1	1.2	3.0	1.4	1.4	3.7
$BR(B^- \to D_s^- D^0)$	91.7	100.0	6.7	−0.0	−5.1	5.4	−5.1	0.4	−2.0
$BR(\bar{B}^0 \to D_s^- D^+)$	6.3	6.7	100.0	58.8	2.1	64.0	−0.4	19.7	38.8
$BR(\bar{B}_s \to D^- D_s^+)$	5.1	−0.0	58.8	100.0	1.3	59.0	15.7	12.6	40.0
$BR(\bar{B}^0 \to D^- D^+)$	1.2	−5.1	2.1	1.3	100.0	−2.6	43.6	−0.8	−1.7
$BR(\bar{B}_s \to D_s^- D_s^+)$	3.0	5.4	64.0	59.0	−2.6	100.0	15.2	13.2	42.4
$BR(\bar{B}_s \to D^- D^+)$	1.4	−5.1	−0.4	15.7	43.6	15.2	100.0	0.1	12.2
$BR(\bar{B}^0 \to \bar{D}^0 D^0)$	1.4	0.4	19.7	12.6	−0.8	13.2	0.1	100.0	12.7
$BR(\bar{B}_s \to \bar{D}^0 D^0)$	3.7	−2.0	38.8	40.0	−1.7	42.4	12.2	12.7	100.0

TABLE 6.8: Summary of the results of our fit with no theoretical assumptions (an averaging procedure) to the available experimental $B \to DD'$ branching ratios [3]. Central values and uncertainties are shown in the table in units of 10^{-3}, and below we present the corresponding correlations, given in percent. Our treatment of production fractions outlined above introduces additional uncertainties in these results. We also display the results for the scenario where f_d/f_u is assumed to be unity and also give the current PDG values, for means of comparison. We symmetrised the uncertainties, which correspond with the correlation matrix below. Comparing with Table 6.10 shows that this approximation is reasonable. No fit results are shown for $\mathcal{B}(\bar{B}^0 \to D_s^- D_s^+)$ since an experimental central value for this does not currently exist. The PDG presents a limit on this quantity, though this was not included in the fits. †: Our fit has a larger uncertainty than the PDG for this input, as we included a recent LHCb measurement that superseded Ref. [253].

The future prospects for measurements of this quantity rely on an LHCb measurement of the ratio [232],

$$\frac{f_u}{f_d}\frac{\mathcal{B}(B^- \to D^0 D_s^-)}{\mathcal{B}(\bar{B}^0 \to D^+ D_s^-)},$$

since the individual branching fractions can be determined precisely at the B factories. This reference also provides the ratios

$$\frac{f_s}{f_d}\frac{f_d}{f_u}\frac{\mathcal{B}(\bar{B}_s^0 \to D^0 \bar{D}^0)}{\mathcal{B}(B^- \to D^0 D_s^-)} \quad \text{and} \quad \frac{f_d}{f_u}\frac{\mathcal{B}(\bar{B}^0 \to D^0 \bar{D}^0)}{\mathcal{B}(B^- \to D^0 D_s^-)}.$$

In this instance, the branching ratios in the numerators of these expressions have not yet been measured individually and so cannot currently be isolated from changes in f_d/f_u, though this could change in the future.

6.5 Validation of Theory Assumptions

We construct a χ^2 function using the experimental inputs outlined in Tables 6.6 and C.1, and the parameterisation in terms of the topological amplitudes introduced in Section 6.2.5. Confidence intervals on the parameters can be determined from the variation of the χ^2 from the minimum value (as in the Rfit approach [255]).

Using Tables 6.1 and 6.3, and with reference to Eq. (2.89) and the expressions in Section 2.3, one can then make predictions for the observables of study as a function of the topological parameters. These parameters are complex (exception for T, which we assume to be real without loss of generality), so each one can be split into real and imaginary parts. These predictions can then be combined with the experimental inputs outlined in Tables 6.6 and C.1 to construct a χ^2 function that can be minimised with respect to the topological parameters[3]. The global minimum designates central values for the estimates of the observables of interest, while uncertainties come from performing profiled scans, minimising the χ^2 while one parameter or observable is held at a fixed value that is then varied. The values that increase the profiled χ^2 by one [256], relative to the minimum, give the upper and lower bounds of the parameter estimate or observable value at 1σ. In setting up this formalism, theoretical assumptions have been made and it is necessary to verify that the data support these assumptions before performing any fits.

6.5.1 $\mathbf{SU(3)_F}$ Symmetry

The entirety of this analysis relies on the assumption of SU(3)$_F$ as a good symmetry for $B \to DD'$ decays, so it is essential to check the validity of this assumption. If this symmetry was an exact one, then U-spin partners, i.e. amplitudes related by a complete

[3]Richard Feynman's infamous quote is most relevant here- "It does not make any difference how beautiful your guess is, it does not make any difference how smart you are, who made the guess, or what his name is - if it disagrees with experiment, it is wrong."

Relative rate	$b \to s$	$b \to d$
Tree-dominated	1	$\bar{\lambda}^2$
Annihilation-dominated	ϵ^3	$\bar{\lambda}^2\epsilon^3$

CP asymmetry	$b \to s$	$b \to d$
Tree-dominated	$\bar{\lambda}^2\epsilon^{2.5}$	$\epsilon^{2.5}$
Annihilation-dominated	$\bar{\lambda}^2\epsilon^2$	ϵ^2

TABLE 6.9: Expectations from power counting for the approximate respective sizes, with respect to the leading tree-dominated $b \to s$ decays, for both decay rates (above) and for the CP asymmetries A_{CP} and ΔS (below). Taken from Ref. [3].

interchange of s and d quarks [257–259], would differ only by CKM factors;

$$\frac{\Gamma_{\mathcal{D}_{b\to s}}}{\Gamma_{\mathcal{D}_{b\to d}}} = -\frac{A_{CP}^{\mathcal{D}_{b\to d}}}{A_{CP}^{\mathcal{D}_{b\to s}}}\,. \tag{6.47}$$

Direct CP asymmetries such as these rely on the interference of $\mathcal{A}_c$ topologies (governed by λ_{cD}) with $\mathcal{A}_u$ topologies (governed by λ_{uD}). The small size of this latter set of parameters mean that it is not currently feasible to test such relations. It is, though, possible to instead test U-spin symmetry using the following relations, which can be easily seen from Table 6.3:

$$\begin{aligned}\left|\frac{\lambda_{cs}}{\lambda_{cd}}\right|^2 \frac{\Gamma(B^- \to D^- D^0)}{\Gamma(B^- \to D_s^- D^0)} &\overset{\text{U-spin limit}}{\simeq} \left|\frac{\lambda_{cs}}{\lambda_{cd}}\right|^2 \frac{\Gamma(\bar{B}_s^0 \to D^- D_s^+)}{\Gamma(\bar{B}^0 \to D_s^- D^+)} \\ &\overset{\text{U-spin limit}}{\simeq} \left|\frac{\lambda_{cs}}{\lambda_{cd}}\right|^2 \frac{\Gamma(\bar{B}^0 \to D^- D^+)}{\Gamma(\bar{B}_s^0 \to D_s^- D_s^+)} \overset{\text{U-spin limit}}{\simeq} 1 + \mathcal{O}(\epsilon^{2.5})\,, \quad (6.48)\end{aligned}$$

$$\left|\frac{\lambda_{cs}}{\lambda_{cd}}\right|^2 \frac{\Gamma(\bar{B}^0 \to \bar{D}^0 D^0)}{\Gamma(\bar{B}_s^0 \to \bar{D}^0 D^0)} \overset{\text{U-spin limit}}{\simeq} \left|\frac{\lambda_{cs}}{\lambda_{cd}}\right|^2 \frac{\Gamma(\bar{B}^0 \to D_s^+ D_s^-)}{\Gamma(\bar{B}_s^0 \to D^+ D^-)} \overset{\text{U-spin limit}}{\simeq} 1 + \mathcal{O}(\epsilon^2)\,. \quad (6.49)$$

The appropriate corrections in these relations come from the breaking contributions to the $\mathcal{A}_c$ parameters, which are dominant in comparison to the corrections to the amplitudes $\mathcal{A}_u$ that were neglected in this analysis.

Measuring suppression relative to a tree-dominated $b \to s$ mode, in this case $\bar{B}^0 \to D_s^- D^+$ (as in Table 6.9), we find that the experimental decay rates agree with our expectations from power counting typically within $\sim$ 30% $\approx \epsilon$, so are consistent with our assumptions. Slightly larger deviations of $\sim$ 40% are seen for $\bar{B}^0 \to D^+ D^-$ and $\bar{B}_s^0 \to D_s^+ D_s^-$, which may indicate significant negative interference with the annihilation amplitude A^c. Indeed such an effect has already been pointed out in Ref. [9] and later confirmed in Ref. [218]. Despite this, the results are generally in agreement with what is expected, since 30% is only an approximate scaling. Since most of the CP asymmetry inputs (A_{CP} and ΔS_{CP}) lie within 1σ of zero, their relative scaling cannot easily be deduced, and so we are more limited in the conclusions we can draw. However, the recent LHCb measurement of $A_{CP}(B^- \to D^0 D^-) \sim 2\%$ displays some small deviation from

zero ($\sim 2\sigma$) but also lies below our assumed scaling of $\epsilon^{2.5} \sim 5\%$. This is a sign that our treatment of penguin amplitudes is conservative.

SU(3)$_F$-breaking corrections at $\mathcal{O}(\epsilon)$ are expected to apply at the amplitude level, so the effect is amplified when one takes a ratio, as already noted in the context of D meson decays in Ref. [260,261]. We applied the experimental values to the square roots of ratios of branching ratios in Eqs. (6.48) and (6.49) and show these in Figure 6.5. These ratios are consistent with unity within $\sim 30\%$, and so this shows that the corrections are smaller than the limits placed on them, and this serves as another piece of evidence that we treat possible breaking conservatively. These results also agree with the structure expected from the CKM matrix.

6.5.2 $1/N_c$ Power Counting

Another assumption of our method is that $1/N_c$ power counting can provide an accurate description of the $B \to DD'$ decays we study, and one must also verify that this is the case. In this limit, the tree diagrams can be factorised into two parts (see Section 2.5); a transition of $B \to D$, encoded by a momentum-dependent form-factor ($F_0^{B\to D}(q^2)$), and the creation of a D' from the vacuum, which is parameterised by a corresponding meson decay constant ($f_{D'}$). We use [92]

$$f_{D^\pm} = (212.0 \pm 0.7)\,\text{MeV}\,, \qquad f_{D_s^\pm} = (249.9 \pm 0.5)\,\text{MeV}\,, \tag{6.50}$$

and

$$F_0^{B^0\to D^-}(\bar{m}_D^2) = 0.740 \pm 0.010\,, \qquad F_0^{B_s^0\to D_s^-}(\bar{m}_D^2) = 0.720 \pm 0.016\,, \tag{6.51}$$

with $\bar{m}_D^2 = 1/3 \times (m_{D^0}^2 + m_{D^-}^2 + m_{D_s^-}^2)$. These form factors were determined using the BGL method introduced in Section 2.5. One should note that these decays cannot be well described by factorisation in the heavy-quark limit [89,90], which have smaller corrections than $1/N_c$ expansion. Our results have corrections at $\mathcal{O}(1/N_c^2)$ that are not included in the error bars shown.

Figure 6.5 shows the results of this study for tree contributions only; all other diagrams are either heavily suppressed or are not factorisable in any N_c regime. One can see overall consistency between the data and the $1/N_c$ limit. The small difference for $|\lambda_{cs}A(B^0 \to D^-D^+)|/|\lambda_{cd}A(B_s \to D_s^-D_s^+)|$ can be understood as coming from the presence of an annihilation contribution (as well as breaking terms) to the amplitudes. As well as the ratios, the individual amplitudes involved were found to be in keeping with the large-N_c limit, which consistently predicted larger rates than the averaged experimental values (from Table 6.8). For the modes without annihilation contributions, the central values of the amplitude sizes differed by around $17-28\%$, reasonably large to be explained by $1/N_c^2$ corrections, though they were consistent with this expectation within their uncertainties. Similar behaviour has already been identified in Ref. [58] in $b \to c\bar{u}d/s$ transitions, however in this instance QCD factorisation is not expected to

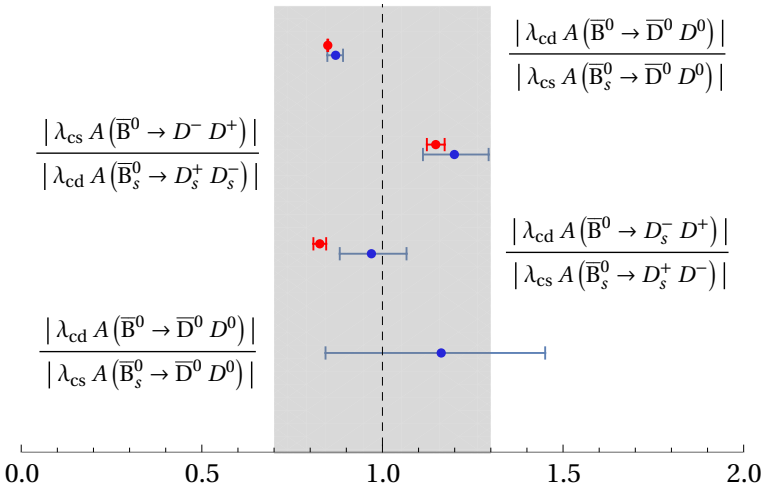

FIGURE 6.5: Naïve factorisation results (red) compared to the predictions from the U-spin limit (blue), as shown in Ref. [3].

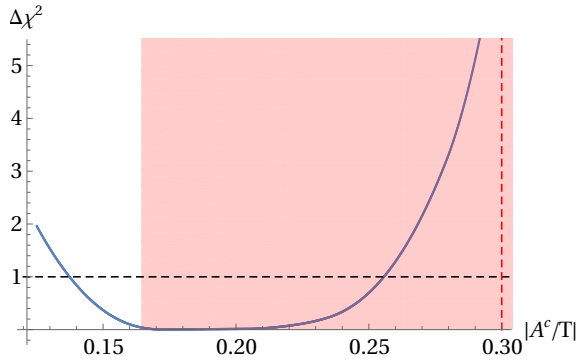

FIGURE 6.6: $\Delta\chi^2$-profile of $|A^c/T|$ as resulting from our global fit, overlaid with vertical lines showing the applied theory constraints resulting from the power counting imposed here (dashed red line) and region excluded in Ref. [9] (red shaded region).

work well, so the disagreement holds much less significance. Overall, our consistency checks have confirmed that our $1/N_c$ power-counting assumptions are valid. Please note that these results were not included in our global fit.

It is also important to check that the assumed power counting for the topological parameters is valid. Figure 6.6 shows a $\Delta\chi^2$ scan of $|A^c/T|$ and it can be seen that the minimum lies well within the allowed parameter space.

6.6 Global Fit

Having validated the method, we perform a global fit to all available experimental inputs, as summarised in Tables 6.6, 6.7, C.1, and C.2, assuming the power counting given in Section 6.2.5. This allows us to take a more general, bigger-picture view of $B \to DD'$ decays as a whole, in terms of consistency of expected flavour symmetries with experimental data. The quality of fit is good, as will be discussed further later on.

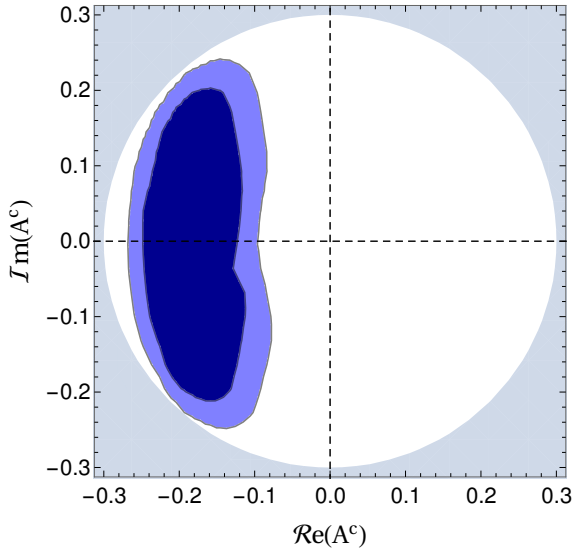

FIGURE 6.7: Two-dimensional contour plot for the real and imaginary parts of A^c. The 68% and 95% confidence regions are shown in dark- and light-blue, respectively.

6.6.1 Constraints on parameters

The parameter T sets the overall scale of the observables and, being the dominant parameter, is well-constrained, with a 68% confidence-interval of [0.97, 1.09] keV. The sub-dominant $\mathrm{SU}(3)_F$ parameter A^c also receives significant constraints beyond those imposed by power counting, with 68% confidence-intervals of $|A^c/T| \in [0.14, 0.27]$ and $\arg(A^c) - \pi \in [-0.86, 0.90]$. The two-dimensional contour plot is shown in Figure 6.7. One of the $\mathrm{SU}(3)_F$-breaking corrections to T receives a small constraint on its absolute value ($|\delta T_1| > 0.08$), with the real part being constrained more strongly (and predicted to be positive only) than the imaginary part, despite the latter having tighter constraints from power-counting. As previously mentioned, the magnitudes and phases of the remaining parameters are largely unconstrained beyond power counting. Figure 6.8 summarises the one-dimensional constraints on the parameters in terms of both magnitudes and real/imaginary parts.

6.6.2 Branching Ratios

Table 6.10 summarises the predictions of the branching ratios resulting from the global fit, with Figure 6.9 illustrating this graphically. Note that the upper bound on $\mathcal{B}(\bar{B}^0 \to D_s^- D_s^+)$ was not used as input to the fit, but its 68% confidence interval could be predicted to be

$$\mathcal{B}(\bar{B}^0 \to D_s^- D_s^+) \in [0.004, 0.037] \times 10^{-3},$$

which agrees with the current upper limit $\mathcal{B}(\bar{B}^0 \to D_s^- D_s^+) \leq 0.036 \times 10^{-3}$ [238]. Imposing our $\mathrm{SU}(3)_F$ assumptions does not significantly change the central values of all the branching ratios with respect to the experiment-only fit, but the precision is improved.

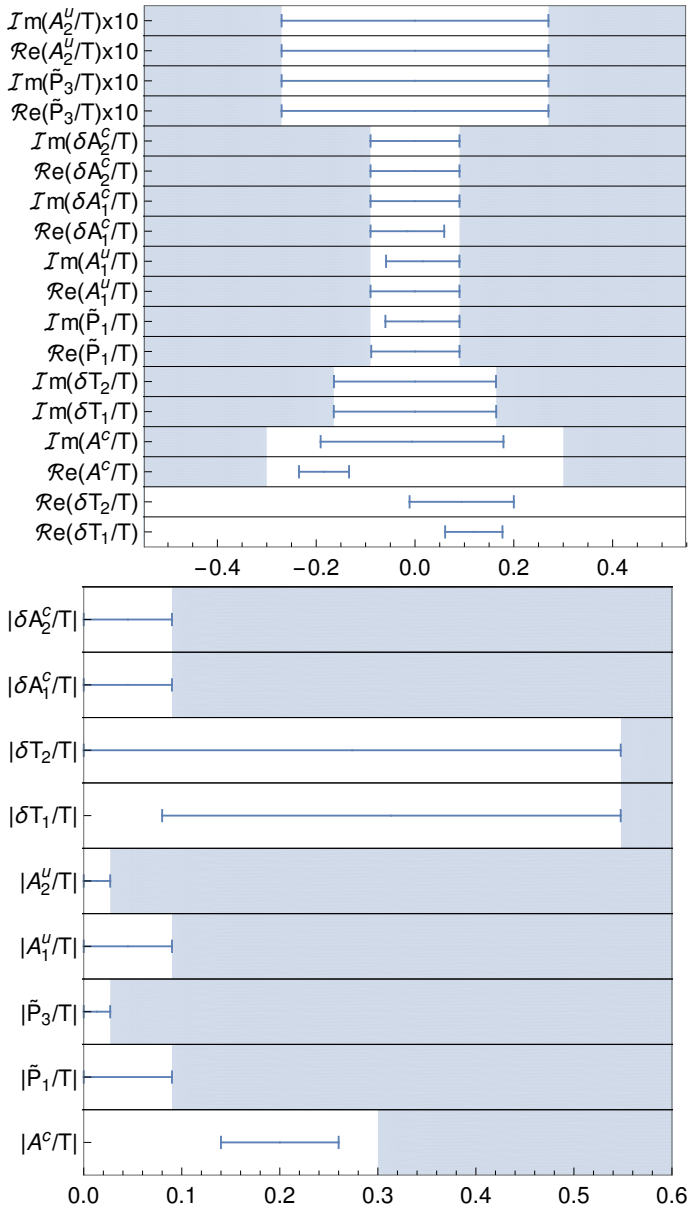

FIGURE 6.8: Constraints on the topological parameters in terms of real/imaginary parts (top) and magnitudes (bottom). The shaded regions show the constraints placed on each of the parameters in the fit.

Since the data agrees with the SU(3) power counting, the U-spin ratios in Figure 6.5 do not give much non-trivial information.

Isospin Breaking

Using isospin symmetry and also applying conservative assumptions on the relative sizes of the topological amplitudes, one can find yet more *quasi-isospin* sum-rules. For the scenario already outlined and focusing on the observables discussed in the previous work (Ref. [9]), one finds

$$\Gamma(\bar{B}^0 \to D_s^- D^+) = \Gamma(B^- \to D_s^- D^0)(1 + \mathcal{O}(\bar{\lambda}^2 \epsilon^{2.5})) \tag{6.52}$$

	Observable	Global fit	Exp.-only fit	PDG [14]
1	$\mathcal{B}(B^- \to D^- D^0)$	0.366 ± 0.025	$0.383^{+0.034}_{-0.033}$	0.38 ± 0.04
2	$\mathcal{B}(B^- \to D_s^- D^0)$	8.8 ± 0.6	$9.2^{+0.9}_{-0.8}$	9.0 ± 0.9
3	$\mathcal{B}(\bar{B}^0 \to D_s^- D^+)$	8.2 ± 0.5	7.6 ± 0.7	7.2 ± 0.8
4	$\mathcal{B}(\bar{B}_s^0 \to D^- D_s^+)$	$0.303^{+0.045}_{-0.040}$	$0.280^{+0.047}_{-0.042}$	0.28 ± 0.05
5	$\mathcal{B}(\bar{B}^0 \to D^- D^+)$	$0.224^{+0.022}_{-0.021}$	$0.231^{+0.023}_{-0.022}$	0.211 ± 0.018
6	$\mathcal{B}(\bar{B}_s^0 \to D_s^- D_s^+)$	4.7 ± 0.6	4.4 ± 0.6	4.4 ± 0.5
7	$\mathcal{B}(\bar{B}^0 \to D_s^- D_s^+)$	$0.024^{+0.013}_{-0.020}$	≤ 0.036	≤ 0.036
8	$\mathcal{B}(\bar{B}_s^0 \to D^- D^+)$	$0.204^{+0.036}_{-0.033}$	$0.24^{+0.06}_{-0.05}$	0.22 ± 0.06
9	$\mathcal{B}(\bar{B}^0 \to \bar{D}^0 D^0)$	0.013 ± 0.006	0.012 ± 0.006	0.014 ± 0.007
10	$\mathcal{B}(\bar{B}_s^0 \to \bar{D}^0 D^0)$	$0.203^{+0.036}_{-0.033}$	$0.166^{+0.042}_{-0.037}$	0.19 ± 0.05

TABLE 6.10: Predicted branching ratios in units of 10^{-3} from both our global fit (second column) and our fit without theory input from Sec. 6.3 (third column), compared with global values from the PDG [14] (fourth column). Taken from Ref. [3].

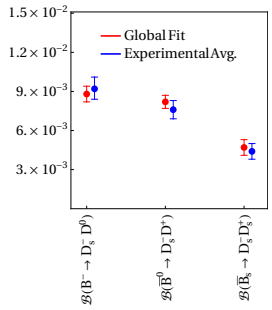

(A) $b \to s$ T-dominated.

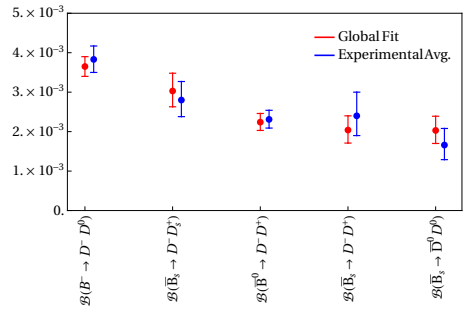

(B) $b \to d$ T- and $b \to s$ A^c-dominated.

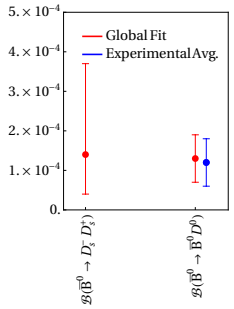

(C) $b \to d$ A^c-dominated

FIGURE 6.9: Branching ratio predictions from the global fit compared to those obtained from our experiment-only fit, as shown in Table 6.10. Taken from Ref. [3].

and

$$\Gamma(\bar{B}_s^0 \to \bar{D}^0 D^0) = \Gamma(\bar{B}_s^0 \to D^- D^+)(1 + \mathcal{O}(\bar{\lambda}^2 \epsilon^2)), \tag{6.53}$$

where some small isospin-breaking contributions have been neglected. These match those determined in the earlier partial analysis of Ref. [262].

Precision measurements of these rates allow for tests for BSM physics with $\Delta I = 1$ or alternatively isopsin breaking in the rates if the SM is assumed. Equally, in the case of

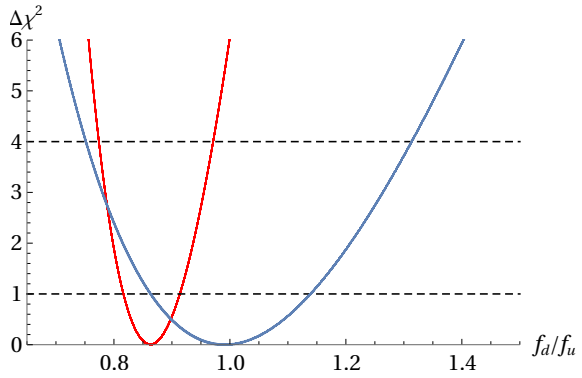

FIGURE 6.10: One-dimensional scans of the parameter f_d/f_u in the case of the full global fit (red) and without theoretical input (blue).

the first relation, one may uncover isospin breaking through a non-unity determination of the ratio of production fractions for $B^\pm$ and B^0, i.e. f_d/f_u at the LHC and f_{+-}/f_{00} at Belle (II).

The experimental value of the ratio

$$\frac{\Gamma_{\bar{B}^0\to D_s^- D^+}}{\Gamma_{B^-\to D_s^- D^0}} = 0.88 \pm 0.05$$

in Table 6.8, assumes $f_d/f_u = 1$, and so Eq. (6.52) means that in the global fit we have

$$(f_d/f_u)^{\text{LHCb, 7 TeV}} = 0.86 \pm 0.05\,.$$

This deviates substantially ($\sim 2.5\sigma$) from the frequently-assumed value of unity. While this tension can be reduced by loosening constraints on A_1^u, it cannot be completely removed; even with $|A_1^u/T| \sim 1$ there remains a deviation of $\sim 1.6\sigma$. A value of f_d/f_u that is non-unity would have serious implications for many LHCb measurements that rely on ratios of B^0 and B_s^0. For example, $\mathcal{B}(\bar{B}_{(s)} \to \mu^+\mu^-)$ uses $B^+ \to J/\psi K^+$ as normalisation mode and involves the production fraction ratio f_s/f_u, which is taken to be equal to f_s/f_d [263,264]. In order to disentangle $f_d/f_u \neq 1$ and $\Gamma(\bar{B}^0 \to D_s^- D^+)/\Gamma(B^- \to D_s^- D^0) \neq 1$, it is important that further determinations of f_d/f_u are made at LHCb with additional data and different decays, such as $\Gamma(B^0 \to J/\psi K^0)/\Gamma(B^+ \to J/\psi K^+)$, making use of precision measurements from Belle(II). There is a similar situation for CMS analyses, like $\mathcal{B}(\bar{B}_{(s)} \to \mu^+\mu^-)$ [263,265], though Ref. [227] found $(f_d/f_u)^{\text{CMS}}$ to be compatible with unity at 13 TeV. This ratio would generally be expected to be different from that of LHCb, since other production fractions display p_T-dependence. Figure 6.10 shows the constraining power of theoretical assumptions on the one-dimensional scans for f_d/f_u.

Since the initial states in the second relation are identical, this one may be used to test the relative detection efficiencies of $D^\pm$ and D^0. These relations also appear "for free" within the global fit, where they also gain from information from other observables in the fit such as production fractions and relative decay rates. As a test of Eq. (6.53), one

can calculate the corresponding ratio

$$\frac{\Gamma_{\bar{B}_s^0 \to \bar{D}^0 D^0}}{\Gamma_{\bar{B}_s^0 \to D^- D^+}} = 0.69^{+0.25}_{-0.18},$$

which has a central value that deviates considerably from unity, but this is only significant at $\sim 1\sigma$.

The quasi-isospin relations above benefit from the fact that the $\Delta I = 1$ contributions that break the symmetry for these $b \to s$ transitions are significantly suppressed by CKM factors. A similar scenario exists for the $\Delta I = 3/2$ contributions in $b \to d$ transitions, but here the suppression is reduced by a factor of $\bar{\lambda}^2$, and so the sum rules receive larger corrections:

$$\frac{\Gamma(\bar{B}^0 \to D^- D^+)}{\Gamma(B^- \to D^- D^0)} = 1 + \mathcal{O}(\epsilon^{3/2}) = 0.65^{+0.09}_{-0.08}. \tag{6.54}$$

This correction would be expected to correspond to $2\mathrm{Re}(A^c)/T$, and so this emphasises the sizeable annihilation amplitude $|\mathrm{Re}(A^c)/T| \sim 18\%$ noted before (see also Ref. [9]). It is therefore clear that improved measurements of $B \to DD'$ branching fractions have a big part to play in testing the SM. The near future looks promising for this, since LHCb is yet to produce measurements for many of the observables for Run 2, and Belle II is yet to produce an analysis of $B \to DD'$.

6.6.3 CP Asymmetries

Through our methodology, it's possible to make predictions for CP asymmetries that are currently unmeasured and improve predictions for those with experimental inputs, due to the non-trivial correlations between observables that is encoded by our parameterisation and power counting. These correlations are particularly strong between CP asymmetries and corresponding branching ratios and between observables related by U-spin symmetry. Through this, we are able to check the consistency of the SM. Table 6.11 and Figures 6.11 and 6.12 summarise the predictions from one-dimensional scans of the CP asymmetries for all the channels of interest. The correlations between these predictions are visualised in Figure 6.13, as well as in Figure 6.14.

With the majority of the CP asymmetries currently unmeasured, in several cases the predictions are constrained predominantly by power-counting (where the branching ratio information is suppressed) and so the shape of the χ^2 around the global minimum appears rather flat when these observables are varied. This deviates from Gaussianity, which would give an approximately quadratic shape. For this reason, in Table 6.11 the results are displayed in terms of $\Delta\chi^2 = 1$ (analogous to a 68% Gaussian confidence interval) so as to not imply that results are at all Gaussian-distributed. This point is especially relevant for the scenario where no CP information is included.

These predictions agree with the experimental values within 2σ and the topological

Mode	Global fit	w/o CP inputs	Exp.
		$A_{CP}(\%)$	
$B^- \to D^- D^0$	[1.2,3.1]	$[-34.0, 34.0]$	2.4 ± 1.1
$B^- \to D_s^- D^0$	[-0.2, 0.3]	$[-1.6, 1.6]$	0.5 ± 0.6
$\bar{B}^0 \to D_s^- D^+$	[-0.8, 0.6]	$[-0.8, 0.8]$	
$\bar{B}_s^0 \to D^- D_s^+$	[-9.3, 18.1]	$[-18.6, 18.6]$	
$\bar{B}^0 \to D^- D^+$	[-3.5, 25.3]	$[-28.2, 28.2]$	13 ± 17
$\bar{B}_s^0 \to D_s^- D_s^+$	[-1.3, 0.7]	$[-1.4, 1.4]$	-8 ± 18
$\bar{B}^0 \to D_s^- D_s^+$	[-43.0,45.1]	[-60.4, 60.4]	
$\bar{B}_s^0 \to D^- D^+$	[-1.5, 1.5]	$[-1.6, 1.6]$	
$\bar{B}^0 \to \bar{D}^0 D^0$	[-62.7,61.3]	$[-64.7, 64.7]$	
$\bar{B}_s^0 \to \bar{D}^0 D^0$	[-3.1,3.1]	$[-3.3, 3.3]$	
		$S_{CP}(\%)$	
$B^- \to D^- D^0$	–	–	–
$B^- \to D_s^- D^0$	–	–	–
$\bar{B}^0 \to D_s^- D^+$	–	–	–
$\bar{B}_s^0 \to D^- D_s^+$	–	–	–
$\bar{B}^0 \to D^- D^+$	[-87.2, -60.4]	$[-87.9, -46.7]$	-81 ± 20
$\bar{B}_s^0 \to D_s^- D_s^+$	[2.9, 5.0]	$[2.3, 5.0]$	-2 ± 17
$\bar{B}^0 \to D_s^- D_s^+$	[-94.2, -31.0]	$[-99.0, -15.1]$	
$\bar{B}_s^0 \to D^- D^+$	[2.1, 5.2]	$[2.1, 5.3]$	
$\bar{B}^0 \to \bar{D}^0 D^0$	[-99.3,-11.7]	[-99.5,-8.1]	
$\bar{B}_s^0 \to \bar{D}^0 D^0$	[0.5,6.8]	$[0.4, 6.9]$	

TABLE 6.11: Fitted CP asymmetries coming from both the global fit (column two) and the fit without experimental CP asymmetry input data (column three), compared to the available experimental measurements. As discussed in the text, many observables showed non-Gaussianity and so we quote the 68% confidence intervals without central values for our predictions. Taken from Ref. [3].

amplitudes did not appear to be significantly pulled towards values outside the constraints we impose from power counting, which again justifies our assumptions. Furthermore, the quality of our fit at the global minimum is good, with $\chi^2_{\text{min}} = 8.6$ almost equal to the number of degrees of freedom ($43 - 35 = 8$). It should be noted, though, that 10 of these parameters were not constrained much beyond the power counting assumptions we directly impose; without them, the minimum χ^2 only increases by 0.7. These parameters were included for generality and to ensure our predictions are conservative. For example, since current experimental uncertainties for the annihilation-dominated modes are large, the SU(3)$_F$-breaking contributions to A^c cannot be well constrained. Setting their values to zero, however, would lead to predicted branching ratios with greatly underestimated uncertainties.

With the current status of experimental measurements, only five topological amplitudes are strictly necessary to describe all available measurements in the fit. These are the leading tree amplitude, the sizeable real part of the annihilation amplitude discussed previously, the (real) SU(3)$_F$-breaking contributions to the leading T amplitude, and a contribution to $A_{CP}(B^- \to D^- D^0)$ (e.g. $\mathcal{I}m(\tilde{P}_1)$). None of these reach their maximal values from the constraints of our power counting. As more precise measurements become available, this situation will change somewhat, and the inclusion of all parameters will

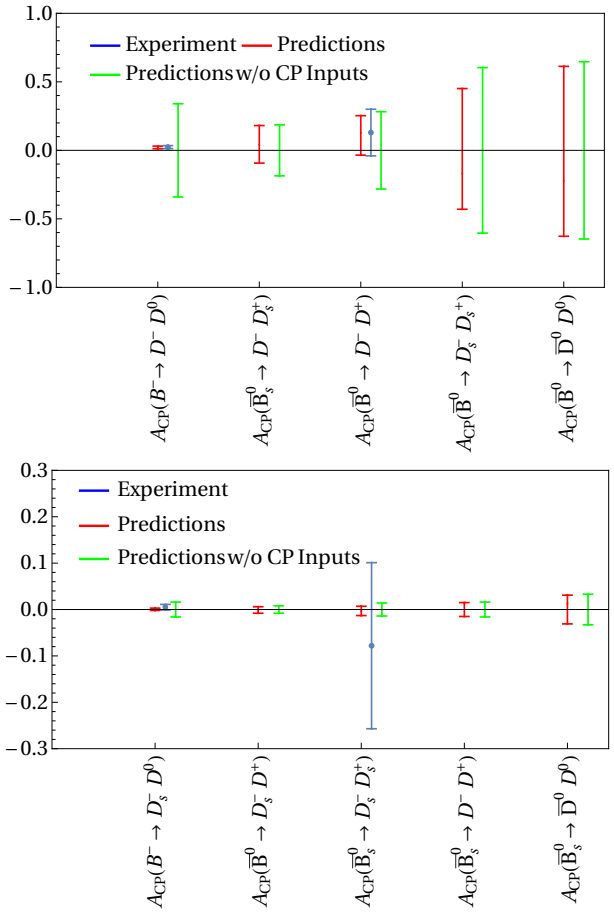

FIGURE 6.11: A_{CP} predictions compared with the latest experimental values for a) $b \to d$ and b) $b \to s$ transitions. Taken from Ref. [3].

become obligatory.

Impact of Measurements

Examining Figure 6.14, we find that, by comparing to the "plain theory" prediction, which relies solely on power counting and no experimental data, the information from measured branching ratios considerably constrains the available parameter space for the CP asymmetries. Including the available CP asymmetry inputs then constrains the system further. Indeed, the constraining effect of CP asymmetry measurements for the charged B decays and $\bar{B}^0 \to D^- D^+$ is clear in Figures 6.11 and 6.12. $\bar{B}^0_s \to D_s^+ D_s^-$ is an exception to this and will be discussed separately later.

These few measurements alone allow the global fit to further constrain most of the CP asymmetries with respect to the information from the branching-ratio-only fit, as can be seen by comparing the red and green ranges. $A_{CP}(B^- \to D^- D^0)$ in particular shows the dramatic improvement we have from constraining penguin pollution with our method. As seen in the top-middle of Figure 6.13 and the zoomed-in 1D scan in Figure 6.15, $A_{CP}(B^- \to D_s^- D^0)$ is significantly more strongly constrained in the global fit

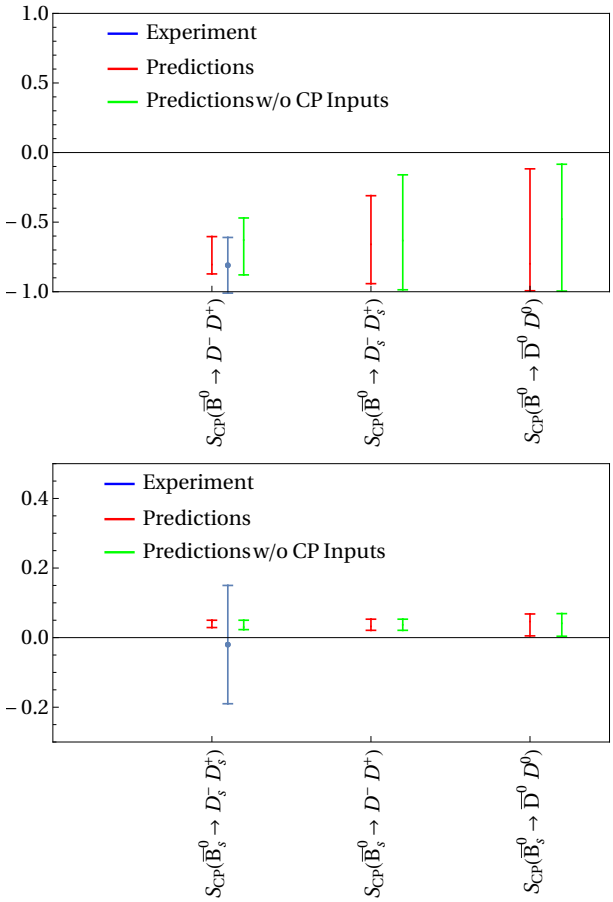

FIGURE 6.12: S_{CP} predictions compared with the latest experimental values for a) $b \to d$ and b) $b \to s$ transitions. Taken from Ref. [3].

than by its measurement, despite having been measured more precisely than our extraction from branching ratio inputs alone. This is due to its correlation with $B^- \to D^- D^0$, and such connections between $b \to d$ and $b \to s$ transitions apply for other SU(3)$_F$ partners, especially for U-spin partners. When CP asymmetry measurements for more of the channels become available, any future CP asymmetries measured to be outside the ranges given in Table 6.11 or Figures 6.11 and 6.12 would indicate BSM physics and not a misunderstanding of hadronic effects, since our assumptions of power counting have been shown to be very conservative.

Time-dependent CP asymmetry in $\bar{B}_s^0 \to D_s^+ D_s^-$

This observable was a key motivator for the use of $B \to DD'$ decays, as explained in Section 6.1, since ϕ_s can be determined very cleanly. Neglecting $\mathcal{A}_u$ terms, one finds the approximate relations

$$S_{CP}(\bar{B}_s^0 \to D_s^- D_s^+) = -\sin(\phi_s) \qquad \text{and} \qquad A_{CP}(\bar{B}_s^0 \to D_s^- D_s^+) = 0. \tag{6.55}$$

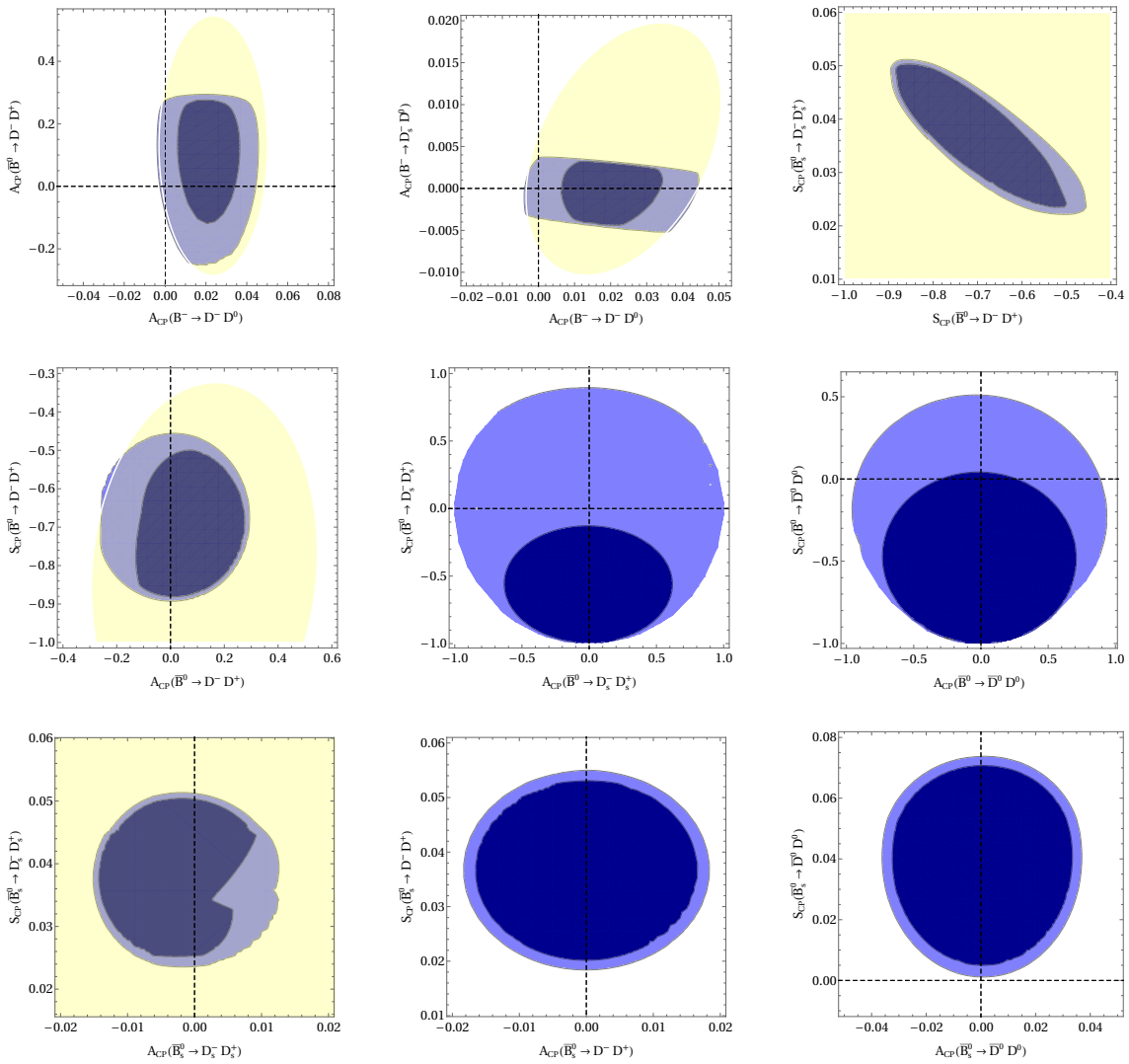

FIGURE 6.13: Two-dimensional theory predictions for CP asymmetries from the global fit at 68% ($\Delta\chi^2 = 2.30$, dark blue) and 95% CL ($\Delta\chi^2 = 5.99$ light blue), compared to the experimental data at 95% confidence-level(light yellow) if available. Taken from Ref. [3].

Corrections to these relations can be found with reference to Tables 6.3 and 6.9, the largest contribution being [3]

$$\Delta S(\bar{B}_s^0 \to D_s^- D_s^+) \sim \bar{\lambda}^2 \epsilon^{2.5} \lesssim 1\% \,. \tag{6.56}$$

The power of our methodology becomes apparent here since one can relate this mode to the corresponding $b \to d$ one, i.e. $\bar{B}^0 \to D^- D^+$ [9, 218, 252, 266, 267]. This can provide further constraining power when the global fit is applied and manage such corrections.

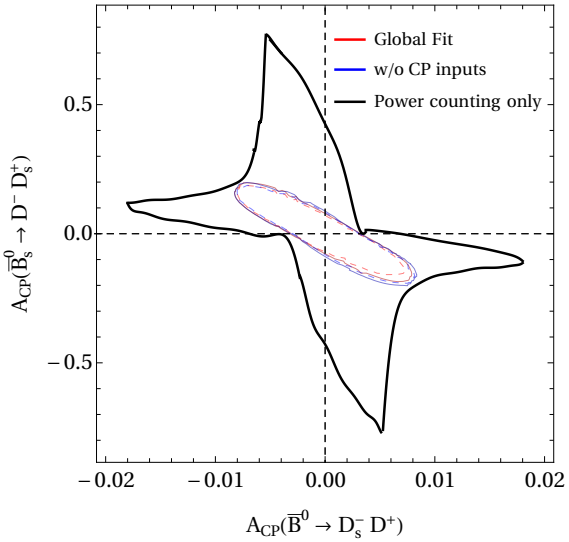

FIGURE 6.14: Correlation between $A_{CP}(\bar{B}^0 \to D_s^- D^+)$ and $A_{CP}(\bar{B}_s^0 \to D^- D_s^+)$ as illustration of the impact of different experimental inputs on the fit, taken from Ref. [3]. We show the global fit result at 68% CL (red-dashed) and 95% CL (red-solid), the fit w/o CP inputs at 68% CL (blue-dashed) and 95% CL (blue-solid) as well as the constraints from power counting only without any experimental inputs (black-solid).

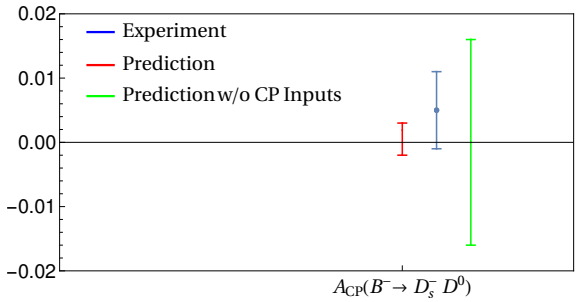

FIGURE 6.15: Zoomed-in one-dimensional bounds on $A_{CP}(B^- \to D_s^- D^0)$ from fits and from experiment.

With an external input of the mixing phase ϕ_d, and making use of the fact that ϕ_s is small, one can arrive at the following approximate formula; [3]

$$\sin(\phi_s) \approx -\left[S_{CP}(\bar{B}_s^0 \to D_s^- D_s^+) + \frac{\bar{\lambda}^2}{\cos(\phi_d)}\left(S_{CP}(\bar{B}^0 \to D^- D^+) + \sin(\phi_d)\right)\right], \quad (6.57)$$

which receives corrections of $\mathcal{O}(\bar{\lambda}^2\epsilon^{3.5})$. There is a similar relation between $\bar{B}^0 \to J/\psi K_S$ and $\bar{B}^0 \to J/\psi\pi^0$ [219] (see also Ref. [268]), though this is simpler, involving only a single mixing phase. With additional SU(3)$_F$ correction terms, this relation is implicitly included in the global fit, where using an external input for ϕ_s leads to greatly improved precision for $S_{CP}(\bar{B}_s^0 \to D_s^- D_s^+)$ (and the corresponding A_{CP} in turn). In future, when experimental precision on CP violation in this channel is improved, it may be possible to remove the

external input for ϕ_s, and instead predict it, using Eq. (6.57). Such an extraction using a fit similar to the one described here would have negligible theory uncertainties and even account for the small penguin pollution.

These statements for $\bar{B}_s^0 \to D_s^- D_s^+$ are also valid for CP asymmetries in other $b \to s$ transitions (see Table 6.9). Of particular note is the fact that there is yet to be a test of a CP asymmetry for an annihilation-dominated mode, which would constitute a New Physics test complementary to the tree-dominated modes.

6.6.4 Future Measurements

The need for further CP asymmetries in $B \to DD'$ decays is clear. An example of this is the current lack of constraint for $A_{CP}(\bar{B}^0 \to D^- D^+)$ in the global fit. This direct asymmetry, coming from interference of $\mathcal{A}_c$ diagrams with $\mathcal{A}_u$ diagrams, has one dominant contribution, namely T with $\tilde{P}_1$. This mode is then correlated with $B^- \to D^- D^0$ (measured to $\sim 1\%$), which shares this contribution but also receives a second contribution, at the same order, from interference of T with A_u^1. This has the result that the correlation, and so the constraint, is weakened, as is evident from a comparison of the first two plots on the top line of Figure 6.13. Measurement of the direct CP asymmetry for $\bar{B}_s^0 \to D^- D_s^+$ would allow this second contribution to be constrained separately, leading to improved precision for $A_{CP}(\bar{B}^0 \to D^- D^+)$ and other modes.

The ranges in Figures 6.11, 6.12 and two-dimensional correlation plots in Figure 6.13 show that much progress can still be made to constrain the allowed parameter space for the measurements. Most of the CP asymmetries are yet to be measured experimentally. In particular, there are currently no values for annihilation-dominated modes, leaving much potential for new physics to be uncovered here, since we are currently insensitive to any BSM contributions here. What's more, since the precision of the predictions for the $b \to d$ modes is relatively low, any experimental measurements in these channels would have a noticeable effect on the global fit. The connection, via relations shown above, to corresponding $b \to s$ modes, whose SM contributions are well understood, means that any BSM contributions could become quite evident.

In summary, we have confirmed that our methodology is sufficiently conservative so as to not over-constrain the system but equally has predictive power and can tell us new things about the status of the SM in this sector. Of course, additional and more precise future measurements of both branching fractions and CP asymmetries in $B \to DD'$ will mean this analysis will only improve. Our analysis has demonstrated the power of symmetry parameterisation for probing new physics, which is by no means specific to $B \to DD'$. The next chapter describes a similar approach that was taken to investigate the $B \to Dh$ tensions presented in Chapter 4.

7

B → Dh Phenomenology

"Just when the caterpillar thought the world was ending, he turned into a butterfly."

- Anonymous Proverb

7.1 Introduction

As discussed in Chapter 4, predictions from QCD factorisation (QCDF) for branching ratios of $B^0_{(s)} \to D_{(s)}h$, $h = \{\pi, K, \rho, K^*\}$ significantly disagree with experimental measurements [58, 59]. There has, therefore, been much recent interest in these decays, both theoretically [206–213] and experimentally [194, 269–272]. Anomalies have also been seen [214–217] in other hadronic B decays. Some of the largest discrepancies are shown by $\bar{B}^0_s \to D^+_s \pi^-$, as discussed in Chapter 4, and $\bar{B}^0 \to D^+ K^-$. Both modes are considered to be "theoretically clean", since they're dominated by colour-allowed tree topologies and lack contributions from penguin or annihilation processes (as introduced in Chapter 6), and so QCDF would have been expected to hold well in these cases. Consistency with experimental data is, however, seen for ratios of these branching ratios,

$$\mathcal{R}^{P(V)}_{s/d} = \frac{\mathcal{B}(\bar{B}^0_s \to \pi^- D^{(*)+}_s)}{\mathcal{B}(\bar{B}^0 \to K^- D^{(*)+})}, \tag{7.1}$$

as noted in Ref. [58], which would suggest that any BSM effects are common to all $b \to c\bar{u}q$ weak transitions.

If BSM effects were confirmed to be present in these channels, this would have substantial physics implications. The "clean" nature of these transitions means that they already play a key role in measurements of CP-violation in the SM, notably interference between the amplitudes of $b \to c\bar{u}s$ and $b \to u\bar{c}s$ allow a very clean extraction of the CKM phase γ within the SM, with a theoretical uncertainty of $< 10^{-7}$ [273]. Indeed, $B^\pm \to D^0 K^\pm$ is often described as an SM "golden" mode for measurements of this phase [274–278]. Model-independent constraints [279] on BSM contributions in these

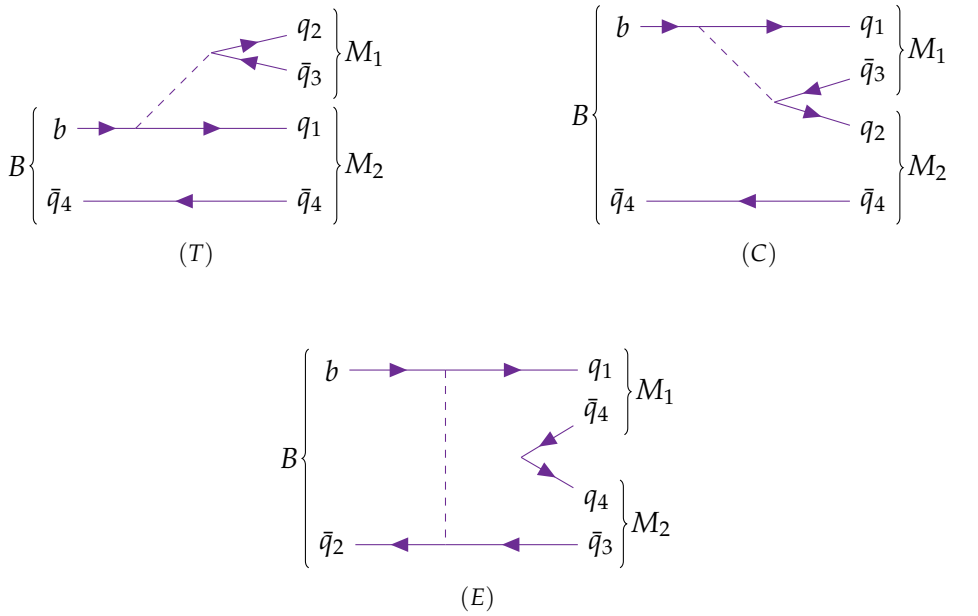

FIGURE 7.1: Topological amplitudes for $B \to Dh$ decays. Figure adapted from Ref. [262].

modes permit possible deviations of as much as 10° from the SM in direct experimental extractions of this phase. This is to be compared with an uncertainty of $\sim 5°$ [37] in LHCb's current, global, direct experimental determination, which assumes the SM, a value expected to reduce to $\sim 0.35°$ with the final data set of LHCb Upgrade II [280].

There is much existing literature on $B \to Dh$ decays, with past studies including; sensitivity to mixing phases and γ [281–283], rescattering effects [210, 284–286], QCD factorisation and soft-collinear effective theory (SCET) [58, 59, 90, 287–289], the factorisation-assisted topological (FAT) approach [290], SU(3)$_F$ methods [224, 262, 291–307] including plain SU(3)$_F$ fits [293, 297, 308], and new physics sensitivities [209]. This problem can be tackled in a similar way to that of the $B \to DD'$ decays by examining the consistency of the SU(3)$_F$ expansion, and I performed such a study in Ref. [4], the details of which are elaborated in this chapter.

7.2 Theoretical parameterisation

7.2.1 Topological Amplitudes

As in the previous chapter, Table 7.1 gives the decomposition of the amplitudes for the decays of interest into topological diagrams, both SU(3)$_F$-conserving (T, C, E) and $SU(3)_F$-breaking (T_1, T_2, C_1, C_2, E_1, E_2), using the parameterisation from Ref. [262]. Figure 7.1 shows how these SU(3)$_F$-conserving diagrams are defined, while the breaking terms can be deduced in a similar way to before. As before, we are free to choose T to be real and positive, and since our interest will be primarily restricted to the parameters themselves, here we consider a parameterisation in terms of magnitudes and phases. We then have

the following fit parameters:

$$T\,,\ |C/T|\,,\ |E/T|\,,\ |T_1/T|\,,\ |T_2/T|\,,\ |C_1/C|\,,\ |C_2/C|\,,\ |E_1/E|\,,\ |E_2/E|\,,$$
$$\phi_C\,,\ \phi_E\ \phi_{T_1}\,,\ \phi_{T_2}\,,\ \phi_{C_1}\,,\ \phi_{C_2}\,,\ \phi_{E_1}\,,\ \phi_{E_2}\,,$$

with

$$\phi_C \equiv \arg(C/T)\,,\ \phi_E \equiv \arg(E/T)\,,\ \phi_{T_i} \equiv \arg(T_i/T)\,,$$
$$\phi_{C_i} \equiv \arg(C_i/T)\,,\ \phi_{E_i} \equiv \arg(E_i/T)\,.$$

We also consider the expected relative sizes of these parameters, similar to the power counting applied in Chapter 6, and use this information to constrain the system. We, once again, assume that $SU(3)_F$-breaking parameters are suppressed by a single power of the counting parameter δ_X, i.e.

$$|T_i/T| \leq \delta_X, \quad |C_i/C| \leq \delta_X, \quad |E_i/E| \leq \delta_X.$$

As before, the default value for δ_X was 0.3. Ref. [262] suggests the hierarchy $|C/T| \sim \delta_X$, $|E/T| \sim \delta_X^2$. To be on the conservative side, we chose not to impose such constraints but did then evaluate the compatibility of such assumptions with the data. As in the previous chapter, Eq. (2.89) can be used to convert these amplitudes into measurable branching ratios and the CKM elements are considered under the Wolfenstein expansion:

$$\lambda_d \equiv V_{cb}V_{ud}^* = A\lambda^2(1-\lambda^2/2), \quad \lambda_s \equiv V_{cb}V_{us}^* = A\lambda^3\,. \tag{7.2}$$

7.2.2 Isospin Decomposition

We can also decompose the decay amplitudes according to isospin, as performed in Ref. [262]:

$$A_{\pi D}^{-0} \equiv A(B^- \to \pi^- D^0) = A_{3/2}\,, \tag{7.3}$$
$$A_{\pi D}^{-+} \equiv A(\bar{B}^0 \to \pi^- D^+) = \frac{2}{3}A_{1/2} + \frac{1}{3}A_{3/2}\,, \tag{7.4}$$
$$A_{\pi D}^{00} \equiv A(\bar{B}^0 \to \pi^0 D^0) = -\frac{\sqrt{2}}{3}A_{1/2} + \frac{\sqrt{2}}{3}A_{3/2}\,, \tag{7.5}$$

and

$$A_{KD}^{-0} \equiv A(B^- \to K^- D^0) = A_1\,, \tag{7.6}$$
$$A_{KD}^{-+} \equiv A(\bar{B}^0 \to K^- D^+) = \frac{1}{2}A_1 + \frac{1}{2}A_0\,, \tag{7.7}$$
$$A_{KD}^{00} \equiv A(\bar{B}^0 \to \bar{K}^0 D^0) = \frac{1}{2}A_1 - \frac{1}{2}A_0\,. \tag{7.8}$$

$\mathcal{A}(\mathcal{D})$	T	C	E	T_1	T_2	C_1	C_2	E_1	E_2
$\sim V_{cb}V_{ud}^* = \mathcal{O}(\lambda^2)$									
$B^- \to \pi^- D^0$	-1	-1	0	0	0	0	0	0	0
$\bar{B}^0 \to \pi^- D^+$	-1	0	-1	0	0	0	0	0	0
$\bar{B}^0 \to \pi^0 D^0$	0	$-\frac{1}{\sqrt{2}}$	$\frac{1}{\sqrt{2}}$	0	0	0	0	0	0
$\bar{B}^0 \to K^- D_s^+$	0	0	-1	0	0	0	0	0	-1
$\bar{B}_s^0 \to K^0 D^0$	0	-1	0	0	0	0	-1	0	0
$\bar{B}_s^0 \to \pi^- D_s^+$	-1	0	0	0	-1	0	0	0	0
$\sim V_{cb}V_{us}^* = \mathcal{O}(\lambda^3)$									
$B^- \to K^- D^0$	-1	-1	0	-1	0	-1	0	0	0
$\bar{B}^0 \to K^- D^+$	-1	0	0	-1	0	0	0	0	0
$\bar{B}^0 \to \bar{K}^0 D^0$	0	-1	0	0	0	-1	0	0	0
$\bar{B}_s^0 \to \pi^- D^+$	0	0	-1	0	0	0	0	-1	0
$\bar{B}_s^0 \to \pi^0 D^0$	0	0	$\frac{1}{\sqrt{2}}$	0	0	0	0	$\frac{1}{\sqrt{2}}$	0
$\bar{B}_s^0 \to K^- D_s^+$	-1	0	-1	-1	-1	0	0	-1	-1

TABLE 7.1: Summary of $B \to Dh$ amplitude decomposition, as found in Ref. [262].

These were also parameterised according to magnitudes and phases, explicitly

$$|A_{1/2}|, |A_{3/2}|, \cos(\arg(A_{1/2}/A_{3/2})) \quad \text{and} \quad |A_0|, |A_1|, \cos(\arg(A_0/A_1))$$

for the two systems. In such a simplified scenario, it is straightforward to solve these systems of equations to give, for the first set [303],

$$\left|\frac{A_{1/2}}{A_{3/2}}\right| = \sqrt{\frac{3\left|A_{\pi D}^{-+}\right|^2 + 3\left|A_{\pi D}^{00}\right|^2 - \left|A_{\pi D}^{-0}\right|^2}{2\left|A_{\pi D}^{-0}\right|^2}}, \tag{7.9}$$

$$\cos\left(\arg\left(\frac{A_{1/2}}{A_{3/2}}\right)\right) = \frac{3\left|A_{\pi D}^{-+}\right|^2 + \left|A_{\pi D}^{-0}\right|^2 - 6\left|A_{\pi D}^{00}\right|^2}{2\sqrt{2}\left|A_{\pi D}^{-0}\right|\sqrt{3\left|A_{\pi D}^{-+}\right|^2 + 3\left|A_{\pi D}^{00}\right|^2 - \left|A_{\pi D}^{-0}\right|^2}}, \tag{7.10}$$

and for the second set [304]

$$\left|\frac{A_0}{A_1}\right| = \sqrt{\frac{2\left|A_{KD}^{-+}\right|^2 + 2\left|A_{KD}^{00}\right|^2 - \left|A_{KD}^{-0}\right|^2}{\left|A_{KD}^{-0}\right|^2}}, \tag{7.11}$$

$$\cos\left(\arg\left(\frac{A_0}{A_1}\right)\right) = \frac{\left|A_{KD}^{00}\right|^2 - \left|A_{KD}^{-+}\right|^2}{\left|A_{KD}^{-0}\right|\sqrt{2\left|A_{KD}^{-+}\right|^2 + 2\left|A_{KD}^{00}\right|^2 - \left|A_{KD}^{-0}\right|^2}}. \tag{7.12}$$

7.2.3 Measures of SU(3)$_F$ Breaking

In addition to parameterising SU(3)$_F$-breaking contributions in terms of the contributions

$$|T_1/T|, |T_2/T|, |C_1/C|, |C_2/C|, |E_1/E|, |E_2/E|,$$

one can also measure SU(3)$_F$ breaking in a parameterisation-independent way by testing known SU(3)$_F$ sum rules [262]. For two amplitudes, A_1 and A_2, that are expected to be equal according to a sum rule, one can use the splitting around their average value [4]

$$\begin{aligned}\varepsilon(A_1/A_2) &\equiv \left|\frac{|A_1| - \frac{1}{2}(|A_1| + |A_2|)}{\frac{1}{2}(|A_1| + |A_2|)}\right| = \left|\frac{|A_1| - |A_2|}{|A_1| + |A_2|}\right| \\ &= \left|\frac{1 - |A_1/A_2|}{1 + |A_1/A_2|}\right| .\end{aligned} \tag{7.13}$$

These splittings are clearly symmetric i.e. $\varepsilon(A_1/A_2) = \varepsilon(A_2/A_1)$ and the sum rules can then be converted into appropriate ratios [4]

$$s_1 \equiv \frac{1}{\sqrt{2}} \frac{|A(\bar{B}_s^0 \to \pi^- D^+)|}{|A(\bar{B}_s^0 \to \pi^0 D^0)|} , \tag{7.14a}$$

$$s_2 \equiv \frac{|A(\bar{B}^0 \to K^- D_s^+)|/|\lambda_d|}{|A(\bar{B}_s^0 \to \pi^- D^+)|/|\lambda_s|} , \tag{7.14b}$$

$$s_3 \equiv \frac{|A(B^- \to \pi^- D^0)|/|\lambda_d|}{|A(B^- \to K^- D^0)|/|\lambda_s|} , \tag{7.14c}$$

$$s_4 \equiv \frac{|A(\bar{B}^0 \to \pi^- D^+)|/|\lambda_d|}{A(\bar{B}_s^0 \to K^- D_s^+)|/|\lambda_s|} , \tag{7.14d}$$

$$s_5 \equiv \frac{|A(\bar{B}_s^0 \to K^0 D^0)|/|\lambda_d|}{|A(\bar{B}^0 \to \bar{K}^0 D^0)|/|\lambda_s|} , \tag{7.14e}$$

$$s_6 \equiv \frac{|A(\bar{B}_s^0 \to \pi^- D_s^+)|/|\lambda_d|}{|A(\bar{B}^0 \to K^- D^+)|/|\lambda_s|} , \tag{7.14f}$$

where in the SU(3)$_F$ (including isospin) limit

$$s_i = 1 \quad \text{and} \quad \varepsilon_i \equiv \varepsilon(s_i) = 0 . \tag{7.15}$$

The size of the values of ε_i, therefore, indicates the degree of SU(3)$_F$ breaking. Ref. [262] shows sum rules that relate more than two decays, though these are not considered here.

Observable	Value	Ref.
$\sim V_{cb}V_{ud}^* = \mathcal{O}(\lambda^2)$		[14]
$\mathcal{B}(B^- \to \pi^- D^0)$	$(4.61 \pm 0.10) \cdot 10^{-3}$	[14]
$\mathcal{B}(\bar{B}^0 \to \pi^- D^+)$	$(2.51 \pm 0.08) \cdot 10^{-3}$	[14]
$\mathcal{B}(\bar{B}^0 \to \pi^0 D^0)$	$(2.67 \pm 0.09) \cdot 10^{-4}$	[14]
$\mathcal{B}(\bar{B}^0 \to K^- D_s^+)$	$(2.7 \pm 0.5) \cdot 10^{-5}$	[14]
$\mathcal{B}(\bar{B}_s^0 \to K^0 D^0)$	$(4.3 \pm 0.9) \cdot 10^{-4}$	[14]
$\mathcal{B}(\bar{B}_s^0 \to \pi^- D_s^+)$	$(2.98 \pm 0.14) \cdot 10^{-3}$	[14]
$\sim V_{cb}V_{us}^* = \mathcal{O}(\lambda^3)$		[14]
$\mathcal{B}(B^- \to K^- D^0)$	$(3.64 \pm 0.15) \cdot 10^{-4}$	[14]
$\mathcal{B}(\bar{B}^0 \to K^- D^+)$	$(2.05 \pm 0.08) \cdot 10^{-4}$	[14]
$\mathcal{B}(\bar{B}^0 \to \bar{K}^0 D^0)$	$(5.2 \pm 0.7) \cdot 10^{-5}$	[14]
$\mathcal{B}(\bar{B}_s^0 \to \pi^- D^+)$	n.a.	-
$\mathcal{B}(\bar{B}_s^0 \to \pi^0 D^0)$	n.a.	-
$\mathcal{B}(\bar{B}_s^0 \to K^- D_s^+)$	$(1.94 \pm 0.21) \cdot 10^{-4}$	[211]

TABLE 7.2: Input $B \to Dh$ branching ratios from experiment. The modes involving the $\bar{B}_s^0$ meson required consideration of its width. See text for details.

7.3 Numerical Results

7.3.1 Experimental Inputs

Once again, our theoretical parameterisation can be confronted with experimental data and Table 7.2 summarises the input values used. Unlike for $B \to DD'$, we do not perform our own averaging but take the values directly from the PDG. Such an averaging could, though, be performed in future work on these decays. The B_s decays are, however, treated in the same way, accounting for the finite width difference between the mass eigenstates through an additional correction factor when comparing "theoretical" branching ratios at $t = 0$ with "experimental" time-integrated branching ratios. This effect applies differently to the different B_s modes under study:

- The effect on $\bar{B}_s^0 \to K^- D_s^+$ has already been studied in Ref. [211], which presents a "theoretical" value that is shifted by $\sim 14\%$ with respect to the "experimental" value of $\mathcal{B}(\bar{B}_s^0 \to K^- D_s^+) = (2.25 \pm 0.12) \cdot 10^{-4}$ [14, 309]. We take this "theoretical" value as input to our analysis.

- The decay $\bar{B}_s^0 \to \pi^- D_s^+$ is flavour-specific, and so the correction factor here is $1 - y_s^2$, as seen earlier. As $y_s^2 \sim 0.004$ is an order of magnitude smaller than the relative error on the measurements, one can comfortably neglect this additional effect.

- The decay channel $\bar{B}_s^0 \to K^0 D^0$ is not flavour-specific, since it can interfere with $B_s^0 \to \bar{K}^0 D^0$ through B_s and kaon mixing, though the latter channel is suppressed by a relative factor of $\mathcal{O}(\lambda^2)$ [262]. Again, considering the size of the relative error on this measurement ($\sim 20\%$), the width-difference effect is neglected for this analysis.

Parameter	Value
$\|C/T\|$	[0.39, 0.63]
$\|E/T\|$	[0.07, 0.16]
ϕ_C	$[-84,-64]^\circ$, $[64,84]^\circ$
ϕ_E	$[-165,-79]^\circ$, $[75,165]^\circ$
$\|T_1/T\|$	[0.10, 0.30]
$\|T_2/T\|$	[0.0, 0.3]
ϕ_{T_1}	$[-85,85]^\circ$
ϕ_{T_2}	$[-180.0,180.0]^\circ$
$\|C_1/C\|$	[0.00, 0.30]
$\|C_2/C\|$	[0.02, 0.30]
ϕ_{C_1}	$[-180.0,180.0]^\circ$
ϕ_{C_2}	$[-180,-22]^\circ$, $[22,180]^\circ$
$\|E_1/E\|$	[0.0, 0.3]
$\|E_2/E\|$	[0.0, 0.3]
ϕ_{E_1}	$[-180.0,180.0]^\circ$
ϕ_{E_2}	$[-180.0,180.0]^\circ$

TABLE 7.3: Numerical results for the SU(3)$_F$ parameters for $B \to Dh$ [4]. SU(3)$_F$ breaking is constrained not to exceed 30%, though the experimental inputs do not exclude more significant breaking. The χ^2 profiles are non-Gaussian and flat around the minimum. Entries in grey correspond to parameters not constrained by the fit. All strong phases are measured relative to the one of the tree diagram, whose phase is set to zero without loss of generality.

Using these inputs, we perform profiled scans of the respective observables, the results of which are shown in Table 7.3, where uncertainties were again obtained through profiled scans on this function. Since the system is under-constrained, with 17 parameters and only ten observables, the global minimum is at $\chi^2 = 0$, with a high degree of degeneracy. It should, however, be stressed that achieving $\chi^2 = 0$ is not a trivial result, due to the bounds that are placed on the parameters. Scans show non-Gaussianity, appearing flat around the minimum and then sharply increasing near parameter boundaries. T is, though, the dominant contribution to many of the decays and so is well-constrained, particularly by $\mathcal{B}(\bar{B}^0 \to \pi^- D^+)$; we find T in the range [14, 16] keV. From the above, there are several consistency checks:

$$\left|\frac{T+T_1}{T+T_2}\right| - 1 = \frac{|\lambda_d||\mathcal{A}(\bar{B}^0 \to K^- D^+)|}{|\lambda_s||\mathcal{A}(\bar{B}^0_s \to \pi^- D^+_s)|} - 1 = \mathcal{O}(2\delta_X) = [0.09, 0.18] \tag{7.16}$$

$$\left|\frac{C+C_1}{C+C_2}\right| - 1 = \frac{|\lambda_d||\mathcal{A}(\bar{B}^0 \to \bar{K}^0 D^0)|}{|\lambda_s||\mathcal{A}(\bar{B}^0_s \to K^0 D^0)|} - 1 = \mathcal{O}(2\delta_X) = [0.32, 0.73] \tag{7.17}$$

$$\left|\frac{E+E_1}{E+E_2}\right| - 1 = \frac{|\lambda_d||\mathcal{A}(\bar{B}^0_s \to \pi^- D^+)|}{|\lambda_s||\mathcal{A}(\bar{B}^0 \to K^- D^+_s)|} - 1 = \mathcal{O}(2\delta_X), \tag{7.18}$$

which are consistent for both T and C. Since neither $\mathcal{B}(\bar{B}^0_s(t=0) \to \pi^- D^+)$ nor $\mathcal{B}(\bar{B}^0_s(t =$

$0) \to \pi^0 D^0)$ have been experimentally determined, it is currently not possible to test the isospin relation for E_i, however one can obtain approximate predictions for these observables

$$\begin{aligned}\mathcal{B}(\bar{B}_s^0(t=0) \to \pi^- D^+) &= 2\mathcal{B}(\bar{B}_s^0(t=0) \to \pi^0 D^0) \\ &= [0.4, 6.0] \cdot 10^{-6}\,.\end{aligned} \tag{7.19}$$

Following the correction found for $\bar{B}_s^0 \to D_s^+ K^-$ in Ref. [211], we apply a relative 20% uncertainty to account for the effect of $\Delta\Gamma_s \neq 0$. We obtain

$$\begin{aligned}\mathcal{B}(\bar{B}_s^0 \to \pi^- D^+) &= 2\mathcal{B}(\bar{B}_s^0 \to \pi^0 D^0) \\ &= [0.3, 7.2] \cdot 10^{-6}\,.\end{aligned} \tag{7.20}$$

These small values help to explain why these branching ratios have not yet been measured.

7.3.2 $\mathbf{SU(3)_F}$ Limit Parameters

Clearly, future measurements of these unmeasured modes would improve the extracted bound on $|E/T|$. The data supports the expected scaling of $|E/T| \sim \mathcal{O}(\epsilon) \sim f_B/m_B$ [262]. The extracted 1σ range for $|E/T|$ roughly corresponds with the expectation from the approximate relation

$$\sqrt{\frac{\mathcal{B}(\bar{B}^0 \to K^- D_s^+)}{\mathcal{B}(\bar{B}^0 \to \pi^- D^+)}} \approx \left|\frac{E}{T}\right| \left(1 + \left|\frac{E_2}{E}\right| \cos(\phi_{E_2})\right), \tag{7.21}$$

and the imposed constraint $|E_2/E| < 0.3$.

Attempting a similar trick gives for C/T, plus breaking, a value of 0.42, though the situation here is more complicated due to experimental inputs for both $\mathcal{B}(\bar{B}_s^0 \to K^0 D^0)$ and $\mathcal{B}(\bar{B}^0 \to \bar{K}^0 D^0)$. There is also the approximate relation

$$\frac{\mathcal{B}(B^- \to \pi^- D^0)}{\mathcal{B}(\bar{B}^0 \to \pi^- D^+)} - 1 \approx 2|C/T| \cos(\phi_C) + |C/T|^2 = 0.86, \tag{7.22}$$

which provides a lower bound on $|C/T|$ (when $\phi_C = 0$) of 0.364 ($= -1 + \sqrt{1 + 0.86}$). The result from a profiled-χ^2 scan for $|C/T|$, with a 1σ lower bound of 0.39, is at the upper end of the expected scaling of $\sim 1/N_c$.

Our results for $|C/T|$ and $|E/T|$ including all first order corrections show consistency with Ref. [297], which extracts these parameters in the $\mathrm{SU(3)}_F$ limit, and Ref. [293], which accounts for partial $\mathrm{SU(3)}_F$-breaking effects, however we find larger errors for $|C/T|$ due to including such additional breaking parameters. The phases ϕ_C and ϕ_E are also considerable, which indicates possible large rescattering effects. The $B \to D\pi$ isospin amplitude ratio remains consistent with the limit estimate from heavy-quark expansion

Parameter	Value
$\lvert A_{1/2}/A_{3/2}\rvert$	0.69 ± 0.03
$\lvert\arg(A_{1/2}/A_{3/2})\rvert$	$(30^{+1}_{-2})^\circ$
$\lvert A_0/A_1\rvert$	0.72 ± 0.06
$\lvert\arg(A_0/A_1)\rvert$	$(51 \pm 4)^\circ$

TABLE 7.4: Numerical constraints for the isospin matrix elements.

Hypothesis	$\Delta\chi^2$	Δdof	Significance of rejection
$T_i = C_i = E_i = 0$	103.2	12	$> 5\sigma$
$T_i = C_i = 0$	91.4	8	$> 5\sigma$
$T_i = E_i = 0$	50.8	8	$> 5\sigma$
$C_i = E_i = 0$	12.5	8	1.5σ
$T_i = 0$	37.3	4	$> 5\sigma$
$C_i = 0$	12.0	4	2.4σ
$E_i = 0$	0.0	4	0σ

TABLE 7.5: Effect on global fit quality, $\Delta\chi^2$, of removing SU(3)$_F$ breaking from selected diagrams, compared to the nominal fit. In all cases, $\delta_X = 0.3$ is used. The corresponding significance of rejection for each hypothesis is shown, considering the number of degrees of freedom, Δdof, removed in each. Taken from Ref. [4].

methods [299]

$$|A_{1/2}/A_{3/2}| \overset{\text{HQ-limit}}{=} 1 + \mathcal{O}(\Lambda_{\text{QCD}}/m_c)\,. \tag{7.23}$$

with the full results of the isospin fit given in Table 7.4.

7.3.3 SU(3)$_F$ Breaking

As shown in Table 7.5, the scenario of complete SU(3)$_F$ symmetry of the system is rejected at more than 5σ, which is driven predominantly by the need for deviations with this same significance from the SU(3)$_F$ limit in the tree diagrams. Viewed another way, the scenario that the SU(3)$_F$ breaking comes solely from tree diagrams is consistent with data within 1.5σ. The currently available data gives 2.4σ evidence for SU(3)$_F$ breaking in C diagrams only but does not give any sensitivity to the same effect in E diagrams. With this said, the data does not require SU(3)$_F$ breaking of more than $\sim 20\%$ for an excellent description. This is true for both parameter-dependent or parameter-independent approaches to SU(3)$_F$ breaking, as can be seen from Figure 7.2 and Table 7.6. This is consistent with the findings of Refs. [58] and [224], which use a factorisation-based approach and estimate the breaking effect from decay constants as $f_K/f_\pi - 1 \sim 20\%$ [92]. See also Ref. [294]. There is no evidence of multiple SU(3)$_F$-breaking contributions accumulating in any of the measures we consider. A clear example of this is our quantity ϵ_4 (see Table 7.6), which compares $\bar{B}_s^{\,0} \to K^- D_s^+$, with numerous breaking contributions, to $\bar{B}^0 \to \pi^- D^+$, which has none. The data places a 1σ lower bound on $|T_1/T|$ at 0.1, driven primarily by the measurement of $\mathcal{B}(B^- \to K^- D^0)$. Conversely, the parameter $|T_2/T|$ does not have an

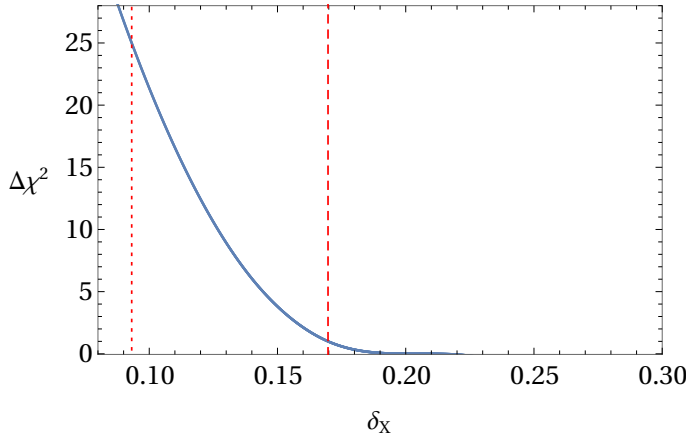

FIGURE 7.2: Effect on $\Delta\chi^2$ for varying degrees of allowed SU(3) breaking, δ_X. $\Delta\chi^2 = 1\,(25)$, i.e. $1\,(5)\sigma$, corresponds to $\delta_X = 0.17(0.09)$, indicated by the dashed (dotted) line, and $\Delta\chi^2 < 1 \times 10^{-3}$ is reached for $\delta_X > 0.2$. Figure taken from Ref. [4].

	$B \to Dh$
ε_1	–
ε_2	–
ε_3	0.10 ± 0.03
ε_4	0.10 ± 0.03
ε_5	0.20 ± 0.06
ε_6	0.06 ± 0.02

TABLE 7.6: Numerical results of tests of the $SU(3)_F$ sum-rules in Eq. (7.15), according to Eq. (7.13). In the $SU(3)_F$-limit, these should all evaluate to zero. The first two sum-rules remain untested due to missing experimental inputs. Taken from Ref. [4].

equivalent experimental input to determine its value, and so is hardly constrained in the fit. One might have expected that the measurement of $\mathcal{B}(\bar{B}_s^0 \to \pi^- D_s^+)$ could have given good sensitivity to this parameter, however this input is currently sufficiently similar to $\mathcal{B}(\bar{B}^0 \to \pi^- D^+)$, which constrains T, and so $|T_2/T| = 0$ is allowed. The phases of the $SU(3)_F$-breaking topologies cannot be constrained by our method with the available data.

7.4 Conclusions

Measurements of branching ratios of $\bar{B}^0_{(s)} \to D^{(*)+}_{(s)} h^-$, $h \in \{K, \pi\}$ have been recently found to be in tension with SM predictions from QCDF, and two of the most significant disagreements come from tree-dominated modes that are theoretically well-described. This motivates an assessment of the data with a different theoretical approach, to complement further experimental analyses like the one described in Chapter 4. A similar method to the previous chapter was used here, testing consistency with the approximate $SU(3)_F$ symmetry of the SM. While this symmetry must be broken (at $> 5\sigma$), the degree of symmetry breaking required to describe the data is moderate ($\sim 20\%$) and well within the level expected by the SM. The conclusion that the branching ratio anomalies cannot

be explained by excess symmetry breaking has implications for New Physics theories that may be proposed to explain them; they must not predict significantly different couplings to the light quarks. It is also consistent with the findings of Ref. [58], which saw no tensions in the ratios of branching ratios given in Eq. (7.1).

It should be noted from Table 7.3, though, that the values of the individual $SU(3)_F$-breaking parameters are largely unconstrained beyond the power counting imposed on them. In only a few cases are small regions of phase-space excluded at 1σ. Having a complete set of precisely measured experimental observables is essential to unlock the full power of this method and probe the $SU(3)_F$ structure of these decays in a far more in-depth way. Indeed, there is certainly plenty of room for increased precision, particularly for $\bar{B}^0 \to K^- D_s^+$, $\bar{B}_s^0 \to K^0 D^0$, $\bar{B}^0 \to \bar{K}^0 D^0$ and $\bar{B}_s^0 \to K^- D_s^+$, which all still have relative uncertainties of $> 10\%$.

In addition to this, the analysis was limited by the lack of experimental inputs for two of the branching ratios under study, namely the suppressed modes of $\bar{B}_s^0 \to \pi^- D^+$ and $\bar{B}_s^0 \to \pi^0 D^0$. The measurement of these observables would not only provide information on the size of $SU(3)_F$ breaking in exchange diagrams, but also allow a direct test of isospin symmetry through the relation that connects the two, i.e. Eq. (7.14a). The $SU(3)_F$ sum rule Eq. (7.14b) also remains untested due to the lack of input for $\mathcal{B}(\bar{B}_s^0 \to \pi^- D^+)$. Both of these missing branching ratios are estimated from the $SU(3)_F$ limit to be $\mathcal{O}(10^{-6})$. With expected yields in Run 3 of $\sim 10^3$, estimated from results in Chapter 5, it may well be possible to make a measurement of $\mathcal{B}(\bar{B}_s^0 \to \pi^- D^+)$, relative to $\mathcal{B}(\bar{B}^0 \to \pi^- D^+)$ with this data. Neutral pions are more challenging to reconstruct so the other missing mode may take longer to measure. If the statistics of Runs 3 and 4 are insufficient for this, then Upgrade II, which is planned to conclude in 2035, is expected to provide improved electromagnetic calorimeter granularity and energy resolution [280], so that LHCb can make full use of the LHC's "high-luminosity" phase. The total data sample collected by LHCb is expected to exceed 300 fb^{-1}.

8 Conclusion

"It is not the critic who counts; not the man who points out how the strong man stumbles... The credit belongs to the man who is actually in the arena...if he fails, at least [he] fails while daring greatly, so that his place shall never be with those cold and timid souls who neither know victory nor defeat."

- Theodore Roosevelt

To conclude, this thesis has presented investigations of Beauty to Open Charm modes from a range of complementary angles. The primary focus of particle physics at the moment is towards reconciling a theory that by many metrics is incredibly successful, in terms of the precision and accuracy of its predictions and its elegance, with the fact that it fails dramatically in explaining several observed phenomena. Theoretical predictions and experimental measurements must therefore be made with ever increased precision in the hope of uncovering exactly what has so far been missed. LHCb is an experiment that is specialised for the "precision" paradigm, with its design ensuring optimal sensitivity to the interactions it was built to study. Measuring CP violation is one of its main topics of interest, a phenomenon that both offers a solution to the puzzle of the overwhelming abundance of matter with respect to antimatter, and which could be an observable where "new physics" is most obvious. This experiment was designed for the study of particles containing the beauty quark i.e. the heaviest quark flavour that hadronises, and the consistency of the Standard Model was studied through CP-violation in b decays, namely $B \to DD'$.

Making precise predictions from first principles for fully hadronic decays such as these are challenging on account of the non-perturbative effects of QCD - the theory governing the strong interaction that binds hadrons together. The situation can be significantly simplified by making a few (conservative) assumptions, particularly through the use of the approximate SU(3)-flavour symmetry involving u, d, and s quarks, which applies exactly in the regime that their masses can be neglected in comparison to the characteristic energy-scale of QCD. Thus the full "family" of decays related by this symmetry

may be expressed in terms of a few parameters, and in this instance these refer to different decay topologies, the relative size of which is reasonably straightforward to estimate. Through this parameterisation, and using the full range of relevant inputs from various experiments, one may perform fits to extract predictions for CP asymmetries, as well as branching ratios, and the consistency of theory and experiment may be probed. While no significant inconsistencies were seen, this method provides predictions more precise than that of the experimental inputs, and can predict many observables that are yet to be measured experimentally. These predictions can be tested at a later date, as more precise experimental measurements are made.

There have, though, been recent hints of significant deviations between theory and experiment for branching ratios of a similar family of Beauty to Open Charm decays, those of $B_{(s)} \to D_{(s)}\pi/K$. Unlike $B \to DD'$ decays, and particularly for two modes with the largest tensions ($\bar{B}^0 \to D^- K^-$ and $\bar{B}^0_s \to D^+_s \pi^-$), QCDF is expected to describe data well, and so these tensions were a big surprise to the community. Since these decays are related to the "golden modes" for the extraction of γ in the SM, the implications of New Physics here are considerable. In the same way to $B \to DD'$, though, the data showed consistency with symmetry assumptions, suggesting only moderate $\mathrm{SU}(3)_F$ breaking, well within the expectations of this symmetry. As such, we can make the statement that the observed tensions are not due to excess $\mathrm{SU}(3)_F$ symmetry breaking, at least not on its own. This finding places important constraints on potential new physics theories that may be used to explain the tensions. Availability and precision of experimental inputs were the limiting factors of this analysis, especially unmeasured $\mathcal{B}(\bar{B}^0_s \to \pi^- D^+)$ and $\mathcal{B}(\bar{B}^0_s \to \pi^0 D^0)$, and so new data from LHCb and other experiments will have substantial impact on the conclusions we can draw. Most of the breaking parameters, for example, are currently unconstrained, with several modes having relative uncertainties greater than 10%. Both phenomenological analyses showed indications of enhancements to the subleading topological parameters, compared to what is often assumed for their magnitudes.

BSM effects in these decays were also probed for experimentally, using the full LHCb Run 2 dataset, through measurements of CP violation in $\bar{B}^0_s \to D^+_s \pi^-$ (A^s_{fs}), since such observables have excellent sensitivity to such phenomena. New Physics, if present, would be easily seen through the observation of direct CP violation in this mode, on top of the contribution from meson-oscillations. The rapid nature of these oscillations for B_s mesons meant that the effect of a charge asymmetry in production was negligible. An imperfect LHCb detector was accounted for by correcting the measured naïve raw asymmetry by numerous sources of detection asymmetry. While the final results are currently blinded, the uncertainties have been estimated, which indicate the possibility of being sensitive to New Physics effects if they are large. This analysis also required the evaluation of many sources of systematic uncertainty, and some of the most significant of these stem from the hardware trigger that rapidly filtered the incoming data. This effect was particularly harsh for hadronic final states.

The newest incarnation of the LHCb detector has removed this trigger, largely to benefit such hadronic analyses. This was a significant step to make and required upgrades

Run	Integrated Luminosity (fb^{-1})
1	3 (measured)
2	6 (measured)
3	14 (expected)
4	$\sim$ 30(expected)
5	$\sim$ 125 (projected)
6	$\sim 150 - 200$ (projected)

TABLE 8.1: Measured, expected, or projected luminosities at LHCb for each run.

to much of the detector. With so many new additions, validation at the start of the new data run was essential to ensure reliable results going forward. Measuring quantities that are already well-understood is a very appropriate way to do this and production asymmetries of beauty hadrons, reconstructed through Beauty to Open Charm decays, are excellent candidates. Such measurements have been made previously using leptonic final states but the new detector allows these to be performed for the first time with hadronic final states, hopefully at a competitive precision with a relatively small amount of data. Indeed, preliminary results on a small subset of the anticipated data indicate very clear invariant mass peaks. The quality of data in 2023 was limited by unforeseen circumstances, most notably running with the VELO subdetector in the open position. This issue has now been fixed, with the early 2024 data showing greatly improved efficiencies compared to Run 2, and prospects look good for Beauty to Open Charm measurements in 2024 and 2025. The early measurements should, therefore, be able to be completed with a subset of the expected 2024 data, and the projected precision of a Run 3 measurement of A_{fs}^{s}, a flagship of the Upgrade I detector, would enable BSM effects to be probed well within expected magnitudes. Data taken with this upgraded detector, and the next, should also help to better constrain phenomenological analyses such as in $B \to DD'$ and $B \to Dh$.

The LHCb detector will be upgraded once again [280], in the long shutdown following Run 4, in preparation for the "high-luminosity" phase of the LHC. The projected luminosity for this phase is compared to those of the other LHC runs in Table 8.1. In the same way that adapting the detector to manage a higher data rate was necessary ahead of Run 3, there are considerable technical challenges that must be overcome if LHCb is to cope with an even greater rate, as well as a more intense radiation environment. Though the technologies will become more sophisticated, the general structure of the detector will not change significantly and will still consist of; a VELO, tracking stations and RICH detectors placed both upstream and downstream of the magnet, an electromagnetic calorimeter (ECAL), and 4 muon stations (M2-M5). The design is, though, not expected to include an HCAL, which will be replaced by additional shielding and a time-of-flight detector (TORCH). The downstream tracker, the Mighty Tracker, will have an outer part with a similar design to the current SciFi, while the inner part will be silicon-based. The side walls of the magnets will also be instrumented with tracking detectors.

The most prominent change from Upgrade I will be a new focus on precision timing $\sim \mathcal{O}(10\,\text{ps})$, expected to be implemented in the RICH, ECAL and TORCH, which will complement existing precise position resolution to more accurately associate particles to the correct vertices and reduce combinatorial background contributions. Some improvements in the reconstruction of neutral particles is also anticipated. Though the performance of this detector is expected to remain similar to that of Upgrade I, it will do so with the pile-up increased by a factor of 7.5, greatly improving the statistical precision.

A

A_{fs}^{s}

A.1 Kπ Asymmetries

The following figures show illustrate the reweighting of calibration samples to match signal for use in `KPiTwoTrackAsymmetry`. For defining the $K-\pi$ pairs, the signal mode $\bar{B}_s^0 \to (D_s^+ \to K^+K^-\pi^+)\pi^-$, and its conjugate, is notated as $B_s \to (D_s \to K_{D_s,1}K_{D_s,2}\pi_{D_s,3})\pi_{\text{bach}}$.

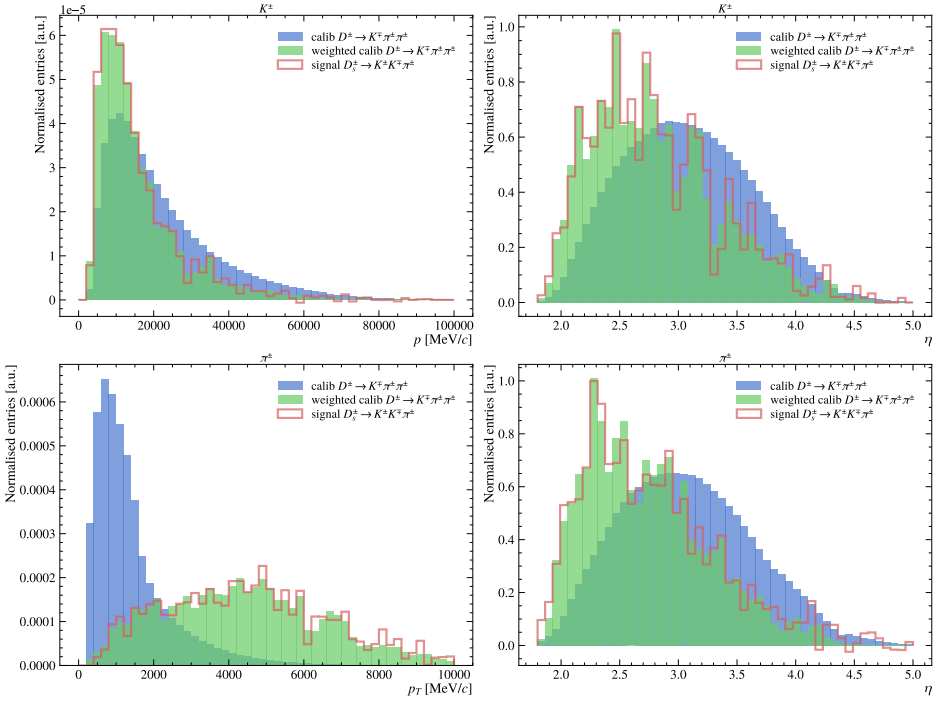

FIGURE A.1: Reweighting of calibration $D^\pm \to K^\mp\pi^\pm\pi^\pm$ to match the signal for 2015 `MagDown`, for use in the `KPiTwoTrackAsymmetry` tool with the pairing ($K_{D_s,1}$, $\pi_{\text{bach.}}$).

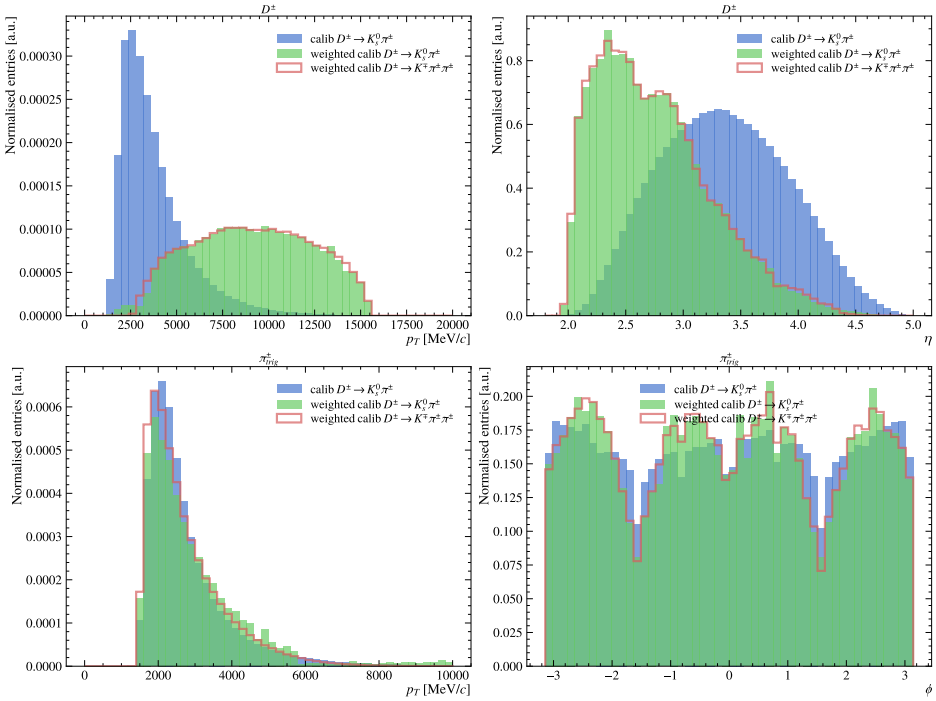

FIGURE A.2: Reweighting of calibration $D^\pm \to K^0_S\pi^\pm$ to match weighted $D^\pm \to K^\mp\pi^\pm\pi^\pm$ for 2015 `MagDown`, for use in the `KPiTwoTrackAsymmetry` tool with the pairing ($K_{D_s}1$, $\pi_{\text{bach.}}$).

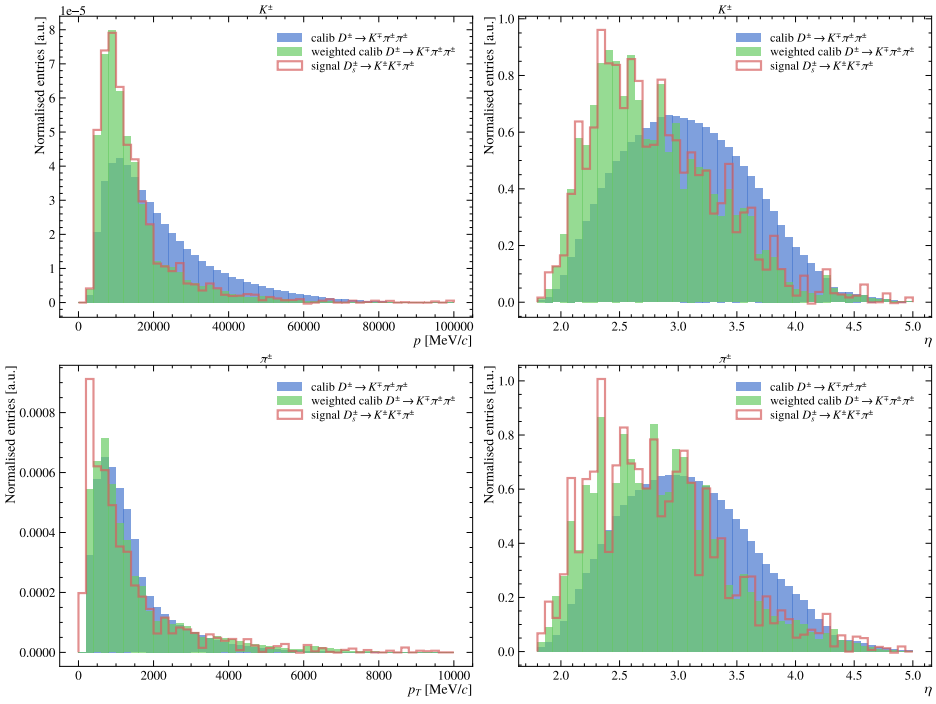

FIGURE A.3: Reweighting of calibration $D^\pm \to K^\mp\pi^\pm\pi^\pm$ to match the signal for 2015 `MagDown`, for use in the `KPiTwoTrackAsymmetry` tool with the pairing ($K_{D_s}2$, $\pi_{D_s}3$).

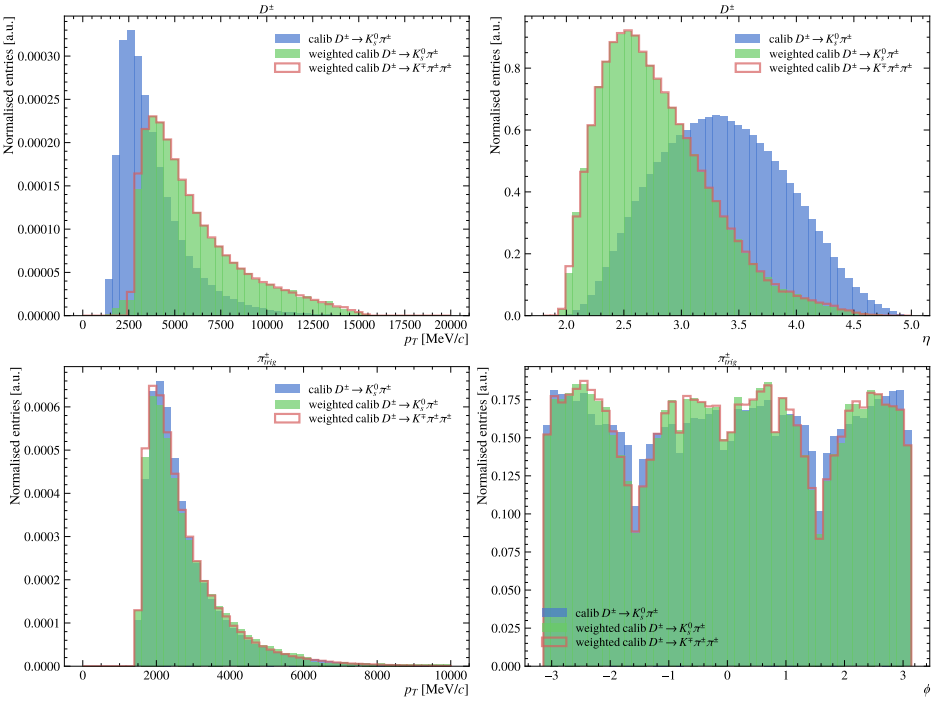

FIGURE A.4: Reweighting of calibration $D^{\pm} \to K^0_S\pi^{\pm}$ to match weighted $D^{\pm} \to K^{\mp}\pi^{\pm}\pi^{\pm}$ for 2015 `MagDown`, for use in the `KPiTwoTrackAsymmetry` tool with the pairing ($K_{D_s}2$, $\pi_{D_s}3$).

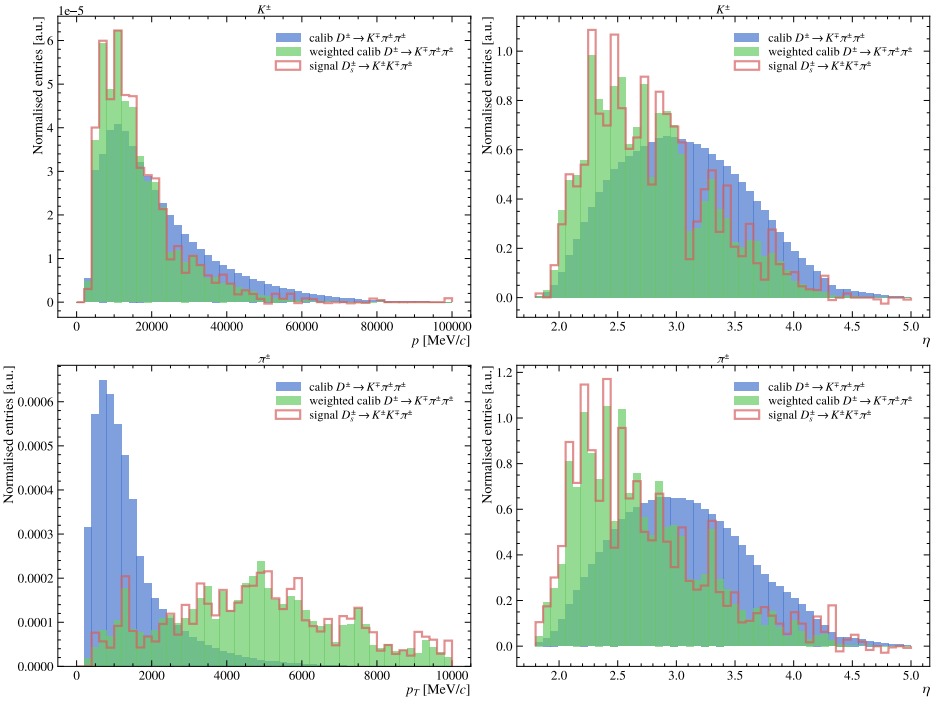

FIGURE A.5: Reweighting of calibration $D^{\pm} \to K^{\mp}\pi^{\pm}\pi^{\pm}$ to match the signal for 2015 `MagUp`, for use in the `KPiTwoTrackAsymmetry` tool with the pairing ($K_{D_s}1$, $\pi_{\text{bach.}}$).

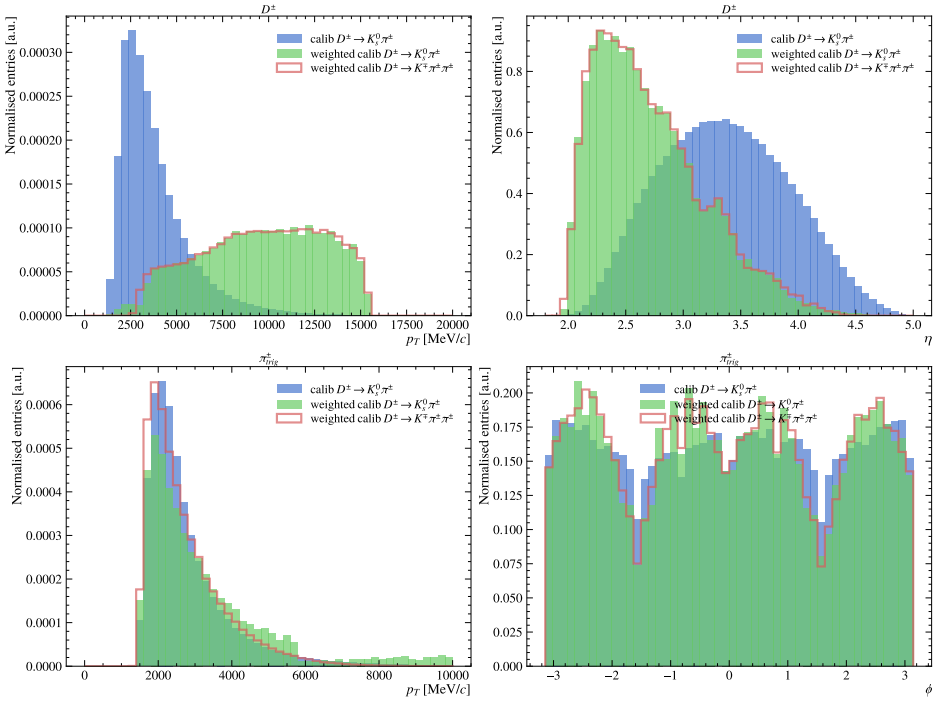

FIGURE A.6: Reweighting of calibration $D^\pm \to K^0_S\pi^\pm$ to match weighted $D^\pm \to K^\mp\pi^\pm\pi^\pm$ for 2015 MagUp, for use in the KPiTwoTrackAsymmetry tool with the pairing ($K_{D_s}1$, $\pi_{\text{bach.}}$).

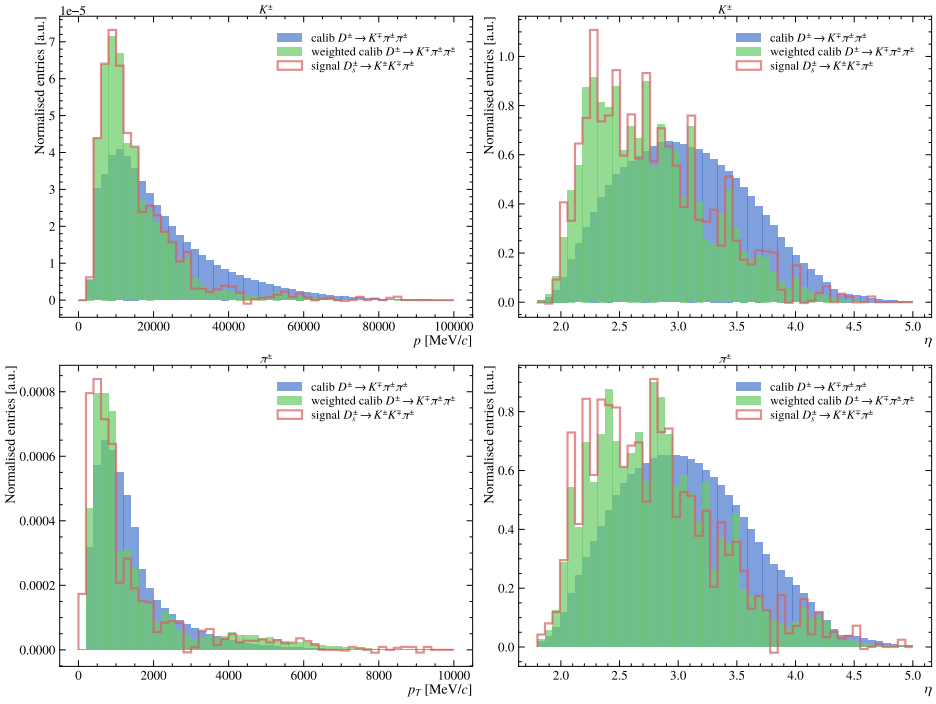

FIGURE A.7: Reweighting of calibration $D^\pm \to K^\mp\pi^\pm\pi^\pm$ to match the signal for 2015 MagUp, for use in the KPiTwoTrackAsymmetry tool with the pairing ($K_{D_s}2$, $\pi_{D_s}3$).

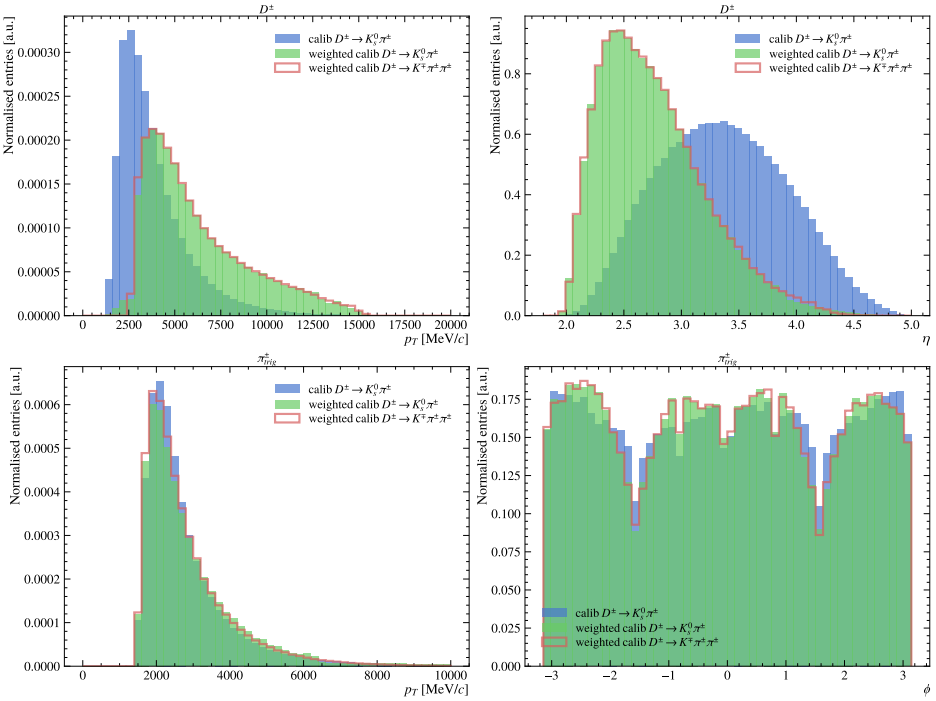

FIGURE A.8: Reweighting of calibration $D^{\pm} \to K^0_S\pi^{\pm}$ to match weighted $D^{\pm} \to K^{\mp}\pi^{\pm}\pi^{\pm}$ for 2015 `MagUp`, for use in the `KPiTwoTrackAsymmetry` tool with the pairing (K_{D_s}2, π_{D_s}3).

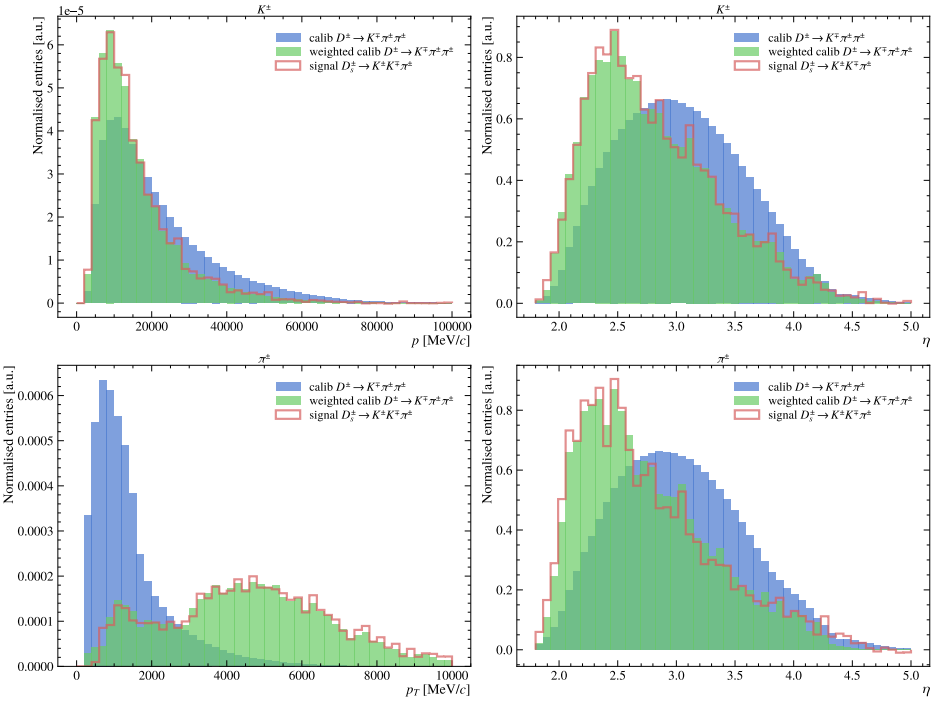

FIGURE A.9: Reweighting of calibration $D^{\pm} \to K^{\mp}\pi^{\pm}\pi^{\pm}$ to match the signal for 2016 `MagDown`, for use in the `KPiTwoTrackAsymmetry` tool with the pairing (K_{D_s}1, $\pi_{\text{bach.}}$).

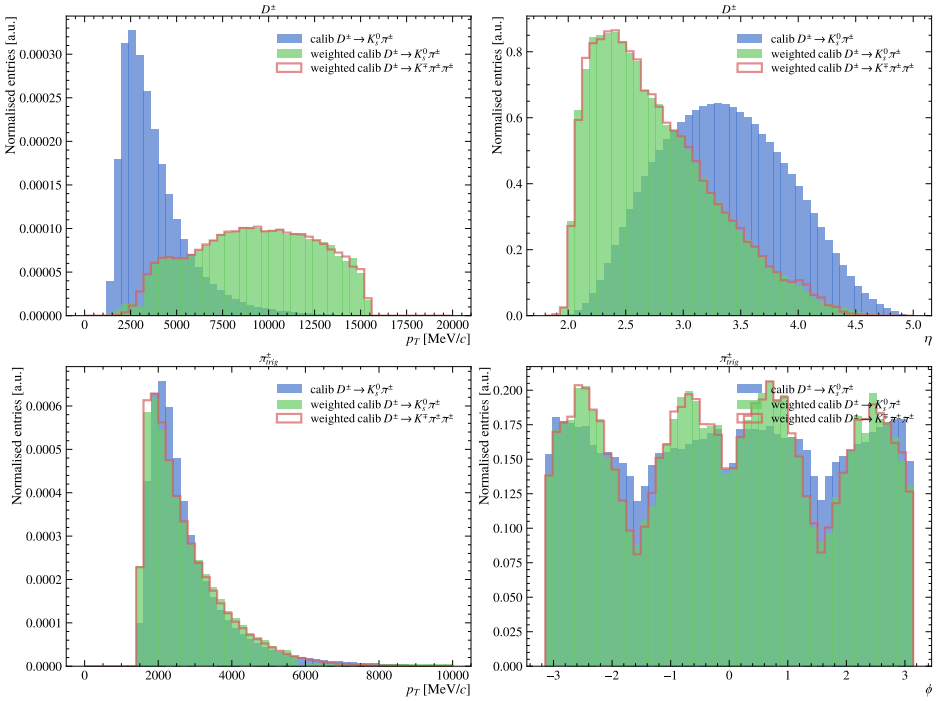

FIGURE A.10: Reweighting of calibration $D^\pm \to K^0_S\pi^\pm$ to match weighted $D^\pm \to K^\mp\pi^\pm\pi^\pm$ for 2016 `MagDown`, for use in the `KPiTwoTrackAsymmetry` tool with the pairing (K_{D_s},1, $\pi_{\text{bach.}}$).

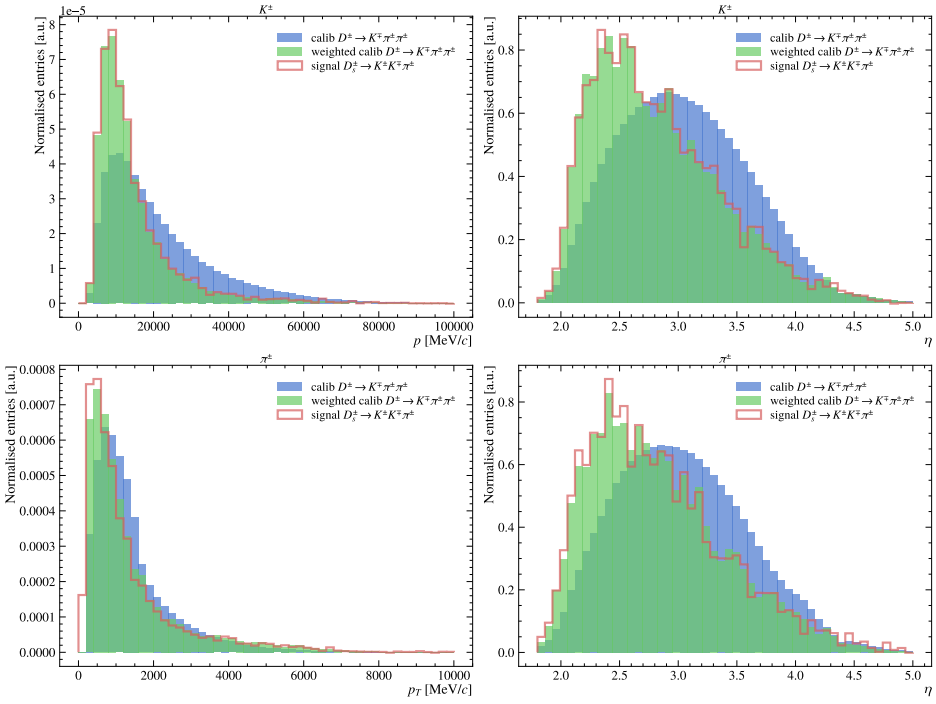

FIGURE A.11: Reweighting of calibration $D^\pm \to K^\mp\pi^\pm\pi^\pm$ to match the signal for 2016 `MagDown`, for use in the `KPiTwoTrackAsymmetry` tool with the pairing (K_{D_s},2, π_{D_s},3).

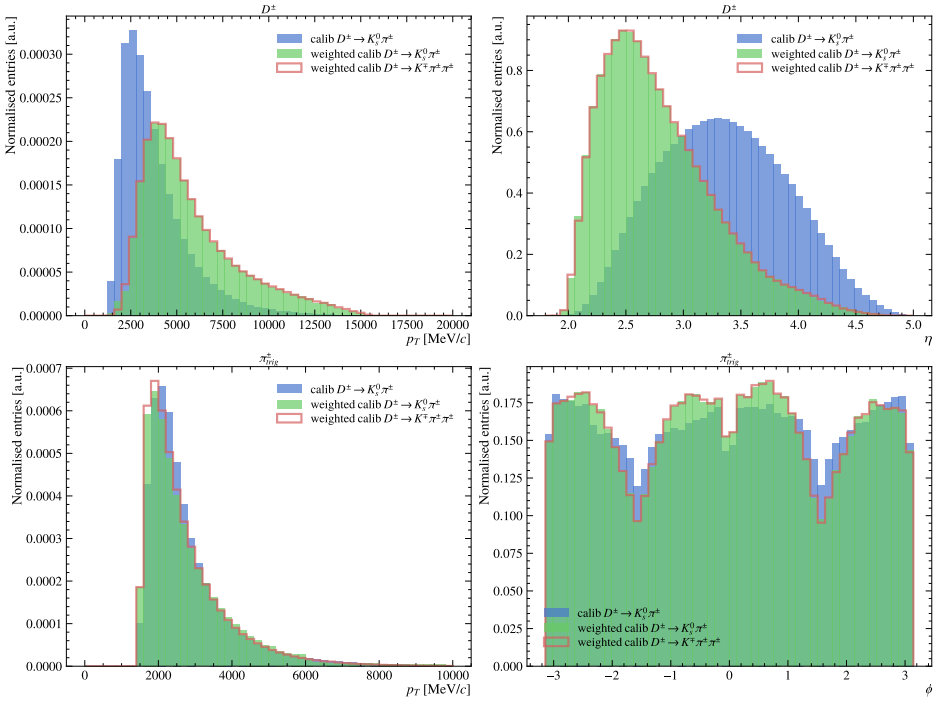

FIGURE A.12: Reweighting of calibration $D^{\pm} \to K^0_S\pi^{\pm}$ to match weighted $D^{\pm} \to K^{\mp}\pi^{\pm}\pi^{\pm}$ for 2016 `MagDown`, for use in the `KPiTwoTrackAsymmetry` tool with the pairing ($K_{D_s}2$, $\pi_{D_s}3$).

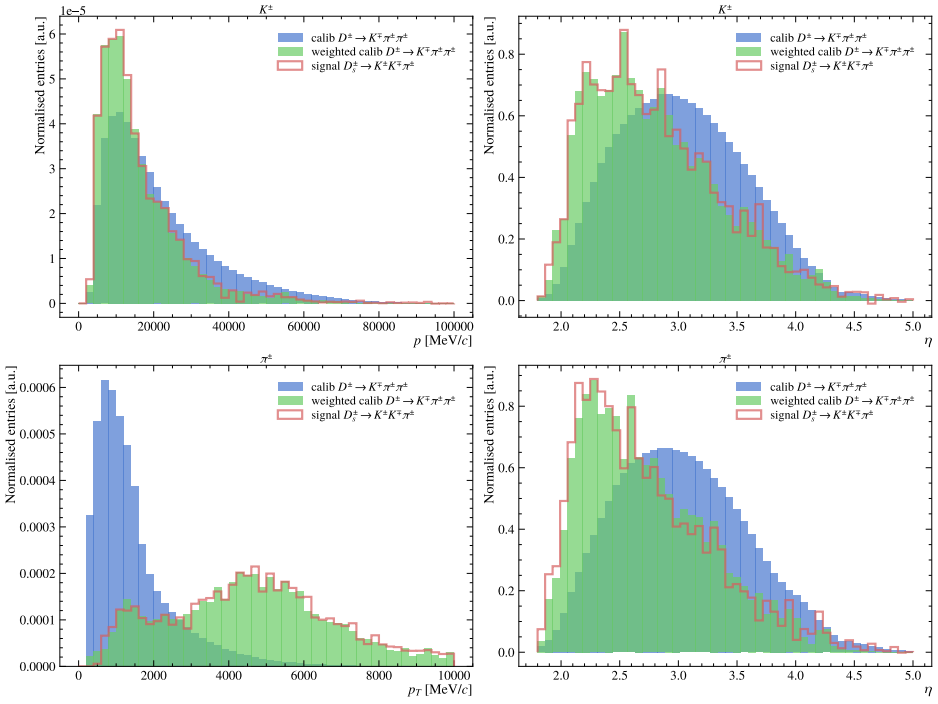

FIGURE A.13: Reweighting of calibration $D^{\pm} \to K^{\mp}\pi^{\pm}\pi^{\pm}$ to match the signal for 2016 `MagUp`, for use in the `KPiTwoTrackAsymmetry` tool with the pairing ($K_{D_s}1$, $\pi_{\text{bach.}}$).

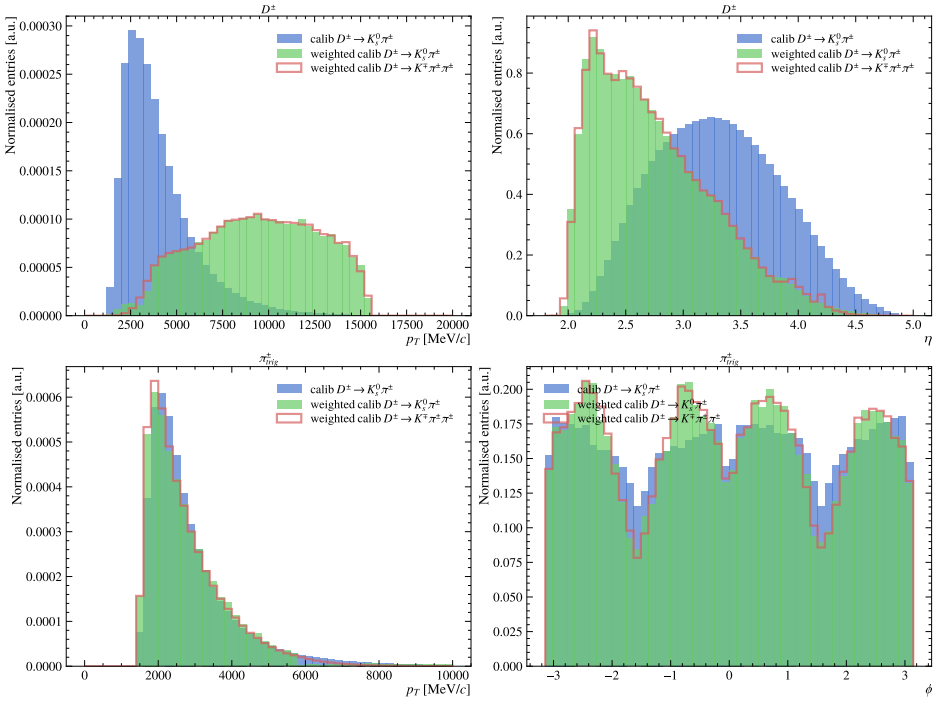

FIGURE A.14: Reweighting of calibration $D^\pm \to K^0_S\pi^\pm$ to match weighted $D^\pm \to K^\mp\pi^\pm\pi^\pm$ for 2016 `MagUp`, for use in the `KPiTwoTrackAsymmetry` tool with the pairing ($K_{D_s}1$, $\pi_{\text{bach.}}$).

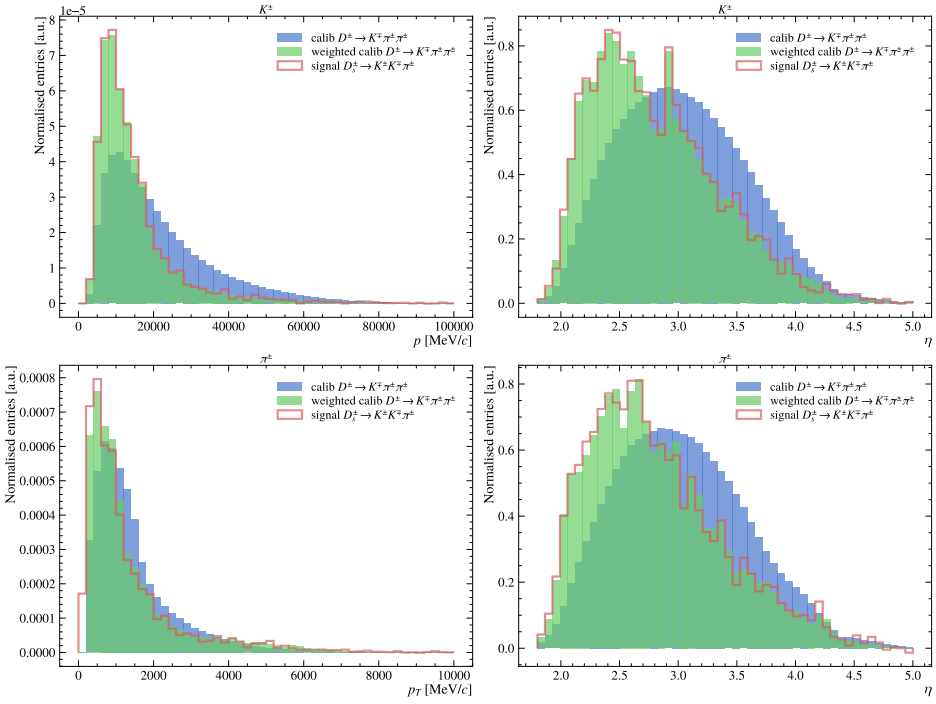

FIGURE A.15: Reweighting of calibration $D^\pm \to K^\mp\pi^\pm\pi^\pm$ to match the signal for 2016 `MagUp`, for use in the `KPiTwoTrackAsymmetry` tool with the pairing ($K_{D_s}2$, $\pi_{D_s}3$).

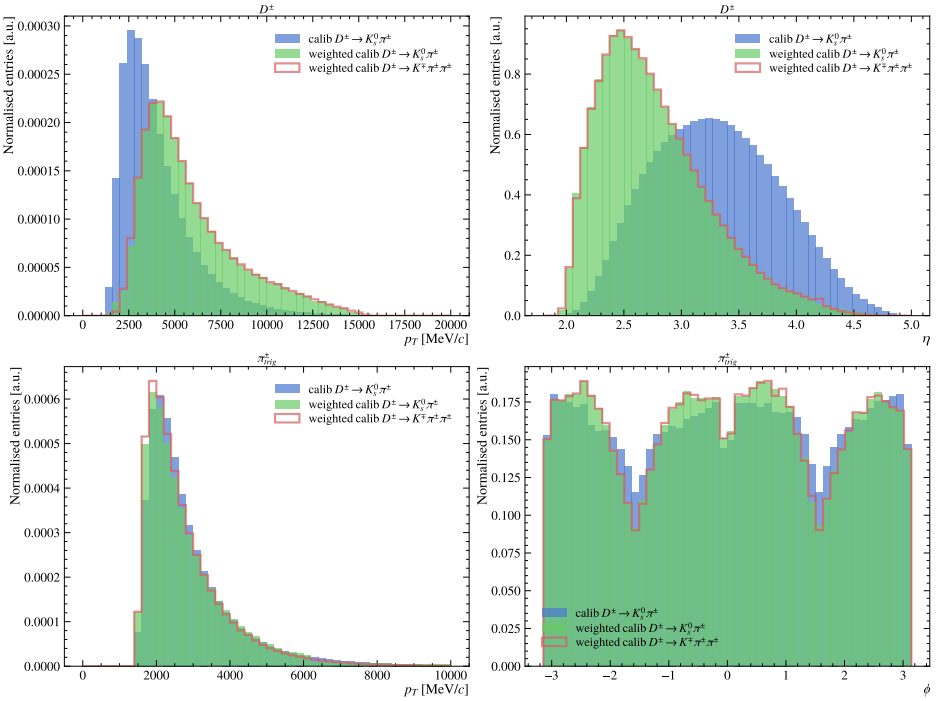

FIGURE A.16: Reweighting of calibration $D^{\pm} \to K^0_S\pi^{\pm}$ to match weighted $D^{\pm} \to K^{\mp}\pi^{\pm}\pi^{\pm}$ for 2016 `MagUp`, for use in the `KPiTwoTrackAsymmetry` tool with the pairing (K_{D_s}2, π_{D_s}3).

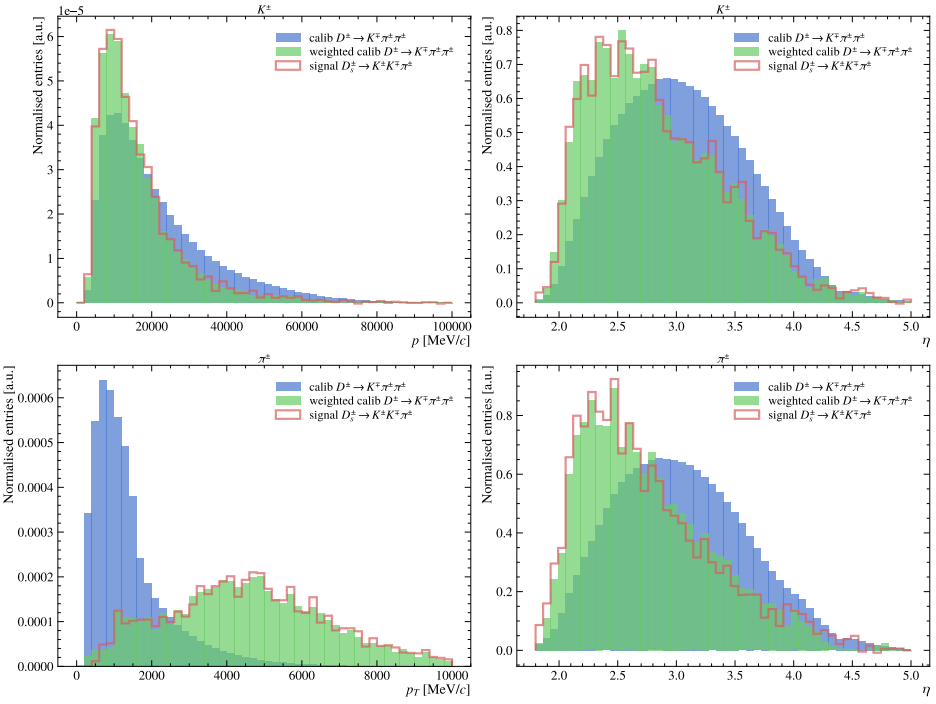

FIGURE A.17: Reweighting of calibration $D^{\pm} \to K^{\mp}\pi^{\pm}\pi^{\pm}$ to match the signal for 2017 `MagDown`, for use in the `KPiTwoTrackAsymmetry` tool with the pairing (K_{D_s}1, $\pi_{\text{bach.}}$).

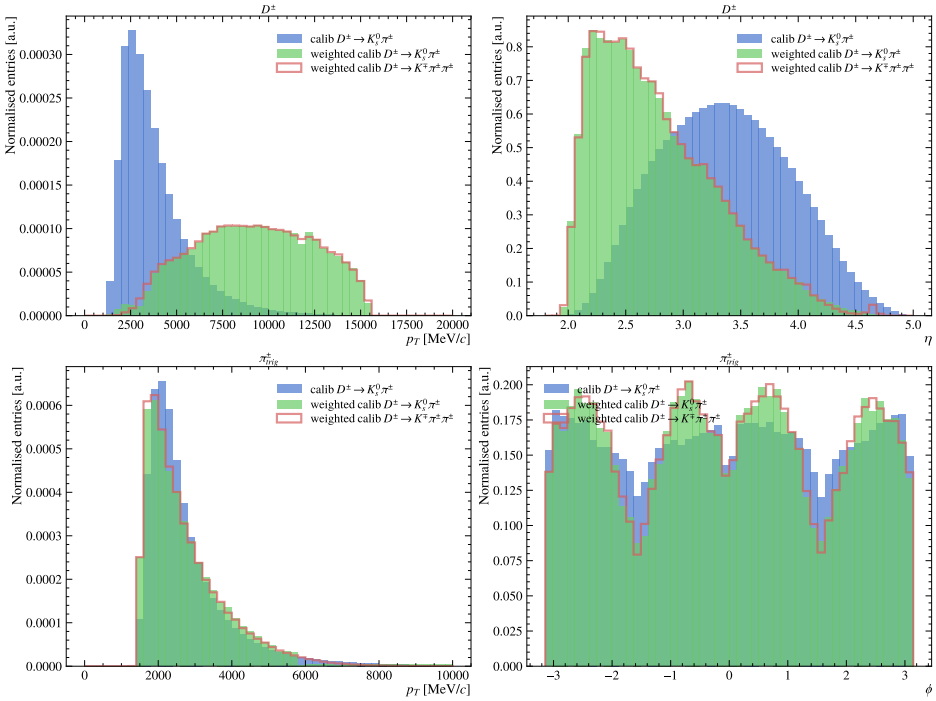

FIGURE A.18: Reweighting of calibration $D^\pm \to K^0_S\pi^\pm$ to match weighted $D^\pm \to K^\mp\pi^\pm\pi^\pm$ for 2017 `MagDown`, for use in the `KPiTwoTrackAsymmetry` tool with the pairing ($K_{D_s}1$, $\pi_{\text{bach.}}$).

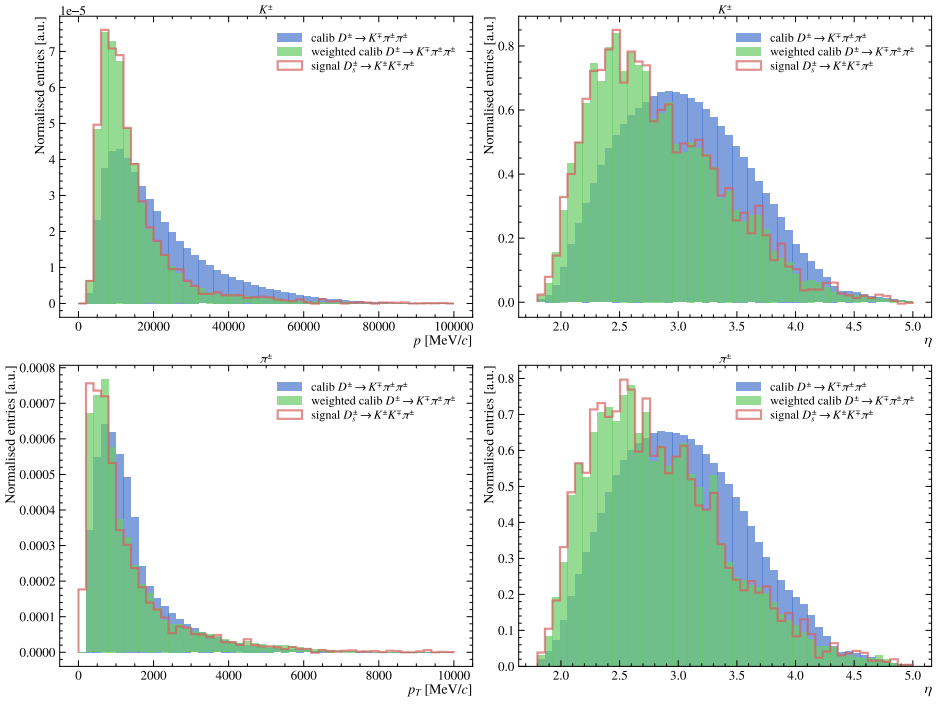

FIGURE A.19: Reweighting of calibration $D^\pm \to K^\mp\pi^\pm\pi^\pm$ to match the signal for 2017 `MagDown`, for use in the `KPiTwoTrackAsymmetry` tool with the pairing ($K_{D_s}2$, $\pi_{D_s}3$).

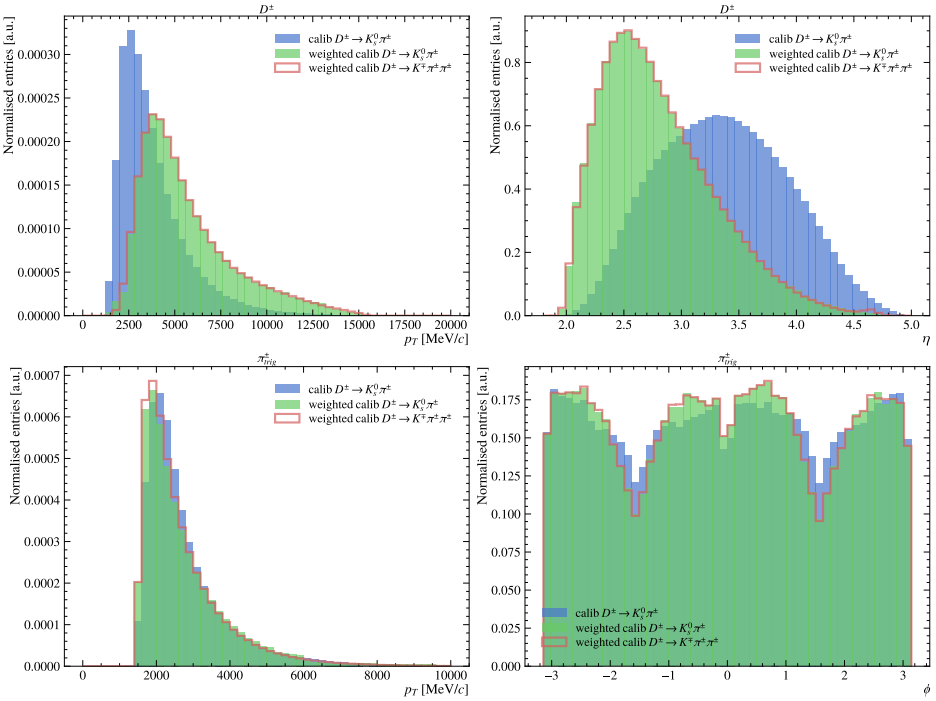

FIGURE A.20: Reweighting of calibration $D^{\pm} \to K^0_S\pi^{\pm}$ to match weighted $D^{\pm} \to K^{\mp}\pi^{\pm}\pi^{\pm}$ for 2017 `MagDown`, for use in the `KPiTwoTrackAsymmetry` tool with the pairing ($K_{D_s}2$, $\pi_{D_s}3$).

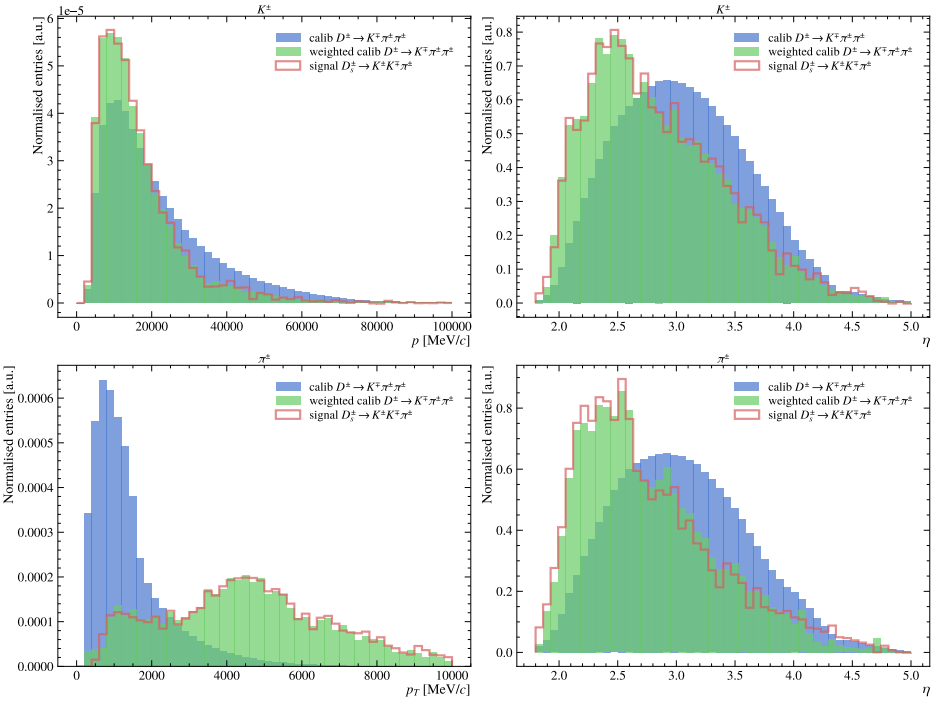

FIGURE A.21: Reweighting of calibration $D^{\pm} \to K^{\mp}\pi^{\pm}\pi^{\pm}$ to match the signal for 2017 `MagUp`, for use in the `KPiTwoTrackAsymmetry` tool with the pairing ($K_{D_s}1$, $\pi_{\text{bach.}}$).

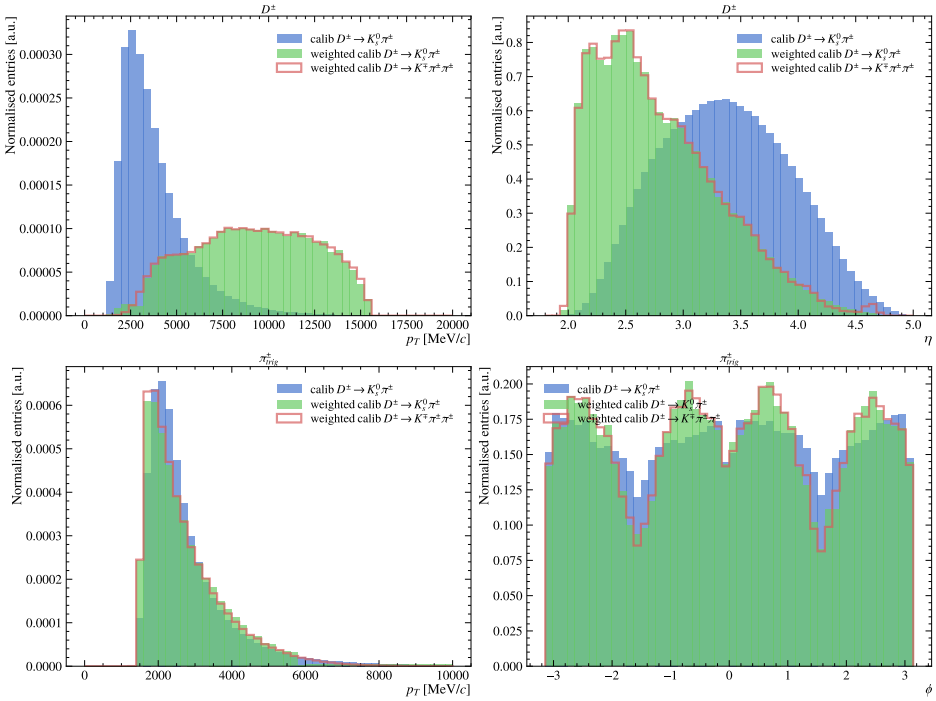

FIGURE A.22: Reweighting of calibration $D^\pm \to K^0_S\pi^\pm$ to match weighted $D^\pm \to K^\mp\pi^\pm\pi^\pm$ for 2017 `MagUp`, for use in the `KPiTwoTrackAsymmetry` tool with the pairing ($K_{D_s}1$, $\pi_{\text{bach.}}$).

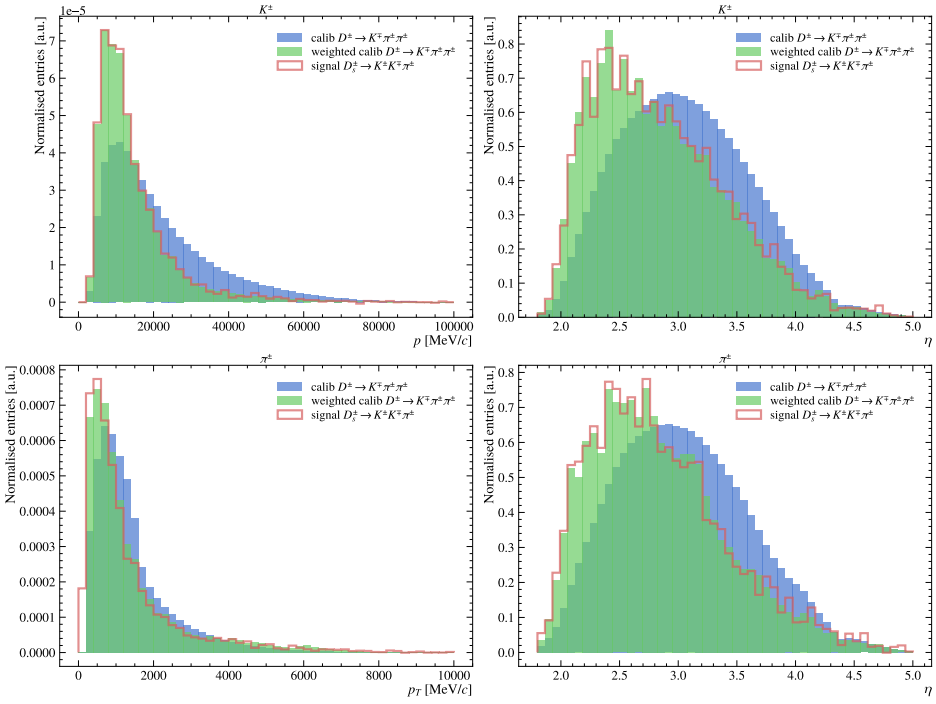

FIGURE A.23: Reweighting of calibration $D^\pm \to K^\mp\pi^\pm\pi^\pm$ to match the signal for 2017 `MagUp`, for use in the `KPiTwoTrackAsymmetry` tool with the pairing ($K_{D_s}2$, $\pi_{D_s}3$).

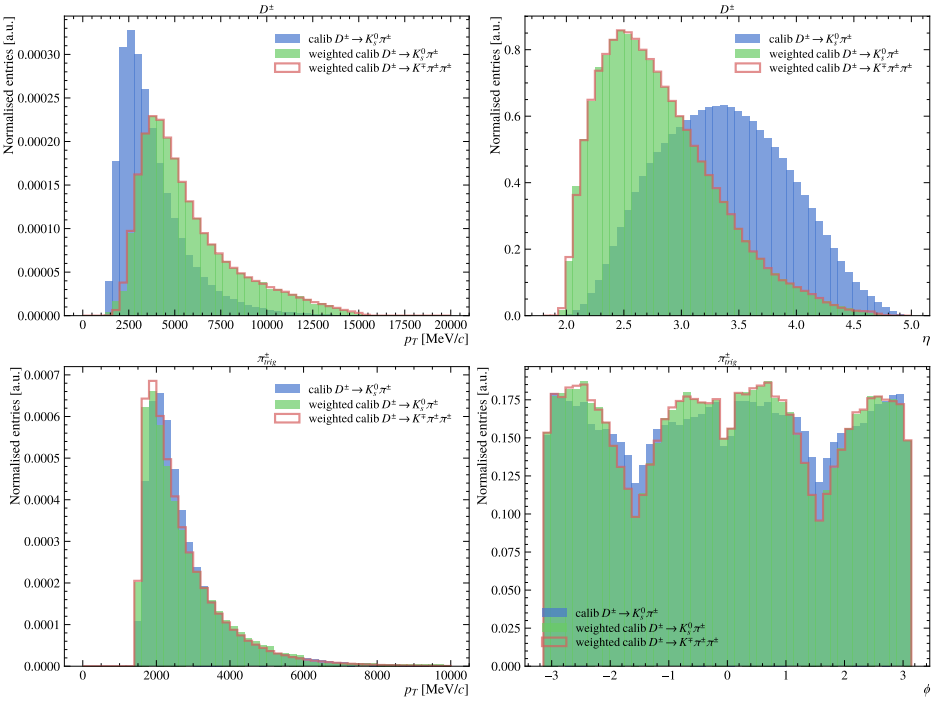

FIGURE A.24: Reweighting of calibration $D^{\pm} \to K^0_S\pi^{\pm}$ to match weighted $D^{\pm} \to K^{\mp}\pi^{\pm}\pi^{\pm}$ for 2017 `MagUp`, for use in the `KPiTwoTrackAsymmetry` tool with the pairing ($K_{D_s}2$, $\pi_{D_s}3$).

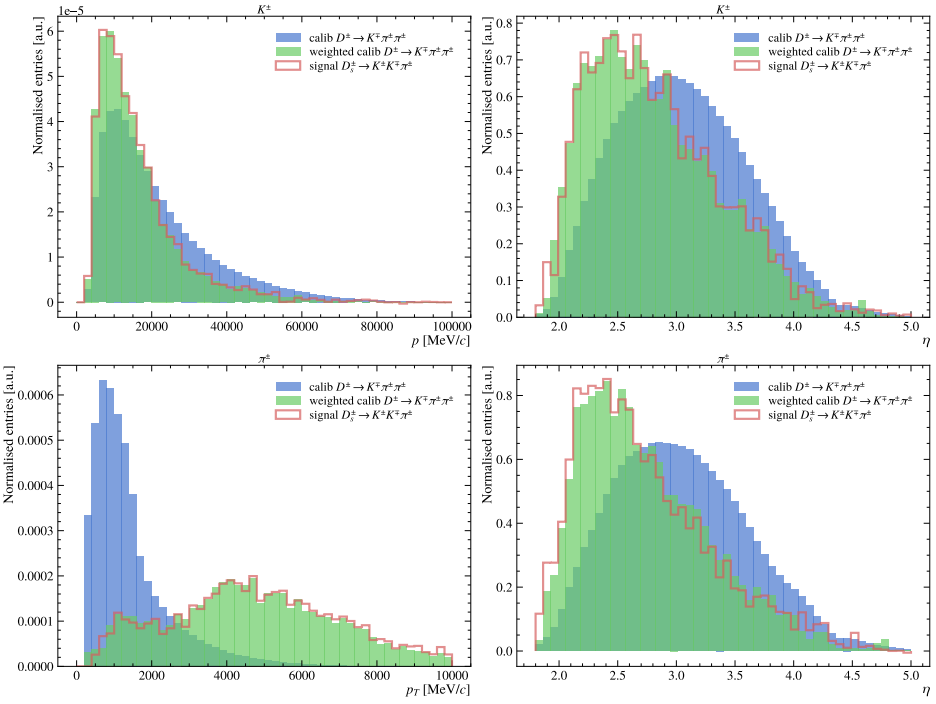

FIGURE A.25: Reweighting of calibration $D^{\pm} \to K^{\mp}\pi^{\pm}\pi^{\pm}$ to match the signal for 2018 `MagDown`, for use in the `KPiTwoTrackAsymmetry` tool with the pairing ($K_{D_s}1$, $\pi_{\text{bach.}}$).

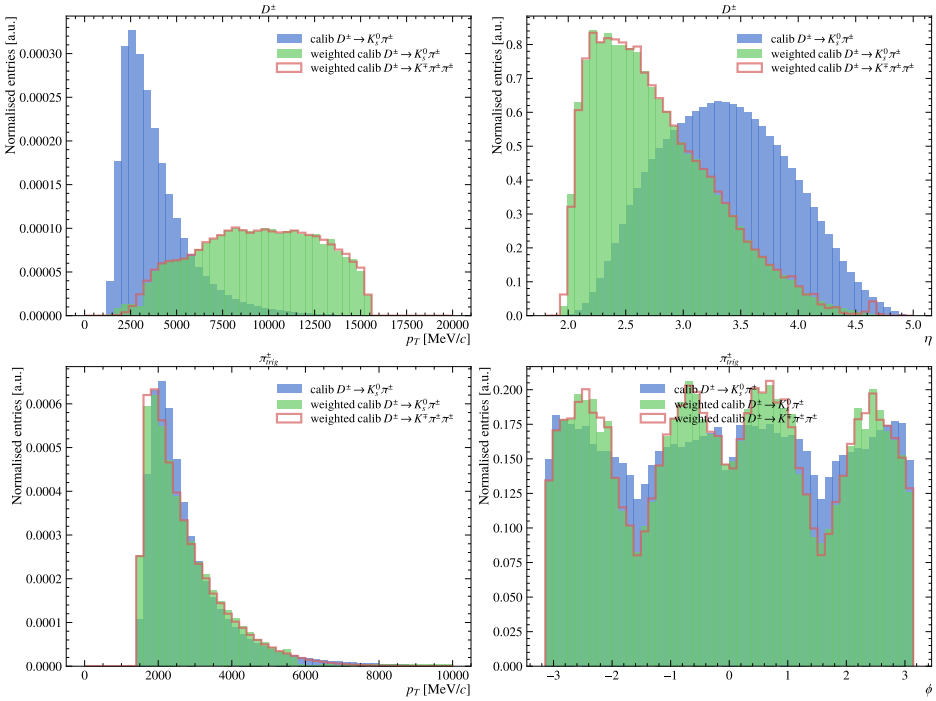

FIGURE A.26: Reweighting of calibration $D^\pm \to K^0_S\pi^\pm$ to match weighted $D^\pm \to K^\mp\pi^\pm\pi^\pm$ for 2018 `MagDown`, for use in the `KPiTwoTrackAsymmetry` tool with the pairing (K_{D_s},1, $\pi_{\text{bach.}}$).

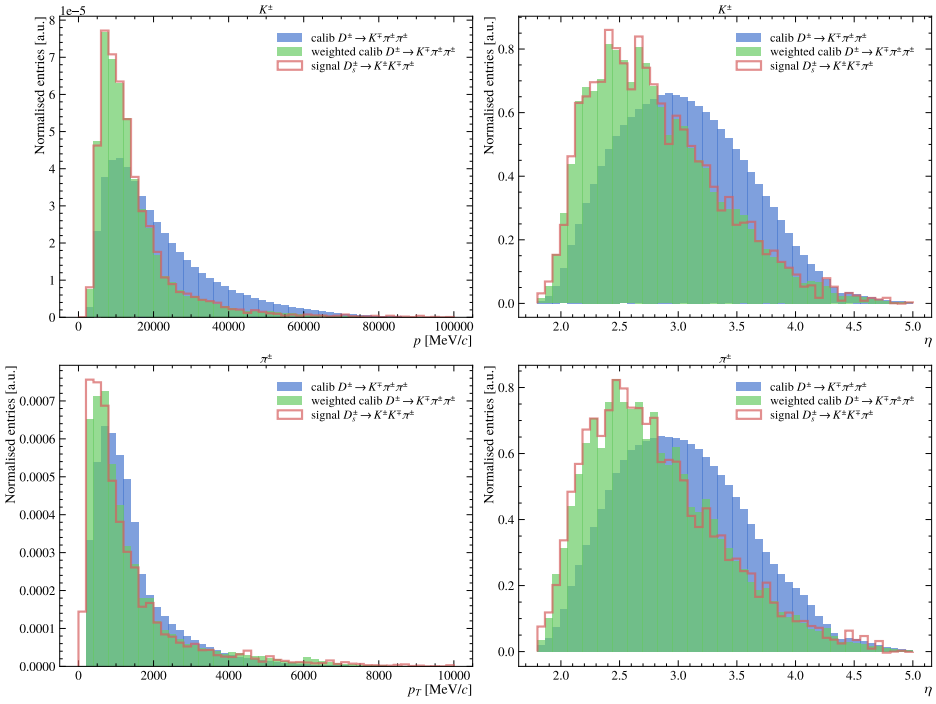

FIGURE A.27: Reweighting of calibration $D^\pm \to K^\mp\pi^\pm\pi^\pm$ to match the signal for 2018 `MagDown`, for use in the `KPiTwoTrackAsymmetry` tool with the pairing (K_{D_s},2, π_{D_s},3).

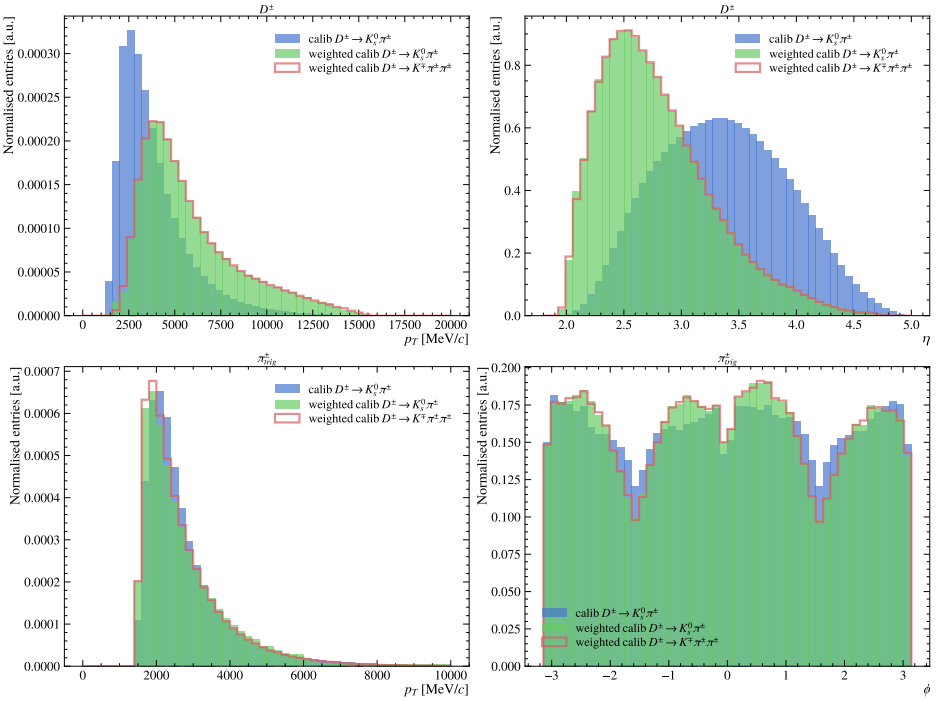

FIGURE A.28: Reweighting of calibration $D^{\pm} \to K^0_S\pi^{\pm}$ to match weighted $D^{\pm} \to K^{\mp}\pi^{\pm}\pi^{\pm}$ for 2018 `MagDown`, for use in the `KPiTwoTrackAsymmetry` tool with the pairing ($K_{D_s}2$, $\pi_{D_s}3$).

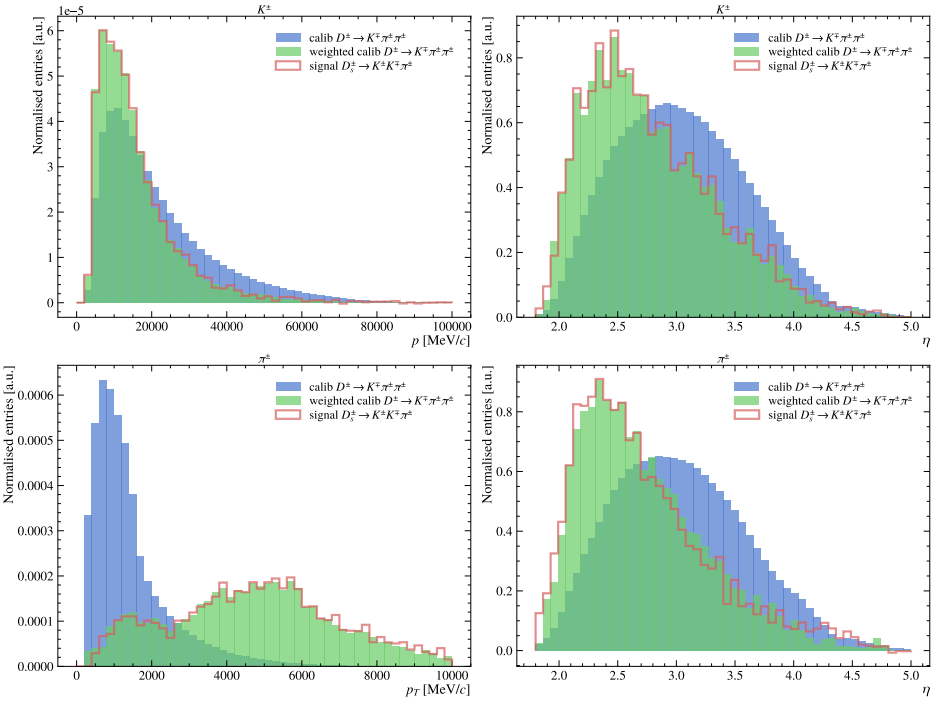

FIGURE A.29: Reweighting of calibration $D^{\pm} \to K^{\mp}\pi^{\pm}\pi^{\pm}$ to match the signal for 2018 `MagUp`, for use in the `KPiTwoTrackAsymmetry` tool with the pairing ($K_{D_s}1$, $\pi_{\text{bach.}}$).

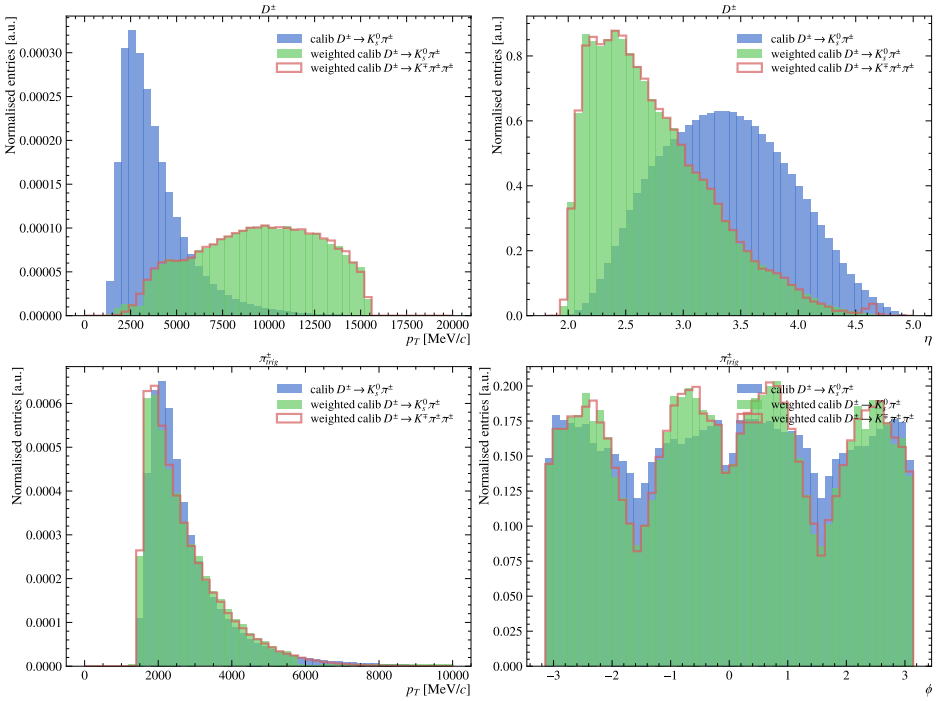

FIGURE A.30: Reweighting of calibration $D^\pm \to K^0_S\pi^\pm$ to match weighted $D^\pm \to K^\mp\pi^\pm\pi^\pm$ for 2018 MagUp, for use in the KPiTwoTrackAsymmetry tool with the pairing ($K_{D_s}1$, $\pi_{\text{bach.}}$).

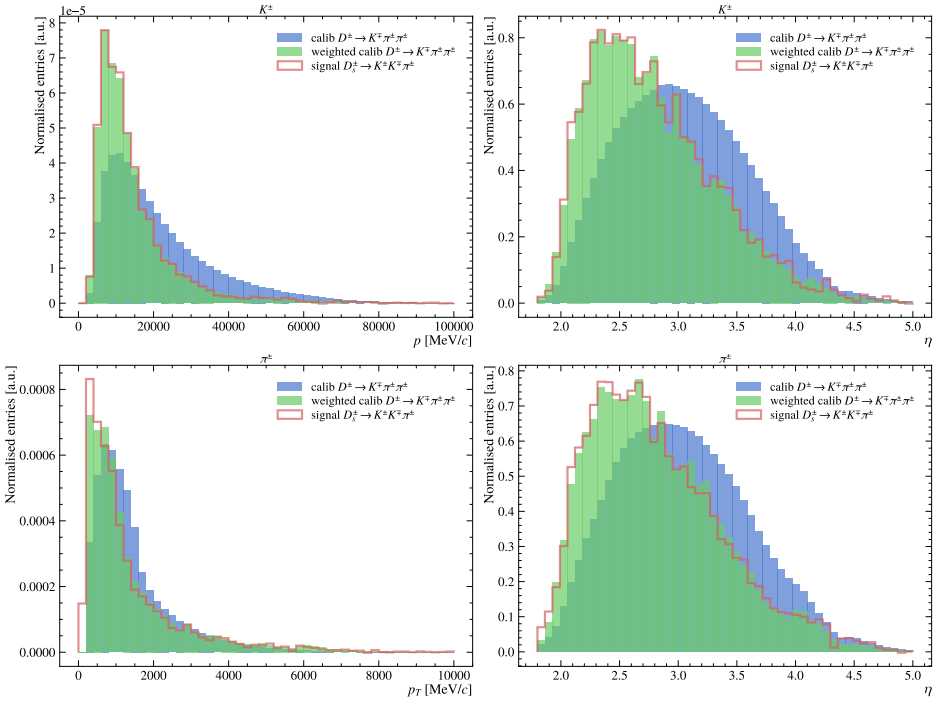

FIGURE A.31: Reweighting of calibration $D^\pm \to K^\mp\pi^\pm\pi^\pm$ to match the signal for 2018 MagUp, for use in the KPiTwoTrackAsymmetry tool with the pairing ($K_{D_s}2$, $\pi_{D_s}3$).

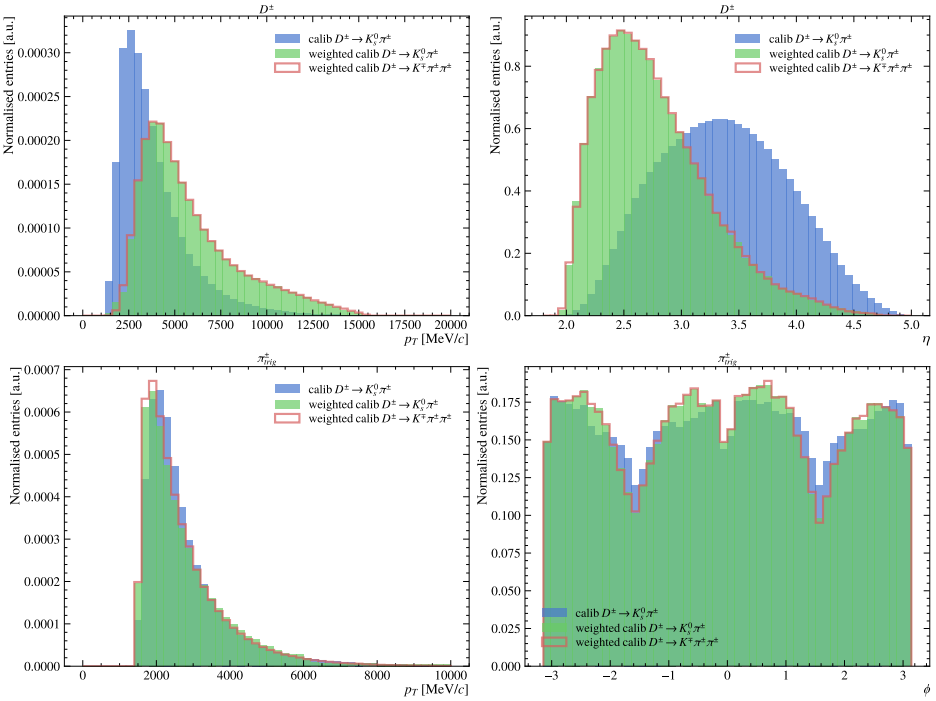

FIGURE A.32: Reweighting of calibration $D^\pm \to K^0_S\pi^\pm$ to match weighted $D^\pm \to K^\mp\pi^\pm\pi^\pm$ for 2018 `MagUp`, for use in the `KPiTwoTrackAsymmetry` tool with the pairing ($K_{D_s}2$, $\pi_{D_s}3$).

A.2 PID Asymmetries

The following tables summarise the PID efficiencies (as percentages) for each of the final state particles in the A^s_{fs} analysis of Chapter 4 for samples split by year, magnet polarity, phase-space region and D_s charge. The labelling `lab{i}`, where i is an integer between 0 and 5, corresponds to the order of particles in the signal decay $\bar{B}^0_s \to \pi^-(D^+_s \to K^+K^-\pi^+)$ or its conjugate, i.e. $\bar{B}^0_s$ is `lab0` and the π^+ from D^+_s is `lab5`.

Phase-space	Weak		Strong	
	In	Out	In	Out
`lab1`	87.49	87.46	76.33	75.51
`lab3`	73.17	61.81	63.85	54.23
`lab4`	87.01	85.78	76.99	75.14
`lab5`	94.07	92.39	87.35	85.86
comb.	52.40	42.84	32.78	26.42

TABLE A.1: PID efficiencies (as percentages) for each final state of $B^0_s \to (D^-_s \to K^+K^-\pi^-)\pi^+$ and combined for 2015 `MagDown`, in regions of phase-space with "weak" and "strong" PID, and "in" and "out" of the $\overline{\Lambda}^-_c$ peak.

Phase-space	Weak		Strong	
	In	Out	In	Out
lab1	87.59	87.23	76.05	75.70
lab3	73.29	61.62	60.96	51.94
lab4	86.61	85.19	72.77	73.49
lab5	94.53	92.59	88.25	86.16
comb.	52.56	42.40	29.77	24.90

TABLE A.3: PID efficiencies (as percentages) for each final state of $B_s^0 \to (D_s^- \to K^+K^-\pi^-)\pi^+$ and combined for 2015 MagUp, in regions of phase-space with "weak" and "strong" PID, and "in" and "out" of the $\overline{\Lambda}_c^-$ peak.

Phase-space	Weak		Strong	
	In	Out	In	Out
lab1	88.00	87.59	77.96	75.28
lab3	74.27	61.65	65.29	52.52
lab4	86.20	85.24	77.07	73.06
lab5	94.03	92.38	87.45	85.90
comb.	52.97	42.52	34.31	24.81

TABLE A.4: PID efficiencies (as percentages) for each final state of $\bar{B}_s^0 \to (D_s^+ \to K^+K^-\pi^+)\pi^-$ and combined for 2015 MagUp, in regions of phase-space with "weak" and "strong" PID, and "in" and "out" of the Λ_c^+ peak.

Phase-space	Weak		Strong	
	In	Out	In	Out
lab1	87.70	87.29	74.13	74.91
lab3	73.91	61.71	64.37	53.52
lab4	86.36	85.58	75.44	74.04
lab5	94.19	92.57	87.40	86.23
comb.	52.73	42.67	31.46	25.60

TABLE A.2: PID efficiencies (as percentages) for each final state of $\overline{B}_s^0 \to (D_s^+ \to K^+K^-\pi^+)\pi^-$ and combined for 2015 MagDown, in regions of phase-space with "weak" and "strong" PID, and "in" and "out" of the Λ_c^+ peak.

Phase-space	Weak		Strong	
	In	Out	In	Out
lab1	86.58	86.78	76.13	76.28
lab3	72.21	59.91	64.67	53.00
lab4	85.67	84.84	75.42	74.26
lab5	94.05	92.32	87.40	85.99
comb.	50.37	40.72	32.45	25.82

TABLE A.5: PID efficiencies (as percentages) for each final state of $B_s^0 \to (D_s^- \to K^+K^-\pi^-)\pi^+$ and combined for 2016 MagDown, in regions of phase-space with "weak" and "strong" PID, and "in" and "out" of the $\overline{\Lambda}_c^-$ peak.

Phase-space	Weak		Strong	
	In	Out	In	Out
lab1	86.42	86.55	75.45	75.74
lab3	72.57	59.99	64.52	53.15
lab4	85.37	84.43	74.78	73.55
lab5	94.20	92.47	87.67	86.24
comb.	50.43	40.54	31.91	25.53

TABLE A.6: PID efficiencies (as percentages) for each final state of $\bar{B}_s^0 \to (D_s^+ \to K^+K^-\pi^+)\pi^-$ and combined for 2016 MagDown, in regions of phase-space with "weak" and "strong" PID, and "in" and "out" of the Λ_c^+ peak.

Phase-space	Weak		Strong	
	In	Out	In	Out
lab1	86.67	86.82	75.80	76.16
lab3	72.21	59.86	63.65	52.74
lab4	85.31	84.31	74.76	73.24
lab5	94.28	92.63	87.66	86.38
comb.	50.34	40.59	31.62	25.41

TABLE A.7: PDIDID efficiencies for each final state of $B_s^0 \to (D_s^- \to K^+K^-\pi^-)\pi^+$ and combined for 2016 MagUp, in regions of phase-space with "weak" and "strong" PID, and "in" and "out" of the $\overline{\Lambda}_c^-$ peak.

Phase-space	Weak		Strong	
	In	Out	In	Out
lab1	86.98	87.12	76.03	76.34
lab3	72.33	59.81	55.34	48.35
lab4	85.22	84.34	74.47	73.61
lab5	93.99	92.35	87.29	85.88
comb.	50.39	40.58	27.35	23.33

TABLE A.8: PID efficiencies (as percentages) for each final state of $\bar{B}_s^0 \to (D_s^+ \to K^+K^-\pi^+)\pi^-$ and combined for 2016 MagUp, in regions of phase-space with "weak" and "strong" PID, and "in" and "out" of the Λ_c^+ peak.

Phase-space	Weak		Strong	
	In	Out	In	Out
lab1	86.92	87.06	76.69	76.62
lab3	72.28	59.80	64.21	52.87
lab4	85.80	84.90	75.91	74.29
lab5	94.08	92.37	87.62	86.05
comb.	50.71	40.83	32.75	25.90

TABLE A.9: PID efficiencies (as percentages) for each final state of $B_s^0 \to (D_s^- \to K^+K^-\pi^-)\pi^+$ and combined for 2017 MagDown, in regions of phase-space with "weak" and "strong" PID, and "in" and "out" of the $\overline{\Lambda}_c^-$ peak.

Phase-space	Weak		Strong	
	In	Out	In	Out
lab1	86.66	86.82	75.90	76.19
lab3	72.60	59.97	64.57	53.12
lab4	85.36	84.55	74.78	73.70
lab5	94.19	92.51	87.73	86.26
comb.	50.58	40.72	32.15	25.73

TABLE A.10: PID efficiencies (as percentages) for each final state of $\bar{B}_s^0 \to (D_s^+ \to K^+K^-\pi^+)\pi^-$ and combined for 2017 MagDown, in regions of phase-space with "weak" and "strong" PID, and "in" and "out" of the Λ_c^+ peak.

Phase-space	Weak		Strong	
	In	Out	In	Out
lab1	86.89	87.06	75.91	76.47
lab3	72.29	59.81	64.16	52.80
lab4	85.30	84.38	74.94	73.44
lab5	94.30	92.64	87.97	86.48
comb.	50.53	40.7	32.11	25.64

TABLE A.11: PID efficiencies (as percentages) for each final state of $B_s^0 \to (D_s^- \to K^+K^-\pi^-)\pi^+$ and combined for 2017 MagUp, in regions of phase-space with "weak" and "strong" PID, and "in" and "out" of the $\overline{\Lambda}_c^-$ peak.

Phase-space	Weak		Strong	
	In	Out	In	Out
lab1	87.20	87.39	76.91	76.89
lab3	72.23	59.75	64.10	51.72
lab4	85.39	84.42	75.22	73.64
lab5	94.01	92.37	87.44	85.93
comb.	50.56	40.72	32.43	25.16

TABLE A.12: PID efficiencies (as percentages) for each final state of $\bar{B}_s^0 \to (D_s^+ \to K^+K^-\pi^+)\pi^-$ and combined for 2017 MagUp, in regions of phase-space with "weak" and "strong" PID, and "in" and "out" of the Λ_c^+ peak.

Phase-space	Weak		Strong	
	In	Out	In	Out
lab1	86.34	86.47	75.33	75.85
lab3	72.21	60.04	64.45	52.83
lab4	85.66	84.80	75.76	74.27
lab5	94.02	92.27	87.35	85.89
comb.	50.21	40.62	32.13	25.56

TABLE A.13: PID efficiencies (as percentages) for each final state of $B_s^0 \to (D_s^- \to K^+K^-\pi^-)\pi^+$ and combined for 2018 MagDown, in regions of phase-space with "weak" and "strong" PID, and "in" and "out" of the $\overline{\Lambda}_c^-$ peak.

Phase-space	Weak		Strong	
	In	Out	In	Out
lab1	86.09	86.28	75.35	75.39
lab3	72.58	60.02	64.14	53.12
lab4	85.43	84.43	74.93	73.61
lab5	94.20	92.42	87.79	86.23
comb.	50.28	40.41	31.79	25.42

TABLE A.14: PID efficiencies (as percentages) for each final state of $\bar{B}_s^0 \to (D_s^+ \to K^+K^-\pi^+)\pi^-$ and combined for 2017 MagDown, in regions of phase-space with "weak" and "strong" PID, and "in" and "out" of the Λ_c^+ peak.

Phase-space	Weak		Strong	
	In	Out	In	Out
lab1	86.31	86.54	75.80	75.55
lab3	72.17	59.89	64.04	52.89
lab4	85.21	84.28	74.52	73.32
lab5	94.27	92.56	87.91	86.33
comb.	50.04	40.43	31.80	25.29

TABLE A.15: PID efficiencies (as percentages) for each final state of $B_s^0 \to (D_s^- \to K^+K^-\pi^-)\pi^+$ and combined for 2017 MagUp, in regions of phase-space with "weak" and "strong" PID, and "in" and "out" of the $\overline{\Lambda}_c^-$ peak.

Phase-space	Weak		Strong	
	In	Out	In	Out
lab1	86.58	86.86	75.90	76.10
lab3	72.08	59.78	55.90	52.75
lab4	85.20	84.33	75.12	73.49
lab5	93.95	92.31	87.25	85.83
comb.	49.95	40.42	27.81	25.32

TABLE A.16: PID efficiencies (as percentages) for each final state of $\bar{B}_s^0 \to (D_s^+ \to K^+K^-\pi^+)\pi^-$ and combined for 2018 MagUp, in regions of phase-space with "weak" and "strong" PID, and "in" and "out" of the Λ_c^+ peak.

Phase-space	In	Out
lab1	86.64	76.56
lab3	90.43	85.15
lab4	93.63	84.22
lab5	91.49	85.31
comb.	67.12	46.84

TABLE A.17: PID efficiencies (as percentages) for each final state of $B_s^0 \to (D_s^- \to \pi^+\pi^-\pi^-)\pi^+$ and combined for 2015 MagDown, in regions of phase-space "in" and "out" of the resonance region.

Phase-space	In	Out
lab1	84.83	75.41
lab3	92.11	85.58
lab4	93.15	83.75
lab5	91.10	85.33
comb.	66.31	46.12

TABLE A.18: PID efficiencies (as percentages) for each final state of $\bar{B}_s^0 \to (D_s^+ \to \pi^-\pi^+\pi^+)\pi^-$ and combined for 2016 MagDown, in regions of phase-space "in" and "out" of the resonance region

Phase-space	In	Out
lab1	85.14	75.80
lab3	92.78	85.69
lab4	93.58	83.78
lab5	92.93	86.01
comb.	68.70	46.80

TABLE A.19: PID efficiencies (as percentages) for each final state of $B_s^0 \to (D_s^- \to \pi^+\pi^-\pi^-)\pi^+$ and combined for 2015 MagUp, in regions of phase-space "in" and "out" of the resonance region.

Phase-space	In	Out
lab1	86.16	76.27
lab3	91.35	85.02
lab4	93.96	84.66
lab5	90.27	85.15
comb.	66.76	46.75

TABLE A.20: PID efficiencies (as percentages) for each final state of $\bar{B}_s^0 \to (D_s^+ \to \pi^-\pi^+\pi^+)\pi^-$ and combined for 2015 MagUp, in regions of phase-space "in" and "out" of the resonance region.

Phase-space	In	Out
lab1	86.58	76.41
lab3	91.33	85.18
lab4	93.44	84.15
lab5	91.26	85.20
comb.	67.43	46.66

TABLE A.21: PID efficiencies (as percentages) for each final state of $B_s^0 \to (D_s^- \to \pi^+\pi^-\pi^-)\pi^+$ and combined for 2016 MagDown, in regions of phase-space "in" and "out" of the resonance region.

Phase-space	In	Out
lab1	86.70	76.05
lab3	91.39	85.57
lab4	93.27	83.90
lab5	91.36	85.47
comb.	67.52	46.67

TABLE A.22: PID efficiencies (as percentages) for each final state of $\bar{B}_s^0 \to (D_s^+ \to \pi^-\pi^+\pi^+)\pi^-$ and combined for 2016 MagDown, in regions of phase-space "in" and "out" of the resonance region

Phase-space	In	Out
lab1	87.28	76.29
lab3	91.98	85.80
lab4	93.21	83.89
lab5	91.80	85.69
comb.	68.69	47.05

TABLE A.23: PID efficiencies (as percentages) for each final state of $B_s^0 \to (D_s^- \to \pi^+\pi^-\pi^-)\pi^+$ and combined for 2016 MagUp, in regions of phase-space "in" and "out" of the resonance region.

Phase-space	In	Out
lab1	87.38	76.59
lab3	91.42	85.23
lab4	93.84	84.46
lab5	91.63	85.25
comb.	68.69	47.00

TABLE A.24: PID efficiencies (as percentages) for each final state of $\bar{B}_s^0 \to (D_s^+ \to \pi^-\pi^+\pi^+)\pi^-$ and combined for 2016 MagUp, in regions of phase-space "in" and "out" of the resonance region.

Phase-space	In	Out
lab1	87.54	76.87
lab3	91.54	85.27
lab4	93.58	84.35
lab5	91.40	85.28
comb.	68.54	47.15

TABLE A.25: PID efficiencies (as percentages) for each final state of $B_s^0 \to (D_s^- \to \pi^+\pi^-\pi^-)\pi^+$ and combined for 2017 MagDown, in regions of phase-space "in" and "out" of the resonance region.

Phase-space	In	Out
lab1	87.23	76.44
lab3	91.52	85.56
lab4	93.50	84.18
lab5	91.48	85.60
comb.	68.28	47.13

TABLE A.26: PID efficiencies (as percentages) for each final state of $\bar{B}_s^0 \to (D_s^+ \to \pi^-\pi^+\pi^+)\pi^-$ and combined for 2017 MagDown, in regions of phase-space "in" and "out" of the resonance region

Phase-space	In	Out
lab1	86.95	76.62
lab3	91.70	85.79
lab4	93.19	84.08
lab5	92.01	85.80
comb.	68.37	47.42

TABLE A.27: PID efficiencies (as percentages) for each final state of $B_s^0 \to (D_s^- \to \pi^+\pi^-\pi^-)\pi^+$ and combined for 2017 MagUp, in regions of phase-space "in" and "out" of the resonance region.

Phase-space	In	Out
lab1	87.59	77.06
lab3	91.68	85.38
lab4	93.71	84.48
lab5	91.78	85.24
comb.	69.07	47.38

TABLE A.28: PID efficiencies (as percentages) for each final state of $\bar{B}_s^0 \to (D_s^+ \to \pi^-\pi^+\pi^+)\pi^-$ and combined for 2017 MagUp, in regions of phase-space "in" and "out" of the resonance region.

Phase-space	In	Out
lab1	86.49	76.03
lab3	91.31	85.12
lab4	93.58	84.21
lab5	91.11	85.12
comb.	67.33	46.39

TABLE A.29: PID efficiencies (as percentages) for each final state of $B_s^0 \to (D_s^- \to \pi^+\pi^-\pi^-)\pi^+$ and combined for 2018 MagDown, in regions of phase-space "in" and "out" of the resonance region.

Phase-space	In	Out
lab1	86.71	75.72
lab3	91.17	85.50
lab4	93.35	83.86
lab5	91.47	85.56
comb.	67.50	46.45

TABLE A.30: PID efficiencies (as percentages) for each final state of $\bar{B}_s^0 \to (D_s^+ \to \pi^-\pi^+\pi^+)\pi^-$ and combined for 2018 MagDown, in regions of phase-space "in" and "out" of the resonance region.

Phase-space	In	Out
lab1	86.87	75.88
lab3	91.84	85.66
lab4	93.40	83.93
lab5	91.60	85.67
comb.	68.26	46.74

TABLE A.31: PID efficiencies (as percentages) for each final state of $B_s^0 \to (D_s^- \to \pi^+\pi^-\pi^-)\pi^+$ and combined for 2018 MagUp, in regions of phase-space "in" and "out" of the resonance region.

Phase-space	In	Out
lab1	86.65	76.46
lab3	91.68	85.17
lab4	93.69	84.42
lab5	91.45	85.21
comb.	68.06	46.84

TABLE A.32: PID efficiencies (as percentages) for each final state of $\bar{B}_s^0 \to (D_s^+ \to \pi^-\pi^+\pi^+)\pi^-$ and combined for 2018 MagUp, in regions of phase-space "in" and "out" of the resonance region.

B

Efficiency Tables

The following tables summarise the binned generator and trigger efficiencies for each mode of interest considered in the early measurements analysis of Chapter 5.

p_T (GeV/c)	$2.0 < y < 2.625$	$2.625 < y < 3.25$	$3.25 < y < 3.875$	$3.875 < y < 4.5$
0.0 - 10.0	0.2921 ± 0.0019	0.6407 ± 0.002	0.818 ± 0.0018	0.8497 ± 0.0019
10.0 - 20.0	0.8381 ± 0.0038	0.9757 ± 0.0018	0.9871 ± 0.0016	0.9412 ± 0.0043
20.0 - 30.0	0.9593 ± 0.0063	0.9908 ± 0.0037	0.9975 ± 0.0025	0.9834 ± 0.0095
30.0 - 40.0	0.9581 ± 0.0155	1.0000 ± 0.0000	1.0000 ± 0.0	1.0000 ± 0.0000

TABLE B.1: Binned generator efficiencies for $B_s^0 \to (D_s^- \to K^+K^-\pi^-)\pi^+$

p_T (GeV/c)	$2.0 < y < 2.625$	$2.625 < y < 3.25$	$3.25 < y < 3.875$	$3.875 < y < 4.5$
0.0 - 10.0	0.2554 ± 0.0018	0.6021 ± 0.0021	0.7942 ± 0.0019	0.8341 ± 0.0019
10.0 - 20.0	0.8105 ± 0.0041	0.9723 ± 0.0020	0.9815 ± 0.0019	0.9430 ± 0.0043
20.0 - 30.0	0.9440 ± 0.0076	0.9985 ± 0.0015	0.9974 ± 0.0026	0.9800 ± 0.0110
30.0 - 40.0	0.9839 ± 0.0092	1.0000 ± 0.0000	1.0000 ± 0.0000	1.0000 ± 0.0000

TABLE B.2: Binned generator efficiencies for $B^0 \to (D^- \to K^+\pi^-\pi^-)\pi^+$

p_T (GeV/c)	$2.0 < y < 2.625$	$2.625 < y < 3.25$	$3.25 < y < 3.875$	$3.875 < y < 4.5$
0.0 - 10.0	0.2617 ± 0.0019	0.6202 ± 0.0021	0.8096 ± 0.0019	0.8476 ± 0.0019
10.0 - 20.0	0.8333 ± 0.0042	0.9823 ± 0.0016	0.9833 ± 0.0019	0.9382 ± 0.0046
20.0 - 30.0	0.9557 ± 0.0070	0.9984 ± 0.0016	0.9908 ± 0.0053	0.9933 ± 0.0067
30.0 - 40.0	0.9809 ± 0.0109	1.0000 ± 0.0000	1.0000 ± 0.0000	1.0000 ± 0.0000

TABLE B.3: Binned generator efficiencies for $B^0 \to (D^- \to K^+\pi^-\pi^-)K^+$

p_T (GeV/c)	$2.0 < y < 2.625$	$2.625 < y < 3.25$	$3.25 < y < 3.875$	$3.875 < y < 4.5$
0.0 - 10.0	0.28 ± 0.00	0.62 ± 0.00	0.80 ± 0.00	0.85 ± 0.00
10.0 - 20.0	0.83 ± 0.01	0.98 ± 0.00	0.99 ± 0.00	0.95 ± 0.01
20.0 - 30.0	0.94 ± 0.01	0.99 ± 0.01	1.00 ± 0.00	1.00 ± 0.00
30.0 - 40.0	0.97 ± 0.02	1.00 ± 0.00	1.00 ± 0.00	1.00 ± 0.00

TABLE B.4: Binned generator efficiencies for $B^+ \to (D^0 \to K^+\pi^-)\pi^+$

p_T (GeV/c)	$2.0 < y < 2.625$	$2.625 < y < 3.25$	$3.25 < y < 3.875$	$3.875 < y < 4.5$
0.0 - 10.0	0.2968 ± 0.0019	0.6499 ± 0.002	0.8187 ± 0.0018	0.8453 ± 0.0019
10.0 - 20.0	0.8435 ± 0.0038	0.9781 ± 0.0017	0.987 ± 0.0016	0.9615 ± 0.0035
20.0 - 30.0	0.9549 ± 0.0064	0.9944 ± 0.0028	1.0000 ± 0.0000	0.9943 ± 0.0057
30.0 - 40.0	0.9791 ± 0.0104	1.0000 ± 0.0000	1.0000 ± 0.0000	1.0000 ± 0.0000

TABLE B.5: Binned generator efficiencies for $\Lambda_b^0 \to (\Lambda_c^+ \to pK^-\pi^+)\pi^+$

p_T (GeV/c)	$2.0 < y < 2.625$	$2.625 < y < 3.25$	$3.25 < y < 3.875$	$3.875 < y < 4.5$
0.0 - 10.0	0.0469 ± 0.0022	0.1143 ± 0.0023	0.1319 ± 0.0023	0.0971 ± 0.0022
10.0 - 20.0	0.1243 ± 0.0052	0.2692 ± 0.0071	0.2832 ± 0.0086	0.2116 ± 0.0105
20.0 - 30.0	0.1969 ± 0.0176	0.3280 ± 0.0241	0.3571 ± 0.0311	0.2308 ± 0.0442
30.0 - 40.0	0.3125 ± 0.0473	0.3514 ± 0.0555	0.4500 ± 0.1112	0.3636 ± 0.145

TABLE B.6: Binned HLT2 efficiencies for $B^0 \to (D^- \to K^+\pi^-\pi^-)\pi^+$

p_T (GeV/c)	$2.0 < y < 2.625$	$2.625 < y < 3.25$	$3.25 < y < 3.875$	$3.875 < y < 4.5$
0.0 - 10.0	0.0398 ± 0.002	0.1115 ± 0.0022	0.1307 ± 0.0022	0.0949 ± 0.0021
10.0 - 20.0	0.1335 ± 0.0050	0.2559 ± 0.0068	0.2744 ± 0.0083	0.2263 ± 0.0103
20.0 - 30.0	0.2218 ± 0.0179	0.3664 ± 0.0234	0.3519 ± 0.0325	0.3208 ± 0.0453
30.0 - 40.0	0.2200 ± 0.0414	0.3188 ± 0.0561	0.3889 ± 0.0812	0.3333 ± 0.1571

TABLE B.7: Binned HLT2 efficiencies for $B^0 \to (D^- \to K^+\pi^-\pi^-)K^+$

p_T (GeV/c)	$2.0 < y < 2.625$	$2.625 < y < 3.25$	$3.25 < y < 3.875$	$3.875 < y < 4.5$
0.0 - 10.0	0.0427 ± 0.0021	0.1122 ± 0.0023	0.1387 ± 0.0024	0.0995 ± 0.0023
10.0 - 20.0	0.1272 ± 0.0053	0.2846 ± 0.0074	0.3160 ± 0.0090	0.2234 ± 0.011
20.0 - 30.0	0.2304 ± 0.0205	0.3089 ± 0.0236	0.3731 ± 0.0341	0.2360 ± 0.0450
30.0 - 40.0	0.3229 ± 0.0477	0.2951 ± 0.0584	0.2414 ± 0.0795	0.3333 ± 0.1571

TABLE B.8: Binned HLT2 efficiencies for $B_s^0 \to (D_s^- \to K^+K^-\pi^-)\pi^+$

p_T (GeV/c)	$2.0 < y < 2.625$	$2.625 < y < 3.25$	$3.25 < y < 3.875$	$3.875 < y < 4.5$
0.0 - 10.0	0.0374 ± 0.0019	0.0907 ± 0.002	0.097 ± 0.0019	0.0717 ± 0.0018
10.0 - 20.0	0.0983 ± 0.0044	0.1608 ± 0.0056	0.1683 ± 0.0069	0.1619 ± 0.009
20.0 - 30.0	0.1291 ± 0.0147	0.1887 ± 0.0194	0.2338 ± 0.0278	0.2151 ± 0.0426
30.0 - 40.0	0.1429 ± 0.0353	0.1967 ± 0.0509	0.1724 ± 0.0701	0.0909 ± 0.0867

TABLE B.9: Binned HLT2 efficiencies for $B^+ \to (D^0 \to K^+\pi^-)\pi^+$

p_T (GeV/c)	$2.0 < y < 2.625$	$2.625 < y < 3.25$	$3.25 < y < 3.875$	$3.875 < y < 4.5$
0.0 - 10.0	0.0395 ± 0.002	0.1017 ± 0.0022	0.1167 ± 0.0022	0.0893 ± 0.0022
10.0 - 20.0	0.1316 ± 0.0051	0.2484 ± 0.0069	0.2694 ± 0.0084	0.1843 ± 0.0097
20.0 - 30.0	0.1761 ± 0.0166	0.3278 ± 0.0246	0.3364 ± 0.0319	0.2647 ± 0.0437
30.0 - 40.0	0.2222 ± 0.0418	0.3239 ± 0.0555	0.3784 ± 0.0797	0.2500 ± 0.1531

TABLE B.10: Binned HLT2 efficiencies for $\Lambda_b^0 \to (\Lambda_c^+ \to pK^-\pi^+)\pi^+$

p_T (GeV/c)	$2.0 < y < 2.625$	$2.625 < y < 3.25$	$3.25 < y < 3.875$	$3.875 < y < 4.5$
0.0 - 10.0	0.5886 ± 0.0263	0.6251 ± 0.0112	0.6204 ± 0.0099	0.6046 ± 0.0126
10.0 - 20.0	0.5919 ± 0.024	0.6107 ± 0.0163	0.6006 ± 0.0188	0.5621 ± 0.0291
20.0 - 30.0	0.5326 ± 0.052	0.6441 ± 0.0441	0.5294 ± 0.0541	0.6875 ± 0.1159
30.0 - 40.0	0.7241 ± 0.083	0.6667 ± 0.0962	0.6667 ± 0.1925	1.0000 ± 0.0000

TABLE B.11: Binned HLT1 efficiencies relative to HLT2 for $B^0 \to (D^- \to K^+\pi^-\pi^-)\pi^+$

p_T (GeV/c)	$2.0 < y < 2.625$	$2.625 < y < 3.25$	$3.25 < y < 3.875$	$3.875 < y < 4.5$
0.0 - 10.0	0.6623 ± 0.0272	0.6147 ± 0.0111	0.6256 ± 0.0096	0.6188 ± 0.0126
10.0 - 20.0	0.5842 ± 0.0225	0.602 ± 0.0161	0.5773 ± 0.0186	0.6527 ± 0.027
20.0 - 30.0	0.6909 ± 0.0441	0.5725 ± 0.0421	0.5667 ± 0.064	0.6538 ± 0.0933
30.0 - 40.0	0.6471 ± 0.1159	0.5833 ± 0.1006	0.7692 ± 0.1169	0.0000 ± 0.0000

TABLE B.12: Binned HLT1 efficiencies relative to HLT2 for $B^0 \to (D^- \to K^+\pi^-\pi^-)K^+$

p_T (GeV/c)	$2.0 < y < 2.625$	$2.625 < y < 3.25$	$3.25 < y < 3.875$	$3.875 < y < 4.5$
0.0 - 10.0	0.5939 ± 0.0270	0.6255 ± 0.0114	0.6293 ± 0.0097	0.6424 ± 0.0124
10.0 - 20.0	0.6310 ± 0.0225	0.6226 ± 0.0159	0.6425 ± 0.0176	0.6477 ± 0.0277
20.0 - 30.0	0.5673 ± 0.0486	0.6609 ± 0.0441	0.6316 ± 0.0553	0.6667 ± 0.1111
30.0 - 40.0	0.6400 ± 0.0960	0.6364 ± 0.1026	0.5000 ± 0.2500	1.0000 ± 0.0000

TABLE B.13: Binned HLT1 efficiencies relative to HLT2 for $B_s^0 \to (D_s^- \to K^+K^-\pi^-)\pi^+$

p_T (GeV/c)	$2.0 < y < 2.625$	$2.625 < y < 3.25$	$3.25 < y < 3.875$	$3.875 < y < 4.5$
0.0 - 10.0	0.5788 ± 0.0289	0.6244 ± 0.0123	0.6092 ± 0.0113	0.6117 ± 0.0141
10.0 - 20.0	0.6023 ± 0.0261	0.6007 ± 0.0207	0.5917 ± 0.0235	0.6808 ± 0.0319
20.0 - 30.0	0.6182 ± 0.0655	0.6094 ± 0.061	0.6429 ± 0.0739	0.6316 ± 0.1107
30.0 - 40.0	0.4615 ± 0.1383	0.4286 ± 0.187	0.5714 ± 0.187	0.0 ± 0.0

TABLE B.14: Binned HLT1 efficiencies relative to HLT2 for $B^+ \to (D^0 \to K^+\pi^-)\pi^+$

p_T (GeV/c)	$2.0 < y < 2.625$	$2.625 < y < 3.25$	$3.25 < y < 3.875$	$3.875 < y < 4.5$
0.0 - 10.0	0.5544 ± 0.0294	0.5878 ± 0.0128	0.5924 ± 0.0116	0.5896 ± 0.0146
10.0 - 20.0	0.5961 ± 0.0242	0.5754 ± 0.0184	0.5966 ± 0.0212	0.6714 ± 0.0322
20.0 - 30.0	0.5526 ± 0.057	0.6044 ± 0.0513	0.5357 ± 0.0666	0.5238 ± 0.109
30.0 - 40.0	0.5000 ± 0.1118	0.7222 ± 0.1056	0.5000 ± 0.1768	0.0000 ± 0.0000

TABLE B.15: Binned HLT1 efficiencies relative to HLT2 for $\Lambda_b^0 \to (\Lambda_c^+ \to pK^-\pi^+)\pi^+$

C

$\bar{B} \to \bar{D}D$ Experimental Inputs

The following tables summarise explicitly the experimental inputs, with correlations, that were used in the $B \to DD$ phenomenological analysis of Chapter 6.

Input	Value (%)
$R_1 = \frac{f_s}{f_d}\frac{\mathcal{B}(\bar{B}_s \to D^+ D^-)}{\mathcal{B}(\bar{B}^0 \to D^- D^+)}$	27.6 ± 5.2 [232]
$R_2 = \frac{f_s}{f_d}\frac{f_d}{f_u}\frac{1}{\epsilon'_{\rm rel}}\frac{\mathcal{B}(\bar{B}_s \to \bar{D}^0 D^0)}{\mathcal{B}(B^- \to D^0 D_s^-)}$	$(9.24 \pm 1.01) \times 10^{-1}$ [234]
$R_3 = \frac{f_d}{f_u}\frac{1}{\epsilon'_{\rm rel}}\frac{\mathcal{B}(\bar{B}^0 \to \bar{D}^0 D^0)}{\mathcal{B}(B^- \to D_s^- D^0)}$	$(2.52 \pm 1.17) \times 10^{-1}$ [232]
$R_4 = \frac{f_s}{f_d}\frac{\mathcal{B}(D_s^+ \to K^+K^-\pi^+)}{\mathcal{B}(D^+ \to K^-\pi^+\pi^+)}\frac{\mathcal{B}(\bar{B}_s \to D_s^- D_s^+)}{\mathcal{B}(\bar{B}^0 \to D_s^- D^+)}$	8.59 ± 0.01 [232]
$R_5 = \frac{f_u}{f_d}\frac{\mathcal{B}(D^0 \to K^-\pi^+)}{\mathcal{B}(D^+ \to K^-\pi^+\pi^+)}\frac{\mathcal{B}(B^- \to D_s^- D^0)}{\mathcal{B}(\bar{B}^0 \to D^- D_s^+)}$	51.9 ± 2.9 [232]
$R_6 = \frac{f_s}{f_d}\frac{\mathcal{B}(\bar{B}_s \to D_s^- D^+)}{\mathcal{B}(\bar{B}^0 \to D_s^- D^+)}$	$(9.79 \pm 1.74) \times 10^{-1}$ [232]
$R_7 = \frac{\mathcal{B}(B^- \to D^- D^0)\mathcal{B}(D^- \to K^+\pi^-\pi^-)}{\mathcal{B}(B^- \to D_s^- D^0)\mathcal{B}(D_s^- \to K^+K^-\pi^-)}$	7.25 ± 0.13 [233]
$\mathcal{B}_1^{\rm CLEO} = 2f_{+-}\mathcal{B}(B^- \to D_s^- D^0)\mathcal{B}(D^0 \to K^-\pi^+)\mathcal{B}(D_s^- \to \phi\pi^-)$	$(1.72 \pm 0.46) \times 10^{-3}$ [235]
$\mathcal{B}_2^{\rm CLEO} = 2f_{00}\mathcal{B}(\bar{B}^0 \to D_s^- D^+)\mathcal{B}(D^+ \to K^-\pi^+\pi^+)\mathcal{B}(D_s^- \to \phi\pi^-)$	$(2.80 \pm 1.00) \times 10^{-3}$ [235]
$\mathcal{B}_1^{\rm BaBar}$ (Dir.) $= \mathcal{B}(B^- \to D_s^- D^0)$	$(9.0 \pm 2.28) \times 10^{-1}$ [236]
$\mathcal{B}_1^{\rm BaBar}$ (Re.) $= \mathcal{B}(B^- \to D_s^- D^0)/k$	$(7.4 \pm 2.1) \times 10^{-1}$ [236]
$\mathcal{B}_2^{\rm BaBar}$ (Dir.) $= \mathcal{B}(\bar{B}^0 \to D_s^- D^+)$	1.33 ± 0.37 [236]
$\mathcal{B}_2^{\rm BaBar}$ (Re.) $= \mathcal{B}(\bar{B}^0 \to D_s^- D^+)/k$	1.11 ± 0.24 [236]
$\mathcal{B}_3^{\rm BaBar} = 2f_{00}\mathcal{B}(D^+ \to K^-\pi^+\pi^+)^2\mathcal{B}(\bar{B}^0 \to D^- D^+)$	$(2.37 \pm 0.40) \times 10^{-4}$ [237]
$\mathcal{B}_4^{\rm BaBar} = 2f_{+-}\mathcal{B}(D^+ \to K^-\pi^+\pi^+)\mathcal{B}(B^- \to D^- D^0)$	$(3.50 \pm 0.65) \times 10^{-3}$ [237]
$\mathcal{B}_1^{\rm Belle} = 2f_{+-}\mathcal{B}(B^- \to D^- D^0)$	$(3.85 \pm 0.49) \times 10^{-2}$ [239]
$\mathcal{B}_{2a}^{\rm Belle} = 2f_{00}\mathcal{B}(\bar{B}^0 \to D_s^- D^+)\mathcal{B}(D_s^- \to \phi(\to K^+K^-)\pi^-)$	$(1.68 \pm 0.21) \times 10^{-2}$ [238]
$\mathcal{B}_{2b}^{\rm Belle} = 2f_{00}\mathcal{B}(\bar{B}^0 \to D_s^- D^+)\mathcal{B}(D_s^- \to K^{*0}(\to K^-\pi^+)K^-)$	$(1.83 \pm 0.23) \times 10^{-2}$ [238]
$\mathcal{B}_{2c}^{\rm Belle} = 2f_{00}\mathcal{B}(\bar{B}^0 \to D^- D^+)\mathcal{B}(D^+ \to K^-\pi^+\pi^+)^2$	$(7.60 \pm 1.03) \times 10^{-3}$ [238]
$\mathcal{B}_3^{\rm Belle} = 2f_{00}\mathcal{B}(\bar{B}^0 \to D^- D^+)\mathcal{B}(D^+ \to K^-\pi^+\pi^+)^2$	$(1.87 \pm 0.20) \times 10^{-4}$ [240]
$\mathcal{B}_4^{\rm Belle} = \mathcal{B}(B_s^0 \to D_s^- D_s^+)$	$(5.90 \pm 1.64) \times 10^{-1}$ [241]
$R_4^{\rm CDF} = \frac{f_s}{f_d}\Big\vert_{\rm Tev}\frac{\mathcal{B}(D_s^+ \to \phi(\to K^+K^-)\pi^+)}{\mathcal{B}(D^+ \to K^-\pi^+\pi^+)}\frac{\mathcal{B}(\bar{B}_s \to D_s^- D_s^+)}{\mathcal{B}(\bar{B}^0 \to D_s^- D^+)}$	4.65 ± 0.61 [228]
$\frac{f_s}{f_d}\mathcal{B}(D_s^+ \to K^+K^-\pi^+)$	1.44 ± 0.10 [58, 225, 226]
$\epsilon(B^- \to D_s^- D^0)$	$(1.66 \pm 0.03) \times 10^{-1}$ [232]
$\epsilon(\overline{B}_s^0 \to \overline{D}^0(\to K^+\pi^-)D^0(\to K^-\pi^+))$	$(1.90 \pm 0.03) \times 10^{-1}$ [232]
$\epsilon(\overline{B}_s^- \to \overline{D}^0(\to K^-\pi^+\pi^-\pi^+)D^0(\to K^-\pi^+))$	$(6.1 \pm 0.2) \times 10^{-2}$ [232]
$\mathcal{B}(D_s^- \to K^+K^-\pi^+)$	5.39 ± 0.15 [310]
$\mathcal{B}(D^0 \to K^-\pi^+)$	3.95 ± 0.03 [310]
$\mathcal{B}(D^0 \to K^-\pi^+\pi^-\pi^+)$	8.22 ± 0.14 [310]
$\mathcal{B}(D^+ \to K^+\pi^-\pi^+)$	9.38 ± 0.16 [310]
$\mathcal{B}(D_s^- \to \phi\pi^-)$	4.5 ± 0.4 [14]
$\mathcal{B}(D_s^- \to \phi(\to K^+K^-)\pi^-)$	2.24 ± 0.08 [311]
$\mathcal{B}(D_s^- \to K^{*0}(\to K^+\pi^-)K^-)$	2.58 ± 0.08 [311]
$\mathcal{B}(D_s^- \to K_S^0(\to \pi^+\pi^-)K^-)$	1.01 ± 0.03 [312]
f_{00}	48.8 ± 1.3 [313]

TABLE C.1: B and D decay branching ratio input data from experiment.

Input	Ref	Correlation
R_1	[232]	$\begin{pmatrix} 100 & 2.12 & 0.0 & 4.64 & 0.0 \\ 2.12 & 100 & 0.23 & 4.61 & -1.87 \\ 0.0 & 0.23 & 100 & 0.0 & -0.76 \\ 4.64 & 4.61 & 0.0 & 100 & 3.14 \\ 0.0 & -1.87 & -0.76 & 3.14 & 100 \end{pmatrix}$
R_2	[232]	
R_3	[232]	
R_4	[232]	
R_5	[232]	
$\mathcal{B}_1^{\text{CLEO}}$	[235]	$\begin{pmatrix} 100 & 38 \\ 38 & 100 \end{pmatrix}$
$\mathcal{B}_2^{\text{CLEO}}$	[235]	
$\mathcal{B}_{2a}^{\text{Belle}}$	[238]	$\begin{pmatrix} 100 & 81 & 77 \\ 81 & 100 & 77 \\ 77 & 77 & 100 \end{pmatrix}$
$\mathcal{B}_{2b}^{\text{Belle}}$	[238]	
$\mathcal{B}_{2c}^{\text{Belle}}$	[238]	

TABLE C.2: Correlations in % for the branching ratio data used.

Bibliography

[1] J. Davies, C. Fitzpatrick, J. Gooding, J. Patoc and N. Skidmore, "Measurement of $A_{\rm fs}^{s}$ in $\overline{B}{}_{s}^{0} \to D_{s}^{+}\pi$ at LHCb." LHCb-ANA-2024-031, 2024.

[2] Y. Amhis et al., "Report from the Early Measurements Task Force." LHCb-INT-2024-003, 2024.

[3] J. Davies, M. Jung and S. Schacht, *$\overline{B} \to \overline{D}D$ decays and the extraction of f_d/f_u at hadron colliders*, *JHEP* **01** (2024) 191 [*Erratum ibid JHEP* **01** (2025) 162], [2311.16952].

[4] J. Davies, S. Schacht, N. Skidmore and A. Soni, *Reappraisal of SU(3)-flavor breaking in $B \to DP$*, *Phys. Rev. D* **109** (2024) 113006 [2403.04878].

[5] S. Biscoveanu, C.-J. Haster, S. Vitale and J. Davies, *Quantifying the effect of power spectral density uncertainty on gravitational-wave parameter estimation for compact binary sources*, *Phys. Rev. D* **102** (2020) 023008.

[6] S. Hageboeck et al., *Training and Onboarding initiatives in High Energy Physics experiments*, 2310.07342. Submitted to Frontiers in Big Data.

[7] I. Stewart, *Why Beauty Is Truth: The History of Symmetry*, Basic Books (2007).

[8] K. Schmid, D. Marx and A. Samal, *Computation of a face attractiveness index based on neoclassical canons, symmetry, and golden ratios*, *Pattern Recognition* **41** (2008) 2710.

[9] M. Jung and S. Schacht, *Standard model predictions and new physics sensitivity in $B \to DD$ decays*, *Phys. Rev. D* **91** (2015) 034027 [1410.8396].

[10] Y. Nagashima, *Beyond the standard model of elementary particle physics*, Wiley-VCH Verlag, Weinheim, Germany, first edition. ed. (2014).

[11] J. Joyce, *Finnegans Wake*, Viking Press, New York (1939).

[12] Merriam-Webster, *What Does 'Quark' Have to Do with Finnegans Wake?*, in *Merriam-Webster.com dictionary* (2023), https://www.merriam-webster.com/words-at-play/quark.

[13] A. Kamal, *Particle Physics*, Graduate Texts in Physics, Springer Berlin Heidelberg, Berlin, Heidelberg (2014).

[14] Particle Data Group collaboration, *Review of Particle Physics*, *PTEP* **2022** (2022) 083C01. Online updates at https://pdg.lbl.gov/.

[15] Nobel Prize Outreach, "All Nobel Prizes in Physics." https://www.nobelprize.org/prizes/lists/all-nobel-prizes-in-physics. Accessed 20 June 2024.

[16] Y. Fukuda et al., *Evidence for Oscillation of Atmospheric Neutrinos*, *Phys Rev Lett.* **81** (1998) 1562 [hep-ex/9807003].

[17] KATRIN collaboration, *Direct neutrino-mass measurement with sub-electronvolt sensitivity*, *Nature Phys.* **18** (2022) 160 [2105.08533].

[18] H. Yukawa, *On the Interaction of Elementary Particles I*, *Proc. Phys. Math. Soc. Jap.* **17** (1935) 48.

[19] F. Close, *The Infinity Puzzle: How the quest to understand quantum field theory led to extraordinary science, high politics, and the world's most expensive experiment*, OUP Oxford (2011).

[20] ATLAS collaboration, *Observation of a new particle in the search for the Standard Model Higgs boson with the ATLAS detector at the LHC*, *Phys. Lett. B* **716** (2012) 1 [1207.7214].

[21] CMS collaboration, *Observation of a New Boson at a Mass of 125 GeV with the CMS Experiment at the LHC*, *Phys. Lett. B* **716** (2012) 30 [1207.7235].

[22] T. Aoyama, M. Hayakawa, T. Kinoshita and M. Nio, *Tenth-order electron anomalous magnetic moment - contribution of diagrams without closed lepton loops*, *Physical Review D* **91** (2014) .

[23] M. Vogel, *The anomalous magnetic moment of the electron*, *Contemporary Physics* **50** (2009) 437.

[24] E. Noether, *Invariante variationsprobleme*, *Nachrichten von der Gesellschaft der Wissenschaften zu Göttingen, Mathematisch-Physikalische Klasse* **1918** (1918) 235.

[25] M. Tinkham, *Group Theory and Quantum Mechanics*, Dover Books on Chemistry and Earth Sciences, Dover Publications (2003).

[26] W. Greiner, *Quantum Mechanics : Symmetries*, Springer Berlin Heidelberg, Berlin, Heidelberg, 2nd edition 1994. ed. (1994).

[27] L.A.B. San Martin, *Lie groups*, Latin American mathematics series, Springer, Cham, Switzerland (2021).

[28] S. Khalil, *Standard model phenomenology*, CRC Press, Boca Raton, first edition. ed. (2022).

[29] O.W. Greenberg, *Spin and unitary-spin independence in a paraquark model of baryons and mesons*, *Phys. Rev. Lett.* **13** (1964) 598.

[30] M.Y. Han and Y. Nambu, *Three-triplet model with double* SU(3) *symmetry*, *Phys. Rev.* **139** (1965) B1006.

[31] D. Griffiths, *Introduction to Elementary Particles*, Wiley (2020).

[32] C.A. Baker et al., *An improved experimental limit on the electric dipole moment of the neutron*, *Phys. Rev. Lett.* **97** (2006) 131801 [hep-ex/0602020].

[33] C. Abel et al., *Measurement of the Permanent Electric Dipole Moment of the Neutron*, *Phys. Rev. Lett.* **124** (2020) 081803 [2001.11966].

[34] C.S. Wu, E. Ambler, R.W. Hayward, D.D. Hoppes and R.P. Hudson, *Experimental test of parity conservation in beta decay*, *Phys. Rev.* **105** (1957) 1413.

[35] H.E. Logan, *TASI 2013 lectures on Higgs physics within and beyond the Standard Model*, 1406.1786.

[36] M. Kobayashi and T. Maskawa, *CP-Violation in the Renormalizable Theory of Weak Interaction*, *Progress of Theoretical Physics* **49** (1973) 652 [https://academic.oup.com/ptp/article-pdf/49/2/652/5257692/49-2-652.pdf].

[37] The CKMfitter Group, "Updated Results on the CKM Matrix." http://ckmfitter.in2p3.fr/www/results/plots_spring21/num/ckmEval_results_spring21.html. Accessed 20 June 2024.

[38] CKMFITTER GROUP collaboration, *CP violation and the CKM matrix: Assessing the impact of the asymmetric B factories*, *Eur. Phys. J. C* **41** (2005) 1 [hep-ph/0406184]. Updated results and plots available at http://ckmfitter.in2p3.fr.

[39] M. Kobayashi and T. Maskawa, *CP Violation in the Renormalizable Theory of Weak Interaction*, *Prog. Theor. Phys.* **49** (1973) 652.

[40] UTFIT collaboration, *New UTfit Analysis of the Unitarity Triangle in the Cabibbo-Kobayashi-Maskawa scheme*, *Rend. Lincei Sci. Fis. Nat.* **34** (2023) 37 [2212.03894]. Online updates at www.UTfit.org.

[41] E. Hardy, *The Republic of Plato*, no. bk. 1, Longmans, Green (1882).

[42] V.C. Rubin, W.K. Ford and N. Thonnard, *Rotational properties of 21 SC galaxies with a large range of luminosities and radii, from NGC 4605 (R=4kpc) to UGC 2885 (R=122kpc).*, *Astrophysical Journal* **238** (1980) 471.

[43] L. Koopmans and T. Treu, *The structure and dynamics of luminous and dark matter in the early-type lens galaxy of 0047-281 at z = 0.485*, *Astrophysical Journal* **583** (2003) 606.

[44] C. Kiefer, *Why quantum gravity?*, in *Approaches to Fundamental Physics: An Assessment of Current Theoretical Ideas*, I.-O. Stamatescu and E. Seiler, eds., (Berlin, Heidelberg), pp. 123–130, Springer Berlin Heidelberg (2007).

[45] S. Koren, *New Approaches to the Hierarchy Problem and their Signatures from Microscopic to Cosmic Scales*, Ph.D. thesis, UC, Santa Barbara (main), 2020. 2009.11870.

[46] M. Markevitch, A.H. Gonzalez, D. Clowe, A. Vikhlinin, W. Forman, C. Jones et al., *Direct Constraints on the Dark Matter Self-Interaction Cross Section from the Merging Galaxy Cluster 1E 0657-56*, *Astrophys.J.* **606** (2004) 819 [astro-ph/0309303].

[47] D. Clowe, M. Bradac, A.H. Gonzalez, M. Markevitch, S.W. Randall, C. Jones et al., *A direct empirical proof of the existence of dark matter*, *Astrophys. J. Lett.* **648** (2006) L109 [astro-ph/0608407].

[48] A.D. Sakharov, *Violation of CP Invariance, C asymmetry, and baryon asymmetry of the universe*, *Pisma Zh. Eksp. Teor. Fiz.* **5** (1967) 32.

[49] L. Canetti, M. Drewes and M. Shaposhnikov, *Matter and antimatter in the universe*, *New Journal of Physics* **14** (2012) .

[50] MUON G-2 collaboration, *Measurement of the Positive Muon Anomalous Magnetic Moment to 0.20 ppm*, *Phys. Rev. Lett.* **131** (2023) 161802 [2308.06230].

[51] T. Aoyama et al., *The anomalous magnetic moment of the muon in the Standard Model*, *Phys. Rept.* **887** (2020) 1 [2006.04822].

[52] S. Borsanyi et al., *Leading hadronic contribution to the muon magnetic moment from lattice QCD*, *Nature* **593** (2021) 51 [2002.12347].

[53] CMD-3 collaboration, *Measurement of the $e^+e^- \to \pi^+\pi^-$ cross section from threshold to 1.2 GeV with the CMD-3 detector*, 2302.08834.

[54] G. Colangelo et al., *Prospects for precise predictions of a_μ in the Standard Model*, 2203.15810.

[55] ATLAS, CMS, LHCB collaboration, *Flavour anomalies: a review*, *J. Phys. Conf. Ser.* **1137** (2019) 012025 [1807.11373].

[56] HEAVY FLAVOR AVERAGING GROUP, HFLAV collaboration, *Averages of b-hadron, c-hadron, and τ-lepton properties as of 2021*, *Phys. Rev. D* **107** (2023) 052008 [2206.07501].

[57] LHCB collaboration, *Test of lepton universality in beauty-quark decays*, *Nature Phys.* **18** (2022) 277 [2103.11769]. [Addendum: Nature Phys. 19, (2023)].

[58] M. Bordone, N. Gubernari, T. Huber, M. Jung and D. van Dyk, *A puzzle in $\bar{B}^0_{(s)} \to D^{(*)+}_{(s)}\{\pi^-, K^-\}$ decays and extraction of the f_s/f_d fragmentation fraction*, *Eur. Phys. J. C* **80** (2020) 951 [2007.10338].

[59] F.-M. Cai, W.-J. Deng, X.-Q. Li and Y.-D. Yang, *Probing new physics in class-I B-meson decays into heavy-light final states*, *JHEP* **10** (2021) 235 [2103.04138].

[60] W. Schmitz, *Particles, Fields and Forces: A Conceptual Guide to Quantum Field Theory and the Standard Model*, The Frontiers Collection, Springer International Publishing (2019).

[61] K. Freese, *Status of Dark Matter in the Universe*, *Int. J. Mod. Phys.* **1** (2017) 325 [1701.01840].

[62] J.L. Feng, *The WIMP paradigm: Theme and variations*, *SciPost Phys. Lect. Notes* **71** (2023) 1 [2212.02479].

[63] P. Ilten, Y. Soreq, J. Thaler, M. Williams and W. Xue, *Proposed Inclusive Dark Photon Search at LHCb*, *Phys. Rev. Lett.* **116** (2016) 251803 [1603.08926].

[64] A. Einstein, *Feldgleichungen der Gravitation*, *Preussische Akademie der Wissenschaften, Sitzungsberichte* (1915) 844.

[65] P. Fleury, *Gravitation : from Newton to Einstein*, SpringerBriefs in Physics Ser., Springer, Cham (2020).

[66] R. Feynman, *Feynman Lectures On Gravitation*, CRC Press (2018).

[67] L.D. Landau, *On the conservation laws for weak interactions*, *Nucl. Phys.* **3** (1957) 127.

[68] R.L. Garwin, L.M. Lederman and M. Weinrich, *Observations of the failure of conservation of parity and charge conjugation in meson decays: the magnetic moment of the free muon*, *Phys. Rev.* **105** (1957) 1415.

[69] J.H. Christenson, J.W. Cronin, V.L. Fitch and R. Turlay, *Evidence for the* 2π *Decay of the* K_2^0 *Meson*, *Phys. Rev. Lett.* **13** (1964) 138.

[70] D.H. Perkins, *Introduction to High Energy Physics*, Cambridge University Press, 4 ed. (2000), 10.1017/CBO9780511809040.

[71] G. Luders, *On the Equivalence of Invariance under Time Reversal and under Particle-Antiparticle Conjugation for Relativistic Field Theories*, *Kong. Dan. Vid. Sel. Mat. Fys. Med.* **28N5** (1954) 1.

[72] W. Pauli, L. Rosenfeld and V. Weisskopf, *Niels Bohr and the Development of Physics*, *British Journal for the Philosophy of Science* **7** (1957) 357.

[73] J.M. Cline, *Baryogenesis*, in *Les Houches Summer School - Session 86: Particle Physics and Cosmology: The Fabric of Spacetime*, 9, 2006 [hep-ph/0609145].

[74] W.-S. Hou, *Source of CP Violation for the Baryon Asymmetry of the Universe*, *Chin. J. Phys.* **47** (2009) 134 [0803.1234].

[75] LHCb collaboration, *Observation of CP Violation in Charm Decays*, *Phys. Rev. Lett.* **122** (2019) 211803 [1903.08726].

[76] LHCb collaboration, *A precise measurement of the* B^0 *meson oscillation frequency*, *Eur. Phys. J. C* **76** (2016) 412 [1604.03475].

[77] LHCb collaboration, *Precise determination of the* B_s^0–$\overline{B}_s^0$ *oscillation frequency*, *Nature Phys.* **18** (2022) 1 [2104.04421]. Details in supporting note LHCb-ANA-2020-033.

[78] T. Nakano and K. Nishijima, *Charge Independence for V-particles*, *Progress of Theoretical Physics* **10** (1953) 581 [https://academic.oup.com/ptp/article-pdf/10/5/581/5364926/10-5-581.pdf].

[79] M. Gell-Mann, *The interpretation of the new particles as displaced charge multiplets*, *Nuovo Cim.* **4** (1956) 848.

[80] T.A. Kaeding and H.T. Williams, *Program for generating tables of SU(3) coupling coefficients*, *Comput. Phys. Commun.* **98** (1996) 398 [nucl-th/9511025].

[81] P.R. Berman, *Introductory Quantum Mechanics : A Traditional Approach Emphasizing Connections with Classical Physics*, UNITEXT for Physics, Springer International Publishing, Cham, 1st edition. ed. (2018).

[82] B. Bodhi, ed., *In the Buddha's Words: An Anthology of Discourses from the Pali Canon*, The Teachings of the Buddha, Wisdom Publications (2005).

[83] M. Gell-Mann, *The Eightfold Way: A theory of strong interaction symmetry*, Tech. Rep. CTSL-20, California Institute of Technology, Synchrotron Laboratory, Pasadena, California (3, 1961), DOI.

[84] Y. Ne'eman, *Derivation of strong interactions from a gauge invariance*, *Nuclear Physics* **26** (1961) 222.

[85] S. Müller, U. Nierste and S. Schacht, *Topological amplitudes in D decays to two pseudoscalars: A global analysis with linear $SU(3)_F$ breaking*, *Phys. Rev.* **D92** (2015) 014004 [1503.06759].

[86] K. De Bruyn, R. Fleischer, R. Knegjens, P. Koppenburg, M. Merk and N. Tuning, *Branching Ratio Measurements of B_s Decays*, *Phys. Rev. D* **86** (2012) 014027 [1204.1735].

[87] HFLAV collaboration, *Averages of b-hadron, c-hadron, and τ-lepton properties as of 2021*, 2206.07501.

[88] R. Penco, "An Introduction to Effective Field Theories." arXiv:2006.16285, 6, 2020.

[89] M. Beneke, G. Buchalla, M. Neubert and C.T. Sachrajda, *QCD factorization for $B \to \pi\pi$ decays: Strong phases and CP violation in the heavy quark limit*, *Phys. Rev. Lett.* **83** (1999) 1914 [hep-ph/9905312].

[90] M. Beneke, G. Buchalla, M. Neubert and C.T. Sachrajda, *QCD factorization for exclusive, nonleptonic B meson decays: General arguments and the case of heavy light final states*, *Nucl. Phys. B* **591** (2000) 313 [hep-ph/0006124].

[91] D. Bigi and P. Gambino, *Revisiting $B \to D\ell\nu$*, *Phys. Rev. D* **94** (2016) 094008 [1606.08030].

[92] FLAVOUR LATTICE AVERAGING GROUP (FLAG) collaboration, *FLAG Review 2021*, *Eur. Phys. J. C* **82** (2022) 869 [2111.09849].

[93] A.J. Buras, J.M. Gerard and R. Ruckl, *1/n Expansion for Exclusive and Inclusive Charm Decays*, *Nucl. Phys. B* **268** (1986) 16.

[94] J.J. Aubert, U. Becker, P.J. Biggs, J. Burger, M. Chen, G. Everhart et al., *Experimental Observation of a Heavy Particle J*, *Phys. Rev. Lett.* **33** (1974) 1404.

[95] J.E. Augustin, A.M. Boyarski, M. Breidenbach, F. Bulos, J.T. Dakin, G.J. Feldman et al., *Discovery of a narrow resonance in e^+e^- annihilation*, *Phys. Rev. Lett.* **33** (1974) 1406.

[96] S.L. Glashow, J. Iliopoulos and L. Maiani, *Weak interactions with lepton-hadron symmetry*, *Phys. Rev. D* **2** (1970) 1285.

[97] M. Riordan, *The hunting of the quark*, Simon & Schuster (Sept., 1987).

[98] CLEO collaboration, *The CLEO Detector*, *Nucl. Instrum. Meth.* **211** (1983) 47.

[99] S.W. Herb, D.C. Hom, L.M. Lederman, J.C. Sens, H.D. Snyder, J.K. Yoh et al., *Observation of a Dimuon Resonance at 9.5 GeV in 400-GeV Proton-Nucleus Collisions*, *Phys. Rev. Lett.* **39** (1977) 252.

[100] K. Ueno, B.C. Brown, C.N. Brown, W.R. Innes, R.D. Kephart, T. Yamanouchi et al., *Evidence for the Υ'' and a search for new narrow resonances*, *Phys. Rev. Lett.* **42** (1979) 486.

[101] CLEO collaboration, *Observation of Three Upsilon States*, *Phys. Rev. Lett.* **44** (1980) 1108.

[102] CLEO collaboration, *Observation of a Fourth Upsilon State in e^+ e^- Annihilations*, *Phys. Rev. Lett.* **45** (1980) 219.

[103] S. Behrends et al., *Observation of exclusive decay modes of b-flavored mesons*, *Phys. Rev. Lett.* **50** (1983) 881.

[104] A. Chen et al., *Evidence for the F Meson at 1970 MeV*, *Phys. Rev. Lett.* **51** (1983) 634.

[105] CLEO collaboration, *Charmless hadronic B decays at CLEO*, in *American Physical Society (APS) Meeting of the Division of Particles and Fields (DPF 99)*, 1, 1999 [hep-ex/9904008].

[106] A. Bevan, B. Golob, T. Mannel, S. Prell, B. Yabsley, K. Abe et al., *The physics of the b factories*, *European Physical Journal C* (2014) .

[107] E. Fernandez, W.T. Ford, A.L. Read, J.G. Smith, R. De Sangro, A. Marini et al., *Lifetime of particles containing b quarks*, *Phys. Rev. Lett.* **51** (1983) 1022.

[108] N. Lockyer et al., *Measurement of the Lifetime of Bottom Hadrons*, *Phys. Rev. Lett.* **51** (1983) 1316.

[109] ARGUS collaboration, *Observation of B^0 - $\overline{B}^0$ Mixing*, *Phys. Lett. B* **192** (1987) 245.

[110] J. Brodzicka, T. Browder, P. Chang, S. Eidelman, B. Golob, K. Hayasaka et al., *Physics achievements from the Belle experiment*, *Progress of Theoretical and Experimental Physics* **2012** (2012) 04D001 [https://academic.oup.com/ptep/article-pdf/2012/1/04D001/11595832/pts072.pdf].

[111] J. Lees, V. Poireau, V. Tisserand, E. Grauges, A. Palano, G. Eigen et al., *Time-integrated luminosity recorded by the BABAR detector at the PEP-II e^+e^- collider*, *Nuclear Instruments and Methods in Physics Research Section A Accelerators Spectrometers Detectors and Associated Equipment* **726** (2013) 203.

[112] BABAR collaboration, *Recent BaBar results on B decays*, *Int. J. Mod. Phys. A* **23** (2008) 3218.

[113] BELLE collaboration, *Observation of large CP violation in the neutral B meson system*, *Phys. Rev. Lett.* **87** (2001) 091802 [hep-ex/0107061].

[114] D0 collaboration, *Observation of the top quark*, *Phys. Rev. Lett.* **74** (1995) 2632 [hep-ex/9503003].

[115] FERMILAB collaboration, *Design Report Tevatron 1 project*, Tech. Rep. FERMILAB-DESIGN-1984-01, Fermilab, Batavia (9, 1984).

[116] A. Valishev, *Tevatron Accelerator Physics and Operation Highlights*, *Conf. Proc. C* **110328** (2011) 37 [1202.5525].

[117] D. Bandurin et al., *Review of Physics Results from the Tevatron*, *Int. J. Mod. Phys. A* **30** (2015) 1541001 [1409.4861].

[118] CDF collaboration, *Observation of the B_c meson in $p\bar{p}$ collisions at $\sqrt{s} = 1.8$ TeV*, *Phys. Rev. Lett.* **81** (1998) 2432 [hep-ex/9805034].

[119] CDF collaboration, *Measurement of the $B_s^0 - \bar{B}_s^0$ Oscillation Frequency*, *Phys. Rev. Lett.* **97** (2006) 062003 [hep-ex/0606027].

[120] CDF collaboration, *First Flavor-Tagged Determination of Bounds on Mixing-Induced CP Violation in $B_s^0 \to J/\psi\phi$ Decays*, *Phys. Rev. Lett.* **100** (2008) 161802 [0712.2397].

[121] LHCB collaboration, *Observation of structure in the J/ψ -pair mass spectrum*, *Sci. Bull.* **65** (2020) 1983 [2006.16957].

[122] LHCB collaboration, *Observation of $J/\psi p$ Resonances Consistent with Pentaquark States in $\Lambda_b^0 \to J/\psi K^- p$ Decays*, *Phys. Rev. Lett.* **115** (2015) 072001 [1507.03414].

[123] CMS collaboration, *Measurement of the B^+ hadron production cross section in pp collisions at 13 TeV*, Tech. Rep. CMS-PAS-BPH-15-004, CERN, Geneva (2015).

[124] CMS collaboration, *Measurement of the CP-violating phase ϕ_s in the $B_s^0 \to J/\psi\,\phi(1020) \to \mu^+\mu^-K^+K^-$ channel in proton-proton collisions at $\sqrt{s} = 13$ TeV*, *Phys. Lett. B* **816** (2021) 136188 [2007.02434].

[125] CMS, LHCb, ATLAS collaboration, *Combination of the ATLAS, CMS and LHCb results on the $B^0_{(s)} \to \mu^+\mu^-$ decays*, Tech. Rep. CMS-PAS-BPH-20-003, LHCb-CONF-2020-002, ATLAS-CONF-2020-049, CERN, Geneva (2020).

[126] LHCb collaboration, *Measurement of b-hadron branching fractions for two-body decays into charmless charged hadrons*, *JHEP* **10** (2012) 037 [1206.2794].

[127] LHCb collaboration, *Performance of the LHCb RICH detector at the LHC*, *Eur. Phys. J. C* **73** (2013) 2431 [1211.6759].

[128] M. Vretenar, J. Vollaire, R. Scrivens, C. Rossi, F. Roncarolo, S. Ramberger et al., *Linac4 design report*, vol. 6 of *CERN Yellow Reports: Monographs*, CERN, Geneva (2020), 10.23731/CYRM-2020-006.

[129] J.-P. Burnet et al., *Fifty years of the CERN Proton Synchrotron : Volume 2*, 1309.6923.

[130] D. Cundy and S. Gilardoni, *The Proton Synchrotron (PS): At the Core of the CERN Accelerators*, *Adv. Ser. Direct. High Energy Phys.* **27** (2017) 39.

[131] N. Doble, L. Gatignon, K. Hübner and E. Wilson, *The Super Proton Synchrotron (SPS): A Tale of Two Lives*, *Adv. Ser. Direct. High Energy Phys.* **27** (2017) 135.

[132] L.R. Evans, *The Large Hadron Collider project*, in *16th International Cryogenic Engineering Conference and 1996 International Cryogenic Materials Conference and Industrial Exhibition*, 5, 1996.

[133] LHCb collaboration, *Precision luminosity measurements at LHCb*, *JINST* **9** (2014) P12005 [1410.0149].

[134] E. Graverini, *Luminosity at LHCb in Run 3*, *PoS* **ICHEP2022** (2022) 679 [2211.12405].

[135] O. Brüning, H. Gray, K. Klein, M. Lamont, M. Narain, R. Polifka et al., *The scientific potential and technological challenges of the high-luminosity large hadron collider program*, *Reports on Progress in Physics* **85** (2022) 046201.

[136] ATLAS collaboration, *The ATLAS Experiment at the CERN Large Hadron Collider: A Description of the Detector Configuration for Run 3*, 2305.16623.

[137] CMS collaboration, *CMS detector: Run 3 status and plans for Phase-2*, in *30th International Workshop on Deep-Inelastic Scattering and Related Subjects*, 9, 2023 [2309.02256].

[138] LHC Project Coordination, "Delivered Luminosity 2018." https://lpc.web.cern.ch/plots.html?year=2018&runtype=protons. Accessed 28 June 2024.

[139] M. Hentschinski, *Proton structure functions at small x*, *Journal of Physics: Conference Series* **651** (2015) 012011.

[140] J.J. Ethier and E.R. Nocera, *Parton Distributions in Nucleons and Nuclei*, *Ann. Rev. Nucl. Part. Sci.* **70** (2020) 43 [2001.07722].

[141] LHCb collaboration, C. Elsasser, "$\bar{b}b$ production angle plots." https://lhcb.web.cern.ch/lhcb/speakersbureau/html/bb_ProductionAngles.html. Accessed 26 April 2024.

[142] LHCb collaboration, *LHCb Detector Performance*, *Int. J. Mod. Phys. A* **30** (2015) 1530022 [1412.6352].

[143] LHCb collaboration, *LHCb reoptimized detector design and performance: Technical Design Report*, Tech. Rep. LHCb-TDR-9, LHCb, CERN (9, 2003).

[144] LHCb collaboration, *LHCb VELO Upgrade Technical Design Report*, Tech. Rep. LHCB-TDR-013, LHCb, CERN (Nov, 2013).

[145] LHCb collaboration, *LHCb VELO (VErtex LOcator): Technical Design Report*, Tech. Rep. LHCb-TDR-5, LHCb, CERN (May, 2001).

[146] E. Tamm and I.M. Frank, *Coherent Radiation of a Fast Electron in a Medium*, *Dokl. Akad. Nauk SSSR* **14** (1937) 107.

[147] LHCb collaboration, *LHCb RICH: Technical Design Report*, Tech. Rep. LHCb-TDR-3, LHCb, CERN (Sep, 2000).

[148] LHCb Outer Tracker Group collaboration, *Performance of the LHCb Outer Tracker*, *JINST* **9** (2014) P01002 [1311.3893].

[149] LHCb collaboration, *LHCb calorimeters: Technical Design Report*, Tech. Rep. LHCb-TDR-2, LHCb, CERN (Sep, 2000).

[150] E.P. Olloqui and (on behalf of the LHCb Collaboration), *LHCb Preshower(PS) and Scintillating Pad Detector (SPD): Commissioning, calibration, and monitoring*, *Journal of Physics: Conference Series* **160** (2009) 012046.

[151] LHCb collaboration, *LHCb muon system: Technical Design Report*, Tech. Rep. LHCb-TDR-4, LHCb, CERN (May, 2001).

[152] LHCb collaboration, "Moore project." https://gitlab.cern.ch/lhcb/Moore. Accessed 28 June 2024.

[153] CERN collaboration, "ROOT Reference Documentation." https://root.cern/doc/master/. Accessed 03 October 2024.

[154] LHCb collaboration, "Brunel project." https://gitlab.cern.ch/lhcb/Brunel. Accessed 28 June 2024.

[155] LHCb collaboration, "Davinci project." https://gitlab.cern.ch/lhcb/DaVinci. Accessed 28 June 2024.

[156] LHCb collaboration, "Gauss project." https://gitlab.cern.ch/lhcb/Gauss. Accessed 28 June 2024.

[157] T. Sjöstrand, *The PYTHIA Event Generator: Past, Present and Future*, *Comput. Phys. Commun.* **246** (2020) 106910 [1907.09874].

[158] P. Nason, *A New method for combining NLO QCD with shower Monte Carlo algorithms*, *JHEP* **11** (2004) 040 [hep-ph/0409146].

[159] A. Ryd, D. Lange, N. Kuznetsova, S. Versille, M. Rotondo, D.P. Kirkby et al., "EvtGen: A Monte Carlo Generator for B-Physics." EVTGEN-V00-11-07, 5, 2005.

[160] T. Basaglia, Z.W. Bell, D. DAgostino, P.V. Dressendorfer, S. Giani, M.G. Pia et al., *Geant4: A game changer in high energy physics and related applicative fields*, *Future Generation Computer Systems* **159** (2024) 411.

[161] LHCb collaboration, "Boole project." https://gitlab.cern.ch/lhcb/Boole. Accessed 28 June 2024.

[162] LHCb collaboration, *LHCb trigger system technical design report*, Tech. Rep. LHCb-TDR-10, LHCb, CERN (Sep, 2003).

[163] LHCb collaboration, "Trigger schemes." http://lhcb.web.cern.ch/lhcb/speakersbureau/html/TriggerScheme.html. Accessed 15 April 2024.

[164] S. Tolk, J. Albrecht, F. Dettori and A. Pellegrino, *Data driven trigger efficiency determination at LHCb*, Tech. Rep. LHCb-PUB-2014-039, CERN-LHCb-PUB-2014-039, CERN, Geneva (2014).

[165] LHCb collaboration, *Design and performance of the LHCb trigger and full real-time reconstruction in Run 2 of the LHC*, *JINST* **14** (2019) P04013 [1812.10790].

[166] R. Aaij et al., *Allen: A High-Level Trigger on GPUs for LHCb*, *Computing and Software for Big Science* **4** (2020) .

[167] LHCb collaboration, *LHCb Tracker Upgrade Technical Design Report*, Tech. Rep. LHCB-TDR-015, LHCb, CERN (Feb, 2014).

[168] LHCb collaboration, *LHCb Trigger and Online Upgrade Technical Design Report*, Tech. Rep. LHCB-TDR-016, LHCb, CERN (May, 2014).

[169] T. Gershon, A. Lenz, A.V. Rusov and N. Skidmore, *Testing the Standard Model with CP asymmetries in flavor-specific nonleptonic decays*, *Phys. Rev. D* **105** (2022) 115023 [2111.04478].

[170] HFLAV collaboration, *Averages of b-hadron, c-hadron, and τ-lepton properties as of 2021*, *Phys. Rev. D* **107** (2023) 052008 [2206.07501].

[171] L. Breiman, *Bagging predictors*, *Machine Learning* **24** (1996) 123.

[172] T. Likhomanenko, P. Ilten, E. Khairullin, A. Rogozhnikov, A. Ustyuzhanin and M. Williams, *LHCb Topological Trigger Reoptimization*, *J. Phys.: Conf. Ser.* **664** (2015) 082025 [1510.00572]. 21st International Conference on Computing in High Energy Physics (CHEP2015).

[173] V.V. Gligorov, *Reconstruction of the Channel $B_d^0 \to D^+\pi^-$ and Background Classification at LHCb (revised)*, Tech. Rep. LHCb-2007-044, CERN-LHCb-2007-044, CERN, Geneva (2007).

[174] A. Di Canto, J. Garra Ticó, T. Gershon, N. Jurik, M. Martinelli, T. Pila et al., *Novel method for measuring charm-mixing parameters using multibody decays*, *Phys. Rev. D* **99** (2019) 012007 [1811.01032].

[175] LHCb collaboration, *Measurement of the CKM angle γ in $B^\pm \to DK^\pm$ and $B^\pm \to D\pi^\pm$ decays with $D \to K_S^0 h^+ h^-$*, *JHEP* **02** (2021) 169 [2010.08483].

[176] LHCb collaboration, "PIDCalib2." https://gitlab.cern.ch/lhcb-rta/pidcalib2. Accessed 28 June 2024.

[177] LHCb collaboration, *Measurement of the flavour-specific CP-violating asymmetry a_{sl}^s in B_s^0 decays*, *Phys. Lett. B* **728** (2014) 607 [1308.1048]. Details in supporting note LHCb-ANA-2013-017.

[178] A. Davis, L. Dufour, F. Ferrari, S. Stahl, M.A. Vesterinen and J. Van Tilburg, *Measurement of the $K^-\pi^+$ two-track detection asymmetry in Run 2 using the Turbo stream*, Tech. Rep. LHCb-INT-2017-023, CERN-LHCb-INT-2017-023, CERN, Geneva (2017).

[179] D.R.O. Morrison, *Review of strong interactions of kaons*, *Conf. Proc. C* **690625** (1969) 235.

[180] LHCb collaboration, *Measurement of CP asymmetry in $D^0 \to K^-K^+$ and $D^0 \to \pi^-\pi^+$ decays*, *JHEP* **07** (2014) 041 [1405.2797]. Details in supporting note LHCb-ANA-2013-055.

[181] Y. Li, E.M. Gersabeck, L. Grillo, S. Borghi, A. Davis and B. Mitreska, "Measurement of CP asymmetry in $B^0 - \overline{B}^0$ meson mixing using semileptonic decays in LHCb Run 2 data." https://cds.cern.ch/record/2855478LHCb-ANA-2023-017, 2023.

[182] LHCb collaboration, *Measurement of the CP asymmetry in $B_s^0 - \overline{B}_s^0$ mixing*, *Phys. Rev. Lett.* **117** (2016) 061803 [1605.09768]. [Addendum: Phys.Rev.Lett. 118, 129903 (2017)]. Details in supporting note LHCb-ANA-2016-004.

[183] LHCb collaboration, "L0HadronTables." https://gitlab.cern.ch/lhcb-TrackingAlignment/l0hadrontables. Accessed 28 June 2024.

[184] LHCb collaboration, *Letter of Intent for the LHCb Upgrade*, Tech. Rep. CERN-LHCC-2011-001, LHCC-I-018, CERN, Geneva (2011).

[185] LHCb collaboration, *Measurement of the $B^{\pm}$ production cross-section in pp collisions at $\sqrt{s} = 7$ and 13 TeV*, *JHEP* **12** (2017) 026 [1710.04921].

[186] LHCb collaboration, *Study of the kinematic dependences of Λ_b^0 production in pp collisions and a measurement of the $\Lambda_b^0 \to \Lambda_c^+ \pi^-$ branching fraction*, *JHEP* **08** (2014) 143 [1405.6842]. details in supporting note LHCb-ANA-2013-023.

[187] LHCb collaboration, *Measurement of the branching fraction of the $B^0 \to D_s^+ \pi^-$ decay*, *Eur. Phys. J. C* **81** (2021) 314 [2010.11986].

[188] LHCb collaboration, *Measurement of the fragmentation fraction ratio f_s/f_d and its dependence on B meson kinematics*, *JHEP* **04** (2013) 001 [1301.5286]. Details in supporting note LHCb-ANA-2011-070.

[189] LHCb collaboration, *Measurement of the b-quark production cross-section in 7 and 13 TeV pp collisions*, *Phys. Rev. Lett.* **118** (2017) 052002 [1612.05140]. [Erratum: Phys.Rev.Lett. 119, 169901 (2017)].

[190] Particle Data Group collaboration, *Review of Particle Physics*, *Phys. Rev.* **D98** (2018) 030001.

[191] LHCb collaboration, *Measurement of b hadron fractions in 13 TeV pp collisions*, *Phys. Rev. D* **100** (2019) 031102 [1902.06794].

[192] LHCb collaboration, *Measurement of the $B_s^0 \to \mu^+\mu^-$ branching fraction and effective lifetime and search for $B^0 \to \mu^+\mu^-$ decays*, *Phys. Rev. Lett.* **118** (2017) 191801 [1703.05747].

[193] LHCb collaboration, *Measurement of the fragmentation fraction ratio f_s/f_d and its dependence on B meson kinematics*, *JHEP* **04** (2013) 001 [1301.5286].

[194] LHCb collaboration, *Precise measurement of the f_s/f_d ratio of fragmentation fractions and of B_s^0 decay branching fractions*, *Phys. Rev. D* **104** (2021) 032005 [2103.06810].

[195] R. Aaij et al., *Allen: A high level trigger on GPUs for LHCb*, *Comput. Softw. Big Sci.* **4** (2020) 7 [1912.09161].

[196] Mölder, F and others, *Sustainable data analysis with snakemake [version 2; peer review: 2 approved]*, *F1000Research* **10** (2021) .

[197] D. Martínez Santos and F. Dupertuis, *Mass distributions marginalized over per-event errors*, *Nucl. Instrum. Meth. A* **764** (2014) 150 [1312.5000].

[198] N.L. Johnson, *Systems of frequency curves generated by methods of translation*, *Biometrika* **36** (1949) 149.

[199] LHCb collaboration, *Measurement of CP violation in $B^0 \to D^{\mp}\pi^{\pm}$ decays*, *JHEP* **06** (2018) 084 [1805.03448].

[200] M. Bjorn, *CP Violation in $B^{\pm} \to Dh^{\pm}$ Decays where $D \to K^0_S h'^+ h'^-$*, Ph.D. thesis, Oxford University, 2020. Presented 08 Oct 2020.

[201] I.W. Park, H. Sako, K. Aoki, P. Gubler and S.H. Lee, *Identifying the transverse and longitudinal modes of the K^* and K_1 mesons through their angular dependent decay modes*, 2403.18288.

[202] LHCb collaboration, *First observation and branching fraction measurement of the $\Lambda_b^0 \to D_s^- p$ decay*, *JHEP* **07** (2023) 075 [2212.12574].

[203] LHCb collaboration, *Measurement of CP observables in $B^{\pm} \to D^{(*)}K^{\pm}$ and $B^{\pm} \to D^{(*)}\pi^{\pm}$ decays using two-body D final states*, *JHEP* **04** (2021) 081 [2012.09903]. Details in supporting note LHCb-ANA-2020-024.

[204] LHCb collaboration, *First observation and branching fraction measurement of the $\Lambda_b^0 \to D_s^- p$ decay*, *JHEP* **07** (2023) 075 [2212.12574]. Details in supporting note LHCb-ANA-2021-013.

[205] LHCb collaboration, "B2OC hadronic triggers in Run 3 (TrackMVA and TwoTrackMVA)." LHCB-FIGURE-2024-014, 2024.

[206] T. Gershon, A. Lenz, A.V. Rusov and N. Skidmore, *Testing the Standard Model with CP asymmetries in flavor-specific nonleptonic decays*, *Phys. Rev. D* **105** (2022) 115023 [2111.04478].

[207] M.L. Piscopo and A.V. Rusov, *Non-factorisable effects in the decays $\overline{B}_s^0 \to D_s^+\pi^-$ and $\overline{B}^0 \to D^+K^-$ from LCSR*, *JHEP* **10** (2023) 180 [2307.07594].

[208] A. Lenz, J. Müller, M.L. Piscopo and A.V. Rusov, *Taming new physics in $b \to c\bar{u}d(s)$ with $\tau(B^+)/\tau(B_d)$ and a_{sl}^d*, *JHEP* **09** (2023) 028 [2211.02724].

[209] S. Iguro and T. Kitahara, *Implications for new physics from a novel puzzle in $\bar{B}^0_{(s)} \to D^{(*)+}_{(s)}\{\pi^-, K^-\}$ decays*, *Phys. Rev. D* **102** (2020) 071701 [2008.01086].

[210] M. Endo, S. Iguro and S. Mishima, *Revisiting rescattering contributions to $\overline{B}_{(s)} \to D^{(*)}_{(s)} M$ decays*, *JHEP* **01** (2022) 147 [2109.10811].

[211] R. Fleischer and E. Malami, *Using $B_s^0 \to D_s^{\mp} K^{\pm}$ Decays as a Portal to New Physics*, *Phys. Rev. D* **106** (2022) 056004 [2109.04950].

[212] M. Beneke, P. Böer, G. Finauri and K.K. Vos, *QED factorization of two-body non-leptonic and semi-leptonic B to charm decays*, *JHEP* **10** (2021) 223 [2107.03819].

[213] M. Bordone, A. Greljo and D. Marzocca, *Exploiting dijet resonance searches for flavor physics*, *JHEP* **08** (2021) 036 [2103.10332].

[214] B. Bhattacharya, S. Kumbhakar, D. London and N. Payot, *U-spin puzzle in B decays*, *Phys. Rev. D* **107** (2023) L011505 [2211.06994].

[215] Y. Amhis, Y. Grossman and Y. Nir, *The branching fraction of $B_s^0 \to K^0 \overline{K}^0$: three puzzles*, *JHEP* **02** (2023) 113 [2212.03874].

[216] A. Biswas, S. Descotes-Genon, J. Matias and G. Tetlalmatzi-Xolocotzi, *A new puzzle in non-leptonic B decays*, *JHEP* **06** (2023) 108 [2301.10542].

[217] R. Berthiaume, B. Bhattacharya, R. Boumris, A. Jean, S. Kumbhakar and D. London, *Anomalies in Hadronic B Decays*, 2311.18011.

[218] L. Bel, K. De Bruyn, R. Fleischer, M. Mulder and N. Tuning, *Anatomy of $B \to D\overline{D}$ decays*, *JHEP* **07** (2015) 108 [1505.01361].

[219] M. Jung, *Determining weak phases from $B \to J/\psi P$ decays*, *Phys. Rev. D* **86** (2012) 053008 [1206.2050].

[220] G. Buchalla, A.J. Buras and M.E. Lautenbacher, *Weak decays beyond leading logarithms*, *Rev. Mod. Phys.* **68** (1996) 1125 [hep-ph/9512380].

[221] K. Izlar, *The march of the penguin diagrams*, *Symmetry Magazine* (2013) . Online at https://www.symmetrymagazine.org/article/june-2013/the-march-of-the-penguin-diagrams. Accessed 16 June 2023.

[222] A.J. Buras and L. Silvestrini, *Nonleptonic two-body B decays beyond factorization*, *Nucl. Phys. B* **569** (2000) 3 [hep-ph/9812392].

[223] G. 't Hooft, *A Planar Diagram Theory for Strong Interactions*, *Nucl. Phys. B* **72** (1974) 461.

[224] R. Fleischer, N. Serra and N. Tuning, *Tests of Factorization and SU(3) Relations in B Decays into Heavy-Light Final States*, *Phys. Rev. D* **83** (2011) 014017 [1012.2784].

[225] LHCb collaboration, *Measurement of b-hadron production fractions in 7 TeV pp collisions*, *Phys. Rev. D* **85** (2012) 032008 [1111.2357].

[226] LHCb collaboration, *Updated average f_s/f_d b-hadron production fraction ratio for 7 TeV pp collisions*, in *EPS-HEP 2013 European Physical Society Conference on High Energy Physics*, 7, 2013 LHCb-CONF-2013-011.

[227] CMS collaboration, *Measurement of the dependence of the hadron production fraction ratio f_s/f_u and f_d/f_u on B meson kinematic variables in proton-proton collisions at $\sqrt{s}$ = 13 TeV*, Phys. Rev. Lett. **131** (2023) 121901 [2212.02309].

[228] CDF collaboration, *Measurement of $B_s^0 \to D_s^{(*)+} D_s^{(*)-}$ Branching Ratios*, Phys. Rev. Lett. **108** (2012) 201801 [1204.0536].

[229] D. Atwood and W.J. Marciano, *Radiative Corrections and Semileptonic B Decays*, Phys. Rev. D **41** (1990) 1736.

[230] G.P. Lepage, *Coulomb corrections for $\Upsilon_{(4S)} \to B\overline{B}$*, Phys. Rev. D **42** (1990) 3251.

[231] F. Bernlochner, M. Jung, M. Khan, G. Landsberg and Z. Ligeti, *Novel approaches to determine $B^{\pm}$ and B^0 meson production fractions*, 2306.04686.

[232] LHCb collaboration, *First observations of $\bar{B}_s^0 \to D^+D^-$, $D_s^+D^-$ and $D^0\bar{D}^0$ decays*, Phys. Rev. D **87** (2013) 092007 [1302.5854].

[233] LHCb collaboration, *Measurement of CP asymmetries and branching fraction ratios of B decays to two charm mesons*, JHEP **09** (2023) 202 [2306.09945].

[234] LHCb collaboration, *Study of beauty hadron decays into pairs of charm hadrons*, Phys. Rev. Lett. **112** (2014) 202001 [1403.3606].

[235] CLEO collaboration, *Measurements of $B \to D_s^+ X$ decays*, Phys. Rev. D **53** (1996) 4734.

[236] BaBar collaboration, *Study of $B \to D^{(*)} D_{(s(J)}^{(*)}$ Decays and Measurement of D_s^- and $D_{sJ}^-(2460)$ Branching Fractions*, Phys. Rev. D **74** (2006) 031103 [hep-ex/0605036].

[237] BaBar collaboration, *Measurement of branching fractions and CP-violating charge asymmetries for B meson decays to $D^{(*)}\overline{D}^{(*)}$, and implications for the CKM angle gamma*, Phys. Rev. D **73** (2006) 112004 [hep-ex/0604037].

[238] A. Zupanc et al., *Improved measurement of $\overline{B}^0 \to D_{(s)}^- D^+$ and search for $\overline{B}^0 \to D_{(s)}^+ D_{(s)}^-$ at Belle*, Phys. Rev. D **75** (2007) 091102 [hep-ex/0703040].

[239] Belle collaboration, *Measurement of the branching fraction and charge asymmetry of the decay $B^+ \to D^+\overline{D}^0$ and search for $B^0 \to D^0\overline{D}^0$*, Phys. Rev. D **77** (2008) 091101 [0802.2988].

[240] Belle collaboration, *Measurements of Branching Fractions and Time-dependent CP Violating Asymmetries in $B^0 \to D^{(*)\pm} D^{\mp}$ Decays*, Phys. Rev. D **85** (2012) 091106 [1203.6647].

[241] Belle collaboration, *Precise measurement of the branching fractions for $B_s \to D_s^{(*)+} D_s^{(*)-}$ and first measurement of the $D_s^{*+} D_s^{*-}$ polarization using e^+e^- collisions*, Phys. Rev. D **87** (2013) 031101 [1208.0323].

[242] BELLE COLLABORATION collaboration, *Evidence for CP Violation in $B^0 \to D^+D^-$ Decays*, *Phys. Rev. Lett.* **98** (2007) 221802.

[243] LHCB collaboration, *Measurement of CP violation in $B^0 \to D^+D^-$ decays*, *Phys. Rev. Lett.* **117** (2016) 261801 [1608.06620].

[244] BABAR collaboration, *Measurements of time-dependent CP asymmetries in $B^0 \to D^{(*)} + D^{(*)}$ - decays*, *Phys. Rev. D* **79** (2009) 032002 [0808.1866].

[245] LHCB collaboration, *Measurement of the CP-violating phase ϕ_s in $\bar{B}^0_s \to D^+_s D^-_s$ decays*, *Phys. Rev. Lett.* **113** (2014) 211801 [1409.4619].

[246] LHCB collaboration, *Measurement of the CP asymmetry in $B^- \to D^-_s D^0$ and $B^- \to D^- D^0$ decays*, *JHEP* **05** (2018) 160 [1803.10990].

[247] M. Schmelling, *Averaging correlated data*, *Phys. Scripta* **51** (1995) 676.

[248] LHCB collaboration, *Improved measurement of CP violation parameters in $B^0_s \to J/\psi K^+K^-$ decays in the vicinity of the $\phi(1020)$ resonance*, 2308.01468.

[249] D. London, N. Sinha and R. Sinha, *Can one measure the weak phase of a penguin diagram?*, *Phys. Rev. D* **60** (1999) 074020 [hep-ph/9905404].

[250] F.J. Botella and J.P. Silva, *Reparametrization invariance of B decay amplitudes and implications for new physics searches in B decays*, *Phys. Rev. D* **71** (2005) 094008 [hep-ph/0503136].

[251] T. Feldmann, M. Jung and T. Mannel, *Is there a non-Standard-Model contribution in non-leptonic $b \to s$ decays?*, *JHEP* **08** (2008) 066 [0803.3729].

[252] M. Gronau, J.L. Rosner and D. Pirjol, *Small amplitude effects in $B^0 \to D^+D^-$ and related decays*, *Phys. Rev. D* **78** (2008) 033011 [0805.4601].

[253] BELLE collaboration, *Evidence for CP violation in $B^0 \to D^+D^-$ decays*, *Phys. Rev. Lett.* **98** (2007) 221802 [hep-ex/0702031].

[254] HFLAV collaboration, *Averages of b-hadron, c-hadron, and τ-lepton properties as of 2018*, *Eur. Phys. J. C* **81** (2021) 226 [1909.12524]. Online update May 2024 at https://hflav.web.cern.ch/.

[255] A. Hocker, H. Lacker, S. Laplace and F. Le Diberder, *A new approach to a global fit of the CKM matrix*, *Eur. Phys. J. C* **21** (2001) 225 [hep-ph/0104062].

[256] R.J. Barlow, *Practical Statistics for Particle Physics*, *CERN Yellow Rep. School Proc.* **5** (2020) 149 [1905.12362].

[257] R. Fleischer, *New strategies to extract β and γ from $B_d \to \pi^+\pi^-$ and $B_s \to K^+K^-$*, *Phys. Lett. B* **459** (1999) 306 [hep-ph/9903456].

[258] M. Gronau, *U spin symmetry in charmless B decays*, *Phys. Lett. B* **492** (2000) 297 [hep-ph/0008292].

[259] M. Gronau and J.L. Rosner, *The role of $B_s \to K\pi$ in determining the weak phase γ*, *Phys. Lett. B* **482** (2000) 71 [hep-ph/0003119].

[260] M.J. Savage, *SU(3) violations in the nonleptonic decay of charmed hadrons*, *Phys. Lett. B* **257** (1991) 414.

[261] G. Hiller, M. Jung and S. Schacht, *SU(3)-flavor anatomy of nonleptonic charm decays*, *Phys. Rev. D* **87** (2013) 014024 [1211.3734].

[262] M. Gronau, O.F. Hernandez, D. London and J.L. Rosner, *Broken SU(3) symmetry in two-body B decays*, *Phys. Rev. D* **52** (1995) 6356 [hep-ph/9504326].

[263] CMS, LHCb collaboration, *Observation of the rare $B_s^0 \to \mu^+\mu^-$ decay from the combined analysis of CMS and LHCb data*, *Nature* **522** (2015) 68 [1411.4413].

[264] LHCb collaboration, *Measurement of the $B_s^0 \to \mu^+\mu^-$ decay properties and search for the $B^0 \to \mu^+\mu^-$ and $B_s^0 \to \mu^+\mu^-\gamma$ decays*, *Phys. Rev. D* **105** (2022) 012010 [2108.09283].

[265] CMS collaboration, *Measurement of the $B_s^0 \to \mu^+\mu^-$ decay properties and search for the $B^0 \to \mu^+\mu^-$ decay in proton-proton collisions at $\sqrt{s} = 13$ TeV*, *Phys. Lett. B* **842** (2023) 137955 [2212.10311].

[266] R. Fleischer, *Extracting γ from $B_{s(d)} \to J/\psi K_S$ and $B_{d(s)} \to D_{d(s)}^+ D_{d(s)}^-$*, *Eur. Phys. J. C* **10** (1999) 299 [hep-ph/9903455].

[267] R. Fleischer, *Exploring CP violation and penguin effects through $B_d^0 \to D^+D^-$ and $B_s^0 \to D_s^+D_s^-$*, *Eur. Phys. J. C* **51** (2007) 849 [0705.4421].

[268] Z. Ligeti and D.J. Robinson, *Towards more precise determinations of the quark mixing phase β*, *Phys. Rev. Lett.* **115** (2015) 251801 [1507.06671].

[269] Belle collaboration, *Measurements of the branching fractions $\mathcal{B}(\bar{B}^0 \to D^{*+}\pi^-)$ and $\mathcal{B}(\bar{B}^0 \to D^{*+}K^-)$ and tests of QCD factorization*, *Phys. Rev. D* **107** (2023) 012003 [2207.00134].

[270] LHCb collaboration, *Observation of the decays $B_{(s)}^0 \to D_{s1}(2536)K$*, *JHEP* **10** (2023) 106 [2308.00587].

[271] C.O. Dib, C.S. Kim and N.A. Neill, *The b quark fragmentation fractions at LHCb and meson decays with heavy quark spectators*, *Eur. Phys. J. C* **83** (2023) 793 [2306.12635].

[272] Belle collaboration, *Study of $\overline{B}^0 \to D^+h^-(h = K/\pi)$ decays at Belle*, *Phys. Rev. D* **105** (2022) 012003 [2111.04978].

[273] J. Brod and J. Zupan, *The ultimate theoretical error on γ from $B \to DK$ decays*, *JHEP* **01** (2014) 051 [1308.5663].

[274] A. Bondar, *Improved Gronau–Wyler method for ϕ_3 extraction*, in *BINP special analysis meeting on Dalitz analysis, Sep. 24–26*, 9, 2002 unpublished.

[275] A. Giri, Y. Grossman, A. Soffer and J. Zupan, *Determining gamma using $B^\pm \to DK^\pm$ with multibody D decays*, *Phys. Rev. D* **68** (2003) 054018 [hep-ph/0303187].

[276] BELLE collaboration, *Measurement of ϕ_3 with Dalitz plot analysis of $B^\pm \to D^{(*)}K^\pm$ decay*, *Phys. Rev. D* **70** (2004) 072003 [hep-ex/0406067].

[277] A. Bondar and A. Poluektov, *Feasibility study of model-independent approach to ϕ_3 measurement using Dalitz plot analysis*, *Eur. Phys. J. C* **47** (2006) 347 [hep-ph/0510246].

[278] A. Ceccucci, T. Gershon, M. Kenzie, Z. Ligeti, Y. Sakai and K. Trabelsi, *Origins of the method to determine the CKM angle γ using $B^\pm \to DK^\pm$, $D \to K^0_S\pi^+\pi^-$ decays*, 2006.12404.

[279] A. Lenz and G. Tetlalmatzi-Xolocotzi, *Model-independent bounds on new physics effects in non-leptonic tree-level decays of b-mesons*, *Journal of High Energy Physics* **2020** (2020) .

[280] LHCB collaboration, *Physics case for an LHCb Upgrade II - Opportunities in flavour physics, and beyond, in the HL-LHC era*, 1808.08865.

[281] I. Dunietz, *Clean CKM information from $B_d(t) \to D^{(*)\mp}\pi^\pm$*, *Phys. Lett. B* **427** (1998) 179 [hep-ph/9712401].

[282] R. Fleischer, *New strategies to obtain insights into CP violation through $B_{(s)} \to D^\pm_{(s)}K^\mp$, $D^{*\pm}_{(s)}K^\mp$, and $B_{(d)} \to D^\pm\pi^\mp$, $D^{*\pm}\pi^\mp$ decays*, *Nucl. Phys. B* **671** (2003) 459 [hep-ph/0304027].

[283] R. Fleischer, *New, efficient and clean strategies to explore CP violation through neutral B decays*, *Phys. Lett. B* **562** (2003) 234 [hep-ph/0301255].

[284] C.-K. Chua and W.-S. Hou, *Rescattering effects in $\overline{B}_{(u,d,s)} \to DP, \overline{D}P$ decays*, *Phys. Rev. D* **77** (2008) 116001 [0712.1882].

[285] H.-Y. Cheng, C.-K. Chua and A. Soni, *Final state interactions in hadronic B decays*, *Phys. Rev. D* **71** (2005) 014030 [hep-ph/0409317].

[286] C.-K. Chua, W.-S. Hou and K.-C. Yang, *Final state rescattering and color suppressed $\overline{B}^0 \to D^{(*)0}h^0$ decays*, *Phys. Rev. D* **65** (2002) 096007 [hep-ph/0112148].

[287] C.W. Bauer, D. Pirjol and I.W. Stewart, *A proof of factorization for $B \to D\pi$*, *Phys. Rev. Lett.* **87** (2001) 201806 [hep-ph/0107002].

[288] Y.-Y. Keum, T. Kurimoto, H.N. Li, C.-D. Lu and A.I. Sanda, *Nonfactorizable contributions to $B \to D^{(*)}M$ decays*, *Phys. Rev. D* **69** (2004) 094018 [hep-ph/0305335].

[289] S. Mantry, D. Pirjol and I.W. Stewart, *Strong phases and factorization for color suppressed decays*, *Phys. Rev. D* **68** (2003) 114009 [hep-ph/0306254].

[290] S.-H. Zhou, Y.-B. Wei, Q. Qin, Y. Li, F.-S. Yu and C.-D. Lu, *Analysis of Two-body Charmed B Meson Decays in Factorization-Assisted Topological-Amplitude Approach*, *Phys. Rev. D* **92** (2015) 094016 [1509.04060].

[291] D. Zeppenfeld, *SU(3) Relations for B Meson Decays*, *Z. Phys. C* **8** (1981) 77.

[292] M.J. Savage and M.B. Wise, *SU(3) Predictions for Nonleptonic B Meson Decays*, *Phys. Rev. D* **39** (1989) 3346. [Erratum: Phys.Rev.D 40, 3127 (1989)].

[293] C.-W. Chiang and E. Senaha, *Update analysis of two-body charmed B meson decays*, *Phys. Rev. D* **75** (2007) 074021 [hep-ph/0702007].

[294] M. Jung and T. Mannel, *General Analysis of U-Spin Breaking in B Decays*, *Phys. Rev. D* **80** (2009) 116002 [0907.0117].

[295] M. Kenzie, M. Martinelli and N. Tuning, *Estimating $r_B^{D\pi}$ as an input to the determination of the CKM angle γ*, *Phys. Rev. D* **94** (2016) 054021 [1606.09129].

[296] N. Kitazawa, K.-S. Masukawa and Y. Sakai, *Extraction of $|V_{cb}|$ from two-body hadronic B decays*, *PTEP* **2019** (2019) 013B02 [1802.05417].

[297] P. Colangelo and R. Ferrandes, *Model independent analysis of a class of $\overline{B}^0_{(s)}$ decay modes*, *Phys. Lett. B* **627** (2005) 77 [hep-ph/0508033].

[298] B. Grinstein and R.F. Lebed, *SU(3) decomposition of two-body B decay amplitudes*, *Phys. Rev. D* **53** (1996) 6344 [hep-ph/9602218].

[299] M. Neubert and A.A. Petrov, *Comments on color suppressed hadronic B decays*, *Phys. Lett. B* **519** (2001) 50 [hep-ph/0108103].

[300] Z.-Z. Xing, *Determining the factorization parameter and strong phase differences in $B \to D^{(*)}\pi$ decays*, *HEPNP* **26** (2002) 100 [hep-ph/0107257].

[301] H.-Y. Cheng, *Implications of recent $\overline{B}^0 \to D^{*0}X^0$ measurements*, *Phys. Rev. D* **65** (2002) 094012 [hep-ph/0108096].

[302] L. Wolfenstein, *Strong phases in the decays $B \to D\pi$*, *Phys. Rev. D* **69** (2004) 016006 [hep-ph/0309166].

[303] C.-W. Chiang and J.L. Rosner, *Final state phases in $B \to D\pi, D^*\pi$, and $D\rho$ decays*, *Phys. Rev. D* **67** (2003) 074013 [hep-ph/0212274].

[304] Z.-Z. Xing, *Final state rescattering and SU(3) symmetry breaking in $B \to DK$ and $B \to DK^*$ decays*, *Eur. Phys. J. C* **28** (2003) 63 [hep-ph/0301024].

[305] H. Yamamoto, *Isospin analysis of two-body B decays and test of factorization*, hep-ph/9403255.

[306] Z.-Z. Xing, *An isospin analysis of CP violation in $B_d \to D\pi, D^*\pi$ and $D\rho$*, *Phys. Lett. B* **364** (1995) 55 [hep-ph/9507310].

[307] C.S. Kim, S. Oh and C. Yu, *Strong phase shifts and color-suppressed tree amplitudes in $B \to DK^{(*)}$ and $B \to D\pi, D\rho$ decays*, *Phys. Lett. B* **621** (2005) 259 [hep-ph/0412418].

[308] P. Colangelo, F. De Fazio and R. Ferrandes, *Two topics for a discussion on the $b\bar{s}$ and $b\bar{q}$ systems*, *Nucl. Phys. B Proc. Suppl.* **163** (2007) 177 [hep-ph/0609072].

[309] K. De Bruyn, R. Fleischer, R. Knegjens, M. Merk, M. Schiller and N. Tuning, *Exploring $B_s \to D_s^{(*)\pm}K^{\mp}$ Decays in the Presence of a Sizable Width Difference $\Delta\Gamma_s$*, *Nucl. Phys. B* **868** (2013) 351 [1208.6463].

[310] PARTICLE DATA GROUP collaboration, *Review of particle physics*, *Phys. Rev. D* **86** (2012) 010001.

[311] W. Yao et al., *Review of particle physics*, *Journal of Physics G: Nuclear and Particle Physics* **33** (2006) .

[312] CLEO collaboration, *Measurement of Absolute Hadronic Branching Fractions of D_s Mesons*, in *33rd International Conference on High Energy Physics*, 7, 2006 [hep-ex/0607079].

[313] M. Jung, *Branching ratio measurements and isospin violation in B-meson decays*, *Phys. Lett. B* **753** (2016) 187 [1510.03423].